



Politecnico di Bari

Repository Istituzionale dei Prodotti della Ricerca del Politecnico di Bari

Innovative design of the Press-Hardening process by means of physical simulation

This is a PhD Thesis

Original Citation:

Innovative design of the Press-Hardening process by means of physical simulation / Palmieri, Maria Emanuela. - ELETTRONICO. - (2022). [10.60576/poliba/iris/palmieri-maria-emanuela_phd2022]

Availability:

This version is available at <http://hdl.handle.net/11589/236660> since: 2022-03-22

Published version

DOI:10.60576/poliba/iris/palmieri-maria-emanuela_phd2022

Publisher: Politecnico di Bari

Terms of use:

(Article begins on next page)



Politecnico
di Bari

Department of Mechanics, Mathematics and Management
MECHANICAL AND MANAGEMENT ENGINEERING

Ph.D. Program

SSD: ING-IND/16–MANUFACTURING
TECHNOLOGY AND SYSTEMS

Final Dissertation

Innovative design of the Press- Hardening process by means of physical simulation

by

Palmieri Maria Emanuela

Supervisor:

Prof. Luigi Tricarico

Coordinator of Ph.D. Program:

Prof. Giuseppe Demelio

Course n°34, 01/11/2018-02/01/2022



Politecnico
di Bari

Department of Mechanics, Mathematics and Management
MECHANICAL AND MANAGEMENT ENGINEERING

Ph.D. Program

SSD: ING-IND/16–MANUFACTURING
TECHNOLOGY AND SYSTEMS

Final Dissertation

Innovative design of the Press- Hardening process by means of physical simulation

by

Palmieri Maria Emanuela

Supervisor:

Prof. Luigi Tricarico

Coordinator of Ph.D. Program:

Prof. Giuseppe Demelio



LIBERATORIA PER L'ARCHIVIAZIONE DELLA TESI DI DOTTORATO

Al Magnifico Rettore
del Politecnico di Bari

Il/la sottoscritto/a Palmieri Maria Emanuela nato/a a Grumo Appula il 11/02/1993

residente a Bitonto in via Corte Zuavo, 3 e-mail mariaemanuela.palmieri@poliba.it
iscritto al 3° anno di Corso di Dottorato di Ricerca in Ingegneria Meccanica e Gestionale ciclo XXXIV

ed essendo stato ammesso a sostenere l'esame finale con la prevista discussione della tesi dal titolo:

Innovative design of the Press-Hardening process by means of physical simulation

DICHIARA

- 1) di essere consapevole che, ai sensi del D.P.R. n. 445 del 28.12.2000, le dichiarazioni mendaci, la falsità negli atti e l'uso di atti falsi sono puniti ai sensi del codice penale e delle Leggi speciali in materia, e che nel caso ricorressero dette ipotesi, decade fin dall'inizio e senza necessità di nessuna formalità dai benefici conseguenti al provvedimento emanato sulla base di tali dichiarazioni;
- 2) di essere iscritto al Corso di Dottorato di ricerca in Ingegneria Meccanica e Gestionale ciclo 34°, corso attivato ai sensi del "Regolamento dei Corsi di Dottorato di ricerca del Politecnico di Bari", emanato con D.R. n.286 del 01.07.2013;
- 3) di essere pienamente a conoscenza delle disposizioni contenute nel predetto Regolamento in merito alla procedura di deposito, pubblicazione e autoarchiviazione della tesi di dottorato nell'Archivio Istituzionale ad accesso aperto alla letteratura scientifica;
- 4) di essere consapevole che attraverso l'autoarchiviazione delle tesi nell'Archivio Istituzionale ad accesso aperto alla letteratura scientifica del Politecnico di Bari (IRIS-POLIBA), l'Ateneo archiverà e renderà consultabile in rete (nel rispetto della Policy di Ateneo di cui al D.R. 642 del 13.11.2015) il testo completo della tesi di dottorato, fatta salva la possibilità di sottoscrizione di apposite licenze per le relative condizioni di utilizzo (di cui al sito <http://www.creativecommons.it/Licenze>), e fatte salve, altresì, le eventuali esigenze di "embargo", legate a strette considerazioni sulla tutelabilità e sfruttamento industriale/commerciale dei contenuti della tesi, da rappresentarsi mediante compilazione e sottoscrizione del modulo in calce (Richiesta di embargo);
- 5) che la tesi da depositare in IRIS-POLIBA, in formato digitale (PDF/A) sarà del tutto identica a quelle **consegnate**/inviata/da inviarsi ai componenti della commissione per l'esame finale e a qualsiasi altra copia depositata presso gli Uffici del Politecnico di Bari in forma cartacea o digitale, ovvero a quella da discutere in sede di esame finale, a quella da depositare, a cura dell'Ateneo, presso le Biblioteche Nazionali Centrali di Roma e Firenze e presso tutti gli Uffici competenti per legge al momento del deposito stesso, e che di conseguenza va esclusa qualsiasi responsabilità del Politecnico di Bari per quanto riguarda eventuali errori, imprecisioni o omissioni nei contenuti della tesi;
- 6) che il contenuto e l'organizzazione della tesi è opera originale realizzata dal sottoscritto e non compromette in alcun modo i diritti di terzi, ivi compresi quelli relativi alla sicurezza dei dati personali; che pertanto il Politecnico di Bari ed i suoi funzionari sono in ogni caso esenti da responsabilità di qualsivoglia natura: civile, amministrativa e penale e saranno dal sottoscritto tenuti indenni da qualsiasi richiesta o rivendicazione da parte di terzi;
- 7) che il contenuto della tesi non infrange in alcun modo il diritto d'Autore né gli obblighi connessi alla salvaguardia di diritti morali od economici di altri autori o di altri aventi diritto, sia per testi, immagini, foto, tabelle, o altre parti di cui la tesi è composta.

Luogo e data Bari,21/03/22

Firma

Il/La sottoscritto, con l'autoarchiviazione della propria tesi di dottorato nell'Archivio Istituzionale ad accesso aperto del Politecnico di Bari (POLIBA-IRIS), pur mantenendo su di essa tutti i diritti d'autore, morali ed economici, ai sensi della normativa vigente (Legge 633/1941 e ss.mm.ii.),

CONCEDE

- al Politecnico di Bari il permesso di trasferire l'opera su qualsiasi supporto e di convertirla in qualsiasi formato al fine di una corretta conservazione nel tempo. Il Politecnico di Bari garantisce che non verrà effettuata alcuna modifica al contenuto e alla struttura dell'opera.
- al Politecnico di Bari la possibilità di riprodurre l'opera in più di una copia per fini di sicurezza, back-up e conservazione.

Luogo e data Bari,21/03/22

Firma



RICHIESTA DI EMBARGO

Sottoscrivere solo nel caso in cui si intenda auto-archiviare la tesi di dottorato nell'Archivio Istituzionale ad accesso aperto alla letteratura scientifica POLIBA-IRIS (<https://iris.poliba.it>) non in modalità "Accesso Aperto", per motivi di segretezza e/o di proprietà dei risultati e/o informazioni sensibili o sussistano motivi di segretezza e/o di proprietà dei risultati e informazioni di Enti esterni o Aziende private che hanno partecipato alla realizzazione della ricerca.

Il/la sottoscritto/a Palmieri Maria Emanuela nato/a Grumo Appula (BA)

Il 11/02/1993 residente a Bitonto alla via Corte Zuavo, 3 indirizzo e-mail mariaemanuela.palmieri@poliba.it

iscritto/a al corso di dottorato di ricerca in Ingegneria Meccanica e Gestionale ciclo 34

Autore della tesi di dottorato dal titolo Innovative design of the Press-Hardening process by means of physical simulation

e ammesso a sostenere l'esame finale:

NON AUTORIZZA

Il Politecnico di Bari a pubblicare nell'Archivio Istituzionale di Ateneo ad accesso aperto il testo completo della tesi depositata per un periodo comunque non superiore a 12 (dodici) mesi decorrenti dalla data di esame finale.

Specificare la motivazione (*apporre una crocetta sulla motivazione*):

Brevetto

(*indicare nel campo libero la data della domanda di deposito*) _____

Segreto industriale, se è stato firmato un accordo di non divulgazione.

(*indicare nel campo libero gli estremi dell'accordo*) _____

Segreto d'ufficio a tutela di progetti _____

Motivi di priorità nella ricerca (previo accordo con terze parti) _____

Motivi editoriali _____

Altro (*specificare*) _____

Saranno comunque consultabili ad accesso aperto i dati bibliografici e l'abstract.

Il sottoscritto dottorando dichiara in virtù di quanto sopra che si rende opportuno procrastinare la pubblicazione della tesi attraverso l'Archivio Istituzionale ad accesso aperto (POLIBA -IRIS) e di impostare la data di embargo, in fase di deposito della tesi di dottorato in formato elettronico (pdf/A) per un periodo *di embargo* non superiore a 12 (dodici) mesi decorrenti dalla data di esame finale.

Il sottoscritto dottorando dichiara di essere a conoscenza che a scadenza della data di embargo su riportata, la tesi verrà pubblicata attraverso l'Archivio Istituzionale ad accesso aperto alla letteratura scientifica del Politecnico di Bari.

Luogo e data Bari, 21/03/22

Firma Dottorando

Firma Relatore



Politecnico
di Bari

Declaration of originality

This is to certify that, to the best of my knowledge, the content of this thesis is my own work. This thesis has not been submitted for any degree or other purposes. I certify that the intellectual content of this thesis is the product of my own work and that all the assistance received in preparing this thesis and sources have been acknowledged.

Contents

Declaration of originality	1
LIST OF FIGURES	4
INTRODUCTION	14
1. STATE OF THE ART	16
1.1. Press-Hardening process	16
1.2 Tailored Technologies	20
2. MATERIALS AND METHOD	26
2.1 Investigated advanced high strength steels (AHSS).....	27
2.2 The Finite Element (FE) Approach	30
2.3 Physical simulation by means of Gleeble 3180 system	33
2.4 Tools for the evaluation of mechanical properties	37
2.5 Method to develop metamodel	39
3. DESIGN OF PHYSICAL SIMULATION TESTS.....	44
3.1 Specimen design for physical simulation tests of laser thermal cycle on EN AW 5754 H32 aluminium alloy	44
3.1.1 Analysis of softening effect induced on ENAW5754 H32 aluminium alloy	48
3.1.2 Analysis of softening effect induced on precipitation hardened ENAW6082 T6 aluminium alloy	54
3.2 Specimen design for mechanical characterization of Advanced High Strength Steel (AHSS) by means of Gleeble system.....	59
3.2.1 Flow curve of the AHSS USIBOR®2000	64
3.2.2 Constitutive model of USIBOR®2000	67
3.2.3 Comparison between USIBOR®2000 AND USIBOR®1500.....	72
3.2.4 Constitutive model of dynamic recovery	73
4. FE ANALYSIS OF PRESS-HARDENING TO OBTAIN TAILORED PROPERTIES	80
4.1 FE model of tailored tool tempering approach	80
4.1.1 Investigation of process parameters on mechanical properties of the part at the end of Press-Hardening process with tailored tool tempering approach.....	85
4.1.2 Design of air gap between cooled and heated tool.....	87
4.1.3 Design of conformal cooling channels (CCC) and evaluation of CCC parameters on mechanical properties of the final part.....	91
4.2 FE model of tailored TemperBox® approach.....	98
4.3 FE thermo-mechanical cycles	102

5. Physical simulation test.....	107
5.1 Analysis of transition zone by means of physical simulation tests	107
5.2 Design of Press-Hardening process by means of physical simulation tests.....	111
5.2.1. Physical simulation tests of Tailored Tool Tempering approach	111
5.2.2. Physical simulation tests of TemperBox [®] approach	117
5.3. Process map.....	122
Conclusion	127
References	131

LIST OF FIGURES

Figure 1.1a: Steps of direct press hardening process.....	17
Figure 1.1b: Steps of indirect press hardening process.....	17
Figure 1.2: Different heating system: (a) roller heat furnace, (b) induction heating, (c) conduction heating.....	18
Figure 1.3: A car structural components stamped by means Press-Hardening process.....	21
Figure 1.4: B-Pillar with tailored properties.....	21
Figure 1.5: Schematic example of tailored welded blank	22
Figure 1.6: Patchwork blank.....	22
Figure 1.7: scheme of tailored blank heating.....	23
Figure 1.8a: Definition of the operating principle of the TemperBox approach.....	24
Figure 1.8b: Scheme of Press-Hardening process by means TemperBox approach.....	24
Figure 1.9a: Line solution for new Multi-layer furnace (MLF) Press-Hardening lines.....	24
Figure 1.9b: Line solution for new Roller heat furnace (RHF) press-Hardening lines.....	25
Figure 1.10: scheme of the tools (die and punch) for a Tailored Tool Tempering approach.....	25
Figure 1.11: Scheme of tailored tool tempering.....	26
Figure 2.1: Scheme of adopted methodology.....	27
Figure 2.2: Increase in the application of high-strength steels for body in white components.....	28
Figure 2.3: Fe-C phase diagram.....	29
Figure 2.4: Comparison of CCT curves of USIBOR®2000 and USIBOR®1500.....	31
Figure 2.5: Scheme of function mode of the refinement algorithm.....	32
Figure 2.6: Radius penetration.....	33
Figure 2.7: Max Element Angle.....	33
Figure 2.8: Gleeble system 3180.....	35
Figure 2.9: scheme of specimen between grips and scheme of thermal gradient recorded by the thermocouples welded on the specimen.....	35
Figure 2.10: Gleeble grips in copper and in stainless steel.....	36
Figure 2.11: Detail of quenching spray hands in Gleeble vacuum chamber.....	36

Figure 2.12: Schematic experimental setup of ISO-QTM specimen for simulation of laser welding thermal cycle.....	37
Figure 2.13: Setup for Gleeble tests.....	37
Figure 2.14: Experimental setup for hardness test.....	38
Figure 2.15a: Experimental equipment for uniaxial tensile test.....	39
Figure 2.15b: speckled specimen.....	39
Figure 2.16: Scheme of a typical ANN architecture.....	41
Figure 2.17: Diagram of the operations performed by a single neuron.....	42
Figure 2.18: Curve of error on training data set and on validation data set.....	43
Figure 3.1a: Thermal cycles investigated for pulsed mode treatment.....	45
Fig. 3.2a Flat dog bone specimen with L0 (length) of 150mm and W0 (width) of 20mm.....	46
Figure 3.2b Comparison between the laser thermal cycle and the Gleeble thermal cycle simulated with the FEM model for P=0.75kW and $\tau=3.5s$ conditions.....	46
Figure 3.3: Geometric parameters of the Gleeble specimen.....	46
Figure 3.4a: Temperature profiles for not shaped (dash-dot line) and shaped specimens (solid lines).....	47
Figure 3.4b: Cooling curves for not shaped (dash-dot line) and shaped specimens (solid lines). The red dashed line represents the cooling curve of laser cycle (P=0.75kW, t=3.5s).....	47
Figure 3.5a: Effects of the geometry of the shaped sample in terms of maximum cooling rate in the control point (response surface).....	47
Figure 3.5b: Effects of the geometry of the shaped sample in terms of maximum cooling rate in the control point (isolines).....	47
Figure 3.6: Microhardness values according to the distance from the specimen centre.....	48
Figure 3.7a: Average grain size in the central area depending on the interaction time of the laser treatment.....	49
Figure 3.7b: Microstructure 500x in Central Zone for 0.5kW,6s (1). Microstructure 500x in Lateral Zone for 0.5kW,6s (2).....	49
Figure 3.8: Comparison of thermal cycles along the longitudinal direction of specimen between FE model and physical simulation test.....	49
Figure 3.9: Hardness curve function of peak temperature.....	50
Figure 3.10: Relationship between the laser interaction time and the maximum softening.....	51

Figure 3.11a: Numerical-experimental comparison of the thermal cycle in the PM treatment realized with a laser power of 1.0kW and a treatment speed of 7.5mm/s.....	52
Figure 3.11b: Numerical-experimental comparison of the thermal cycle in the PM treatment realized with a laser power of 0.5kW and a pulse time of 6s.....	52
Figure 3.12: Temperature distribution in the FE simulation of the CM laser surface treatment, when the laser beam is in the specimen centre (Figure 3.12a), and of PM laser surface treatment at the end of the pulse time (Figure 3.12b).....	53
Figure 3.13: FE thermal profiles along the longitudinal (longAxs) and transverse axes (transAxs) of the specimens, simulated in the laser and physical simulation tests of the treatments P0.75kWt3.5s (Fig. 3.13a) and P1kWv7.5mm/s (Fig. 3.13b).....	53
Figure 3.14: Laser source distribution.....	54
Figure 3.15: Mesh distribution on the treated blank.....	54
Figure 3.16: Laser thermal cycles investigated.....	55
Figure 3.17a: Geometry of tapered specimens.....	56
Figure 3.17b: Geometry of notched specimens.....	56
Figure 3.18a: Hardness values recorded at specimen centre after physical simulation test for different treatment speed and peak temperature.....	56
Figure 3.18b: Hardness values recorded at specimen centre after physical simulation and natural ageing for different treatment speed and peak temperature.....	56
Figure 3.19a: Von Mises equivalent strain after physical simulation for all laser condition investigated and comparison with material base.....	57
Figure 3.19b: Von Mises equivalent strain after natural ageing for all laser condition investigated and comparison with material base.....	57
Figure 3.20a: equivalent Von Mises strain across specimen longitudinal section.....	57
Figure 3.20b: load versus time curve and the equivalent strain versus time curve in correspondence of rupture point.....	57
Figure 3.21: Scheme of cycles for mechanical characterization.....	59
Figure 3.22: Parameters (w and L) considered to optimize geometry of Gleeble specimen for mechanical characterization test.....	59
Figure 3.23a: Metamodel of thermal gradient at the end of keeping phase at 930°C as a function of L and w.....	60
Figure 3.23b: Metamodel of thermal gradient at the end of keeping phase at 700°C as a function of L and w.....	60

Figure 3.23c: Metamodel of cooling rate (from 930°C to 700°C) as a function of L and w.....	60
Figure 3.23d: Effect of the L and w parameters on the cooling rate (isolines).....	60
Figure 3.24: Effect of sheet metal thickness on cooling rate and thermal gradient.....	61
Figure 3.25: Current density distribution at the end of the keeping phase at 930°C.....	61
Figure 3.26: Electric potential and current density profile at the end of the austenitization phase.....	61
Figure 3.27: Temperature distribution on sample at the end of austenitization phase (930 °C).....	62
Figure 3.28: geometry of sample in USIBOR®2000 adopted during hot mechanical characterization test.....	62
Figure 3.29a: Flow stress curves in the strain range 1s-1-0.001s-1 at a deformation temperature of 650°C.....	63
Figure 3.29b: Flow stress curves in the strain range 1s-1-0.001s-1 at a deformation temperature of 700°C.....	63
Figure 3.29c: Flow stress curves in the strain range 1s-1-0.001s-1 at a deformation temperature of 750°C.....	63
Figure 3.29d: Flow stress curves in the strain range 1s-1-0.001s-1 at a deformation temperature of 800°C.....	63
Figure 3.29e: Flow stress curves in the strain range 1s-1-0.001s-1 at a deformation temperature of 850°C.....	64
Figure 3.29f: Flow stress curves in the strain range 1s-1-0.001s-1 at a deformation temperature of 900°C.....	64
Figure 3.30: work hardening, dynamic recovery and dynamic recrystallization that occur during hot deformation.....	64
Figure 3.31: CCT diagram of 37MnB5 boron steel and thermal cycle for deformation temperature of 650 °C and strain rate 0.001s-1.....	65
Figure 3.32: CCT diagram of 37MnB5 boron steel and thermal cycle for deformation temperature of 700 °C and strain rate 0.001s-1.....	65
Figure 3.33a: Relationships at different temperatures between $\ln \dot{\epsilon}$ and $\ln \sigma$	67
Figure 3.33b: Relationships at different temperatures between $\ln \dot{\epsilon}$ and σ	67
Figure 3.34a: Relationship at different temperatures between $\ln \dot{\epsilon}$ and $\ln \sinh(\alpha \sigma_{\max})$	67
Figure 3.34b: Relationship at different strain rate between $\sinh^{-1}(\alpha \sigma_{\max})$ and $1/T$	67
Figure 3.35: Polynomial fitting curves of material coefficients as a function of strain: (a) for α (b) n, (c) Q, and (d) $\ln A$	69

Figure 3.36: Comparison between experimental stress-strain curves (solid line) and predicted stress-strain curves (circular markers) by the Arrhenius constitutive equation at various strain rates: (a) 1s-1, (b) 0.1s-1, and (c) 0.01s-1.....	69
Figure 3.37a: Relationship between material coefficient α and the true strain for both USIBOR®2000 and USIBOR®1500.....	71
Figure 3.37b Relationship between material coefficient n and the true strain for both USIBOR®2000 and USIBOR®1500.....	71
Figure 3.37c: Relationship between material coefficient Q and the true strain for both USIBOR®2000 and USIBOR®1500.....	71
Figure 3.37d: Relationship between material coefficient $\ln A$ and the true strain for both USIBOR®2000 and USIBOR®1500.....	71
Fig. 3.38: Work hardening rate curves of different strain rates at temperatures of (a) 750 °C, (b) 800 °C and (c) 850 °C.....	72
Figure 3.39: Curves of $d\theta/d\sigma - \sigma$ under different deformation conditions at temperatures of (a) 750 °C, (b) 800 °C and (c) 850 °C.....	73
Figure 3.40: Relationship between $\theta\sigma - \sigma^2$ for T=750 °C and $\dot{\epsilon}'=1s-1$	75
Figure 3.41: Relationship between $\ln(\sigma_0) - \ln Z$	75
Figure 3.42: Relationship between σ_{sat} and σ_{max}	76
Figure 3.43: Relationship between $\ln(\sigma_{max})$ and $\ln(Z)$	76
Figure 3.44 (a): Comparison between experimental data and predicted results with DRV model under different deformation temperature at 1s-1.....	76
Figure 3.44(b): Comparison between experimental data and predicted results with DRV model under different deformation temperature at 0.1s-1.....	76
Figure 3.44 (c): Comparison between experimental data and predicted results with DRV model under different deformation temperature at 0.01s-1.....	77
Fig. 4.1: B-Pillar investigated as a case study to model in AutoForm a Press-Hardening process with tool tempering approach.....	78
Fig.4.2. Initial blank and pilots.....	79
Figure 4.3: Tool surfaces geometries: (a) die, (b) punch, (c) blank holder, (d) pad.....	79
Figure 4.4: Air gap between heated and cooled tools.....	80
Figure 4.5: Production line of Press Hardening process.....	80
Figure 4.6: FLCs for USIBOR®1500.....	81
Figure 4.7: FLCs for USIBOR®2000.....	82

Figure 4.8: B-Pillar investigated with required mechanical properties.....	83
Figure 4.9: Dominant variable that influences bainitic microstructure percentage on the final stamped component.....	84
Figure 4.10a: Metamodel of bainite percentage in region III as a function of quenching time and temperature of heated tools.....	84
Figure 4.10b: Contour plot of bainite percentage in region III as a function of quenching time and temperature of heated tools.....	84
Figure 4.11a: Metamodel of bainite percentage in region III as a function of transport time and temperature of heated tools.....	85
Figure 4.11b: Contour plot of bainite percentage in region III as a function of transport time and temperature of heated tools.....	85
Figure 4.12: Parameters relating to the transition zone in correspondence of section A-A of the B-Pillar.....	86
Figure 4.13: Twelve points chosen for the analysis of bainite percentage.....	86
Figure 4.14: Percentage of bainitic microstructure as a function of the abscissa x for three different values of air gap.....	86
Figure 4.15: Width of transition zone for three different values of air gap.....	87
Figure 4.16: Values of the parameter "C" for three different values of air gap.....	87
Figure 4.17a:Metamodel of transition zone I width (A) as a function of heated tool temperature and quenching time.....	87
Figure 4.17b:Metamodel of transition zone I width (A) as a function of heated tool temperature and transport time.....	87
Figure 4.18a:Metamodel of shift parameter (C) as a function of heated tool temperature and quenching time.....	88
Figure 4.18b:Metamodel of shift parameter (C) as a function of heated tool temperature and transport time.....	88
Figure 4.19a: Tool insert of investigated B-Pillar with the geometric parameters p and d considered for the optimization.....	89
Figure 4.19b: position of the tool insert in the investigated component.....	89
Figure 4.20: Pressure dependent HTC.....	90
Figure 4.21: Thermal cycles on punch surface with cooling channels in two configuration.....	91
Figure 4.22: Punch temperature difference between two consecutive hot stamping cycles.....	91

Figure 4.23: Thermal cycles in the steady state condition for the two most extreme condition and the respective temperature distribution on the punch.....	92
Figure 4.24: Martensite history during quenching phase (d = 21 mm, p = 24 mm).....	92
Figure 4.25: Metamodel related to the quenching time that guarantees the complete martensitic transformation as p and d vary.....	92
Figure 4.26: Geometric model of the conformal cooling channels, the die, the punch and the blank.....	93
Figure 4.27: Thermal cycles recorded during 20 hot stamping cycles at 30 mm from the punch and die surfaces and on the punch and die surfaces.....	93
Figure 4.28a: Die temperature distribution in the steady condition at the time corresponding to the peak temperature.....	94
Figure 4.28b: Die temperature distribution in the steady condition at the time corresponding to the end of the hot stamping cycle.....	94
Figure 4.28c: Temperature distribution in the cross sections of the die at the end of the stamping cycle in the steady state condition.....	94
Figure 4.29: Process plan for FE simulation of Press Hardening process with Temper Box approach.....	95
Figure 4.30: Thermal history on the blank during Press Hardening with Temper Box approach.....	95
Figure 4.31: FE thermal cycle recorded in soft and hard region.....	96
Figure 4.32a: Phase fractions before forming.....	96
Figure 4.32b: Phase fractions at the end of the process.....	96
Fig.4.33a: Hardness FE results as a function of $t_{\text{temperbox}}$ for a constant $T_{\text{temperbox}}$	97
Fig.4.33b: Hardness FE results as a function of $T_{\text{temperbox}}$ for a constant $t_{\text{temperbox}}$	97
Fig. 4.34: thermal cycles in ductile region III for two different condition (i) $T_{\text{temperbox}}=600$ °C - $t_{\text{temperbox}}=30$ s (ii) $T_{\text{temperbox}}=600$ °C - $t_{\text{temperbox}}=210$ s superimposed on CCT diagram.....	98
Fig.4.35a: thermal cycles of the hard part (region II) as the transport time between the first and second furnace ($t_{\text{transport1}}$) vary.....	98
Fig.4.35b: thermal cycles of the ductile part (region III) as the transport time between the first and second furnace ($t_{\text{transport1}}$) vary.....	98
Figure 4.36: Five points considered near the transition zone for extracting thermo-mechanical cycles.....	99
Figure 4.37a: thermal cycle of five points considered for transition zone analysis.....	100
Figure 4.37b: equivalent plastic strain of five points considered for transition zone analysis.....	100

Figure 4.38: Node chosen to follow thermal and mechanical history of the component during the process.....	101
Figure 4.39a: Example of thermo-mechanical cycle extract from FE model for USIBOR®2000 with quenching time of 50s and tool temperature of 500°C.....	101
Figure 4.39b: Thermal cycle for different condition extract from FE-model in USIBOR®2000....	101
Figure 4.40a: Thermal cycles in the ductile region III as the parameter $t_{\text{temperbox}}$ changes for $T_{\text{temperbox}}$ equal to 600 °C.....	102
Figure 4.40b: Thermal cycles in the resistant region II as the parameter $t_{\text{temperbox}}$ changes for $T_{\text{temperbox}}$ equal to 600 °C.....	102
Figure 4.41: Thermal cycles in the resistant region II as the parameter $t_{\text{temperbox}}$ changes for $T_{\text{temperbox}}$ equal to 600 °C and $t_{\text{transport1}}$ equal to 22 s.....	102
Figure 5.1: Position of thermocouples welded on the specimen for Gleeble test.....	104
Figure 5.2: Thermal cycles recorded by TC2, TC3 and TC4 thermocouples during the physical simulation test related to point 1.....	104
Figure 5.3: Temperature gradient along the longitudinal axis of specimen.....	104
Figure 5.4: Hardness trend as a function of bainite percentage.....	105
Figure 5.5 Microstructure (500x) of the USIBOR®1500 steel obtained in the central section of specimen after physical simulation tests of thermo-mechanical cycles of point 1 (a), point 2 (b) and point 5 (c).....	106
Figure 5.6 Stress-strain curves representative of mechanical properties in three different point near transition zone.....	106
Figure 5.7: Thermal cycles recorded by the thermocouples during the Gleeble tests on USIBOR®2000 specimen in the condition of temperature of heated tools equal to 430 °C and quenching time 20 s.....	108
Figure 5.8: Hardness values along longitudinal direction of USIBOR®2000 specimen for the condition of temperature of heated tools equal to 430 °C and quenching time equal to 20 s.....	108
Figure 5.9: (a)Hardness values for different quenching time at temperature of 430 °C; (b) Hardness values for different quenching time at temperature of 465 °C; (c) Hardness values for different quenching time at temperature of 500 °C.....	109
Figure 5.10a: Microstructure of USIBOR®2000 steel in the supply state (1000x).....	110
Figure 5.10b: Microstructure of the USIBOR®2000 steel obtained in the specimen central point with the T500tq20 condition (1000x).....	110
Figure 5.10c: Microstructure of the USIBOR®2000 steel obtained in the specimen central point with the T500tq250 condition (1000x).....	110

Figure 5.11: Bainite hardness trend (100%) as a function of temperature of heated tools.....	110
Figure 5.12: speckled notched specimen adopted for tensile tests.....	111
Figure 5.13: (a) Stress-strain curves for the two UHSS in the condition of heated tools temperature of 430 °C; (b) Stress-strain curves for the two UHSS in the condition of heated tools temperature of 500 °C.....	112
Figure 5.14: Hardness trend along the longitudinal direction of the specimen in USIBOR®2000 after physical simulation of Tailored Heated Blank approach.....	112
Figure 5.15a: Hardness values for different values of $t_{\text{temperbox}}$ related to the thermal cycles in ductile zone of investigated component.....	113
Figure 5.15b: Hardness values for different values of $t_{\text{temperbox}}$ related to the thermal cycles in hard zone of investigated component.....	113
Figure 5.16a: Microstructure observed with the optical microscope (100X) after the TemperBox® thermal cycle in the resistant part for $t_{\text{temperbox}}$ of 250 s.....	114
Figure 5.16b: Microstructure observed with the optical microscope (100X) after the TemperBox® thermal cycle in the resistant part for $t_{\text{temperbox}}$ of 1000 s.....	114
Figure 5.17: Proposed tailored hot stamping process.....	115
Figure 5.18: Thermal cycles of ductile and hard region in the proposed tailored Press-Hardening process.....	115
Figure 5.19: thermal cycles imposed on Gleeble system to investigate the proposed tailored approach.....	116
Figure 5.20: Hardness value for different holding time values after physical simulation test of tailored Press-Hardening process proposed.....	116
Figure 5.21a: Hardness comparison between temper box and new proposed approach.....	116
Figure 5.21b: Comparison between the thermal cycle of the temper box approach and that of the new proposed approach.....	117
Figure 5.22: Diagram of neural network.....	118
Figure 5.23a: Process window to predict hardness of low strength region as a function of heated tool temperature and quenching time.....	119
Figure 5.23b: Process window to predict tensile strength of low strength region as a function of heated tool temperature and quenching time.....	119
Figure 5.23c: Process window to predict rupture deformability of low strength region as a function of heated tool temperature and quenching time.....	119
Figure 5.24a: Regression plot that shows the neural network predictions (output) with respect to responses (target).....	120

Figure 5.24b: Error histogram for additional verification of neural network performance.....120

INTRODUCTION

Press-Hardening of ultra-high strength steel is an advanced technology that integrates traditional hot stamping process and quenching heat treatment. Currently, this process represents the best solution to increase the strength-mass ratio of components, exhibiting both high mechanical resistance and lightweight. Press-Hardening is widely adopted in automotive industry to manufacture structural component such as body pillars, roof rails, rockers, bumpers and door intrusion beams. In the last years, automotive industry showed an increasing interest in the production of components that guarantee i) a high level of active and passive protection of the vehicle and ii) reduction of emissions. Hot stamped-die quenched structural components provide excellent intrusion resistance, thanks to the martensitic microstructure of the component at the end of the process. However, these components exhibit limited ductility, which may limit the impact performance. To improve impact performance, hot stamped component with *tailored properties* and ductile regions can be designed. For this reason, experts put the attention on new technologies to manufacture tailored components with innovative steels.

In tailored Press-Hardening process, several *process parameters* are involved, as various phases with different mechanical properties coexist in the hot stamped part. Process parameters affect the final microstructure and mechanical properties of the component, as thermal, mechanical and metallurgical phenomena occur during the Press-Hardening. As a result, a preliminary design of the process is required to obtain specific mechanical properties of the component.

Numerical models represent a valid solution to design the process. Several researchers developed Finite Element (FE) models that allow i) to estimate mechanical properties of the component at the end of the process; ii) to define the most important process parameters; iii) to optimize the process. Nowadays, different commercial FE software are available (e.g., AutoForm, Pamp-Stamp, Dynaform). Modelling Press-Hardening process requires coupled thermo-mechanical calculations, capturing how the microstructure and material properties change with temperature, time and deformation; moreover, thermal contact problems occur between the blank and die. Due to the complexity of aforementioned problems, FE models usually adopt theoretical assumptions. For this reason, FE predictions require experimental validations, which are often performed with post-forming tests at the *industrial scale*. Such procedure involves high cost and material waste.

In this dissertation, experimental *physical simulation* is combined with numerical simulation to study the effect of Press-Hardening process parameters; different materials and tailored technologies are investigated at the *laboratory scale*, simulating the manufacturing process of a *B-Pillar* automotive component with tailored properties. The investigated materials are two advanced high strength steels, namely USIBOR®1500 and USIBOR®2000.

First, FE models have been developed in AutoForm to simulate the Press-Hardening. Two tailored technologies are presented to obtain a component with ductile and resistant regions: i) the *Tailored Tool Tempering* approach, where ductility is given by a predominantly bainitic microstructure; ii) the *Tailored Blank Heating*, where ductility is given by a predominantly ferritic-pearlitic mixed microstructure.

Second, numerical thermo-mechanical cycles have been experimentally reproduced using the Gleeble 3180 thermo-mechanical physical simulator. After physical simulation of Press-Hardening,

tensile and hardness tests have been carried out on treated samples, with the aim of measuring their mechanical properties. In general, physical simulation has been used to:

- validation of numerical predictions;
- characterize the rheological behaviour of a new advanced high strength steel, the USIBOR®2000 (implementing its flow curves in FE models);
- design innovative Press-Hardening processes to manufacture component with tailored properties;
- compare the two USIBOR steels, discussing their properties in the light of industrial application in tailored Press-Hardening processes.

Third, a case study is presented for the application of artificial intelligence to the design of Press-Hardening process. Specifically, an *Artificial Neural Network* (ANN) model has been developed to predict the mechanical properties of the ductile part of a B-Pillar component, for different process parameters.

The structure of this dissertation is described in the following. Chapter 1 reviews the state of the art of existing Press-Hardening processes and tailored technologies. Chapter 2 collects all information regarding materials (USIBOR steels) and a general description of methods (FE model, physical simulator, tensile and hardness tester, metamodel for artificial intelligence). Chapter 3 discusses the design of samples geometry for physical simulation tests. Chapter 4 describes in detail FE models that have been adopted for Press-Hardening simulations and contains numerical results. Chapter 5 contains the experimental results of physical simulation tests and describes the development of the ANN model.

1. STATE OF THE ART

1.1. Press-Hardening process

In the automotive sector, the demand for new processes to produce high-strength parts with adequate costs and productivity is growing together with weight reduction and safety improvements. The high-strength advanced boron steel responds to these requests, in fact the elevated strength of hot formed parts allows for the use of thinner gauge sheet metal, which results in vehicle weight reduction while maintaining structural integrity. However, to increase the formability of this alloy, the Press Hardening process (also known as hot stamping) is carried out. There are two general classifications of hot forming: direct and indirect. In the direct hot stamping process heating the blank in a furnace and subsequent forming and quenching in closed tool are involved. Figure 1.1a shows the steps of the direct Press Hardening process.

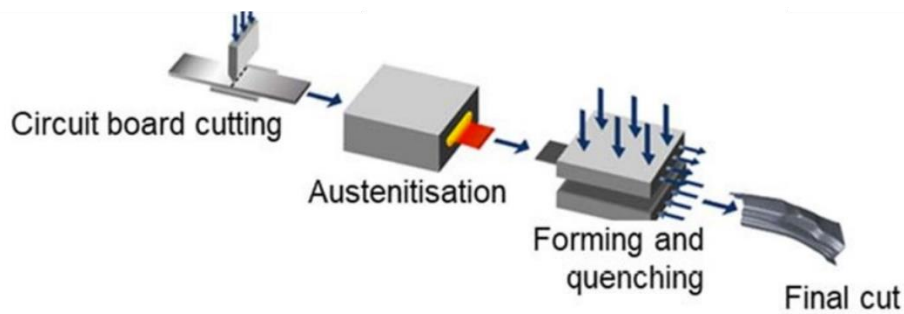


Fig.1.1a: Steps of direct press hardening process

In the indirect hot stamping process, on the other hand, a nearly complete cold pre-formed part is subjected only to a quenching and calibration operation in the press after austenitization (Figure 1.1b).

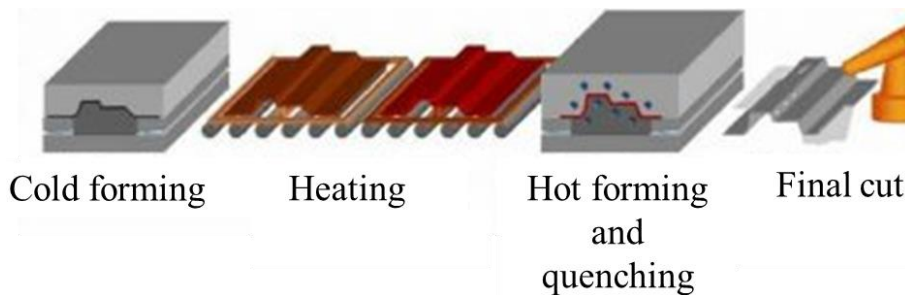


Fig.1.1b: Step of indirect press hardening process

In this thesis the focus will be only on the direct Press Hardening process, therefore phases of direct hot stamping process are analysed in detail below.

The first phase of cutting allows to obtain the blank used for the subsequent forming operations. The shape of the initial blank is defined on the basis of the shape of the stamped part and of the draw-in during the forming phase.

Then, there is the heating phase of the blank in the furnace. The heating step aims to bring the blank to a temperature higher than the austenitizing one (A_{c3}) to ensure a complete transition to the austenitic microstructure into martensitic one during the drawing and quenching phases. The most influential parameters in this heating phase are the temperature and the holding time in the oven. Also

the thickness of the sheet is important; in fact, the greater the thickness the higher the temperature to be reached and the longer the heating time in the furnace. Thickness also affects how homogeneous the deformation is, which in turn also affects M_s , i.e. ease of martensitic transformation. Lechler et al. [1] showed that the heating phase has a greater influence on the process time and on the final part properties. Although it is necessary to reduce the heating time to reduce the cycle times of the process, a homogeneous blank temperature is required to obtain a uniform microstructure at the end of the process. The blank can be heated using different thermal phenomena: radiation in a furnace, induction, and conduction. The different heating techniques are shown in Figure 1.2.

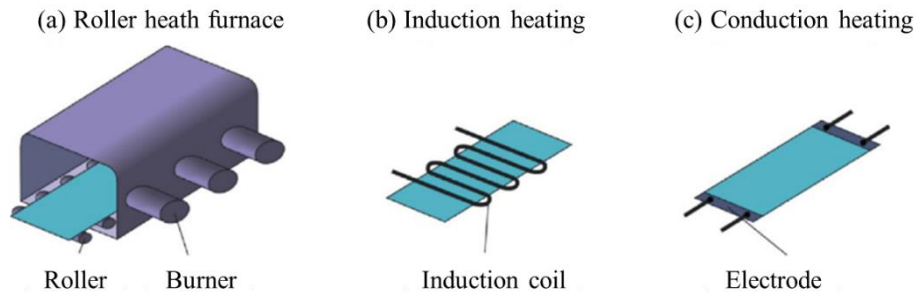


Fig.1.2: Different heating system: (a) roller heat furnace, (b) induction heating, (c) conduction heating [2]

The method of heating by means of roller heat furnace is the most used; these types of furnace reach lengths of 30 – 40 m [2] but the size and connected load of these furnaces depend on the material to be heated. The heating time with this approach is longer, therefore a reduction in furnace residence time can be achieved by the other two heating methods. Compared to roller heat furnaces, the induction heating presents higher efficiency because of the higher losses of the roller heat furnace by exhaust gases and the rollers. The efficiency of this heating system is influenced by the distance between inductor and sheet and the geometry of the inductor. The last heating system is the conduction heating, that is based on Joule's law, therefore the heat generated in an electric circuit is proportional to the electric circuit power. Also the conduction heating method presents a very high efficiency. However, this heating system leads to an inhomogeneous temperature especially for blanks with complex geometry [3].

After the heating phase, there is the transport phase of the blank from the furnace to the press. The blank must be transferred as quickly as possible in order to avoid blank cooling before forming, otherwise undesired metallurgical structures occur.

Then there is the forming phase, during which the blank is positioned on the blank holder, the die blocks the metal sheet on the blank holder and finally the blank-die-blank holder system approaches the punch for the forming phase. This phase is completed when the die is at a certain distance (gap) from the punch. This gap is necessary to avoid immediate cooling of the blank, as the forming process must be completed before the martensitic transformation begins. Furthermore, the gap affects the draw-in of the blank in the die. In particular, for large gap values, a risk of wrinkling occurs; on the contrary, a reduction of the gap reduces the possibility of wrinkling but it can lead to an increase in thinning in the most critical areas of the stamped part. Another parameter that significantly affects the process is the drawing speed. Typically the drawing speed must be high in order to achieve forming at higher temperatures, where the material is less resistant and more deformable. Furthermore, an increase in the forming speed allows a homogeneous temperature distribution on the part.

After forming phase, the part is quenched in the tools until the complete martensitic transformation occurs. The transformation from austenite to martensite causes a change in volume, which affects the distribution of stresses during quenching. The parameters that become important in this phase are: the quenching time (the time for a process step without tool movement and sheet deformation, but with heat exchange between tool and blank), the quenching force (the press force acting during quenching phase), which affects the contact pressure and consequently the heat transfer coefficient (HTC) at the interface blank-tools (i.e., the thermal conductivity at the blank-die interface), and the temperature of the tools.

For the steel most used for this type of process (high strength boron steel 22MnB5) the complete martensitic transformation is obtained for cooling rates higher than about 27 K/s [2, 4-5]. In addition, the temperature of the tools must keep low (approximately 200 °C) to ensure martensitic transformation. To attain this, a production of tools with cooling system is required. In general, the cooling system consist of drilled channels in which water circulates [4,6]. An efficient design of the cooling system is desired in order to reduce the cooling time of the process and allow a uniform distribution of cooling. In fact, reducing the cooling time by means of an increase of the cooling rate, the total cycle time is reduced [7]. Moreover, the need to have a uniformly cooled part arises from the need to avoid dimensional discrepancies [8-9]. To meet these requirements, most of scientific works are mainly focused on optimizing cooling channel diameter, the distance between channels and the distance between tool surface and channel. Shan et al. [10] showed that the depth from the die surface to the cooling channels has the biggest impact on the cooling rate and uniformity of the workpiece. Moreover, they discovered that augmenting the cooling channel diameter near the inlet improved the water flow uniformity. Lin et al. [11] showed that the distance between the cooling channels and the distance between the cooling channel and the tools surface have significant influence on the quenching effect; in particular better quenching effect can be achieved with the shorter distance from the tool surface and with smaller distance between cooling channels. Furthermore, thermal expansion proved to be the main reason for deformation of the hot forming tools, which causes the distortion of the cooling channels, and the stress concentration at corner of the cooling channels. Recently, Hung et al. [12] stated that the blank thickness, the distance from the tool surface to the cooling channel edge, and distance between cooling channel edges are the parameters that have marked effects on cooling performance. These studies mentioned so far are mainly focused on straight drilled channels, however to improve cooling efficiency, conformal cooling channels (CCC) are increasingly adopting thanks to opportunities offered by additive manufacturing (AM) technologies in combination with the development of powders with high thermal conductivity. Cortina et al. [13] investigated the design and manufacturing of conformal cooling ducts via additive manufacturing and they compared the conformal cooling conduits with the traditional straight channels. With regard to thermal results, a more homogeneous temperature distribution within the tool and the stamped part is attained with conformal cooling channels, leading to the enhancement of the dimensional accuracy and features of the produced parts. Moreover, they stated that better temperature distribution also leads to the lowering of the process cycle times in hot stamping and the subsequent improvement of the efficiency of the process and reduction of the costs. Muvunzi et al. [14] proposed a method for designing hot stamping tools with conformal cooling channels. The suggested method involves the evaluation of the part to decide whether it is suitable for AM application, the definition of conformal cooling parameters and the design of alternative layouts. Vallas et al. [15] explored the increase of

cooling capacity of tools by using the new high thermal conductivity tool steel powders FASTCOOL-50 and HTCS-230.

From this analysis of the previous works, it is clear that other important parameters to be considered in the quenching phase are the geometric parameters of the cooling channels in the tools, as well as the tools material.

Finally, after quenching phase, the part is extracted from the tools and it is cooled in air until it reaches room temperature. One of the problems that could arise in this phase is the springback phenomenon. For this reason it is advisable to check the final temperature of the formed part, since if the component is extracted at temperature higher than the ambient one, the springback will be greater because the component will continue to cool free from the constraints represented by the tools.

The cooled part can be subjected to subsequent mechanical processes such as trimming, to obtain the final component.

1.2 Tailored Technologies

The hot stamping process is currently used to manufacture structural components such as bumper beams, door intrusion beams, A-pillar, B-pillar, roof and side rails (Figure 1.3).

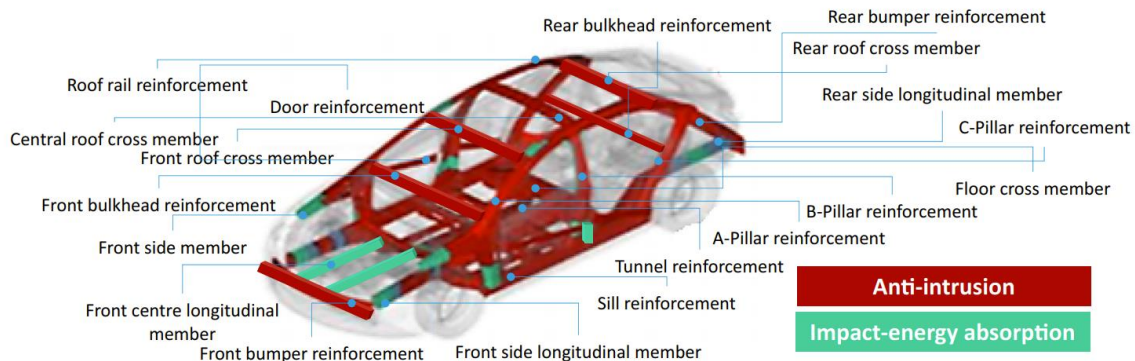


Fig.1.3: A car structural components stamped by means Press-Hardening process [16]

As can be seen in Figure 1.3, there are some components that must have anti-intrusion properties and others that must have the ability to absorb energy during impacts. Current industrial and academic research is studying the possibility of manufacturing components with tailored properties, therefore components that perform both functions. An example of a component that requires the presence of ductile areas and areas with greater mechanical resistance is the B-Pillar (Figure 1.4).

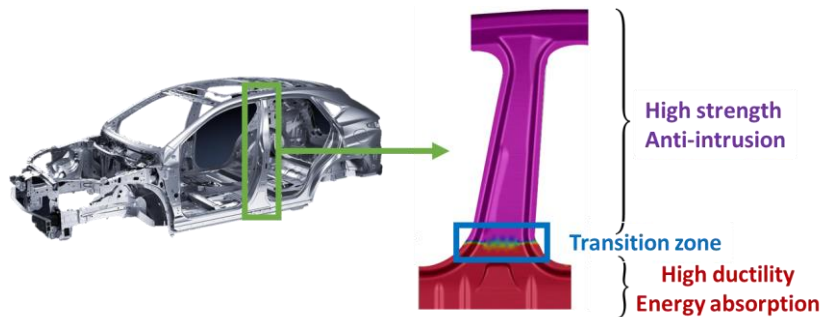


Fig. 1.4: B-Pillar with tailored properties

There are two categories of tailored technologies: tailored blank technologies in which different sheet steels or different sheet thickness are exploited to produce different mechanical (or structural) properties; and tailored process technologies in which different heat treatment within the hot-stamping process are exploited to produce different microstructures and mechanical properties from a single sheet steel.

In this section, an overview of different existing technologies for manufacturing components with tailored properties will be presented.

A. TAILORED-WELDED BLANK

In the tailor-welded blank two or more blank of different thickness or chemistry are laser welded and then subsequently hot stamped. Figure 1.5 shows as an example schematic representation of tailored welded blank.

In literature, Múnera et al. [17] investigated the potential of weight reduction of safety relevant parts produced by hot stamping of tailored welded blanks. Weight savings of 4.1–5.4 kg were achieved

welding the steel-grade USIBOR 1500P with the DUCTIBOR 500P, which is characterized by a high ductility after quenching. The tailor-welded blank approach may be the oldest of the tailored technologies and comprises the added financial cost of manufacturing the tailored blank. Moreover, this technology can lead to fracture in the correspondence of the thinner sheet. However, it is a relatively simple technique, can be applied to a standard hot-stamping line, does not increase cycle time and guarantees reproducibility across a range of part geometries.

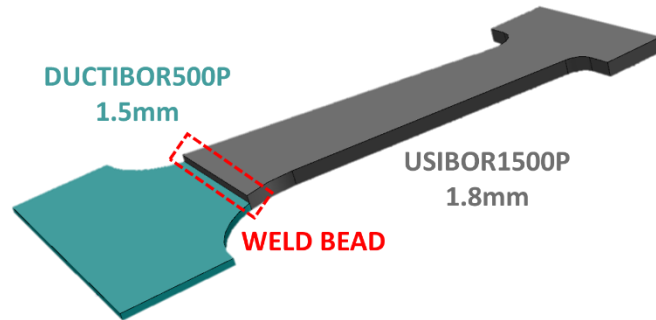


Fig.1.5: Schematic example of tailored welded blank

Before welding process, usually the coating of the weld zone is removed. Important aspects to be considered in the process design of tailor welded blanks is the position of the weld seam and its limited formability during hot stamping.

B. TAILOR-ROLLED BLANK

In the tailor-rolled blank, different regions of the blank are locally rolled to different gauges before hot stamping. This permits to have thicker regions in the part requiring maximum crashworthiness and thinner regions in the part requiring lower stiffness for crashworthiness via impact energy absorption.

The advantage of this technology is related to the continuous transition of sheet thickness, in fact a better load distribution is achieved in the transition zones. However, the tool design is quite complex to ensure, during quenching phase, contact of the blank to the tool surface in the transition zone.

C. PATCHWORK BLANK

In the patchwork blank local patch reinforcements are layered on top and joined (usually by spot welding or laser welding) to the blank before stamping (Figure 1.6). Similar to the tailor-rolled blank, the patchwork blank permits to obtain thicker regions in correspondence of the part with higher local strength. Moreover, reinforcements may be of the same sheet steel as the base blank or may be of a higher strength sheet steel for a twofold local strength increase.

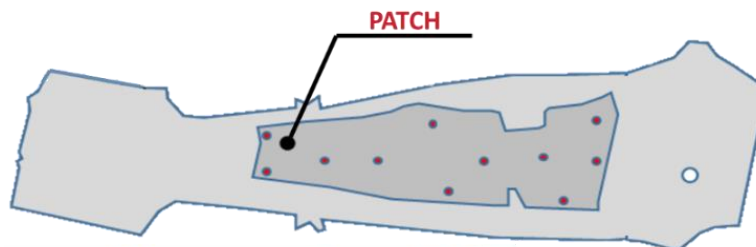


Fig.1.6: Patchwork blank

The patchwork blank presents excellent opportunities for optimised crashworthiness, moreover this technology is more economical than tailor-rolled blanks. However, different local blank gauges can complicate blank heating and die quenching, as demonstrated by Lei et al. [18].

D. TAILORED BLANK HEATING or PARTITIONED HEATING

Tailored blank heating involves that some blank regions are heated to above the Ac3 temperature and others are maintained at the temperature below the Ac3 (Figure 1.7). In this way, during die quenching, the completely austenitic region of the blank hardens to martensite, while the partially austenised region of the blank forms a ferritic–martensitic microstructure (soft-zone) [20].

To achieve this, the only industrially practised method is the shielding with ceramic or stainless steels masks. However, recently research try to find alternative methods such as furnaces with multiple chambers in parallel (separated by an insulating wall). To implement this new technology on an industrial scale would require costs.

Another solution to obtain the tailored blank heating is the use of by-pass resistance heating [21]. By using localised copper by-passes, some regions of the blank are not electrified, and thus not heated.

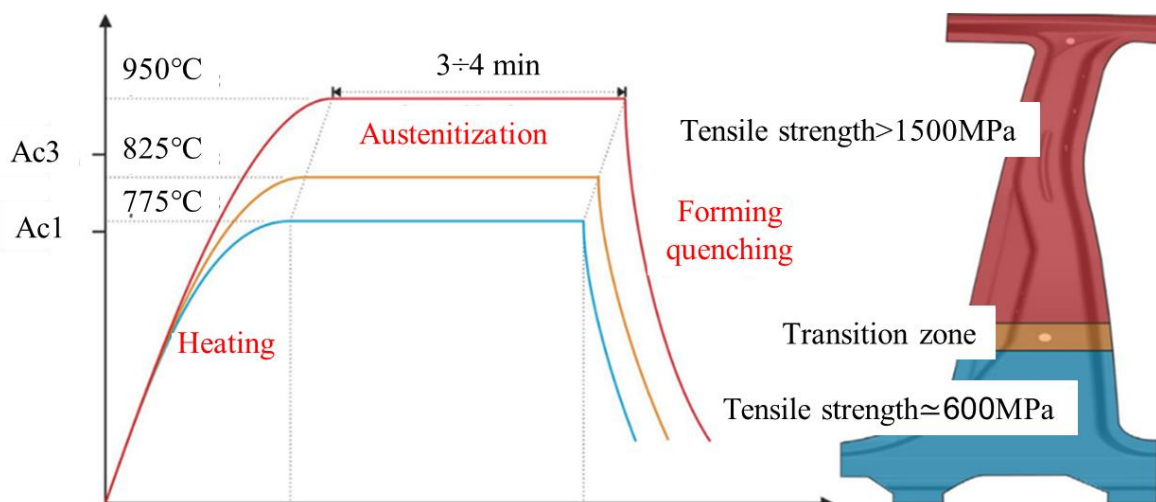


Fig.1.7: scheme of tailored blank heating [19]

The method of tailored heating is not very popular due to the difficulty to precisely control temperatures of the blank. Moreover, when forming at a temperature below the Ac3, formability of the blank is compromised.

A new generation technology can be included in the tailored blank heating category, named TemperBox®.

TemperBox® is a new patented solution by AP&T for tailored press hardening of structural parts for passenger cars. The process involves a controlled heat treatment, which takes place in a second special furnace known as TemperBox®. After being heated up to the complete austenitization temperature in a conventional austenitization furnace, the blank is moved to the temper box station, where selected sections are cooled down by convection while the rest of the part is kept hot. The blank is subsequently formed and quenched into the press to produce the finished part. Finally, a part with properties customized to the required performance is obtained. Figures 1.8a and 1.6b summarize this process.

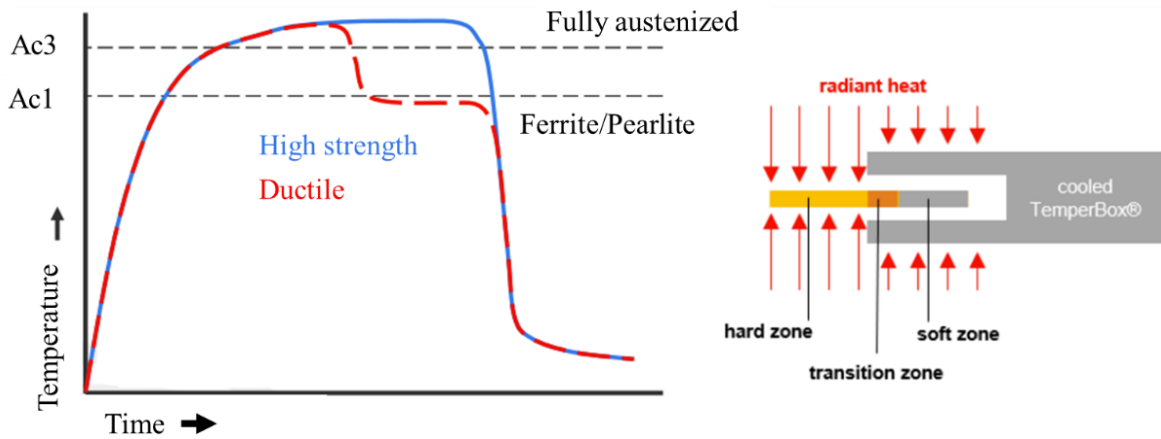


Fig. 1.8a: Definition of the operating principle of the TemperBox approach [22]

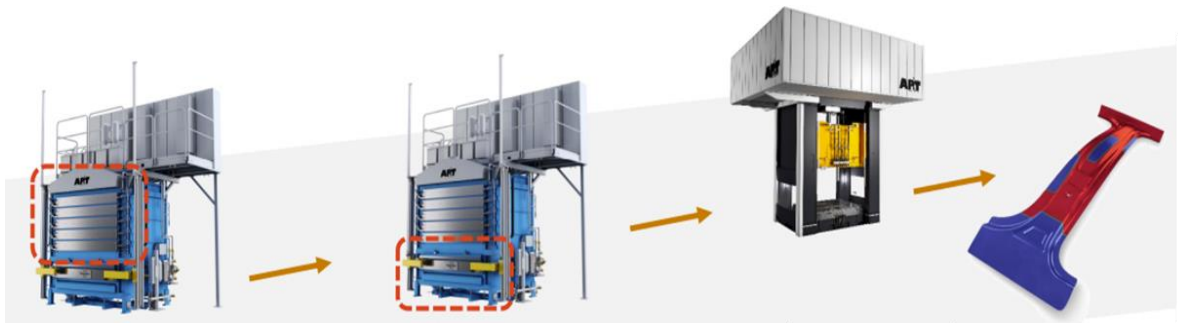


Fig.1.8b: Scheme of Press-Hardening process by means TemperBox approach [22]

This new technology it is very competitive with the other existing tailored technologies, in fact it does not imply an increase in cycle times, moreover it assure high precision of transition areas, no thermal distortion and a high design flexibility.

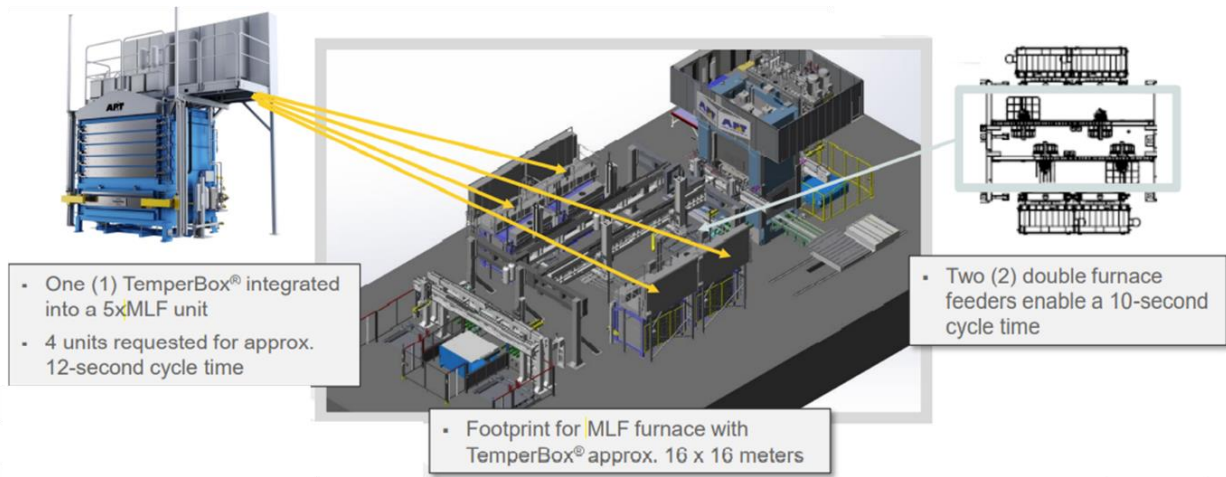


Fig.1.9a: Line solution for new Multi-layer furnace (MLF) Press-Hardening lines [22]

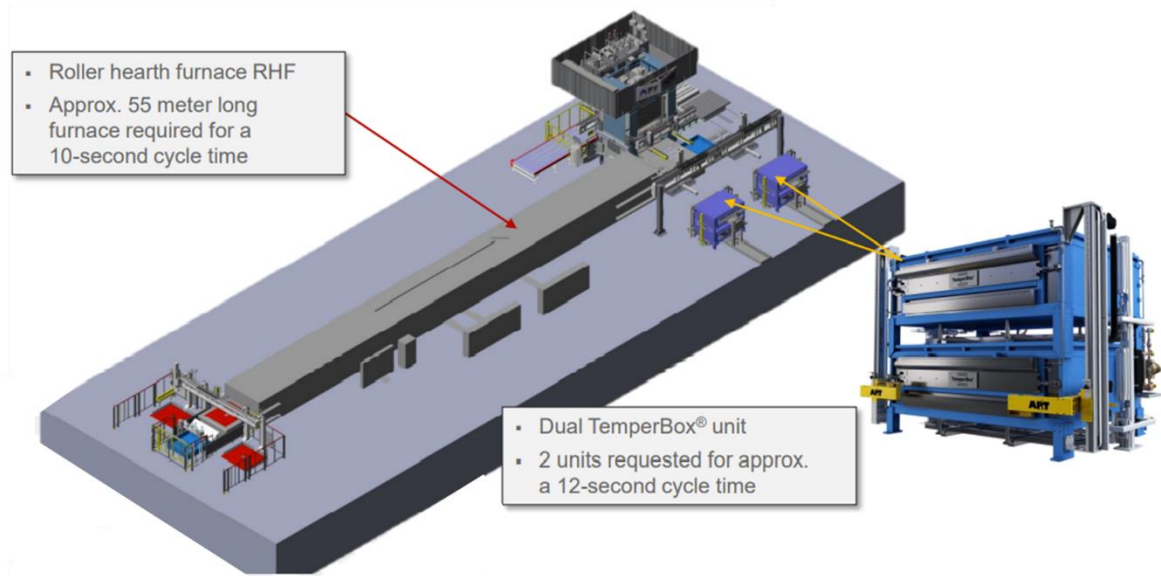


Fig.1.9b: Line solution for new Roller heat furnace (RHF) press-Hardening lines [22]

This new method offers clear production-related advantages also due to the easy integration in new and existing press hardening lines. In fact, Figures 1.9a and 1.9b show some solutions in the Press-Hardening line in which the TemperBox® is introduced together with a multi-layer furnace and a roller heat furnace, respectively.

E. TAILORED TOOL TEMPERING

With the Tailored Tool Tempering approach, the part is cooled differentially, with local regions of the part exposed to different cooling rates (by heating and cooling elements integrated within the forming tools). Generally, cartridge heaters in one half tool are insert to obtain a bainite microstructure on the part and cooling channels are placed in the other half to obtain a martensite microstructure (Figure 1.10).

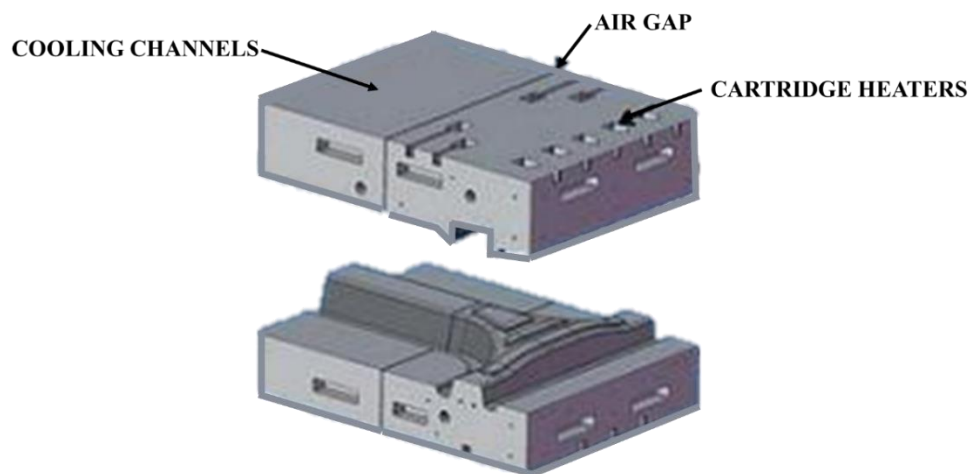


Fig.1.10: scheme of the tools (die and punch) for a Tailored Tool Tempering approach

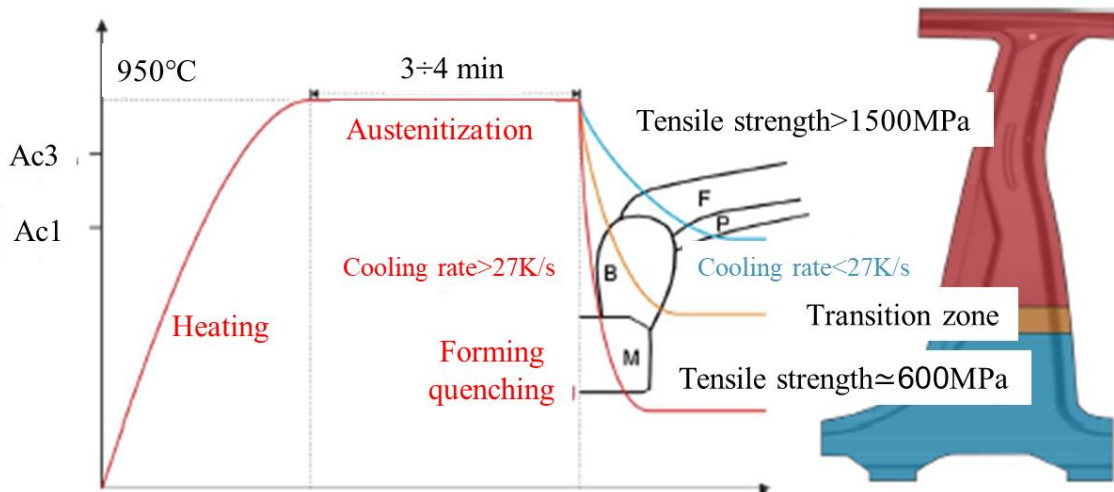


Fig.1.11: Scheme of tailored tool tempering

With this approach, as the temperature of the die is increased, the heat transfer, and thus the cooling rate, is decreased leading to a ductile microstructure (Figure 1.11).

Recently research activities focus on this technology [23-25] because, unlike other technologies, there are no special requirements of blank heating, enabling conventional furnace heating to be used. Moreover, there is no additional process step in comparison to the standard hot-stamping process; the mechanical properties can be tailored over a wide range; it is highly flexibility concerning the size, shape and position of the soft-zone; and in the end formability is not compromised.

2. MATERIALS AND METHOD

The objective of this thesis is to study and reliably design, by means of numerical and physical simulation, a Press-Hardening process to manufacture components with customized properties. As a case study the automotive B-Pillar was considered. This component is composed of some ductile zone together with some other zones of higher strength/hardness.

Two tailored technologies were explored: Tailored Tool Tempering and Tailored Heated Blank. The first technology aims at obtaining ductile regions by differentiating tools temperature, instead, in the second approach ductile regions are obtained by means of different blank temperature.

Materials studied were two advanced high strength steels (AHSS): USIBOR1500 and the recently developed USIBOR2000.

For this study, the method described in Figure 2.1 was adopted.

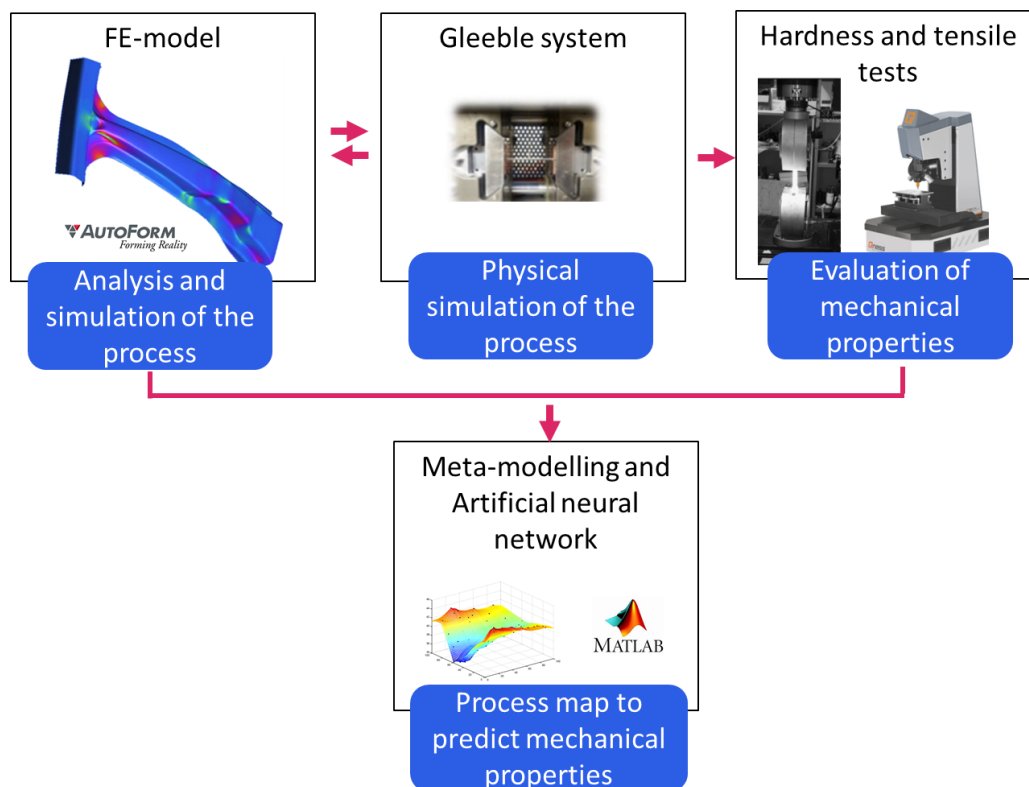


Fig.2.1: Scheme of adopted methodology

First, Finite Element (FE) numerical models of tailored Press-Hardening processes were developed in AutoForm commercial thermo-mechanical metallurgical software. FE analysis was adopted i) to evaluate the most influential process parameters on final mechanical properties (hardness and microstructure) and quality (e.g. splits, thinning, wrinkles) of the final stamped component and ii) to track the thermal and mechanical cycles during the process on specified region of the component.

For a case study, the results of FE analysis were post-processed to obtain metamodels by means of kriging technique, useful to predict the response of unobserved points i.e., those whose response has not been obtained by the simulations. The metamodels allowed to obtain process window that map the relation between input process parameters and final mechanical properties.

Second, FE thermo-mechanical cycles, extracted in specific regions of the component, were reproduced in laboratory on steel samples, thanks to the Gleeble physical simulator. The treated specimens were subsequent subjected to hardness and tensile tests, for experimentally evaluating mechanical properties.

For a case study, experimental results were post-processed to train an Artificial Neural Network (ANN) with the aim to develop the process window.

The presented method allowed i) to study the influence of process parameters on mechanical properties of the component; ii) to compare the two AHSS in the application of tailored Press-Hardening processes; iii) validate a new procedure that can replaces the more expensive and time-consuming classic post-forming tests.

In the following subsections, details about the two investigated AHSS and the tools adopted for this study are presented.

2.1 Investigated advanced high strength steels (AHSS)

The requirements for the design of automotive components include crashworthiness and a high strength/weight ratio to save fuel. To meet this demand, several advanced-high-strength steels (AHSS) are developed. In fact comparing to the other lightweight materials, AHSS has lower cost and high ultimate tensile strength. Thanks to its superior mechanical properties, these steels experiences a very rapid growth in anti-intrusion applications of automotive structures (bumpers, doors, bodies-in-white). Figure 2.2 compares, as an example, the body in white of the 2003 Volvo XC90 to that of the 2014 Volvo XC90, noting an increase in the application of high-strength steels.

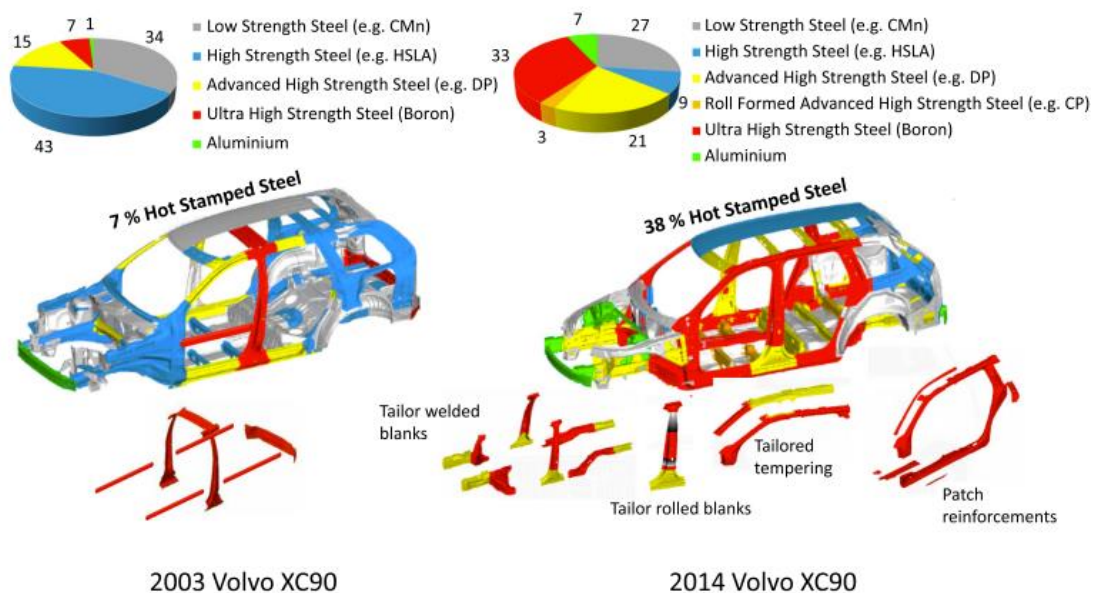


Fig.2.2: Increase in the application of high-strength steels for body in white components [16]

In automotive industry, five classes of AHSS are used: dual phase, complex phase, transformation induced plasticity, martensitic steel and press hardened steels (PHS). This thesis discusses only about PHS also known as hot-formed steel or hot stamped steel.

Press hardened are typically carbon-manganese-boron alloyed steels. Carbon has effects on phase transformations, such as lowering the martensite-start temperature [2,26-29], and on steel strength. In particular, as carbon content increases, the strength and hardness of the steel increases. Manganese has an important effect on the steel hardenability. The presence of boron pushes the CCT (Continuous Cooling Transformation) and TTT (Time Temperature Transformation) to right without lowering the Ms temperature. This greatly increases the hardenability of steels. To achieve ultra-high strength steel at the end of hot stamping process, the transformation of austenite to martensite is required. Two different kinds of phase transformations exist; diffusion-dependent with changes in phase compositions or number of phases, and diffusionless phase transformation where metastable phases are produced.

Quenching phase during the hot stamping process involves the diffusionless transformation of austenite into martensite. The critical cooling rate is the minimum rate of continuous cooling required for the diffusionless transformation of austenite to martensite [30]. Austenite is the face-centered-cubic (FCC, gamma iron) phase and it is not stable below the eutectoid temperatures unless cooled rapidly. The critical temperatures range for hypoeutectoid steels are between A_{c1} and A_{c3} (Figure 2.3), known as the intercritical temperatures.

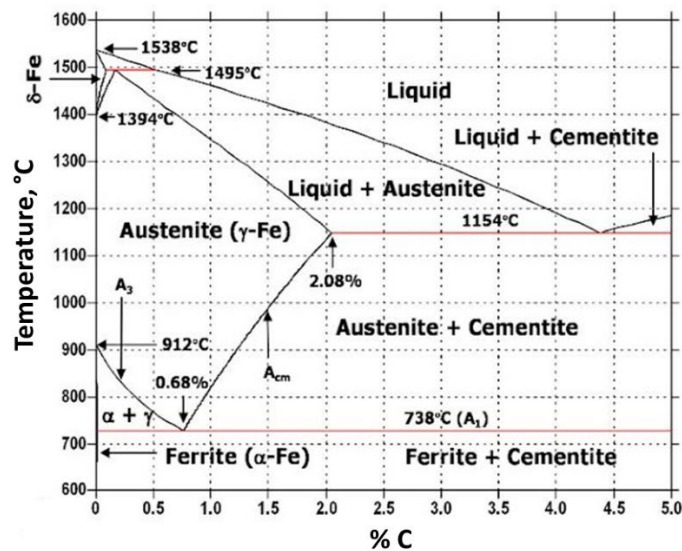


Fig.2.3: Fe-C phase diagram

Between these temperatures, the microstructure exists as austenite and ferrite. Steel must be heated above A_{c3} in order to transform the entire microstructure into austenite, after which cooling can occur to transform the microstructure from austenite into the other phases. Ferrite is a body-centered-cubic (BCC, alpha or delta iron) form of iron. Alpha ferrite is stable at room temperature and, at high temperatures, it transforms into austenite. Delta ferrite has the same structures as alpha ferrite and it is stable at high temperatures. Alpha ferrite forms from slow cooling of austenite and is caused by the rejection of carbon by diffusion.

When steel with a carbon content of at least 0.5% w.t. is heated to 815 °C for sufficient dwell time, the carbon will be dissolved in the interstices of the FCC crystal. If cooling is slow enough, the transformation from FCC to BCC of the crystal begins. This begins to occur when temperatures drop below the A_{c3} . Carbon atoms have minimum solubility in the ferrite alpha crystal lattice and during

slow cooling the alloy is in equilibrium conditions in terms of the phases present. Magnetic changes occur at 770 °C when iron carbon alloy is converted to austenite by heat, and a large absorption of heat occurs at the transformation temperature [31]. M_s is the martensite start temperatures where martensite begins to transform and continues during cooling until the martensite finish temperature (M_f) is reached. When the alloy is cooled rapidly, carbon atoms are trapped in the iron lattice. This results in a distortion of the lattice, and if cooling is fast enough martensite is formed. The austenite to martensite transition does not involve diffusion and no thermal activation is needed. Martensite forms nearly instantaneously when the required low temperature is reached. The FCC gamma austenite transforms into a BCT (Body Centered Tetragonal) unit cell. Martensite is metastable and is unreactive at room temperature [31]. Bainite is formed at cooling rates slower than that for martensite formation and faster for that of ferrite and pearlite. Depending on the temperature, upper and lower bainite exist. Upper bainite generally forms at temperatures between 550 °C and 400 °C. When the carbon concentration in the austenite is high enough, cementite nucleates as discrete particles or discontinuous stringers at ferrite/austenite interfaces. The cementite filaments can become more continuous with the increase of carbon content. At very high carbon contents, the bainitic ferrite laths are finer with the cementite stringers more frequent and continuous which can be described as 'feathery' bainite. Lower bainite generally forms at temperatures between 400 °C and 250 °C and the precise changeover temperature between upper and lower bainite depends on carbon content in steel.

Table 2.1a: Chemistry max, % for USIBOR®2000 and USIBOR®1500

Material	C	Mn	Si	B
USIBOR®2000	0.36	0.80	0.80	0.005
USIBOR®1500	0.25	1.4	0.4	0.005

Table 2.1b: Mechanical properties for USIBOR®2000 and USIBOR®1500

Material	Yield stress Rp0.2 (MPa)	Tensile strength Rm (MPa)	Elongation at break (%)
USIBOR®2000	≥ 1400	≥ 1800	6
USIBOR®1500	≥ 1050	≥ 1400	7

Among the press hardened steels, the most common are the USIBOR®1500 (22MnB5) and the USIBOR®2000 (37MnB5). The first one is the predecessor of the USIBOR®2000, in fact in the last decade, several steelmakers introduced new steel grades with higher carbon levels, leading to a tensile strength between 1800 MPa and 2000 MPa that is higher as compared to the typical 1500 MPa value of USIBOR®1500. For a 2000 MPa press hardened steel, Taylor et al. [32] found that a high quench rate resulted in a complete martensite transformation within 1.5 s. They found that this also correlated the lath size to increased strength for a USIBOR®2000, which also showed greater microstructural homogeneity when compared to 22MnB5.

Due to the higher carbon concentration, the USIBOR®2000 exhibits the continuous cooling transformation (CCT) curves shifted to the right with respect to the CCT of USIBOR®1500 as observed in Figure 2.4.

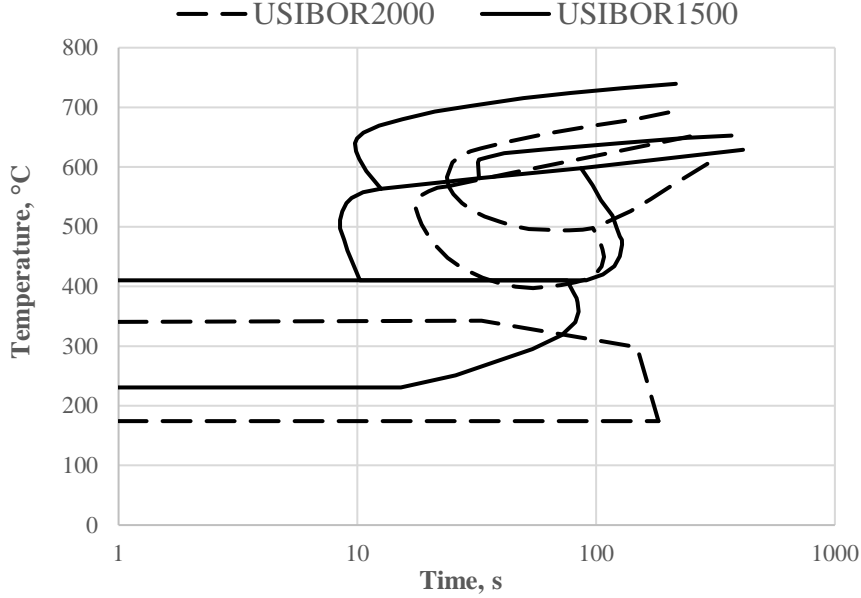


Fig.2.4: Comparison of CCT curves of USIBOR®2000 and USIBOR®1500 [33]

In this thesis, the two ultra-high strength boron steels mentioned have been investigated for the manufacturing of an automotive B-Pillar.

The chemical composition and mechanical properties are reported in Table 2.1a and 2.1b, respectively.

2.2 The Finite Element (FE) Approach

The Finite Element (FE) analysis of manufacturing processes is an efficient tool, because it allows to accurately processing the process design, to define the most influence process parameters, to optimize the process and to solve different technological problems quickly, avoiding the costs of a “trial-and-error” experimental approach.

For the hot stamping process, there are several commercial FE computer codes such as AutoForm, Pam-Stamp, DYNIFORM and JSTAMP. In this thesis, the hot stamping process is modelled in AutoForm software.

AutoForm is an implicit code [34], therefore the method of time integration is based on the solution of the static equilibrium. The dynamic forces are disregarded. The following equilibrium equation is solved to find nodal displacements:

$$R^{t+\Delta t} - P^{t+\Delta t} = 0 \quad (2.1)$$

Where R and P represent, respectively, the internal and the external forces. A state of equilibrium is assumed at time t and at the time $t + \Delta t$ equilibrium is needed.

Considering the current state \hat{u} , the equilibrium equation (2.1) become:

$$R(\hat{u}) - P(\hat{u}) + K(\hat{u})\Delta(\hat{u}) = 0 \quad (2.2)$$

Where K is the stiffness matrix, \hat{u} is the vector of nodal displacements and $\Delta\hat{u}$ is unknown displacement increment.

The principal advantage of implicit solver is related to the fact that the static equilibrium is achieved at each step. However, there are a lot of potential disadvantages. Since a linear set of equations is solved for each iteration, a large memory and long calculating time may be required. Moreover, unlike

an explicit code, the dynamic forces are neglected and consequentially stability problems can occur, especially when there are wrinkling problems. Furthermore, convergence problems can occur due to the relatively large time steps because the contact constraints can change significantly from one time step to the next.

To avoid these problems, special functionalities are implemented in AutoForm. In particular, an effective automatic time step control ensures that the contact constraints are only moderately changed from one increment to the next. Moreover, a special decoupled solution is used for the bending enhanced membrane element. This is characterized by a high calculation speed and relatively low memory requirements. The elastic-plastic shell element is fully compatible with the bending enhanced membrane. Thus, depending on operational demands and accuracy requirements, the user can freely exchange these two element types. The formulation of the shell element in AutoForm and a fast direct solver ensure that calculation time and memory requirements are moderately increased in relation to the bending enhanced membrane.

The time step taken during the simulation is optimized with respect to accuracy and computing time. In AutoForm software, the time step is controlled by the parameter *Max Material Displacement* that represents the tangential distance that the nodes move relative to the contacting tool.

For the simulations of stamping processes with, in general, large and complex sheet metal parts are involved, the spatial discretization with finite elements of varying sizes is required to accelerate computational costs. This means using, for example, small elements only in zones with a strongly curved geometry. For the refinement strategy, AutoForm uses a procedure named h-method [35]. Specifically, the adaptive discretization is carried out by dividing and combining elements.

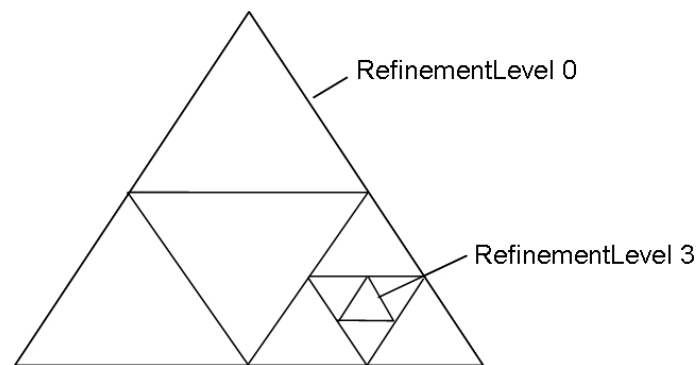


Fig. 2.5: Scheme of function mode of the refinement algorithm

Figure 2.5 shows the function mode of the refinement algorithm. Specifically, initially, a *RefinementLevel 0* is assigned to the triangles of the original mesh. Then, in each simulation time step, each triangle can be divided into 4 sub triangles (*RefinementLevel 1*) and this refinement can be carried out up to the maximum *RefinementLevel*. When this refinement is no longer required, the *RefinementLevel* is decremented (*De-Refinement*).

In AutoForm there are different refinement criteria such as that curvature based and strain based. One control parameter involved is the *Radius Penetration* (Figure 2.6) that defines the permissible penetration p in the length unit used and is independent of the current sheet thickness. For a certain p value, it is possible to calculate the upper and the lower limit for the element side length if the sheet curvature is known. If the actual element side length exceeds lower or upper limit, the element is refined or de-refined.

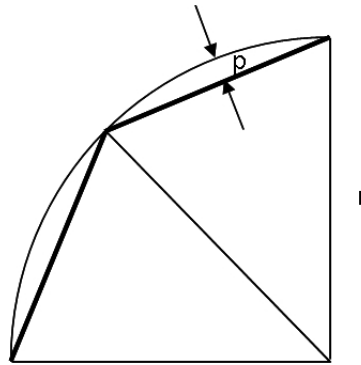


Fig. 2.6: Radius penetration

Another control parameter is the *Max Element Angle* that is associated with the mesh refinement at small radii (Figure 2.7). Before the simulation, an angle value is entered and it represents the number of element on a radius of 90° .

For example in Figure 2.7 a *Max Element Angle* equal to $22,5^\circ$ is chosen, therefore the radius is discretized with 4 element. Based on the curvature, an upper and a lower limit are calculated, therefore if the actual element angle exceeds the lower or the upper limit, the element is refined or de-refined. The *Tangential Refinement* is an advanced control parameter especially used for the elasto-plastic shell element in the entrance/exit area of a radius to obtain a more continuous representation of the stress gradient. In this way, better springback results are achieved.

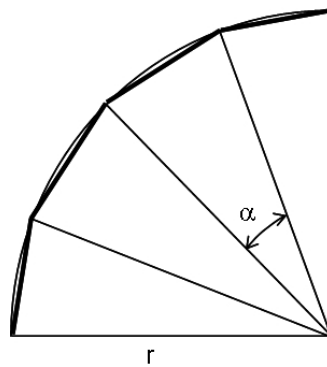


Fig.2.7: Max Element Angle

The AutoForm solver allows to choose the element type such as a membrane element (BEM: Bending Enhanced Membrane), shell element (EPS: Elasto-Plastic Shell) or CPS: Composite Shell element. For the numerical simulation of a sheet metal forming process, BEM or EPS elements are generally better to use. Specifically, the BEM element is suitable for deep drawing processes with thin sheets (up to about 2.5 mm) and for preliminary analysis since this element is characterized by a high degree of efficiency and this means that the simulation can be run in an extremely short time. On the contrary, when thick sheets or small bending radii (radius/blank thickness ratio < 3) are used, the EPS element is preferred due to the increased influence of transverse shear.

In AutoForm software, for the simulation of hot forming processes, the temperature and time dependent material behaviour has to be modelled. In the thermal material model, the hardening is dependent on temperature and on the strain rate. Accordingly a table of temperature dependent r -values characterizes the yield surface. Also for the evaluation of the forming limits, a temperature dependent table of forming limit curves is provided. Moreover, to predict the final properties of hot

stamped parts such as the microstructural phase portions, Vickers hardness and so on, the modelling of the phase transformation is required. To predict those properties, a database with measured CCT diagrams is used in AutoForm. The influence of different chemical composition on the simulation of phase transformation is considered.

As it will be detailed below, in this thesis for the study of the hot stamping process of an automotive B-Pillar, two high strength boron steels were investigated, namely the USIBOR[®]1500 and the USIBOR[®]2000. For the former one, since it is a steel on the market for quite some time, the material data has been imported from the AutoForm library material database. Instead, for the second one, there is no data in AutoForm database. Therefore, material flow behaviour at high temperature was experimentally obtained and then insert in FE model. The forming limit curves and the thermal properties were provided by Fiat Research Centre (CRF). Finally, for the evaluation of the phase transformations, the graph of the continuous cooling transformation curves of 37MnB5 steel was taken as a reference [33].

2.3 Physical simulation by means of Gleeble 3180 system

Worldwide demand of more efficient processes, leading to low costs of their products, stimulates intensive research to reach these goals. Therefore, industrial experiments, from this point of view, appears to be very expensive and inefficient. To overcome this problem, besides numerical simulations, physical simulation too is used. Physical simulation is a tool that is able to reproduce exactly thermal and mechanical processes in the laboratory that a material is subjected to during the real manufacturing process. In this way, it is possible to study metallurgical processes, develop new materials and replicate real world conditions in the laboratory.

The first metallurgical process studied by the physical simulation technique was welding process. Specifically, thermal cycle occurring in the heated affected zone was physically reproduced to study ductility and fracture behaviour of this zone. First studies revealed the influence of thermal gradients on phase transformations and on defects in the crystallographic lattice to adapt plastically to various micro deformations. Consequently, the welder simulator was equipped with a mechanical system capable to deform specimens with adequate speed at exact temperatures. This is how the Gleeble system was born. Over the years, the Gleeble system has undergone several metamorphoses; in fact, recent physical simulators allow the use not only for studying welding process but also for studying others processes, such as continuous casting, hot rolling, forging, extrusion, diffusion bonding, continuous strip annealing, heat treating, quenching, powder metallurgy/sintering and so on.

In fact, nowadays the role of physical simulation has increased in the field of engineering sciences and industrial applications, because it can contribute to design manufacturing systems, to develop and optimize manufacturing processes, and to characterize the different material properties under the conditions of the production line. Applying a desired thermal and mechanical loading profiles physical simulation allow to investigate a wide variety of materials processing technologies and to reproduce the operational loadings of structural materials. Depending on the capability of the physical simulator, the results can be extremely useful. In fact, when the simulation is accurate, the results can be readily transferred from the laboratory to the full size production process.

In particular, the current Gleeble system includes an AC electric resistance heating system, a mechanical deformation system that was previously pneumatic and it is now servo-hydraulic, a vacuum working chamber, and a computerized control for the data acquisition and processing. In

Figure 2.8, the Gleeble 3180 system is illustrated, in particular it is possible to see a digital control console for the user, the load unit in which tests are carried out and the vacuum system.

The Gleeble machine is a fully integrated digital closed-loop control thermal and mechanical testing system to simulate thermal cycles or hot deformation process. Gleeble machine can heat specimens at rates of up to 10000 °C/s. Therefore, Gleeble systems typically can run thermal tests up to ten times faster than conventional furnace equipped machines. Gleeble systems have no problem to guarantee heating rate up to 10000 °C/s, thanks to the AC electric resistance heating system.

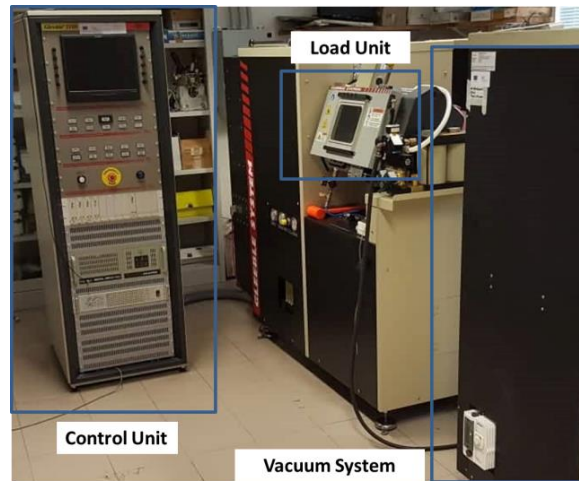


Fig.2.8: Gleeble system 3180

The samples are heated by Joule effect induced by a modulated current flow based on the temperature acquired from a thermocouple welded in the control point. Typically the control thermocouple is placed in the specimen centre and, thanks to the Proportional – Integral – Derivative (PID) control system, the specimen temperature profile follows the set temperature. In fact, this control system is able to modulate the current density at the control point as a function of the difference between the target (set) temperature and the temperature in the specimen. Up to four thermocouples can be welded on the specimen. The thermocouple is a sensor that measures the temperature. Thermocouples consist of two wire legs in different metals that are welded together at one end, creating a junction. This junction is where the temperature is measured. A voltage is generated when the junction experiences a change in temperature. Depending on characteristics in terms of temperature range, durability, vibration resistance, chemical resistance, and application compatibility different types of thermocouples exist. Type J, K, T, and E are the most common types.

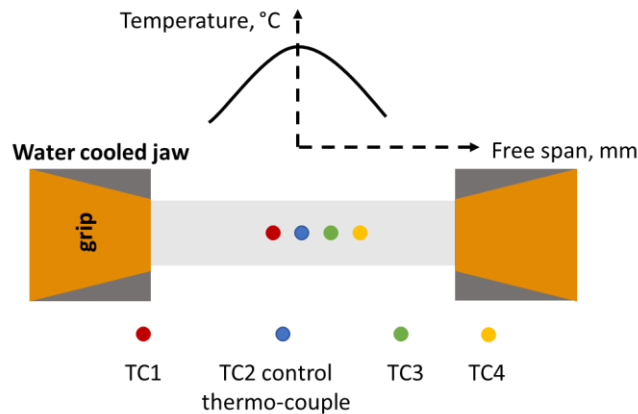


Fig.2.9: scheme of specimen between grips and scheme of thermal gradient recorded by the thermocouples welded on the specimen

It is advisable to weld all four thermocouples on the specimen to record the thermal gradient on the specimen during the test. In fact, during the tests, an axial thermal gradient is found on the specimen. Specifically, a parabolic temperature distribution, with a peak temperature at the point where control thermocouple is welded (in general at the centre of the sample) and a lower temperature near the jaws, can be observed on the specimen, due to the cool water-glycol solution circulating in the jaws (Figure 2.9).

Inside the jaws, the grips hold the specimen. The use of grips with different geometry and conductivity can change the temperature distribution. In addition, the distance between the jaws may affect the thermal gradient, in particular if the free span is small, the parabolic thermal gradient become steeper. The grips can be in copper or in stainless steel (Figure 2.10). The first one conduct heat away from the sample very quickly, instead, the second one has lower thermal conductivity and a small contact area, assuring in this latter case there is a flatter temperature gradient across the sample.

Although there are no problems in simulating cycles with high heating rate, the achievable cooling rates by the water-cooled jaws surrounding the specimen can be insufficient respect to those required for thermal cycle characterized by high cooling rate, i.e. severe thermal cycle typical of welding or laser treatment. For this reason, Gleeble system includes in vacuum chamber quenching spray heads that are mounted on the specimen and they are located to spray on the centre line of the specimen (Figure 2.11).



Fig.2.10: Gleeble grips in copper and in stainless steel

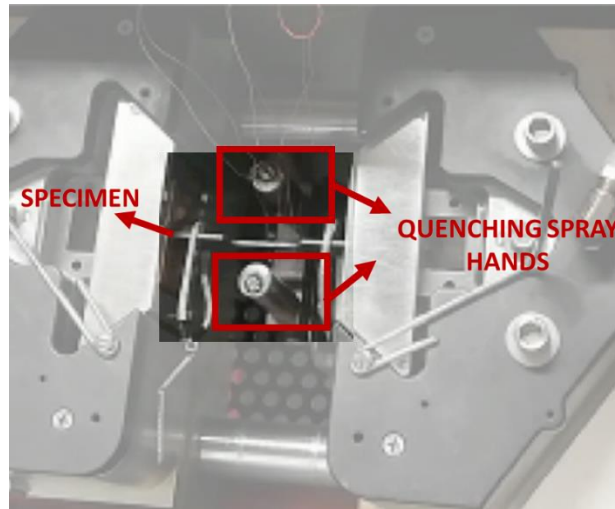


Fig. 2.11: Detail of quenching spray hands in Gleeble vacuum chamber

The air is supplied from the compressed air source with a control valve located at the vacuum chamber connection. The air pressure can be adjusted as necessary.

Often also this solution is not sufficient to guarantee high cooling rate, as in the case of physical simulation of laser welding thermal cycle. To overcome this problem, a solution is offered by ISO-QTM samples [36], that are cylindrical specimens with two holes through which water, regulated by a valve, flows. Figure 2.12 shows the schematic experimental setup and ISO-QTM specimen.

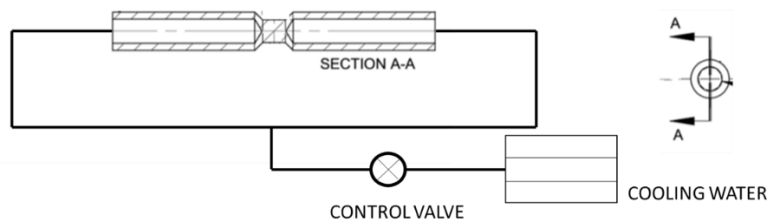


Fig. 2.12: Schematic experimental setup of ISO-QTM specimen for simulation of laser welding thermal cycle

This is a solution adopted on cylindrical specimens, however, on flat specimens, the increase of cooling rate was investigated by reducing the specimen cross section [37-38].

This aspect will be deepened in chapter 3 that explain the design of a physical simulation test. In fact, in this thesis, the properly design of Gleeble specimens is investigated with the aim to characterize USIBOR[®]2000 ultra-high strength steel (UHSS) in the austenitic field and to simulate thermo-mechanical cycle typical of Press-Hardening process. In order to do this, we draw on the experience in designing the geometry of Gleeble specimens to simulate laser thermal cycles on aluminium alloy specimens [37-38].

The mechanical characterization at high temperature of new materials, as well as the physical simulation of the thermo-mechanical hot stamping process, are possible by means of the Gleeble mechanical system, as well as thermal system. The mechanical system is a fully integrated hydraulic servo system capable of exerting static force in dilatation, tension, compression or torsion. Displacement rates as fast as 1000 mm/s can be achieved and the use of transducers, load cells, or non-contact laser extensometer provide feedback to ensure accurate execution and repeatability of the mechanical test program. The hydraulic ram is attached only to one of the sets of copper jaws, in

fact the other set of jaws is fixed. The ram movement can be monitored by stroke, force applied, or strain. Stroke and force are the two most common types of control.

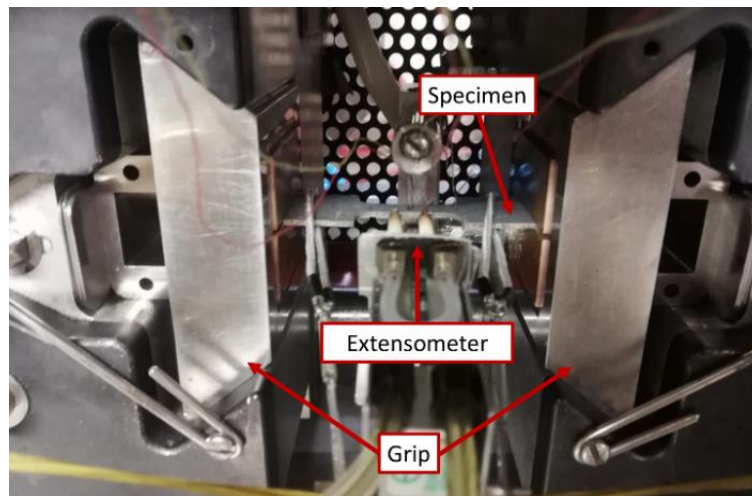


Fig. 2.13: Setup for Gleeble tests

These tests were assisted by the extensometer HZT071 that is characterized by alumina rods in contact with specimen for lengthwise measurement of the strain in the central hot zone of the specimen (gauge length is 10 mm) in which a uniform thermal gradient is present. Moreover, for these tests the ram movement was monitored by strain calculated thanks to the measure of HZT071 extensometer.

Figure 2.13 shows the experimental setup adopted for the mechanical characterization tests and for the physical simulation tests of the Press-Hardening thermo-mechanical cycles. Although the setup is the same for the two types of tests, the thermo-mechanical cycles imposed are different, as it will explain in detail later.

2.4 Tools for the evaluation of mechanical properties

The tools adopted to evaluate the mechanical properties of the material after physical simulation tests of thermal or thermo-mechanical cycles were the QnessQ10+ system for hardness tests and Instron 4485 universal test machine for tensile tests.

The hardness test is the most widely used test for evaluating the mechanical properties of materials. The hardness of a material is usually considered as the resistance to permanent indentation. In fact, during the hardness test, an indenter is pressed into the surface of the material to be tested under a specific load for a definite time interval, and a measurement is made of the size or depth of the indentation. The hardness value can be associated to the ultimate tensile strength of the material. Compared to a tensile test that can give the same information, the hardness test is preferred because it is simple, easy, and relatively non-destructive. The fully automatic Qness Q10+ system allows to carry out Vickers, Knoop or Brinell tests. However, for the hardness tests on specimens subjected to the physical simulation tests a Vickers hardness is adopted. The experimental setup is shown in Figure 2.14. It is recommended to grind and polish specimen before hardness test in order to obtain a planar surface and, consequently, a correct hardness value. The hardness, as already said, can only give the information of the maximum strength of the material. However, for the purposes of this thesis, it was necessary to know the elongation at break (fracture strain) of the material after a specific thermo-mechanical cycle typical of the Press-Hardening process. In fact, for the investigated application, i.e.

the manufacturing of an automotive structural component with tailored properties, it is necessary to guarantee parts able to absorb energy during impacts. Therefore, in addition to the hardness tests, tensile tests by means of the Instron 4485 universal testing machine (200 kN load cell) assisted by the Digital Image Correlation (DIC) system ARAMIS 3D (provided by GOM) were performed. The experimental setup is shown in Figure 2.15a.

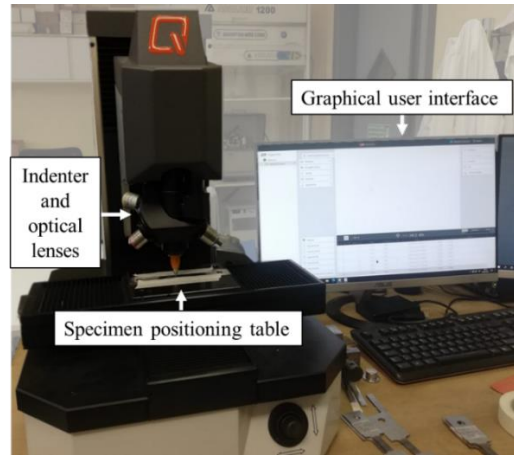


Fig.2.14: Experimental setup for hardness test

Digital Image Correlation (DIC) is a non-contact optical technique adopted for measuring strain and displacement. DIC works by comparing digital photographs of a component or sample at different stages of deformation. By tracking blocks of pixels, the system can measure surface displacement, build up full field 2D and/or 3D deformation vector fields and strain maps. It is generally preferable that the pixel blocks are random and unique with a range of contrast and intensity levels, for an effective work of DIC system. In many cases, before DIC analysis, a special surface preparation is required. In fact, for the tensile tests on specimens after physical simulation tests, the specimens have been sprayed with a white matte layer to avoid reflection and then with a random distribution of small black points, so that the resulting pattern (speckle) could thus be recognized by the two DIC cameras (12M pixel) as a virtual grid. The speckled specimen before tensile test is shown in Figure 2.15b.

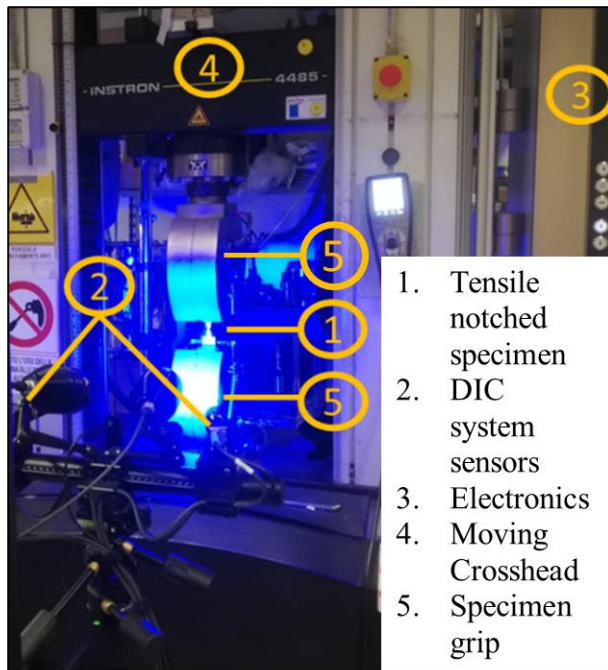


Fig.2.15a: Experimental equipment for uniaxial tensile test



Fig.2.15b: speckled specimen

It was decided to adopt the DIC system in order to evaluate the local fracture strain near to the center of specimen, i.e. near to the point where the control thermocouple was welded during the Gleeble test. In this point, in fact, the thermal cycle recorded is equal to the set one; consequently, it is possible to determine the mechanical properties corresponding exactly to the imposed thermo-mechanical cycle. To force the plastic deformation exactly in this point, specimens with geometry similar to that shown in Figure 15b were adopted. This type of specimen was called *notched* and it was obtained by reducing the center sample section exactly where the control thermocouple was welded. In several papers [39, 40] this solution is proposed to determine the mechanical properties of welded joints.

2.5 Method to develop metamodel

In designing of forming processes, several variables are involved, therefore knowledge of how process parameters affect the final mechanical properties of components can help the design phase. The map that connect the input process parameters and the output variables related to the quality of the final stamped part can be obtained using mathematical models. The metamodels allow to predict numerical or experimental output values, without studying the behaviour of the system over time or carrying out many experimental tests, reducing in this way, computing times and experimental costs. These advantages allow metamodels to be used to support manufacturing decisions, such as manufacturing scheduling and control.

To this end, in this thesis, metamodels have been developed using kriging techniques and artificial neural networks.

For the metamodel by means of kriging technique, the MATLAB package DACE (Design and Analysis of Computer Experiments) was adopted [41]. The Kriging metamodel is the best technique to predict outputs from a computer model that are deterministic, i.e. the response lacks random error, in fact repeated runs for the same input parameters give the same response from the model.

The Kriging model approximation follows the equation 2.3:

$$Y(\theta) = f(\theta) + z(\theta) \quad \forall \theta \in D \quad (2.3)$$

- $Y(\theta)$ is the unknown function of interest;
- $z(\theta)$ is the Gaussian process with zeros mean, variance σ^2 , non-zero covariance and correlation matrix ψ .
- $f(\theta)$ is the regression function constructed based on the data that can be expressed as $f(\theta)^T \beta$ where β denotes the parameter of a polynomial model. Polynomial functions can be of zero degree (constant), of first or second degree. The choice of the type of polynomial function significantly influences the precision obtained in the regression phase.

The covariance of the stochastic function can be written as:

$$Cov[z(\theta^i), z(\theta^j)] = \sigma^2 \psi([\psi(\theta^i, \theta^j)]) \quad (2.4)$$

where $\psi(\theta^i, \theta^j)$ is correlation function between any sampled data points θ^i and θ^j .

The Kriging predictor $\widehat{Y}(\theta)$ and gradient of the prediction $\frac{d\widehat{Y}(\theta)}{d\theta}$ [42-44] are derived untried values of θ respectively, as:

$$\widehat{Y}(\theta) = f(\theta)^T \beta + r^T(\theta) \psi^{-1}(y - F\beta) \quad (2.5)$$

$$\frac{d\widehat{Y}(\theta)}{d\theta} = \left[\frac{df(\theta)}{d\theta} \right]^T \beta + \left[\frac{dr(\theta)}{d\theta} \right]^T \psi^{-1}(y - F\beta) \quad (2.6)$$

$r^T(\theta)$ represents the vector of correlations between the point θ and samples S_N ($r^T(\theta) = [\psi(\theta, \theta^1), \psi(\theta, \theta^2), \dots, \psi(\theta, \theta^N)]^N$). On the other hand, y represents the column vector which contains the values of the response at each sample point and F is the regression matrix.

The parameter of polynomial model β can be determined by generalized least squares (GLS):

$$\beta = (F^T \psi F)^{-1} F^T \psi^{-1} y \quad (2.7)$$

The process variance σ^2 can be calculated as in the equation 2.8:

$$\sigma^2 = \frac{1}{N} (y - F\beta)^T \psi^{-1} (y - F\beta) \quad (2.8)$$

The accuracy of Kriging metamodel depends on the choice of the correlation function. The most adopted correlation function are the Gaussian and the exponential functions.

GAUSSIAN	$-\sum_{j=1}^m (\theta_j^a - \theta_j^b)^2$
EXPONENTIAL	$-\sum_{j=1}^m \theta_j^a - \theta_j^b ^p$

Actually, the toolbox contains others choices: linear, spherical, cubic and spline correlation model. In the metamodel developed for the studies described in this thesis, a Gaussian correlation model is adopted.

After the approximation model is constructed, it should be validated to ensure sufficient accuracy. Therefore, the additional validation points are used to compute error. Where error is defined as the difference between the predicted and actual values in terms of MSE (Mean Square Error).

$$MSE = \sum_{i=1}^N \frac{(Y(\theta) - \widehat{Y}(\theta))^2}{N} \quad (2.9)$$

Another technique in metamodeling is the artificial neural network (ANN) that in this thesis, thanks to the Neural Net Fitting MATLAB application, it was adopted to get metamodels from experimental data.

ANN is so-called because it is a system that learns by using interconnected nodes or neurons in a layered structure, similar to what a human brain does. An example of neural network architecture is shown in Figure 2.16. The network consists of an input layer, one or more hidden layers, and an output layer. In each layer, there are several nodes, or neurons, and therefore the nodes in each layer use the outputs of all nodes within the previous layer as inputs, such all neurons interconnect with one another through the various layers. Each neuron typically is assigned a weight that's adjusted during the training process and reduces or increases within the weight change the strength of that neuron's signal. A neural network of this kind is named the Feedforward NN.

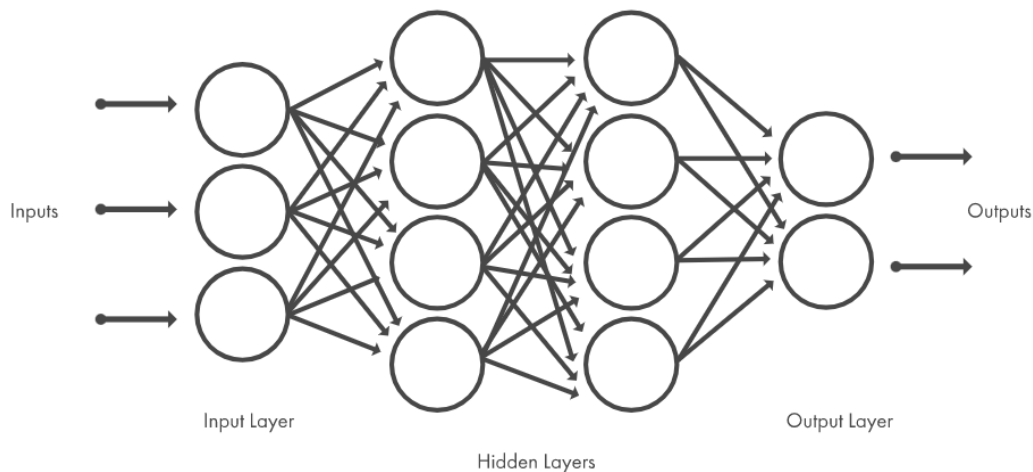


Fig.2.16: Scheme of a typical ANN architecture [45]

Neural networks (NN) can have different structures that approximate a set of data with different accuracies. For example, a NN trained with few neurons on a large data set may not be sufficient to ensure a correct approximation. On the other hand, having an excessive number of neurons can lead to overfitting problems. The best NN can be defined as the NN that guarantees the best compromise between the effectiveness of the approximation avoiding overfitting and assuring a simplicity of the network structure.

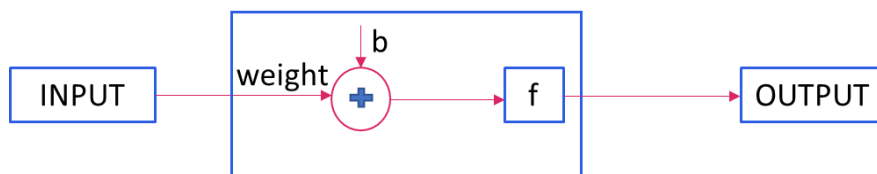


Fig.2.17: Diagram of the operations performed by a single neuron

The operations performed by a single neuron are extremely simple. A neuron processes a scalar input i to obtain a scalar output o . The input is multiplied by a weight w and a deviation b is added. The result is then processed with a transfer function (f), according to the scheme in Figure 2.17. Therefore, the relationship between the input and output of a single neuron is:

$$o = f(wi + b) \quad (2.10)$$

The transfer functions f are generally linear or nonlinear increasing monotone functions. The most common functions are the linear one (which has, as domain, the entire set of real numbers), or the logarithmic sigmoidal one (which has as domain $]0; 1[$).

The training of neural networks is an iterative process. The NN is trained by means of an algorithm that modifies the weights so as to reduce the difference between the expected values of the outputs and the known outputs. Different NN training algorithms exist in the literature. Almost all of them are based on the methodology called back-propagation. This methodology involves that the error between exact output value and the predicted one is propagated within the neural network and the values of the weights of the various neurons are adjusted. Thanks to this procedure, it is possible to iteratively adjust the parameters of the network so that it can 'learn' from the data known for minimize the error of the neural network. The epochs are repeated until the error that the neural network commits in the approximation phase on the set of known data does not fall below a certain threshold, or when a maximum number of epochs established is reached, or a stopping criterion is imposed. The various back-propagation algorithms can be classified according to the time required to carry out the training and the precision. Since Levenberg-Marquardt algorithm is the most rapid one, it was adopted in this thesis.

The Levenberg-Marquardt algorithm was designed to avoid the computation of the Hessian matrix, approaching second-order training speed. When the performance function has the form of a sum of squares (as is typical in training feedforward networks), then the Hessian matrix (H) can be approximated as:

$$H = J^T J \quad (2.11)$$

Where J is the Jacobian matrix that contains first derivatives of the network errors with respect to the weights and biases.

The gradient can be computed as:

$$g = J^T e \quad (2.12)$$

Where e is a vector of network errors.

The Jacobian matrix can be computed through a standard backpropagation technique [46] that is much less complex than computing the Hessian matrix.

The Levenberg-Marquardt algorithm uses this approximation to the Hessian matrix in the following Newton-like update:

$$x_{k+1} = x_k - [J^T J + \mu I]^{-1} J^T e \quad (2.13)$$

When the scalar μ is zero, this is just Newton's method, using the approximate Hessian matrix. When μ is large, this becomes gradient descent with a small step size. Newton's method is faster and more accurate near an error minimum, so the aim is to shift toward Newton's method as quickly as possible. Thus, μ is decreased after each successful step (reduction in performance function) and is increased only when a tentative step would increase the performance function. In this way, the performance function is always reduced at each iteration of the algorithm [47].

Once network is trained, it is necessary to validate the model to avoid the problem of overfitting. The overfitting occurs when the model fits exactly against training data, but it does not describe the general phenomenon well, i.e. the algorithm cannot perform accurately against unseen data. To avoid overfitting issues, one of the most used control techniques during the training phase is the early

stopping one. This method involves carrying out the validation on a data set of the same problem (validation set) not used for the training phase.

By observing the trend of the errors calculated on the training data set and on the validation data set as a function of epochs number in Figure 2.18, it can be seen that the error on the training data set drops constantly.

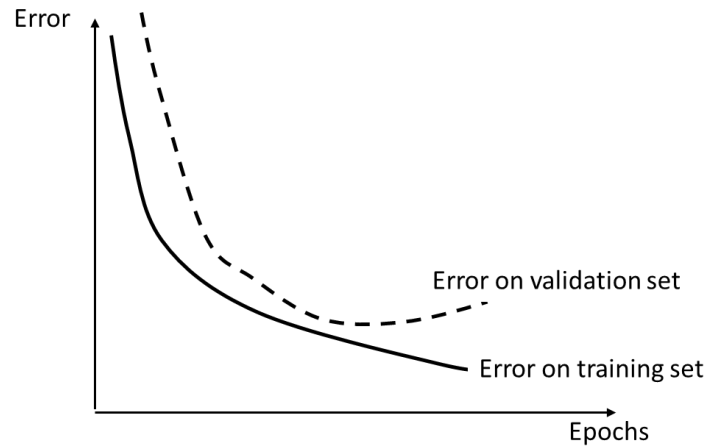


Fig.2.18: Curve of error on training data set and on validation data set

Due to the nature of the training algorithm that adjust the parameters of NN during the training following the error minimization criterion. On the contrary, the error trend on the validation data set decreases in the first section, but then it begins to rise. This behaviour indicates that the approximation in the areas distant from the training data set is no longer adequate. When this signal appears, it is advisable to stop the training process early even if the limit imposed by the stopping criterion has not been reached, to avoid overfitting problem.

3. DESIGN OF PHYSICAL SIMULATION TESTS

The accurately design of physical simulation tests is required to ensure that the Gleeble system correctly reproduce thermal and/or thermo-mechanical cycles imposed. As already highlighted in the introduction section, several variables can influence the test, such as the samples geometry, the grips type and the control mode adopted during the test.

This section focus on the design of geometry specimen to guarantee high cooling rate and low thermal gradient during physical simulation tests. To this end, FE models were developed in COMSOL Multiphysics software.

First, the design of specimen in EN AW5754 H32 and EN AW6085 T6 aluminium alloy is described with the aim to reproduce with physical simulation laser heat treatment characterized by rapid thermal cycle, i.e. high heating and cooling rate.

Second, the design of samples adopted during thermo-mechanical tests for obtaining flow curves of USIBOR®2000 is presented. The geometry resulting from this design was also adopted to carry out the thermo-mechanical cycles of Press-Hardening process.

3.1 Specimen design for physical simulation tests of laser thermal cycle on EN AW 5754 H32 aluminium alloy

This section details the FE model developed to optimize the specimen geometry. To reproduce the severe cooling conditions during Gleeble tests, the idea is to reduce sample central section; thereby the current densities are differentiated between the area to be brought to high temperature (the one with the smallest section) and the adjacent one to be kept cold. With this approach, the heat removed by conduction from the adjacent and cold area is higher respect to the heat removed during a test on constant section specimen, thanks to the smaller area at high temperature. To explore the feasibility and the potential of the proposed solution, rapid thermal cycles typical of laser softening treatment of aluminium EN AW 5754-H32 sheet alloy of 1.5 mm thickness were taken as reference. The thermal cycles investigated are represented in Figure 3.1. These thermal cycles were obtained by interpolation of acquired experimental data from thermocouple at the specimens centre during laser heat treatment (LHT) performed by means of a 2.5 kW CO₂ Laser source on specimens obtained from the sheet metal investigated. A focal length equal to 225 mm, which produced a square spot area (400 mm²) with a top-hat intensity distribution was adopted.

The tests were performed following two different approaches: (i) in pulsed operating mode (laser source stationary with respect the specimen surface) and (ii) in continuous treatment mode (laser source moves with a constant treatment speed). When the pulsed operation mode was adopted, the laser beam was stationed in the centre of a 100 mm x 20 mm rectangular sheet specimen. Instead, during the continuous treatment, the laser beam moved along the central trajectory of a square specimen with a side of 100 mm. The thermal cycles obtained in pulsed operating mode are shown in Figure 3.1a, while the ones obtained in continuous treatment mode are shown in Figure 3.1b. The laser treatments were performed for different values of the laser power and for different values of the treatment speed (in the continuous treatment mode) or for different pulse time (in the pulsed treatment mode). The pulse time represent the dwell time of laser source on specimen surface. The process laser parameters (laser power, treatment speed and pulse time) were varied with the aim of evaluating their influence on the material softening. Generally, laser surface treatment is a process adopted to soft the material, i.e. to reduce hardness of the treated areas by increasing their formability in subsequent

cold-forming operations. Thanks to its flexibility, laser surface treatment is particularly suitable for the production of Tailored Heat Treated Blanks (THTB) that are blanks that locally exhibit different mechanical properties of the material.

Table 3.1 shows the characteristic parameters of the selected thermal cycles and the level of softening achieved after laser treatment, calculated as the ratio between the measured softening value and that associated with the complete softening condition, which is approximately 59 HV0.2. The parameters P, V, t and PT represent respectively the laser power, the treatment speed during continuous laser treatment mode, the pulse time during pulsed laser treatment mode and the peak temperature reached at the sample centre during the laser treatment. The parameter τ represents the interaction time assumed equal to the pulse time in the PM, and equal to the ratio between laser spot size and the treatment speed in the CM treatment. Instead, the parameter CR represent the cooling rate that is, as can be seen from Table 3.1, on average higher than 100 K/s.

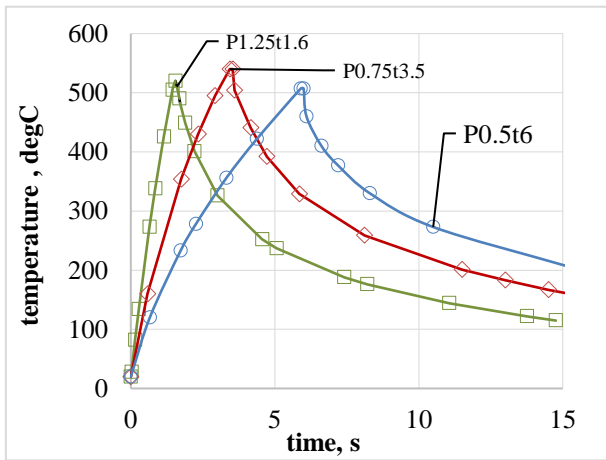


Figure 3.1a: Thermal cycles investigated for pulsed mode treatment

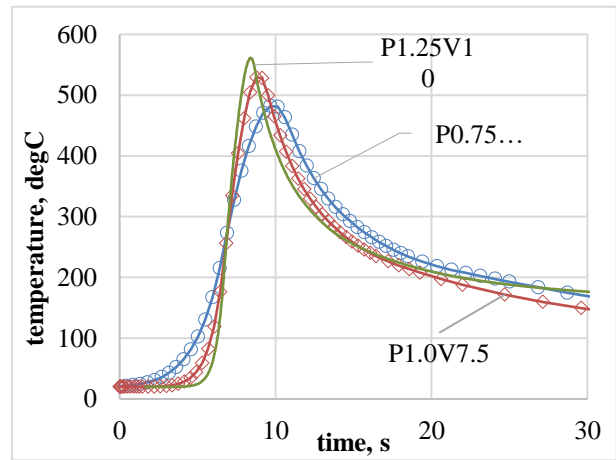


Figure 3.1b: Thermal cycles investigated for continuous mode treatment

Table 3.1: Parameters of the laser thermal cycles

Treatment mode (TM)	P (kW)	V (mm/s)	t (t)	τ (s)	PT ($^{\circ}$ C)	CR (K/s)	Treatment code	Softening (%)
Pulsed (PM)	0.5	-	6.0	6.00	507	105	P0.50t6	93
Pulsed (PM)	0.75	-	3.5	3.50	540	170	P0.75t3.5	86
Pulsed (PM)	1.25	-	1.6	1.6	520	190	P1.25t1.6	78
Continuous (CM)	0.75	5.0	-	4.00	483	72	P0.75V5	68
Continuous (CM)	1.00	7.5	-	2.67	528	110	P1V7.5	73
Continuous (CM)	1.25	10	-	2.0	550	140	P1.25V10	60

Preliminary physical simulations of laser thermal cycles, shown in Figure 3.1, using a classic flat dog bone specimen highlighted the capability of the physical simulator to reproduce in the control point only the heating phase of the thermal cycle, while cooling rates realized are lower to those induced by laser treatment. An increase of the cooling rate was observed reducing the specimen cross section

in the central zone. This because the not shaped zone of the specimen remains at lower temperatures (lower current density) respect to the temperatures of the shaped area (higher current density), during the heating phase; in the next cooling phase the heat removed by conduction from the non-shaped areas of the specimen increases the cooling rates in the shaped area of the specimen.

A 3D transient FE thermo-electric model was developed in COMSOL Multiphysics to sizing the shaped area of the specimen and to analyse physical simulation's results. A Proportional-Integrative-Derivative (PID) controller was implemented in the FE model in order to guarantee the required thermal cycle in the control point. The heat removed from the clamps, which are kept at a low temperature thanks to the use of a water-glycol solution that circulates inside them, was modelled as heat lost by convection in the specimen gripping area.

Figure 3.2 highlights FE model results obtained in the simulation of the PM laser treatment with $P=0.75\text{kW}$ and $t=3.5\text{s}$, when the classic flat dog bone specimen was used (Figure 3.2a). The numerical and experimental thermal cycles compared in Figure 3.2b confirm the capability to reproduce the heating phase of the laser thermal cycle, as well as the difficulty to adapt the cooling phase.

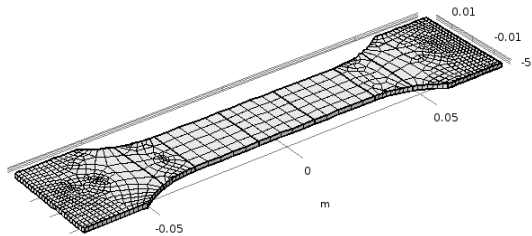


Fig. 3.2a Flat dog bone specimen with L_0 (length) of 150mm and W_0 (width) of 20mm

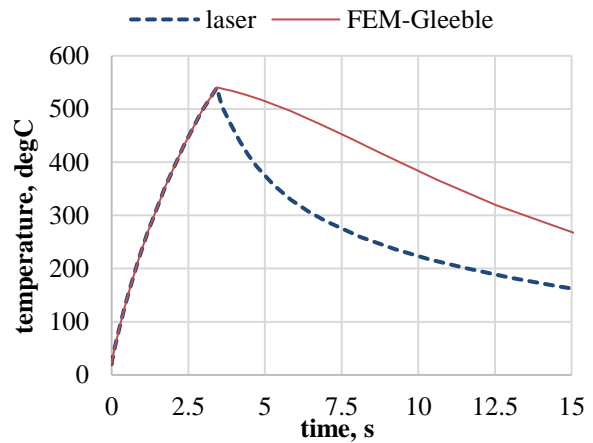


Fig. 3.2b Comparison between the laser thermal cycle and the Gleeble thermal cycle simulated with the FEM model for $P=0.75\text{kW}$ and $\tau=3.5\text{s}$ conditions

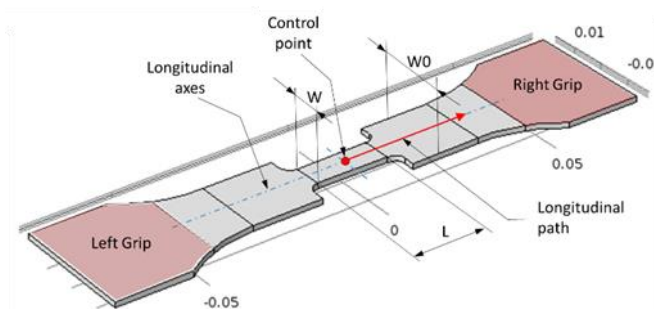


Fig.3.3: Geometric parameters of the Gleeble specimen

Figure 3.3 shows the Gleeble specimen with the shaped area in the central zone (*tapered* specimen). In particular the figure highlights the length (L) and the width (W) of the shaped area and the control point and the specimen gripping areas. A FE simulation plan was realized, varying L and W parameters respectively from 15 mm to 25 mm and from 6 mm to 10 mm. In Figure 3.4a and in Figure 3.4b the temperature profiles at the end of the heating phase and the cooling curves in the control

point for some combinations of L and W are respectively shown. It is observed that by shaping the specimen, the area subjected to high temperatures is reduced and this leads to more drastic cooling curves. The approach allows reaching higher cooling rate than those required during the laser process, by reducing the width and/or the length of the shaped area.

The effect of the geometric parameters was investigated with Kriging techniques through the DACE MATLAB toolbox. A Kriging approximation model based on data from a computer experiment was developed. The results shown in Figure 3.5 quantifying the effects of the shaped area parameters. Results confirms that a reduction in the width and length of the shaped zone leads to an increase of cooling rate and that there is a greater sensitivity to the variation of W rather than L.

The optimal specimen geometry was designed using results shown in Figure 3.5 and the information on the maximum cooling rate required in the experimented laser treatments (Table 3.1).

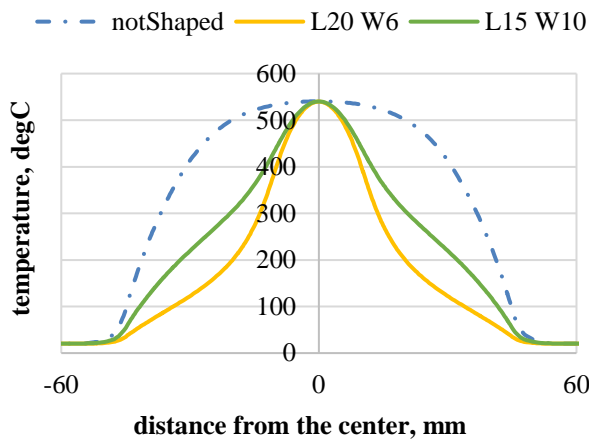


Fig. 3.4a: Temperature profiles for not shaped (dash-dot line) and shaped specimens (solid lines)

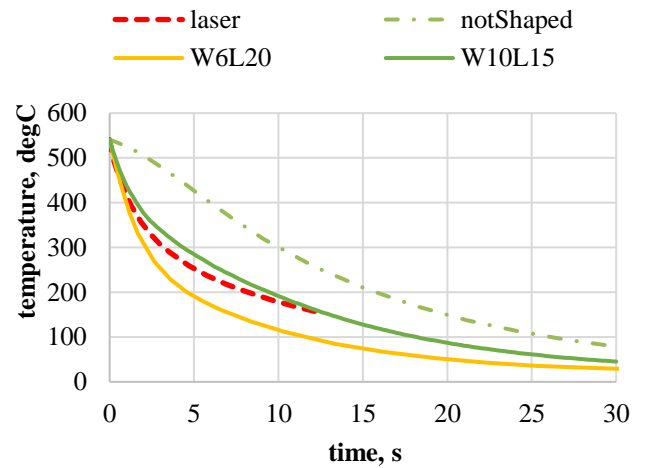


Fig. 3.4b: Cooling curves for not shaped (dash-dot line) and shaped specimens (solid lines). The red dashed line represents the cooling curve of laser cycle ($P=0.75kW$, $t=3.5s$)

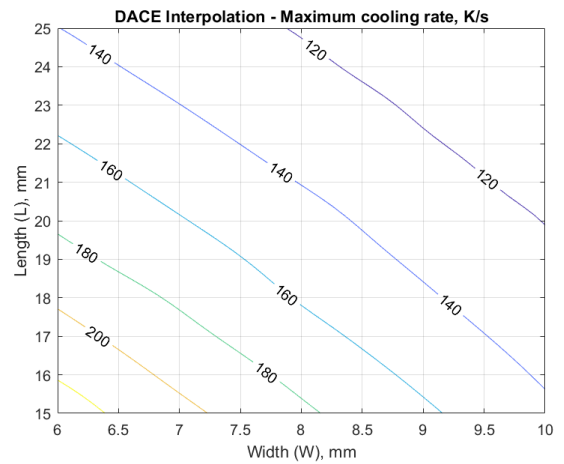
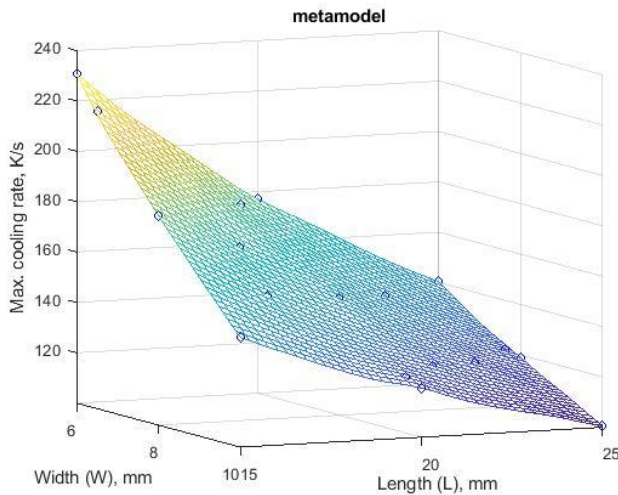


Fig. 3.5a: Effects of the geometry of the shaped sample in terms of maximum cooling rate in the control point (response surface)

Fig. 3.5b: Effects of the geometry of the shaped sample in terms of maximum cooling rate in the control point (isolines)

The used approach was been to create specimens with a geometry of the shaped area able to guarantee a cooling rate greater than that required in the laser thermal cycles. With this approach it was possible to verify that the PID regulator of the Gleeble system was always able to modulate the current density both in the heating and cooling phases, perfectly reproducing the laser thermal cycles highlighted in Figure 3.1.

3.1.1 Analysis of softening effect induced on ENAW5754 H32 aluminium alloy

The need to simulate these rapid laser thermal cycles using the Gleeble physical simulator is due to the possibility of carrying out laser surface heat treatment with a simpler experimental test without the use of CO₂ laser source and without the distortion problems encountered after the laser treatment. Physical simulation allowed to evaluate the softening of the investigated alloy for the different process conditions. In fact, once the different laser heat treatment conditions in term of both laser power and interaction time have been physically simulated, micro-hardness tests and metallographic analyses were carried out. Micro-hardness tests, with Qness Q10+ system, were realized on grinded and polished samples surface after physical simulation test adopting a load equal to 0.2 kg with a dwell time of 5 seconds. For each sample, micro-hardness tests were performed along the longitudinal section of the samples and along a path parallel to the previous one at 2 mm distance. For each path micro-hardness test were realized with a pitch of 0.5 mm. The results of hardness profiles are shown in Figure 3.6 for the different laser treatment condition investigated. In the shaped section and therefore in the section subjected to the maximum temperatures, the minimum hardness is reached; this grows up to the value at the as received state in correspondence of the part of the specimen in contact with the cold clamps.

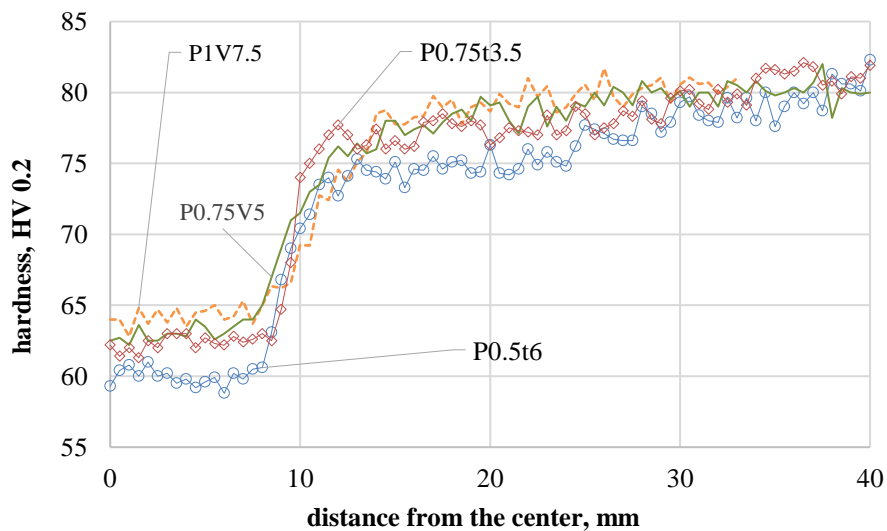


Fig. 3.6: Microhardness values according to the distance from the specimen centre

These results obtained by hardness analysis were confirmed observing microstructural changes in the material as a function of the distance from the specimen centre and of the interaction time. An electrochemical etching procedure was performed using Barker's reagent (675ml water, 23ml of

flour-boric acid (48%)). The anodization process was performed for $90 \div 120$ s at 24V DC. The microstructure was possible to observe using polarized light through the Nikon Ig_ma200In optical microscope.

Considering the section of the specimen with maximum softening, it is possible to correlate the grain size and the hardness to the interaction time of the laser treatment. Figure 3.7a shows how the average grain size varies in the case of a PM laser treatment. Taking P0.5kWt6s as a reference, in Figure 3.7b the micrographs are respectively shown in the central zone of the shaped area and in the zone of the not shaped-area at 30mm from the central point. It is noted that an increase in treatment interaction time leads to an increase in grain size. For the case considered where the minimum hardness recorded in the central area is of 60 HV0.2, there is an average grain size of $30.59 \mu\text{m}$. This value is greater than what is observed in the lateral area. Here the average grain size is of $15.38 \mu\text{m}$.

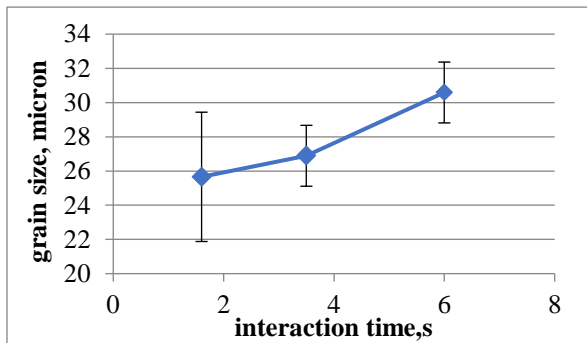


Fig. 3.7a: Average grain size in the central area depending on the interaction time of the laser treatment

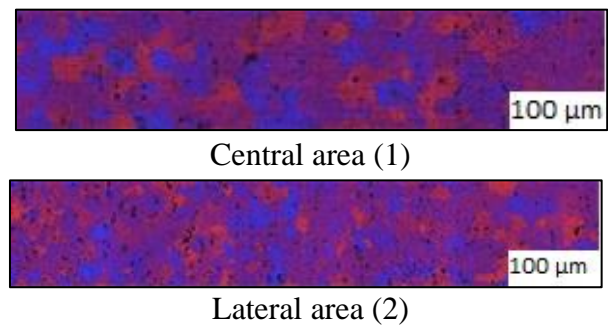


Fig. 3.7b: Microstructure 500x in Central Zone for 0.5kW,6s (1). Microstructure 500x in Lateral Zone for 0.5kW,6s (2)

During the Gleeble test on the specimen, four thermocouples were welded, one in the centre (control thermocouple) and the others at a distance of 8 mm, 14 mm and 30 mm from the centre, respectively. In this way it was possible to control the thermal cycles also in the points near to the central point, that is the point where the recorded thermal cycle coincides with the imposed one.

The experimental results of the temperature acquired by the thermocouples allowed to calibrate the FE model to simulate each Gleeble test and to derive the temperature distribution along the longitudinal specimen section during the test.

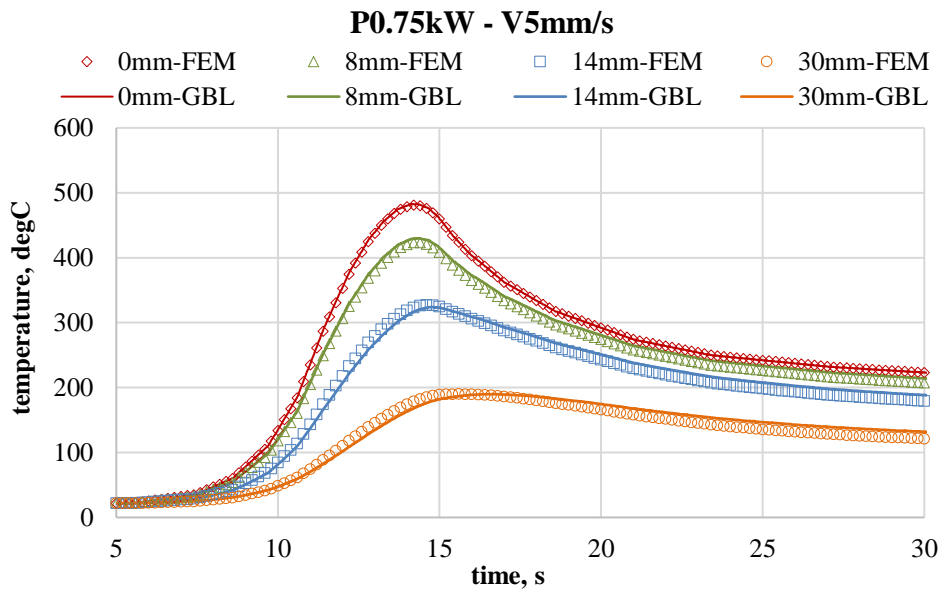


Fig. 3.8: Comparison of thermal cycles along the longitudinal direction of specimen between FE model and physical simulation test

Referred to the continuous surface treatment performed by adopting 0.75 kW laser power and with a treatment speed equal to 5 mms^{-1} , Figure 3.8 shows the thermal cycles calculated with the FE approach in different points along the specimen longitudinal direction and at difference distances from the specimen centre. In the same figure thermal cycles measured by the thermocouple welded in the control point and at 8mm, 14mm and 30mm from the control point, along the longitudinal path were depicted. A good correspondence between the temperature profiles of the maximum temperatures obtained by FE approach and the values of the maximum temperatures recorded by the thermocouples welded on the Gleeble specimens was recorded. These results show the ability of the FE model to also predict the thermal cycles that are generated during the physical simulation test in the specimen points positioned at different distances from the control point; similar results were obtained by simulating other treatment conditions. Especially in the shaped-zone of the specimen, the results further highlight that thermal cycles obtained at the different points of the longitudinal path have the same shape, while peak temperatures are reached at the same time. With increasing distance from the control point, a single physical simulation test is therefore able to reproduce laser thermal treatments made with the same mode (PM or CM), with the same interaction time, but with laser powers, consequently peak temperature, smaller than that corresponding to the control point.

It is possible to associate the hardness profile (Figure 3.6) to the peak temperature profile (Figure 3.8). In fact, Figure 3.9 shows the hardness trend as a function of the peak temperature reached during the Gleeble test in different points of the sample along the longitudinal path. In Figure 3.9 the different effect of recovery and recrystallization phenomena on the softening level of the analysed aluminium alloy is shown. Below a certain peak temperature, there are no softening effects. With the increase in peak temperature, the hardness initially decreases slowly (mild softening domain) and then more markedly. Finally, for each thermal cycle analysed there is a peak temperature value (threshold temperature), in which the hardness reaches a minimum value; this hardness value remains constant even for thermal cycles with peak temperatures higher than the threshold temperature (maximum softening domain).

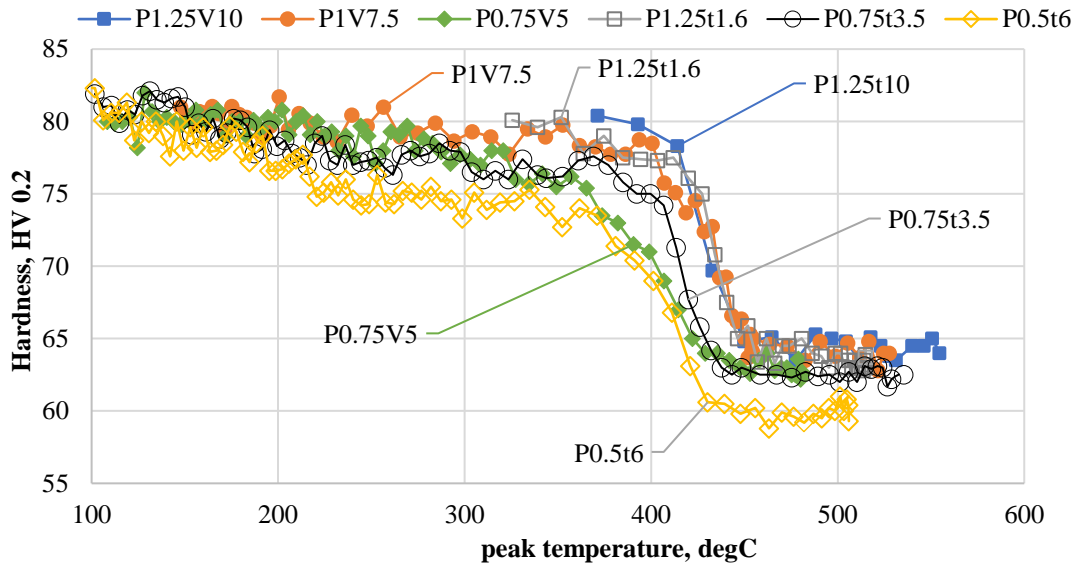


Fig.3.9: Hardness curve function of peak temperature

The severity of the thermal cycle influences the curves trend, which can be described with the following parameters: (i) The peak temperature at which the hardness begins to decrease. (ii) The hardness at the end of the mild softening domain. (iii) The temperature above which the hardness decrease becomes more significant. (iv) The threshold temperature. (v) The hardness value in the maximum softening domain. In particular, the peak temperature in which the softening phenomena start is between approximately 150°C, in correspondence with the less severe thermal cycles (longer interaction times or pulse times), and 390°C for the more severe thermal cycles. Furthermore, increasing the severity of the thermal cycle the hardness reduction at the end of the mild softening domain decreases, while increases the peak temperature beyond which the hardness decreases markedly (approximately from 350°C to 410°C). Finally, as regards the maximum softening domain, it should be noted that: (i) the threshold temperature increases with the increase in the severity of the thermal cycle; in the range of laser parameters examined, the maximum threshold temperature is about 450°C and is obtained in thermal cycles performed with less interaction time. (ii) the value of the minimum hardness decreases reducing the severity of the thermal cycle; the minimum hardness obtained, comparable with that of a complete annealing, is obtained in the physical simulation of the laser treatment carried out with the highest interaction time explored (6s). The softening amount in the maximum softening domain, which indicates the presence of recrystallization phenomena in the material, has been analysed for all the laser heat treatments experimented as a function of the interaction time (continuous laser condition) and the pulses time (pulsed laser condition). For each physically simulated laser heat treatment, the mean hardness corresponding to peak temperatures above 450°C were considered in this analysis. Results obtained are shown in Figure 3.10; as previously highlighted, a decrease in the severity of the thermal cycle determines an increase in maximum softening, with softening values ranging between approximately 75% and 95%. Furthermore, in the range of explored parameters, it is plausible to hypothesize a linear relationship between softening and interaction time or pulsed time. Regarding the softening differences shown in Figure 3.10, comparing the results of the laser treatment in pulsed mode and those in continuous mode at the same time (interaction or pulsed), it is possible to hypothesize that these differences are

probably due to the heat conduction effect. This effect, in the pulsed treatment mode is more limited because the specimen width is equal to the laser spot size. On the contrary, in the continuous treatment mode the effects of heat conduction are greater because of the square sample adopted.

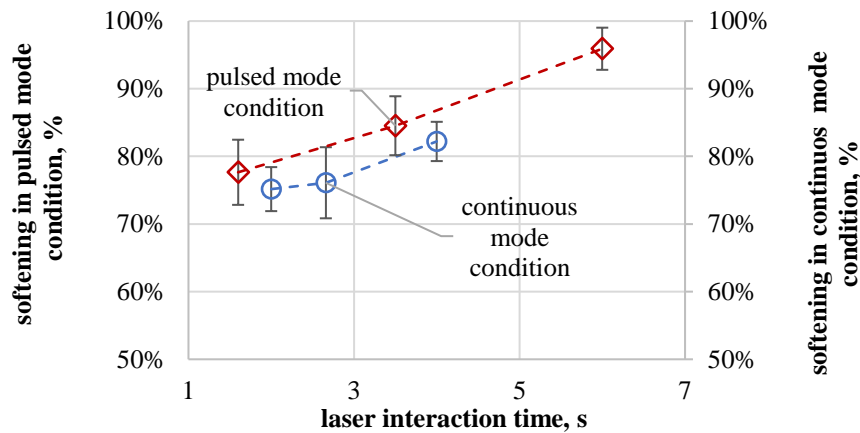


Fig.3.10: Relationship between the laser interaction time and the maximum softening

Finally, comparing the maximum softening obtained in the physical simulation tests (Figure 3.10) with those obtained in laser heat treatment (Table 3.1), a good correspondence is observed when the comparison is made by analyzing the pulsed treatment mode. On the contrary, the differences are sensible for the continuous treatment mode; these differences could be originated by in process variations of the laser beam focal position, due to the sample distortion experimented in this treatment condition. The distortion differences between the two treatment conditions investigated indicate a different thermal flux in the treated area.

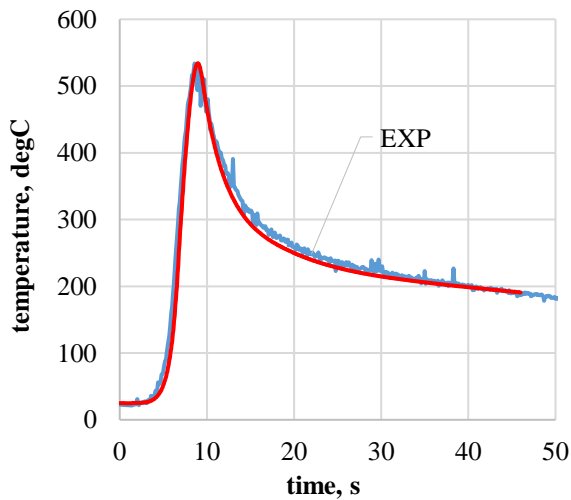


Fig.3.11a: Numerical-experimental comparison of the thermal cycle in the PM treatment realized with a laser power of 1.0kW and a treatment speed of 7.5mm/s

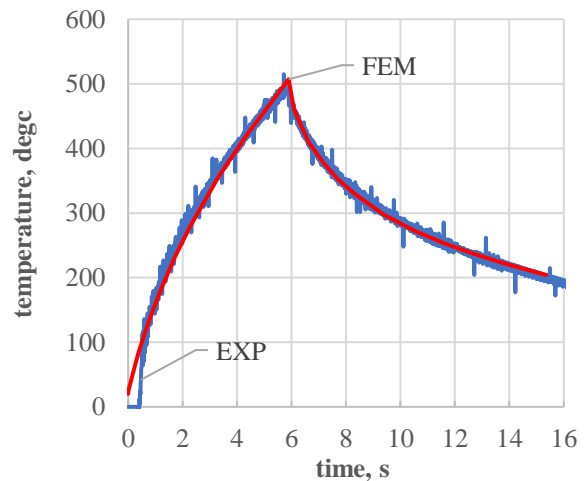


Fig.3.11b: Numerical-experimental comparison of the thermal cycle in the PM treatment realized with a laser power of 0.5kW and a pulse time of 6s

To better understand the differences between the softening results obtained immediately after laser heat treatment and immediately after physical simulation tests, a 3D transient FE thermal model has been developed for the CM and PM laser surface treatment simulation.

The FE model was implemented using COMSOL Multiphysics. The 20x20mm laser source has been modelled as a surface thermal flux with a top hat distribution. In continuous mode treatment, the laser source moves with a constant laser treatment speed while in pulsed mode the laser source is active for time shorter than the pulse time. The thermo-physical parameters were modelled as a function of temperature. Heat loss from the sample surfaces was modelled with a constant convective heat transfer coefficient. Using the thermal cycles acquired in the experimental tests, the calibration of the FE model was obtained by defining the convective heat transfer coefficient and a laser source absorption coefficient, which delimits the portion of the laser power supplied to the specimen. The numerical-experimental comparison of thermal cycles highlighted in Figures 3.11a and 3.11b show the results of this calibration phase for two of the process conditions investigated in PM and CM laser surface treatment. It is possible to observe that the numerical curves are in good agreement with the experimental ones.

As example of FE model simulation results, the Figure 3.12 shows the temperature distribution obtained respectively: (i) when the laser source is on the specimen centre in the CM laser surface treatment (Figure 3.12a), (ii) and at the end of the pulse time in the PM treatment simulation (Figure 3.12b). Due to the reduced thickness of the specimens, the difference in temperature between top (the surface of the specimen irradiated by the laser), and bottom side is a few Celsius degrees.

Thanks to FE models developed to simulate laser heat treatments in PM and CM, the different heat flux in the treated area is confirmed by observing the temperature profiles along axial and transverse specimen directions (Figure 3.13). For both the PM (Figure 3.13a) and CM (Figure 3.13b) treatments, the profiles are obtained at the time in which the peak temperature is reached. The same figures show the longitudinal and transverse temperature profiles obtained in the Gleeble specimens as a result of physical simulation tests of PM and CM treatments. The comparison between laser heat treatment conditions shows a significant difference of the thermal gradients in the transverse direction of the specimens, which are absent in the PM treatment and comparable with that in the longitudinal direction in the CM treatment.

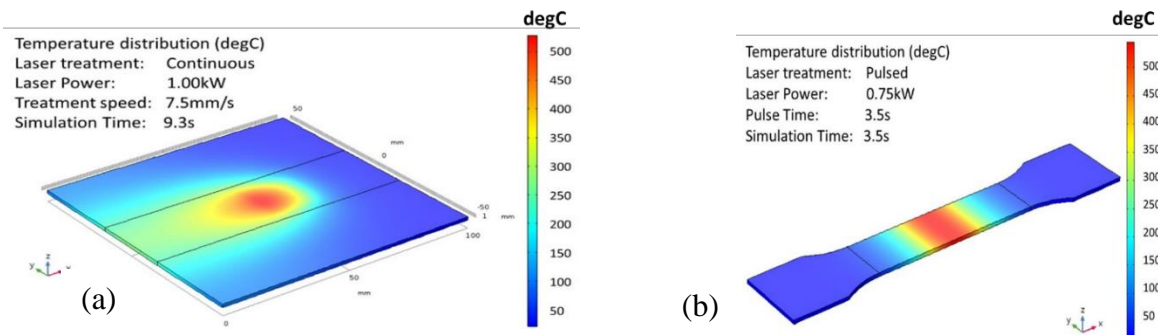


Fig. 3.12: Temperature distribution in the FE simulation of the CM laser surface treatment, when the laser beam is in the specimen centre (figure 3.12a), and of PM laser surface treatment at the end of the pulse time (figure 3.12b)

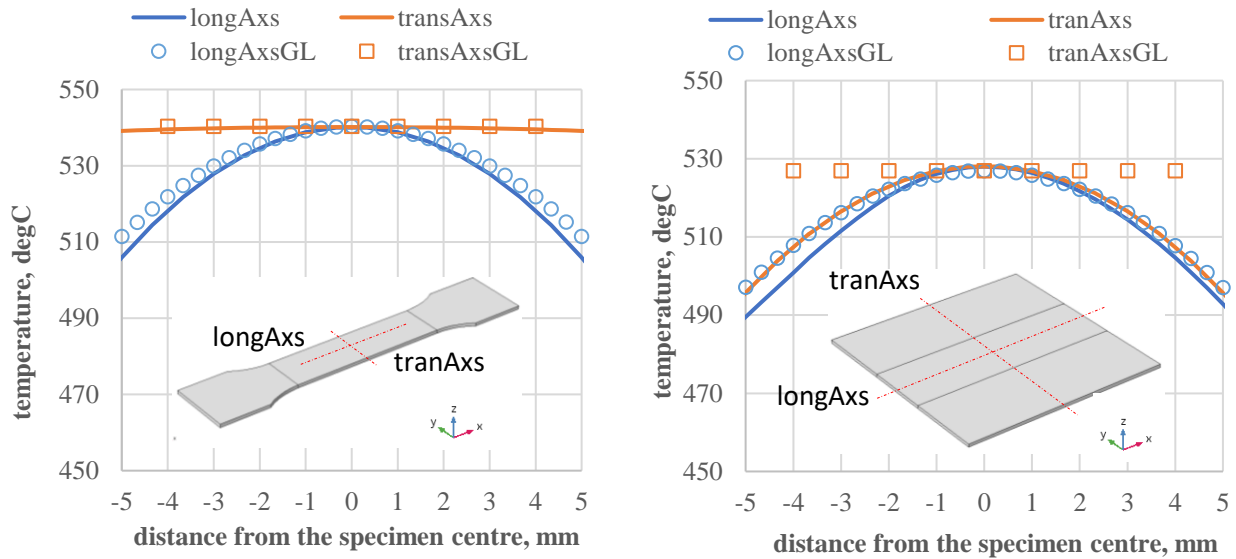


Fig. 3.13: FE thermal profiles along the longitudinal (longAxis) and transverse axes (tranAxis) of the specimens, simulated in the laser and physical simulation tests of the treatments P0.75kWt3.5s (Fig. 3.13a) and P1kWv7.5mm/s (Fig. 3.13b)

The comparison between laser treatment and corresponding physical simulation test shows thermal gradients comparable only in the physical simulation of the PM treatment, justifying the good correspondence of the softening levels obtained (the difference in terms of softening is about 2%). There are greater differences in the physical simulation of the CM treatment (approximately 15%), highlighting how an increase in gradients in the transversal direction of the specimen reduces the level of softening possible in a CM treatment. On the one hand, this reduces the ability of the physical simulation to estimate the softening in a CM treatment, but on the other, it provides indications on the design of the heat treatment, which will have to try to reduce the gradients in the transversal direction. For example, in a single pass treatment this gradient reduction could be obtained by increasing the size of the laser spot, which is transversal to that of the laser treatment direction. In conclusion, after careful specimen design, the Gleeble system was able to simulate the thermal cycles of the laser surface treatment and it allowed to make considerations on the softening effects induced on the investigated aluminium alloy when the process parameters and the type of treatment changed. In addition, this system allowed to understand the problems that could arise during the process. This demonstrates that physical simulation is a fundamental tool in the design phase of manufacturing processes.

For further details about physical simulation and FE results see the scientific work [38].

3.1.2 Analysis of softening effect induced on precipitation hardened ENAW6082 T6 aluminium alloy

Thanks to the study described in subsection 3.1.1, it is clear that the Gleeble system allows to perform laser thermal cycles in a simple way and without distortion problems encountered in laser heat treatment performed with the laser source, obtaining the same results. For this reason, to study the softening effects and the deformability improvement induced by laser heat treatments (LHTs) on the EN AW 6082 T6 aluminium alloy 1 mm thick with a hardness of 110 HV0.2 in the conditions

received, a three-dimensional (3D) transient Finite Element (FE) thermal model was developed. In particular, Gleeble tests were performed directly by taking the results of the numerical simulation without carrying out experimental tests with the CO₂ laser source. This FE model allowed to simulate different laser heating condition and to define thermal cycles with different peak temperature and with different treatment speed. This transient three-dimensional finite element model was used for the numerical simulation of a localized laser surface treatment of a blank 1 mm thick and 150 mm x150 mm wide. The heat treatment was modelled with a 20 mm x 20mm laser spot, which moves with constant treatment speed (v) along a centre line of the blank surface. The power of the laser source, which was modelled with a top hat energy distribution, is calibrated to guarantee a steady state treatment condition and therefore thermal cycles with the same peak temperature along the entire treatment direction. The thermal cycle that occurs in the centre of the blank surface was used for the physical simulation test. In Figure 3.14 the laser source distribution is highlighted, while in Figure 3.15 the mesh on the blank, suitably thickened in the area affected by the major thermal gradients, is shown.

The treatment speeds of 5 mm/s and 7.5 mm/s were investigated, while the absorbed laser power (PL) was varied in order to achieve thermal cycles with peak temperatures (T_{peak}) of about 300 °C, 400 °C and 500 °C. These peak temperatures have been chosen to investigate the softening effects on the alloy. The Table 3.2 shows the characteristic parameters of the investigated thermal cycles.

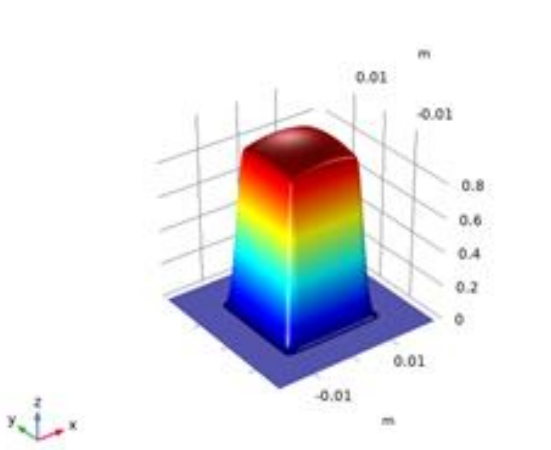


Fig.3.14: Laser source distribution

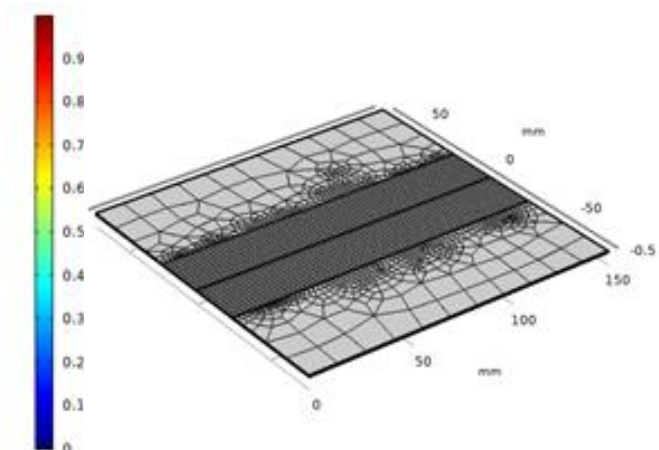


Fig.3.15: Mesh distribution on the treated blank

Table 3.1: Laser heat treatment condition

Treatment code	v [mm/s]	T_{peak} [degC]
T510V5	5	510
T400V5	5	400
T310V5	5	310
T510V7.5	7.5	510
T400V7.5	7.5	400
T310V7.5	7.5	310

The thermal cycles obtained with the laser conditions shown in Table 3.2 are plotted in Figure 3.16. In particular, the thermal cycles obtained with a treatment speed of 5 mm/s were represented with the

solid line, while the cycles obtained with a treatment speed of 7.5 mm/s were represented with the dotted line.

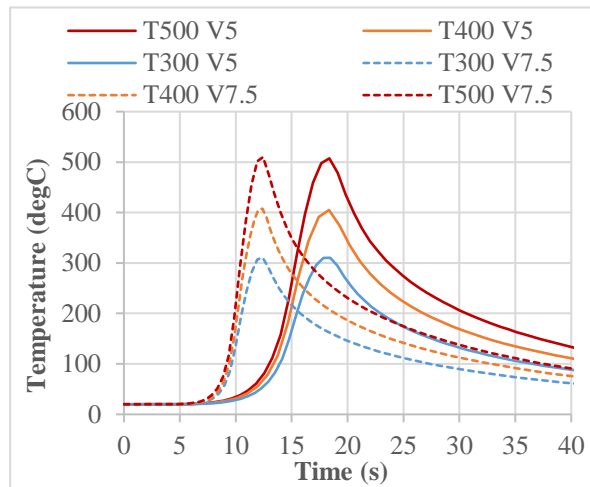


Fig.3.16: Laser thermal cycles investigated

These FE thermal cycles were then physically simulated using the Gleeble system. Since these are rapid thermal cycles, to satisfy cooling rate during Gleeble tests a tapered specimen were adopted (Figure 3.17a). The specimens geometry was defined thanks to optimization of length and width of shaped area by means of thermo-electric FE model described previously. This FE model, in fact, allowed to verify that a reduction in sheet thickness leads to an increase in the achievable cooling rates.

The physical simulation tests were carried out both on the tapered specimens that were subjected to the subsequent micro-hardness test, and on notched specimens that were subjected, instead, to the subsequent tensile test. Micro-hardness Vickers tests were performed in order to evaluate the softening effects induced by different laser simulated thermal cycles after physical simulation treatment (APS) and after physical simulation treatment and natural ageing (T4). Moreover, to evaluate the improvement of formability in APS and T4 conditions, tensile tests were carried out. Notched specimens (Figure 3.17b) were adopted during tensile tests in order to force plastic deformation exactly in the central point of the specimen which is the point where thermal cycle was imposed because it is the point where the control thermocouple was welded during the Gleeble test. Furthermore, tensile tests were assisted by the DIC (Digital Image Correlation) system to continuously acquire locally the strain distribution during the test.

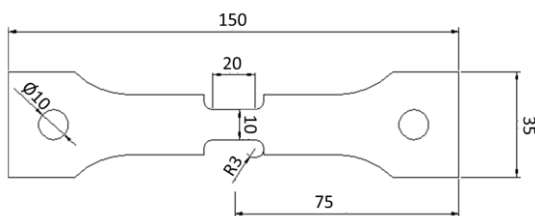


Fig.3.17a: Geometry of tapered specimens

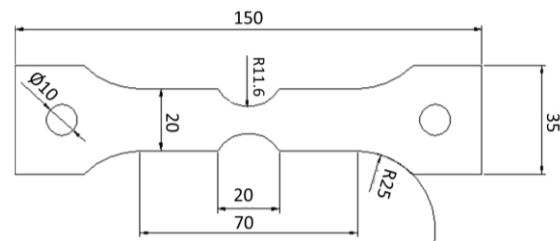


Fig.3.17b: Geometry of notched specimens

The effects of this treatment on the softening and deformability of the investigated alloy were analysed both at the T4 state and immediately after physical simulation (APS), in order to understand whether it is more appropriate to perform plastic deformations immediately after treatment or after natural aging.

Figure 3.18 sums up the hardness values obtained at the centre of tapered specimens immediately after physical simulation (Figure 3.18a) and after physical simulation and natural aging (Figure 3.18b), for each treatment speed and peak temperatures explored.

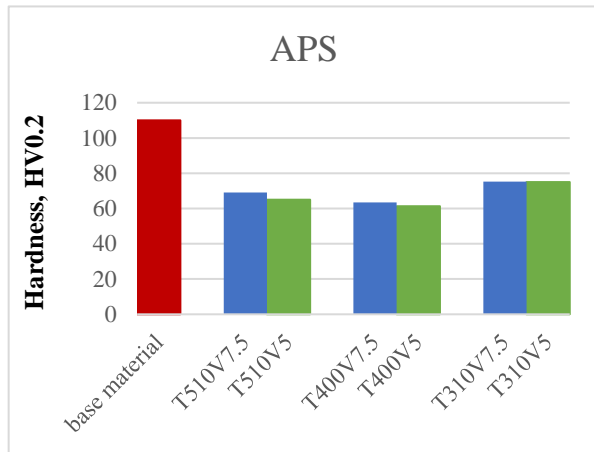


Fig.3.18a: Hardness values recorded at specimen centre after physical simulation test for different treatment speed and peak temperature

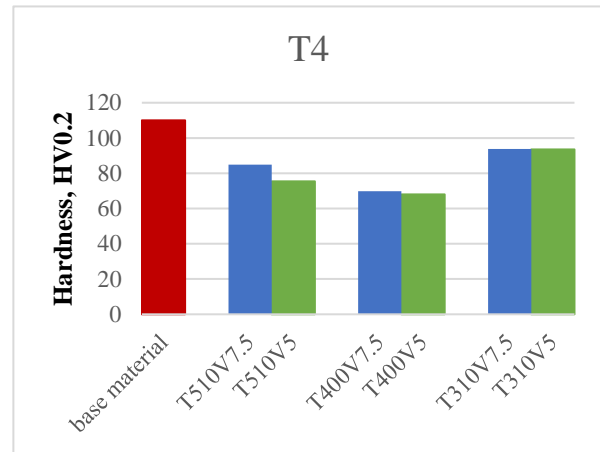


Fig.3.18b: Hardness values recorded at specimen centre after physical simulation and natural ageing for different treatment speed and peak temperature

It is observed that as the treatment speed decreases, the hardness value slightly decreases for all peak temperatures investigated. However, the effect of treatment speed on softening is more evident at the highest peak temperatures tested, especially in the T4 condition. This behaviour is justified by the greater dissolution of precipitates initially present in the alloy. As regards the moment in which the micro-hardness measurements were performed, the softening obtained in T4 condition are constantly lower than those measured in the APS condition, confirming a precipitation of Mg and Si atoms solubilized during thermal cycle imposed with the physical simulation. Finally, a marked influence of peak temperature is observed, with the greatest reduction in hardness at the peak temperature of about 400 °C, especially in T4 condition.

In Figures 3.19a and 3.19b the maximum values of equivalent Von Mises strain of treatments with the two different treatment speed and peak temperatures of about 500 °C, 400 °C and 300 °C recorded immediately after the Gleeble treatment and after natural aging respectively are reported. The maximum value of the Von Mises equivalent strain allows to understand if there has been an improvement in terms of elongation at break.

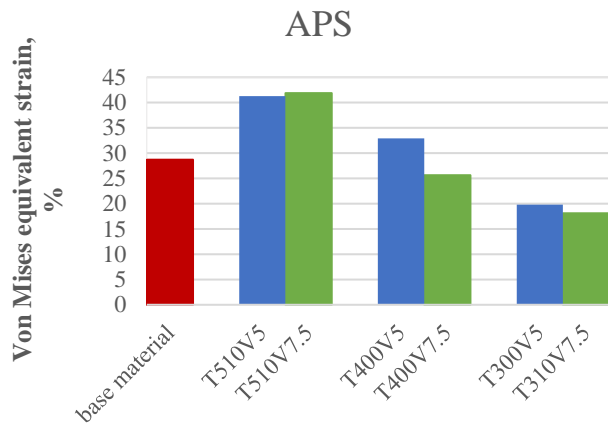


Fig.3.19a: Von Mises equivalent strain after physical simulation for all laser condition investigated and comparison with material base

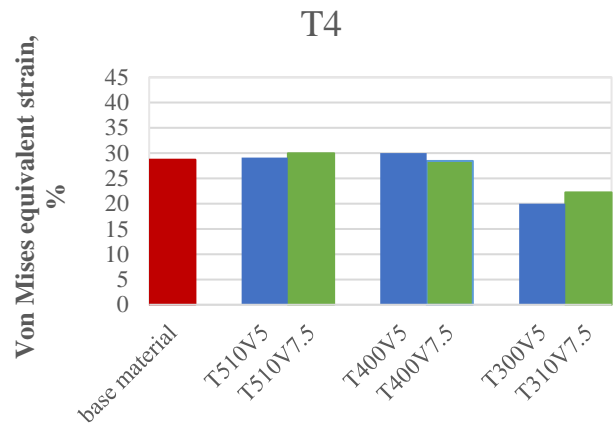


Fig.3.19b: Von Mises equivalent strain after natural ageing for all laser condition investigated and comparison with material base

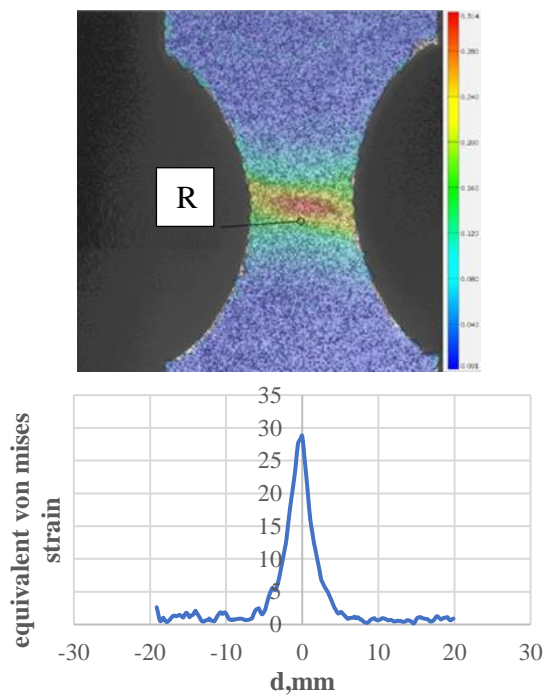


Fig.3.20a: equivalent Von Mises strain across specimen longitudinal section

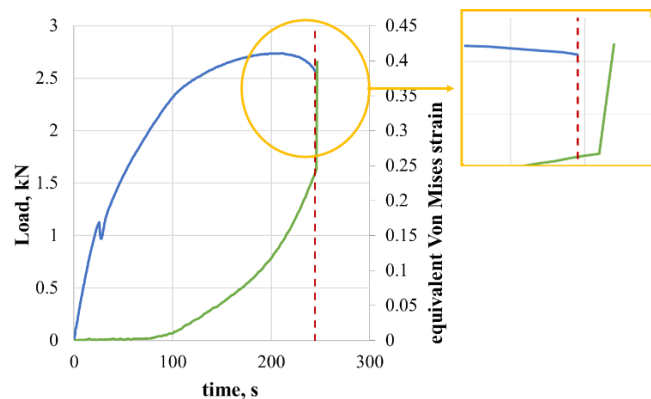


Fig.3.20b: load versus time curve and the equivalent strain versus time curve in correspondence of rupture point

The values of Von Mises equivalent strain are obtained in the rupture point R (Figure 3.20a), at the end of post-necking before failure (Figure 3.20b). In Figure 3.20a, the deformation profile as a function of the distance from the centre of the specimen is shown in addition to the deformation distribution on the specimen and the point in which the rupture occurs. On the other hand, Figure 3.20b shows the trend of force and deformation as a time function; in detail image, the point where the fracture strain (in terms of Von Mises equivalent strain) is considered is better highlighted.

Observing Figure 3.19a it is understood that immediately after physical simulation, a significant increase in deformability is obtained, with respect to the base material, for the cycles that have reached the peak temperature of 500 °C. Even at 400 °C a slight improvement in deformability is observed. For cycles that reached a peak temperature of 300 °C, a decrease in equivalent strain is observed. These results are justified because for peak temperatures between 400 °C and 500 °C the heat flux is sufficiently strong so that the MgSi clusters are increasingly completely dissolved. This leads to greater ductility of the material.

On the other hand, when the peak temperature is 300 °C, the presence of semi-coherent and coherent precipitates leads to a reduction in ductility with respect to the base material. These results are also confirmed by the evaluation of fracture strain after natural aging (Figure 3.19b).

The results are in line with the references. In fact, already in the previous investigations by M. Merklein et al. [48-49] and Geiger et al. [50] there is a reduction of uniform elongation at a temperature of 300 °C. However, it can be observed that in T4 state, for the cycles that have reached a peak temperature of 500 °C, a deformability of the material lower than about 10% is obtained with respect to the elongation obtained immediately after Gleeble treatment. This is due to the reprecipitation of the Mg and Si atoms. Furthermore, both data allow to state that the laser treatment speed did not influence the deformability.

The correct design of the specimen with the FE model described in the paragraph 3.1 allowed to physically simulate the laser thermal cycles with the Gleeble system to study the effect of softening on the aluminium alloy EN AW 6082 T6 as the treatment speed and peak temperature vary.

Also in this case, Gleeble proved to be a valid tool for studying and designing the laser surface heat treatment. In fact, having identified how the process parameters affect the mechanical properties of the investigated alloy, it is possible to choose which process parameters to impose to reach a certain level of softening.

3.2 Specimen design for mechanical characterization of Advanced High Strength Steel (AHSS) by means of Gleeble system

This section explores the use of the Gleeble system in order to derive the rheological behaviour at elevated temperature, in the austenitic field, of an advanced high strength boron steel for hot stamping application.

For the mechanical characterization tests carried out using the Gleeble physical simulator it must be considered that during Gleeble tests, thermal gradients occur on the sample due to the cooled grips (as described in the section 2.3).

Since the aim is the characterization of the flow behaviour of the material at a certain temperature, it is necessary to ensure that in the fracture zone this deformation temperature is respected. This means designing a specimen that guarantees low thermal gradients. In fact, to enhance the temperature uniformity, it is advisable to impose a certain dwell time at the test temperature before imposing a certain deformation.

Moreover, due to thermal gradients on the samples, it is necessary to reduce the gauge length to ensure that the rupture occurs exactly in the zone at the test temperature.

The goal is to identify the rheological behaviour of the material for the hot stamping application, therefore the mechanical characterization should be performed in the austenitic field. To ensure that the mechanical characterization takes place in the austenitic field, it is necessary to guarantee high

cooling rates during the cooling phase from the complete austenitization temperature (930 °C) to the test temperature to avoid that other phase transformations occur.

Therefore, the design of the specimen was performed with the aim of optimizing the width and length of the gauge length to ensure high cooling rates and to minimize, at the same time, the thermal gradient.

A thermo-electric-mechanical FE code in COMSOL Multiphysics was developed to optimize the sample geometry. The material selected for the FE model is USIOR[®]1500 (22MnB5) of 1.8 mm thick. The thermal cycle imposed in the FE code includes (Figure 3.21):

- Heating from ambient temperature to 705 °C with heating rate of 10 K/s;
- Heating up to the complete austenitization temperature of 930 °C with a heating rate of 5 K/s;
- Keeping phase at 930 °C for 240s (4 minutes) to ensure the complete austenitic microstructure;
- Cooling at test temperature with high cooling rate;
- Keeping phase at a dwell time to ensure a uniform deformation temperature;
- Deformation at test temperature for certain strain rate values;
- Cooling at room temperature.

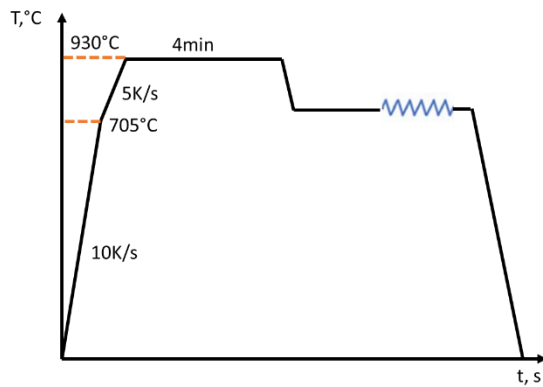


Fig. 3.21: Scheme of cycles for mechanical characterization

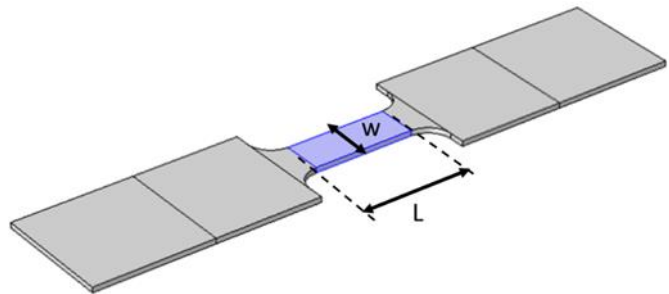


Fig. 3.22: Parameters (w and L) considered to optimize geometry of Gleeble specimen for mechanical characterization test

The choice of the heating rates, the austenitization temperature and the soaking time at this temperature was made based on the work of Jing Zhou et al. [51] for the 22MnB5 steel.

A Proportional-Integrative-Derivative (PID) controller was implemented in the FE model in order to guarantee the required thermal cycle in the control point, during heating and keeping phase at complete austenitization temperature.

The heat removed from the clamps, which are kept at a low temperature thanks to the use of a water-glycol solution that circulates inside them, was modelled as heat lost by convection.

Since one of the two clamps is connected to the hydraulic piston for the subsequent deformation test, mechanical physics was introduced in the model. The area of the specimen in contact with the clamp connected to the hydraulic piston is unconstrained, while the area of the specimen in contact with the opposite clamp is constrained by imposing all displacements equal to zero. FE model can measure thermal expansions that occur as a result of the temperature variation.

The PID parameters and the heat transfer coefficient were set after calibration with preliminary experimental results obtained with a specimen characterized by a length of 25 mm and a width of 10 mm. Figure 3.22 shows the w and L parameters of specimen to optimize the Gleeble sample to carry out mechanical characterization tests.

In this section, as an example, the study of the influence of width (w) and length (L) of the gauge length specimen on thermal gradient and cooling rate is shown for deformation temperature of 700 °C. The L and w values were varied in the range 15 mm – 25 mm and 6 mm – 10 mm, respectively. The numerical results were elaborated to create metamodells using the kriging technique that describe the influence of the parameters w and L on the thermal gradient and on the cooling rate. Figures 3.23a, 3.23b and 3.23c respectively show the thermal gradient at the end of the keeping phase at the temperature of 930 °C, at the end of the keeping phase at the test temperature of 700 °C before starting the deformation phase and the cooling rate during cooling from 930 °C to 700 °C, as L and w vary. The thermal gradient was calculated on a width of 5 mm. Figure 3.23d shows, more clearly, by means of isolines the influence of the specimen geometric parameters w and L as the cooling rate changes during the cooling phase from the complete austenitization temperature to the test temperature, in this case of 700 °C.

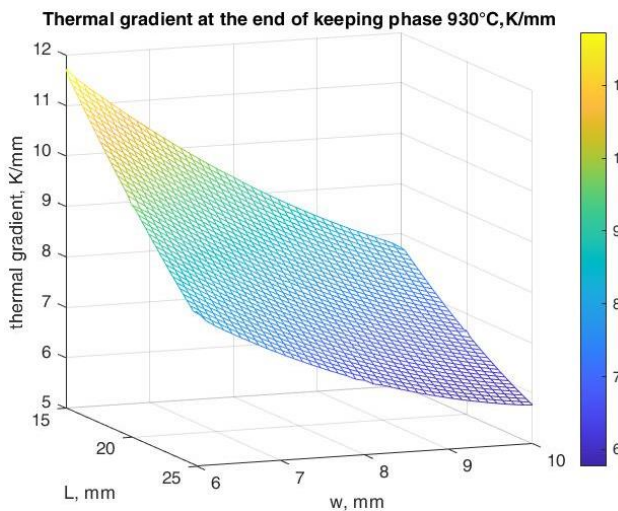


Fig.3.23a: Metamodel of thermal gradient at the end of keeping phase at 930°C as a function of L and w

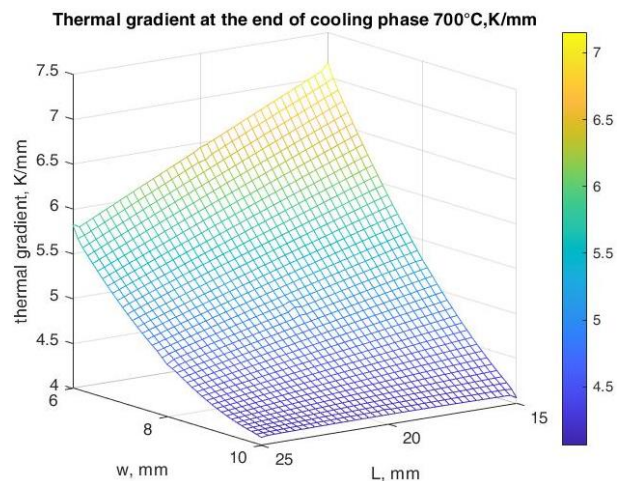


Fig.3.23b: Metamodel of thermal gradient at the end of keeping phase at 700°C as a function of L and w

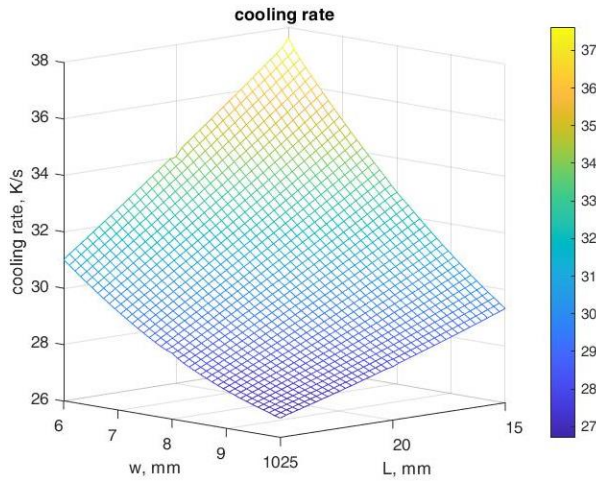


Fig.3.23c: Metamodel of cooling rate (from 930°C to 700°C) as a function of L and w

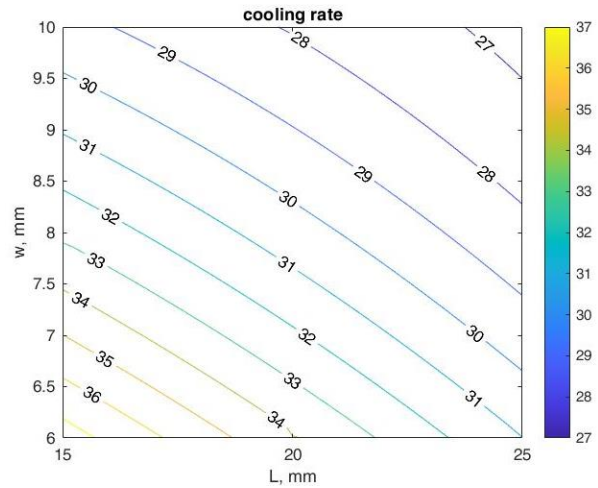


Fig.3.23d: Effect of the L and w parameters on the cooling rate (isolines)

From the metamodels in Figures 3.23a and 3.23b it can be seen that an increase in w and L leads to a reduction in the thermal gradients on the specimen. The geometric configuration characterized by parameters L and w equal to 25 mm and 10 mm, respectively, leads to a thermal gradient before the deformation phase of about 4 K on 5 mm width. This geometric configuration is the optimal one as it leads to low thermal gradients. Instead, from the graphs shown in Figures 3.23c and 3.23d it is observed that the cooling rate increases as the parameters L and w decrease. Therefore, in order to have a cooling rate as high as possible, the optimal geometric configuration involves a values of L and w equal to 15 mm and 6 mm, respectively. However, this geometric configuration would lead to thermal gradients of about 7.5 K/mm before the deformation phase. This thermal gradient is high and it could lead to unreliable data for deriving flow curves after mechanical characterization tests. Therefore, the optimal geometric configuration is the one with the values of L and w equal to 25 mm and 10 mm, respectively. For this geometric configuration, it was evaluated how the cooling rate and the thermal gradient vary as the metal sheet thickness varies (Figure 3.24).

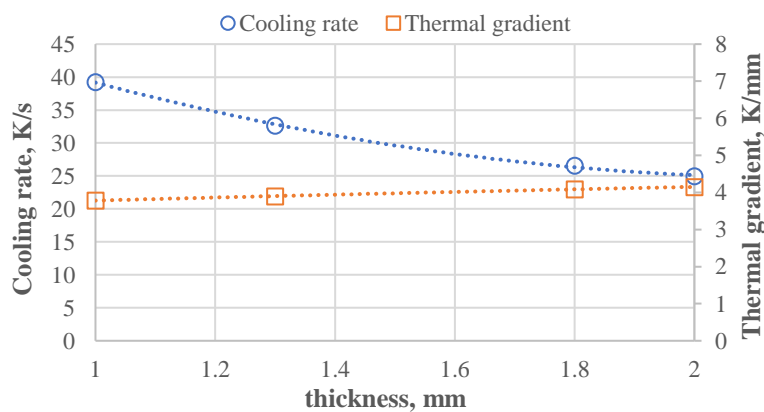


Fig.3.24: Effect of sheet metal thickness on cooling rate and thermal gradient

It is observed that the thickness significantly affects the cooling rate; in particular, as expected, an increase in thickness leads to a reduction in the cooling rate since the masses involved are greater and

the heat is dissipated more slowly. On the other hand, an increase in thickness leads to a slight increase in the thermal gradient. For optimal geometric configuration identified, Figure 3.25 shows the distribution on the specimen of the current density at the end of the keeping phase at 930 °C. Figure 3.26, on the other hand, shows the profiles of current density and electric potential as a function of the length of the specimen.

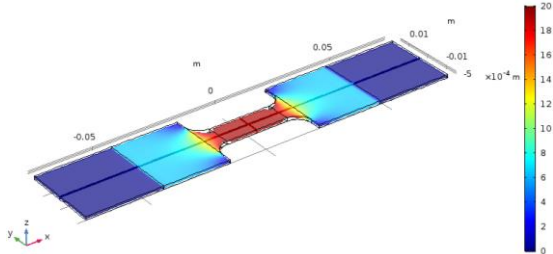


Fig.3.25: Current density distribution at the end of the keeping phase at 930°C

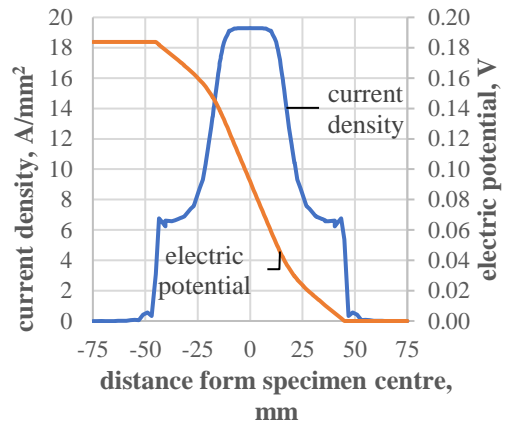


Fig. 3.26: Electric potential and current density profile at the end of the austenitization phase

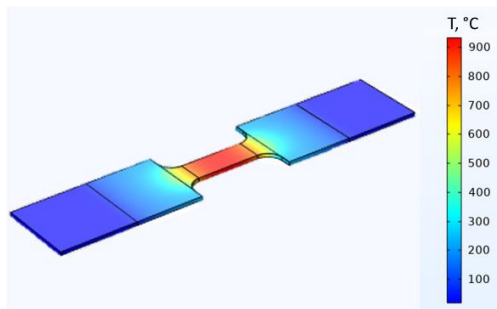


Fig.3.27: Temperature distribution on sample at the end of austenitization phase (930 °C)

From these graphs it is clear the effect of the tapering specimen; this reduction of central section of the specimen allows to differentiate the current density between the tapered zone and the adjacent one, with consequent differentiation of the temperatures between these zones, as can be seen in Figure 3.27. This figure, in fact, shows the temperatures distribution on the specimen at the end of the keeping phase at 930°C. It can be seen that the heating is localized in the central area of the specimen, while the lateral ones are kept at a lower temperature. This is due to the tapering of specimen in the central area that allows, in the subsequent cooling phase, a greater cooling rate.

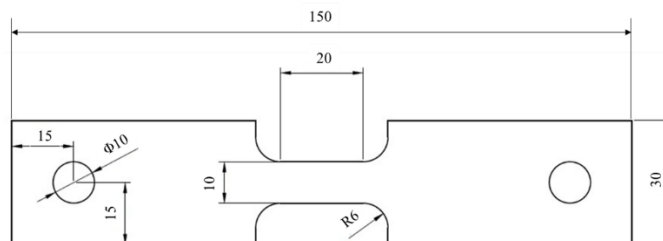


Fig. 3.28: geometry of sample in USIBOR®2000 adopted during hot mechanical characterization test

The FE model described so far allowed to design the mechanical characterization tests in the austenitic field (for the temperatures of 750 °C – 850 °C and for the deformation rates of 0.01s^{-1} – 1s^{-1}) of USIBOR®2000 specimens of 2 mm thick. Although the increase in thickness leads to a reduction in the cooling rate (Figure 3.24), a specimen geometry with w and L equal to 10 mm and 20 mm, respectively, was chosen (Figure 3.28). In this way, low thermal gradients were preferred. Furthermore, for the temperatures and strain rates of interest, the cooling rate of 25 K/s is able to guarantee the characterization in the austenitic field. As it will be explained in the next paragraph, this cooling rate is not sufficient to characterize this steel in the austenitic field, at lower temperatures and strain rate (0.001s^{-1}).

For low temperatures and low strain rates, it is possible to increase the cooling rate by using forced air through the quenching spray hands present in the Gleeble test chamber. However, this solution should be avoided because it would lead to oxidation problems on the specimen.

3.2.1 Flow curve of the AHSS USIBOR®2000

To obtain the flow behaviour of USBIBOR®2000 at high temperatures, thermo-mechanical test were performed on a Gleeble 3180 physical simulator. The experimental setup has been already shown in Figure 2.13 in section 2.3. In particular, the specimen in USIBOR®2000 2mm thick is clamped in a vacuum chamber using copper grips. A NiCr–NiSi thermocouple spot welded at the centre of the specimen was used to ensure that the specimen temperature profile follows the set one. Moreover, these tensile tests were assisted by the extensometer HZT071 that is characterized by alumina rods in contact with specimen for lengthwise measurement of the strain in the central hot zone of the specimen (gauge length is 10 mm) in which a uniform thermal gradient is present. Actually, the results described in the previous section 3.2 reveal that a thermal gradient of 4 K/mm is recorded on the sample. Moreover, these results show that a cooling rate of 25 K/s is assured during cooling rate from complete austenitization temperature to test temperature.

Temperatures investigated are 900°C, 850°C, 800°C, 750°C, 700°C and 650°C; instead strain rate investigated are 1s^{-1} , 0.1s^{-1} , 0.01s^{-1} and 0.001s^{-1} . The imposed thermo-mechanical cycles have been already shown in 3.2.

To describe the relationship between the strain rate, flow stress and temperature, Arrhenius type constitutive equation was derived. For this purpose, a subroutine that processes the results of the physical simulation tests was written in MATLAB, allowing to calculate the material coefficients.

True stress vs true strain curves at different temperatures and strain rates are given in Figures 3.29. It was observed that the temperature and strain rate have significant effects on the mechanical properties of the investigated steel. The increase of temperature and the decrease of strain rate reduce the material resistance. To better understand the trend of the stress-strain curves it is necessary to highlight the phenomena that occur in the material during a hot tensile test.

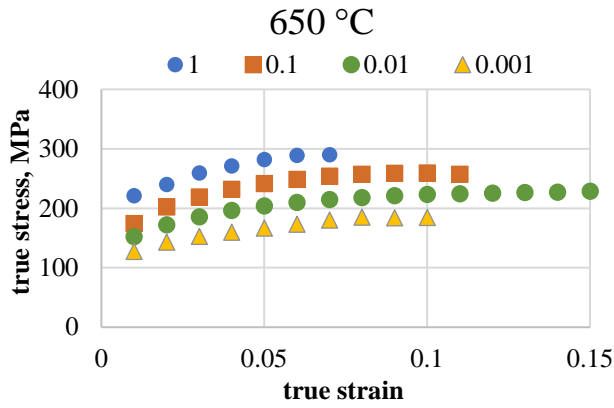


Fig. 3.29a: Flow stress curves in the strain range $1s^{-1}$ - $0.001s^{-1}$ at a deformation temperature of $650^{\circ}C$

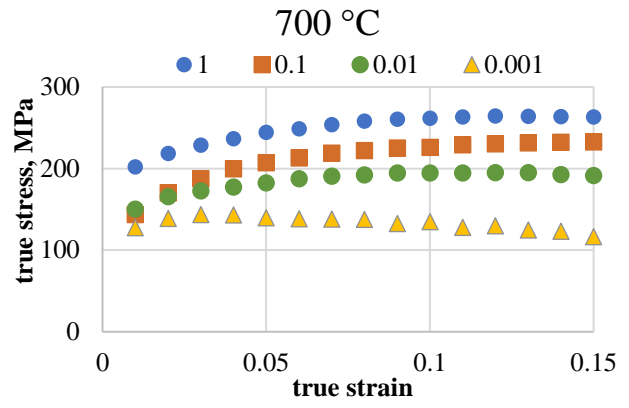


Fig. 3.29b: Flow stress curves in the strain range $1s^{-1}$ - $0.001s^{-1}$ at a deformation temperature of $700^{\circ}C$

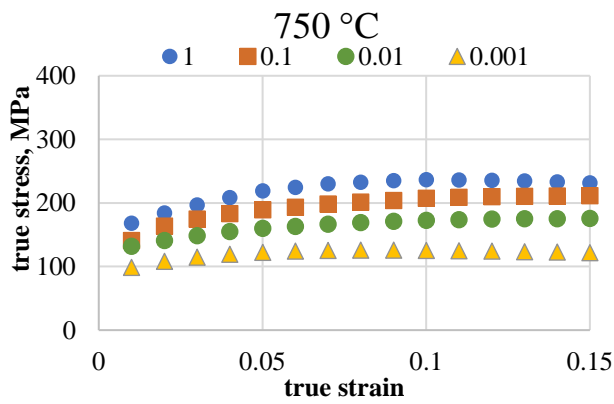


Fig. 3.29c: Flow stress curves in the strain range $1s^{-1}$ - $0.001s^{-1}$ at a deformation temperature of $750^{\circ}C$

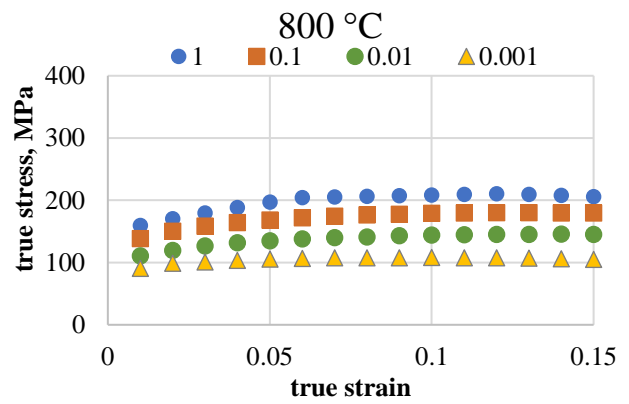


Fig. 3.29d: Flow stress curves in the strain range $1s^{-1}$ - $0.001s^{-1}$ at a deformation temperature of $800^{\circ}C$

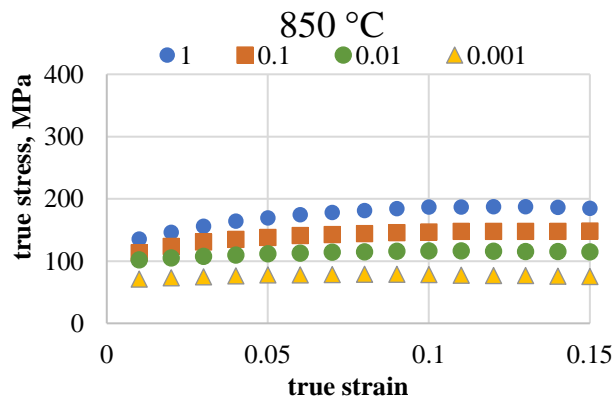


Fig. 3.29e: Flow stress curves in the strain range $1s^{-1}$ - $0.001s^{-1}$ at a deformation temperature of $850^{\circ}C$

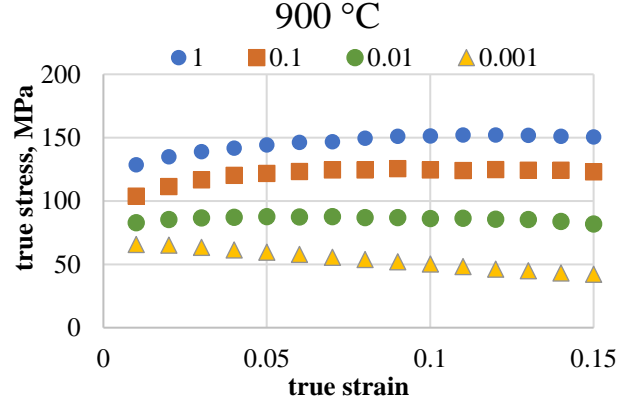


Fig. 3.29f: Flow stress curves in the strain range $1s^{-1}$ - $0.001s^{-1}$ at a deformation temperature of $900^{\circ}C$

These phenomena are schematized in Figure 3.30. In the initial stage of deformation, work hardening phenomenon is present, causing a dislocation multiplication [52]. With the rise of deformation, the work hardening effect becomes negligible and softening effects such as dynamic recovery (DRV) and

dynamic recrystallization (DRX) become predominant. This leads to a reduction in the increased stress with deformation.

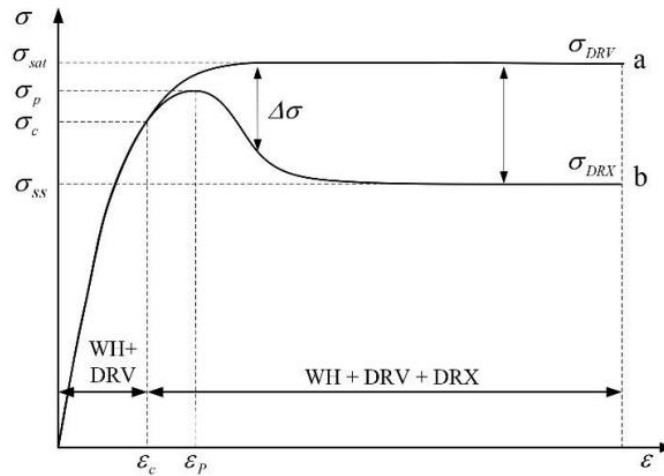


Fig. 3.30: work hardening, dynamic recovery and dynamic recrystallization that occur during hot deformation [53]

When the softening effect caused by dynamic recovery reaches dynamic equilibrium with work hardening, the stress value remains constant, tend to reach to a plateau named saturated stress (σ_{sat}). When the strain reaches critical value (ϵ_c), the DRX phenomenon occurs. This effect becomes more evident when maximum stress (σ_{max}/σ_p) is reached and it leads to a reduction of stress with the increasing of deformation. When the softening mechanism is in equilibrium with the work hardening effect, the stress is equal to a steady stress value (σ_{ss}) [53]. Furthermore, the two described softening effects (DRV+DRX) are more evident at high temperatures and low deformation rates. Observing the curves in Figure 3.28 it is possible to state that in the most cases as the strain increased from 0.01 to 0.15, the flow stress increases and the rate with which the flow stress increases is greater in the first part of the curve and less in the second part. This behaviour is justified by the work hardening and dynamic recovery phenomena. However, there are curves that differ from this behaviour. In fact, for example, continuous strain hardening behaviour of the material could be observed at deformation temperature of 650 °C and strain rate of 1 s^{-1} ($T650^{\circ}\text{C}\epsilon'1\text{s}^{-1}$) because once maximum stress is reached, the specimen breaks. Regarding the flow curves obtained at deformation temperature of 650 °C, it is also observed that the fracture deformation in the condition with a strain rate of 0.001s^{-1} is less than that obtained with a strain rate of 0.01s^{-1} . In fact, during Gleeble tests in the condition $T650^{\circ}\text{C}\epsilon'0.001\text{s}^{-1}$ (temperature deformation of 650 °C and strain rate of 0.001 s^{-1}) the cooling rate at deformation temperature of about 25 K/s is not sufficient to guarantee the characterization in the austenitic field.

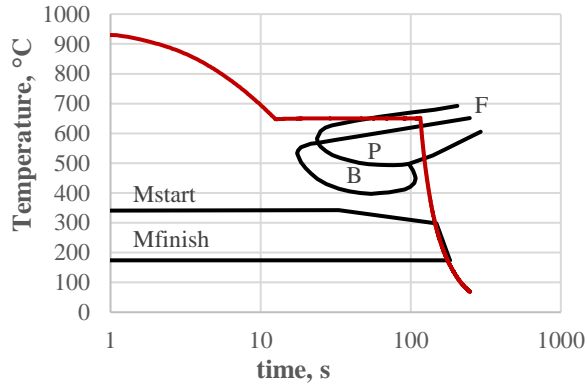


Fig. 3.31: CCT diagram of 37MnB5 boron steel and thermal cycle for deformation temperature of 650 °C and strain rate 0.001s⁻¹

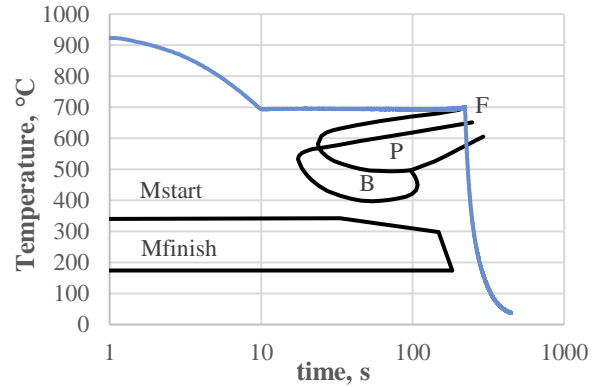


Fig. 3.32: CCT diagram of 37MnB5 boron steel and thermal cycle for deformation temperature of 700 °C and strain rate 0.001s⁻¹

This is highlighted in Figure 3.31 where the thermal cycle recorded by the control central thermocouple during the test is superimposed on the CCT diagram of USIBOR[®]2000 (37MnB5). From Figure 3.31 it is possible to observe that during the hot tensile test, the ferritic transformation took place. This justifies the stress-strain curve obtained in the condition T650°Cε'0.001s⁻¹) shown previously in Figure 3.29a. In fact, in this test condition, it is observed that failure occurs at a deformation of about 0.1.

The stress drop observed at a deformation temperature of 700 °C and low strain rate of 0.001s⁻¹ (T700°Cε'0.001s⁻¹) is due to the ferritic transformation. Figure 3.32 shows the thermal cycle corresponding to the test condition T700°Cε'0.001s⁻¹ to highlight the ferritic transformation that occurs in this case.

Sumit Ghosh et al. [54] had already observed a stress drop after peak stress for ferrite flow stress curves at high temperatures and low strain rates for Ti+Nb stabilized interstitial free steel.

The effects of DRX begin to be evident in the flow curves obtained at the temperature of 900 °C for a strain rate range of 0.1s⁻¹ and 0.001s⁻¹ and for the temperature test of 850 °C and strain rate of 0.001 s⁻¹. However, in no condition the flow stress becomes steady. The characteristics of dynamic recrystallization are more easily observed during compression tests rather than during tensile tests, since during hot compression tests there is enough deformation to ensure the occurrence of DRX [53].

3.2.2 Constitutive model of USIBOR[®]2000

Considering only a range of deformation temperature and strain rate of interest for applications in the Press-Hardening process, the constitutive equations of USIBOR[®]2000 as a function of the Zener-Hollomon [55] factor have been obtained. The range of temperatures and strain rates adopted are 750 °C -850 °C and 1 s⁻¹ - 0.01 s⁻¹, respectively. In these test conditions, the mechanical characterization took place in the austenitic field.

The Zener-Hollomon parameter used to represent the effect of strain rate and temperature on hot deformation is described by the equation (3.1):

$$Z = \dot{\epsilon} * \exp\left(\frac{Q}{RT}\right) \quad (3.1)$$

Where $\dot{\epsilon}$ is the strain rate (s^{-1}), R is the gas constant ($\frac{J}{mol \cdot K}$), T is the absolute temperature (K) and Q is the activation energy ($\frac{J}{mol}$).

The Arrhenius constitutive equation that describes the relationship between strain rate, flow stress and temperature is:

$$\dot{\epsilon} = AF(\sigma) * \exp\left(-\frac{Q}{RT}\right) \quad (3.2)$$

Where:

$$F(\sigma) = \begin{cases} \sigma_{max}^{n'} & \alpha\sigma < 0.8 \quad (3.3) \\ \exp(\beta\sigma_{max}) & \alpha\sigma > 1.2 \quad (3.4) \end{cases}$$

$$(\sinh(\alpha\sigma_{max}))^n \text{ for all stress levels} \quad (3.5)$$

n' , β , α , n are material constants and α can be expressed as $\frac{\beta}{n'}$. Moreover, σ_{max} is the peak stress.

Replacing equations (3.3), (3.4), (3.5) in equation (3.2), the following expressions are obtained:

$$\dot{\epsilon} = A_1 \sigma_{max}^{n'} * \exp\left(-\frac{Q}{RT}\right) \quad \alpha\sigma < 0.8 \quad (3.6)$$

$$\dot{\epsilon} = A_2 \exp(\beta\sigma_{max}) * \exp\left(-\frac{Q}{RT}\right) \quad \alpha\sigma > 1.2 \quad (3.7)$$

$$\dot{\epsilon} = A (\sinh(\alpha\sigma_{max}))^n * \exp\left(-\frac{Q}{RT}\right) \text{ for all stress level} \quad (3.8)$$

Turning to logarithmic expressions for equation (3.6), (3.7) and (3.8), the following expressions are obtained:

$$\ln\dot{\epsilon} = \ln A_1 + n' \ln \sigma_{max} - \frac{Q}{RT} \quad \alpha\sigma < 0.8 \quad (3.9)$$

$$\ln\dot{\epsilon} = \ln A_2 + \beta \sigma_{max} - \frac{Q}{RT} \quad \alpha\sigma > 1.2 \quad (3.10)$$

$$\ln\dot{\epsilon} = \ln A + n \ln (\sinh(\alpha\sigma_{max})) - \frac{Q}{RT} \text{ for all stress level} \quad (3.11)$$

The relationship between $\ln\dot{\epsilon}$ and $\ln\sigma$ and that between $\ln\dot{\epsilon}$ and σ at different temperatures are shown in the graphs in Figure 3.33a and 3.33b.

There is a linear relationship between $\ln\dot{\epsilon}$ and $\ln\sigma$ as well as between $\ln\dot{\epsilon}$ and σ . In fact, the dashed lines correctly approximate the points. The graphs also show the equations of the trend lines. The parameters n' and β can be obtained from the slope of the lines in Figures 3.33a and 3.33b. At a strain of 0.15, the average values of these coefficients are 13.3743 and 0.0663 MPa^{-1} , respectively.

By considering that $\alpha = \frac{\beta}{n'}$, it is possible to calculate the corresponding value of α coefficient equal to 0.005 MPa^{-1} .

In Figure 3.33a the relationship between $\ln\dot{\epsilon}$ and $\ln(\sinh(\alpha\sigma_{max}))$ at different temperatures is illustrated.

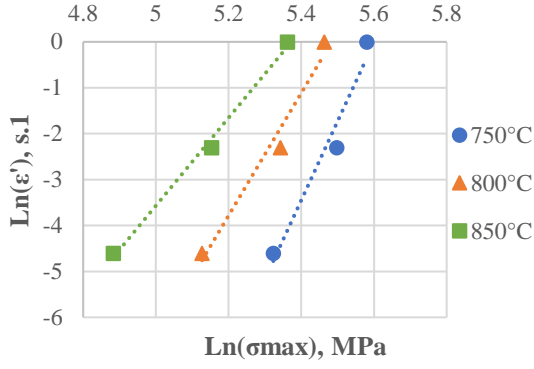


Fig. 3.33a: Relationships at different temperatures between $\ln\dot{\epsilon}$ and $\ln\sigma$

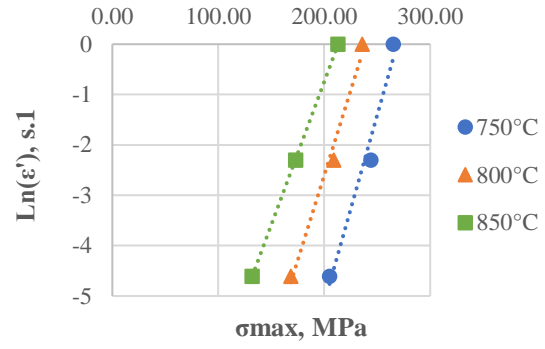


Fig. 3.33b: Relationships at different temperatures between $\ln\dot{\epsilon}$ and σ

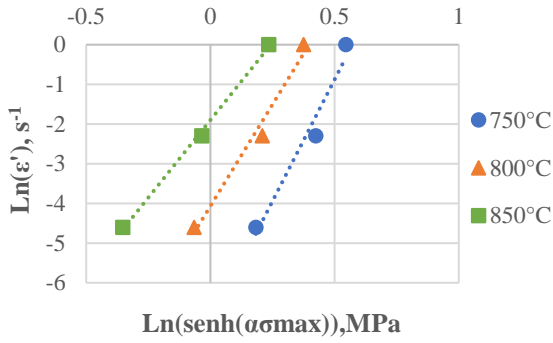


Fig. 3.34a: Relationship at different temperatures between $\ln\dot{\epsilon}$ and $\ln\sinh(\alpha\sigma_{max})$

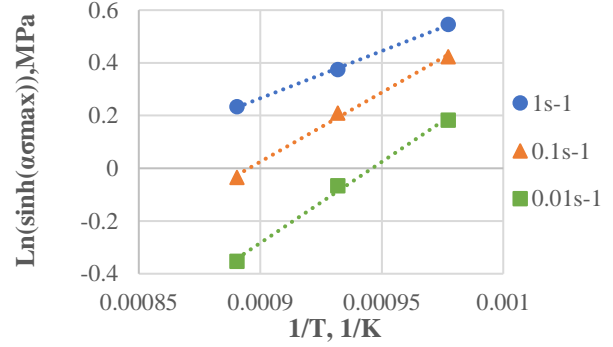


Fig. 3.34b: Relationship at different strain rate between $\sinh(\alpha\sigma_{max})$ and $1/T$

Also between $\ln\dot{\epsilon}$ and $\ln(\sinh(\alpha\sigma_{max}))$ there is a linear relationship. Therefore, the material coefficient n is the slope of the lines shown in Figure 3.34a. The average values, at a strain of 0.15, is 10.1075.

To derive the activation energy Q , equation (3.8) is differentiated and, considering the constant strain rate, the following expression is achieved:

$$Q = Rn * \left[\frac{\partial \ln(\sinh(\alpha\sigma_{max}))}{\partial \frac{1}{T}} \right] \quad (3.12)$$

Hence, in Figure 3.34b, the linear relationship between $(\sinh(\alpha\sigma_{max}))$ and $\frac{1}{T}$ for different strain rate conditions is shown. The material coefficients Q and A can be calculated, respectively, from the slope and intercept of the lines in Figure 3.34b. The average value of Q is 419.75KJ/mol.

Replacing activation energy, temperatures and strain rates values into the equation (3.1), Zener-Hollomon factors are obtained.

However, the Arrhenius equation doesn't take into account the strain effect. Therefore, material coefficient for strains ranging from 0.01 to 0.15 at intervals of 0.01 are determined using the procedure just mentioned above. At the end, a fifth-order polynomial fit (equations 3.13,3.14,3.15 and 3.16) is used to describe the relationship between the strain and the material coefficient (α , n , Q and $\ln A$). In this way, it is possible to calculate the flow stress at different strains.

$$\alpha = A_5\varepsilon^5 + A_4\varepsilon^4 + A_3\varepsilon^3 + A_2\varepsilon^2 + A_1\varepsilon + A_0 \quad (3.13)$$

$$n = B_5\varepsilon^5 + B_4\varepsilon^4 + B_3\varepsilon^3 + B_2\varepsilon^2 + B_1\varepsilon + B_0 \quad (3.14)$$

$$Q = C_5\varepsilon^5 + C_4\varepsilon^4 + C_3\varepsilon^3 + C_2\varepsilon^2 + C_1\varepsilon + C \quad (3.15)$$

$$\ln A = D_5\varepsilon^5 + D_4\varepsilon^4 + D_3\varepsilon^3 + D_2\varepsilon^2 + D_1\varepsilon + D_0 \quad (3.16)$$

The coefficient of polynomial fitting are listed in Table 3.2.

Table 3.2: Polynomial coefficient of α , n , Q , $\ln A$

	α		n		Q		lnA
A_5	-23.404	B_5	53639	C_5	1E+10	D_5	1E+06
A_4	16.638	B_4	-24918	C_4	-6E+09	D_4	-643243
A_3	-4.9209	B_3	2214	C_3	1E+09	D_3	139528
A_2	0.7962	B_2	483.44	C_2	-1E+08	D_2	-13178
A_1	-0.0736	B_1	-83.194	C_1	5E+06	D_1	541.37
A_0	0.0081	B_0	12.403	C_0	299581	D_0	29.752

In Figure 3.35, the fitting curves, represented with the dashed lines, of material coefficient (α , n , Q , $\ln A$) as function of strain are presented.

Considering the equations (3.1) and (3.2), the relationship between the Zener-Hollomon parameter Z and the flow stress can be found. This relationship can be expressed as shown in the equation 3.17:

$$\sigma = \frac{1}{\alpha} \ln \left\{ \left(\frac{Z}{A} \right)^{1/n} + \left[\left(\frac{Z}{A} \right)^{2/n} + 1 \right]^{\frac{1}{2}} \right\} \quad (3.17)$$

Now the flows stress at different temperatures, strain rates and strains can be determined. Figure 3.36 shows the experimental stress-strain curves and the predicted ones. The first curves are highlighted with a solid lines, the second ones, on the other hand, with circular markers. As an example, in Figure 3.36 only the comparison as a function of different strain rate is shown. It follows that the flow stress-strain predicted curves using the Arrhenius constitutive equation is similar to the experimentally determined curves.

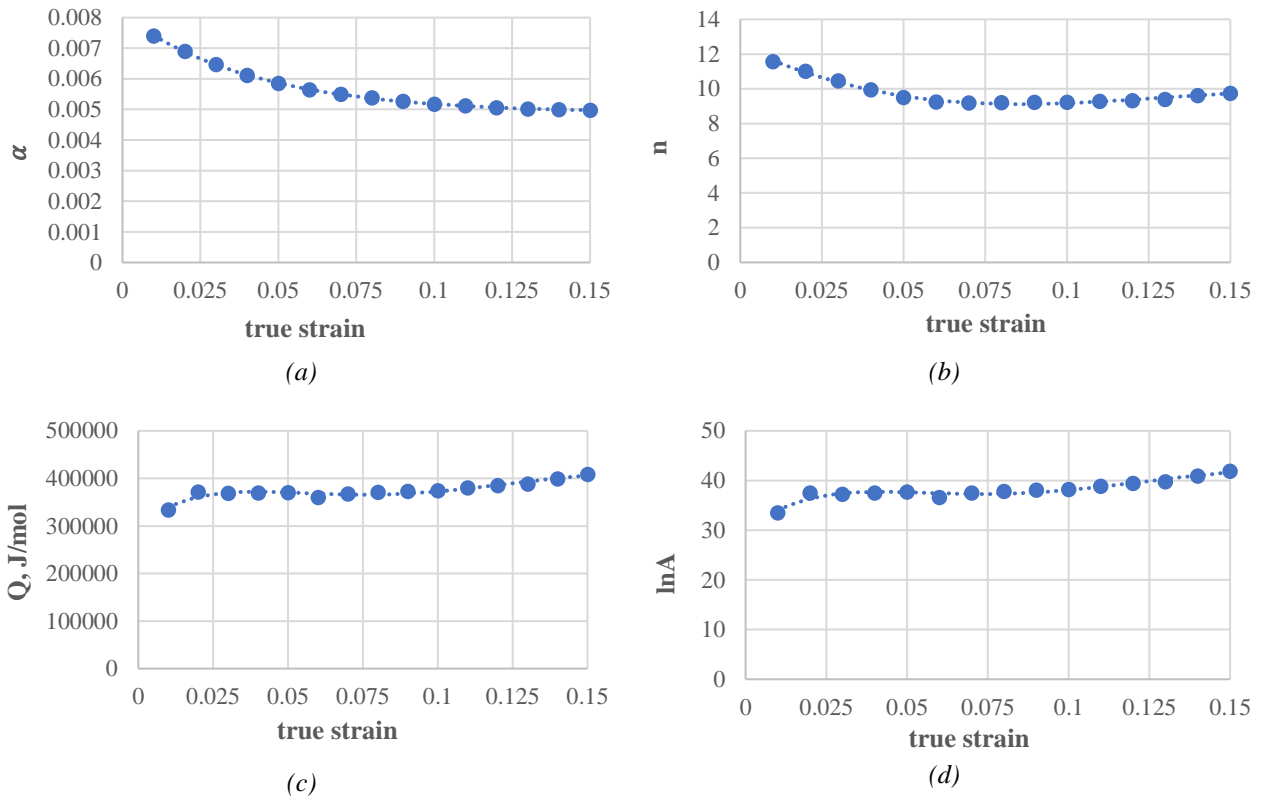


Fig.3.35: Polynomial fitting curves of material coefficients as a function of strain: (a) for α (b) n , (c) Q , and (d) $\ln A$

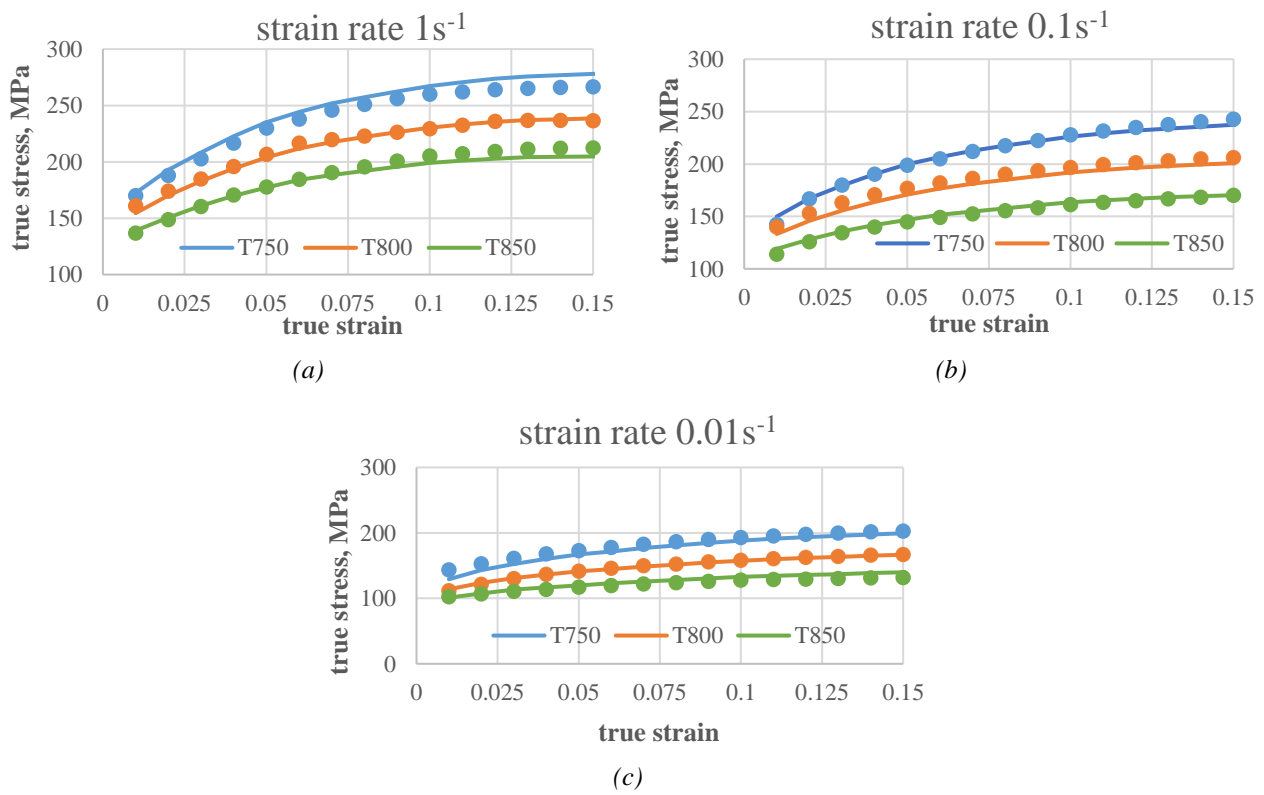


Fig. 3.36: Comparison between experimental stress-strain curves (solid line) and predicted stress-strain curves (circular markers) by the Arrhenius constitutive equation at various strain rates: (a) $1s^{-1}$, (b) $0.1s^{-1}$, and (c) $0.01s^{-1}$.

The quantitative accuracy of the model can be defined using the correlation coefficient R, the average absolute relative error (AARE), and the root mean square error (RMSE). These parameters are defined as follows:

$$R = \frac{\sum_{i=1}^n (E_i - \bar{E}) * (P_i - \bar{P})}{\sqrt{\sum_{i=1}^n (E_i - \bar{E})^2 * \sum_{i=1}^n (P_i - \bar{P})^2}} \quad (3.18)$$

$$AARE (\%) = \frac{1}{N} \sum_{i=1}^n \left| \frac{E_i - P_i}{E_i} \right| \quad (3.19)$$

$$RMSE = \sqrt{\frac{1}{n} * \sum_{i=1}^n (E_i - P_i)^2} \quad (3.20)$$

Where E_i represents the experimental data, P_i the predicted data using the Arrhenius model, \bar{E} and \bar{P} the mean values of the experimental and predicted data, respectively. Moreover n is the total number of samples. The values of R, AARE and RMSE parameters are 0.9992, 0.2512% and 1.2586 MPa, respectively. Since correlation coefficient is nearly to 1 and AARE value is low, it can be stated that the proposed constitutive equations accurately predict the flow behavior of USIBOR[®]2000.

3.2.3 Comparison between USIBOR[®]2000 AND USIBOR[®]1500

The Arrhenius model described so far, that allowed to derive the flow behavior of the USIBOR[®]2000, was also applied to the USIBOR[®]1500 starting from the experimental flow curves found in literature [51,53,56]. To achieve this, the same subroutine created to calculate the Zener-Hollomon factors of USIBOR[®]2000 was used. Figures 3.37 show the graphs of the material coefficients as a function of strains for both USIBOR[®]2000 and USIBOR[®]1500, in order to compare the two high-strength steels, as well as to verify the reliability of the results obtained for the USIBOR[®]2000.

The material coefficients of the two high-strength steels are compared in a deformation range of 0.1-0.15.

The results of the USIBOR[®]1500 Zener-Hollomon factors calculated with the USIBOR[®]2000 subroutine are in agreement with the results of references. Therefore it can be deduced that the subroutine developed in MATLAB is correct and consequently the results obtained for the USIBOR2000 are reliable.

The comparison between the two steels relative to the material coefficients are shown in Figures 3.37. It can be observed that for lower deformation values there is greater variability due to the lack of experimental data in the stress-strain curve. Moreover, from Figures 3.37a and 3.37b it can be observed that there are no great differences for the alpha and n coefficient; however more marked differences are observed for Q and lnA.

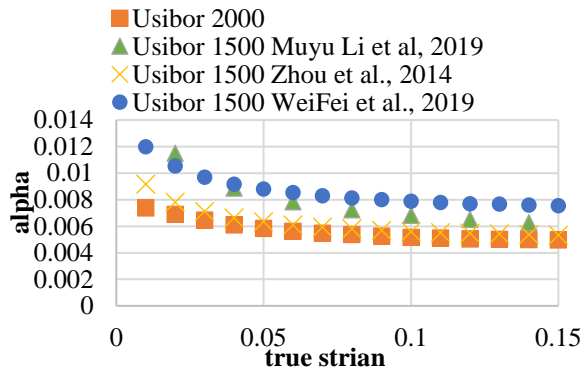


Fig 3.37a: Relationship between material coefficient α and the true strain for both USIBOR[®]2000 and USIBOR[®]1500

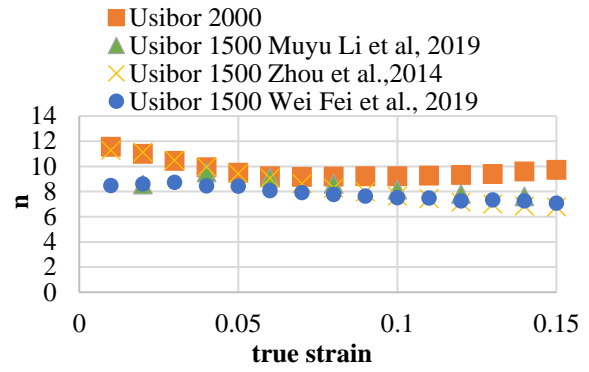


Fig. 3.37b Relationship between material coefficient n and the true strain for both USIBOR[®]2000 and USIBOR[®]1500

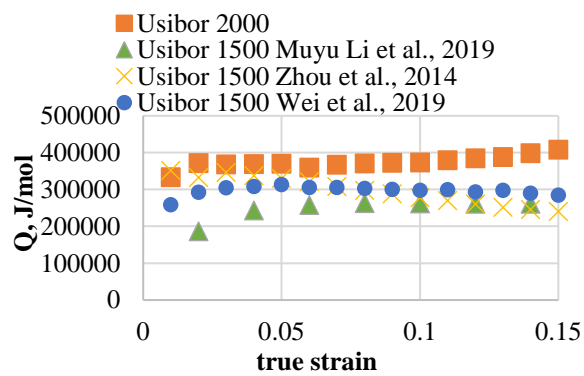


Fig. 3.37c: Relationship between material coefficient Q and the true strain for both USIBOR[®]2000 and USIBOR[®]1500

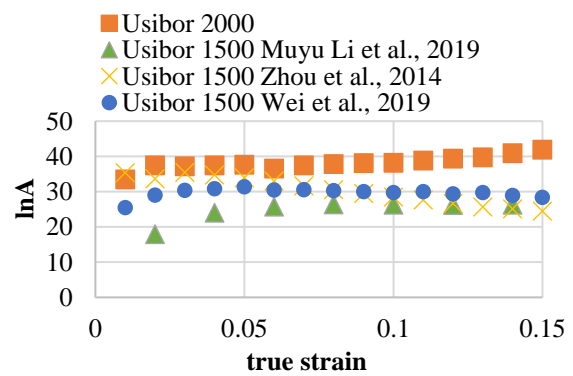


Fig. 3.37d: Relationship between material coefficient $\ln A$ and the true strain for both USIBOR[®]2000 and USIBOR[®]1500

The activation energy Q represents the deformation resistance of material at high temperature. From this comparison in Figure 3.37c it emerges that the activation energy, so the deformation resistance of the material at high temperatures, is greater for the USIBOR[®]2000 than its predecessor USIBOR[®]1500.

3.2.4 Constitutive model of dynamic recovery

Arrhenius constitutive model as well as Johnson-Cook model is the most widely used model to describe the material flow behaviour, however these are phenomenological models that don't describe complex changes in flow curves due to the microstructure evolution. Therefore, to take into account the softening effect due to the dynamic recovery, the theory of dislocation density was implemented to solve the constitutive model as Montazeri-Pour and Parsa [57] did for the constitutive analysis of AA1100 aluminium. Instead, to describe the softening effects due to the combination of DRV and DRX, the kinetic model of dynamic recrystallization can be introduced into the constitutive model of the DRV softening mechanism. This solution was presented by Rakhshkhorshid and Hashemi [58]. In previous works [53-54,59] the constitutive model of dynamic recovery and dynamic recrystallization have been used to estimate the flow behaviour of the material subjected to compression tests. In fact, the tensile tests fail to fully appreciate these softening effects unlike the compression tests, in which no necking instability is encountered [53].

Considering the temperature and strain rate range values of 750 °C - 850 °C and 0.01s⁻¹ - 1s⁻¹ respectively, the constitutive model of dynamic recovery was implemented based on the experimental data obtained with the hot tensile tests carried out with the Gleeble physical simulator.

To develop the dynamic recrystallization model it is necessary to determine some characteristic values including the work hardening rate that indicates the trend with which the flow curves change during the deformation process. The work hardening rate is defined as:

$$\theta = \frac{d\sigma}{d\varepsilon} \quad (3.21)$$

To calculate the work hardening rate, the experimental points of the stress-strain curves were interpolated with a rational function of the third degree for the numerator and first degree for the denominator (equation 3.22).

$$\sigma(p_1, p_2, p_3, p_4, q_1, \varepsilon) = \frac{p_1 * \varepsilon^3 + p_2 * \varepsilon^2 + p_3 * \varepsilon + p_4}{\varepsilon + q_1} \quad (3.22)$$

The plots of strain hardening rate as a function of stress for all investigated conditions are illustrated in Figures 3.38.

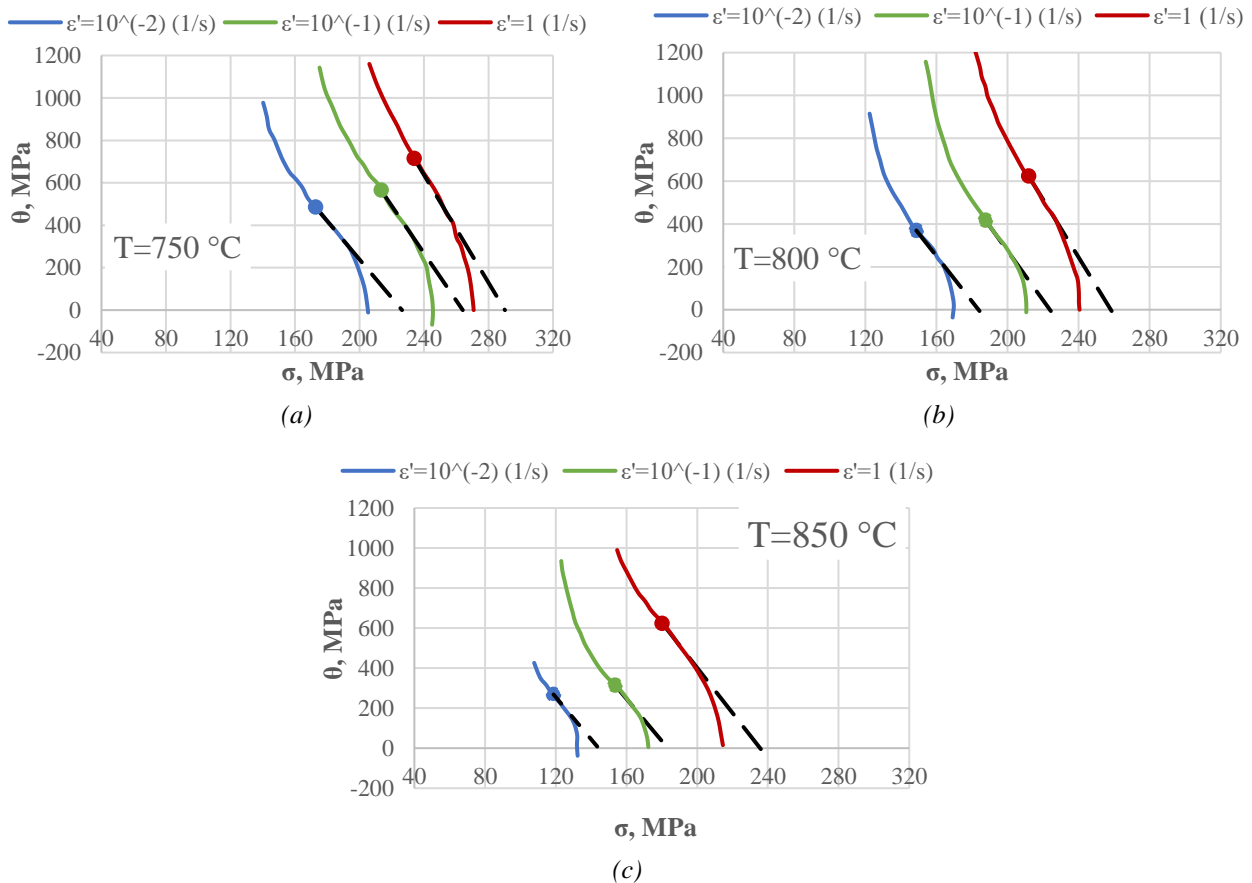


Fig. 3.38: Work hardening rate curves of different strain rates at temperatures of (a) 750 °C, (b) 800 °C and (c) 850 °C

The corresponding stress value in the point of θ - σ curve in which the inflection is observed (indicated with the circular markers in Figures 3.38) represents the critical stress (σ_c) for the initiation of DRX

phenomenon. The value of σ_c can be calculated from the zero point of second derivative of θ - σ plots. Figures 3.37 show the $\frac{d\theta}{d\sigma}$ - σ curves for all deformation temperature and strain rate investigated and, with circular markers, the stress corresponding to the peak value of the $d\theta/d\sigma$ - σ curves are highlighted.

The dashed lines in Figures 3.38 represent the tangent lines at the position corresponding to the critical stress. When the dashed lines reach zero values, the saturated stress (σ_{sat}) of dynamic recovery is achieved.

The simultaneous presence of work hardening and dynamic recovery phenomena influences the evolution of the density of dislocations. The increasing rate of dislocation density with the strain can be represented by the model that Estrin and Mecking [60] proposed:

$$\frac{d\rho}{d\varepsilon} = h - r\rho \quad (3.23)$$

Where h represents the work hardening rate, $r\rho$ represents the dynamic recovery and it reflects the reduction of dislocation density, therefore r is the dynamic recovery coefficient.

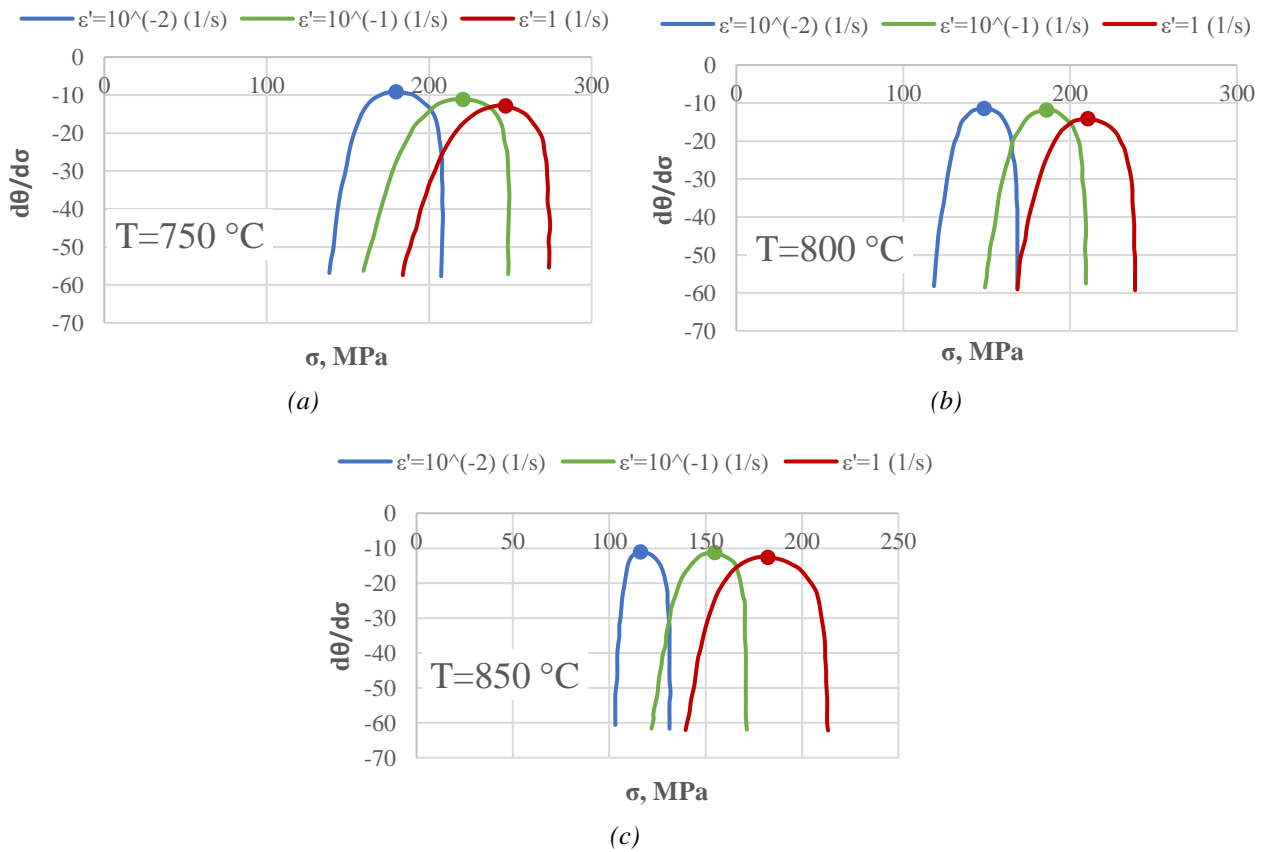


Fig.3.39: Curves of $\frac{d\theta}{d\sigma}$ - σ under different deformation conditions at temperatures of (a) 750 °C, (b) 800 °C and (c) 850 °C

Integrating equation (3.23) gives:

$$\rho = \frac{h}{r} - \left(\frac{h}{r} - \rho_0 \right) * \exp(-r\varepsilon) \quad (3.24)$$

ρ_0 indicates the initial dislocation density. The applied stress can be estimated as a function of dislocation density:

$$\sigma = \alpha * \mu * b * \sqrt{\rho} \quad (3.25)$$

Where α is the material constant, μ is the shear modulus and b is the distance between atoms in the slip direction (Burgers vector).

Substituting equation (3.24) in into equation (3.23) and considering that $\sigma_0 = \alpha\mu b\sqrt{\rho_0}$, the following equation can be obtained:

$$\sigma = \sqrt{\sigma_0^2 * \text{Exp}(-r\varepsilon) + (\alpha\mu b)^2 * \frac{h}{r} * [(1 - \exp(-r\varepsilon))]} \quad (3.26)$$

When the work hardening and dynamic recovery reach equilibrium, the flow stress tends to an asymptotic value σ_{sat} that can be expressed as $\sigma_{sat} = \alpha\mu b\sqrt{\frac{h}{r}}$. Therefore, equation (3.26) can be written in the following way:

$$\sigma = \sqrt{\sigma_{sat}^2 + (\sigma_0^2 - \sigma_{sat}^2) * \exp(-r\varepsilon)} \quad (3.27)$$

Where σ_0 is yield stress.

The r dynamic recovery coefficient can be calculated with the method proposed by Jonas J. J. et al. [61]. By taking derivatives on both sides of equation (3.27):

$$\frac{d\sigma}{d\varepsilon} = \frac{1}{2} * \frac{r * (\sigma_{sat}^2 - \sigma_0^2) * \exp(-r\varepsilon)}{\sqrt{\sigma_{sat}^2 + (\sigma_0^2 - \sigma_{sat}^2) * \exp(-r\varepsilon)}} = \frac{1}{2} * \frac{r * (\sigma_{sat}^2 - \sigma_0^2) * \exp(-r\varepsilon)}{\sigma} \quad (3.28)$$

$$\frac{d\sigma}{d\varepsilon} = \frac{1}{2} * \frac{r * (\sigma_{sat}^2 - \sigma_0^2) * \exp(-r\varepsilon)}{\sigma} \quad (3.29)$$

from equation (3.27):

$$\sigma^2 - \sigma_{sat}^2 = (\sigma_0^2 - \sigma_{sat}^2) * \exp(-r\varepsilon) \quad (3.30)$$

By replacing equation (3.30) into equation (3.29):

$$\theta\sigma = -\frac{1}{2} * r * (\sigma^2 - \sigma_{sat}^2) \quad (3.31)$$

$$\theta\sigma = -0.5 * r * \sigma^2 + 0.5 * r * \sigma_{sat}^2 \quad (3.32)$$

From equation (3.32) it is clear that the dynamic recovery coefficient r can be calculated from the slope of the $\theta\sigma - \sigma^2$ curves, as Figure 3.40 shows.

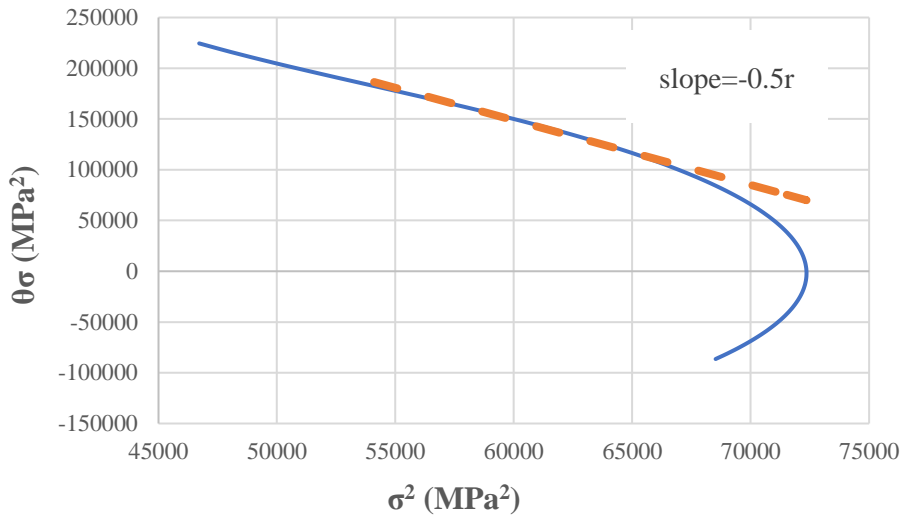


Fig. 3.40: Relationship between $\theta\sigma - \sigma^2$ for $T=750\text{ }^\circ\text{C}$ and $\dot{\epsilon}'=1\text{ s}^{-1}$

The yield stress σ_0 can be expressed as a function of Zener-Hollomon parameter, this relationship is illustrated in Figure 3.41. In this figure, with the dashed line, linear regression line is represented. The correlation coefficient is equal to 0.9747.

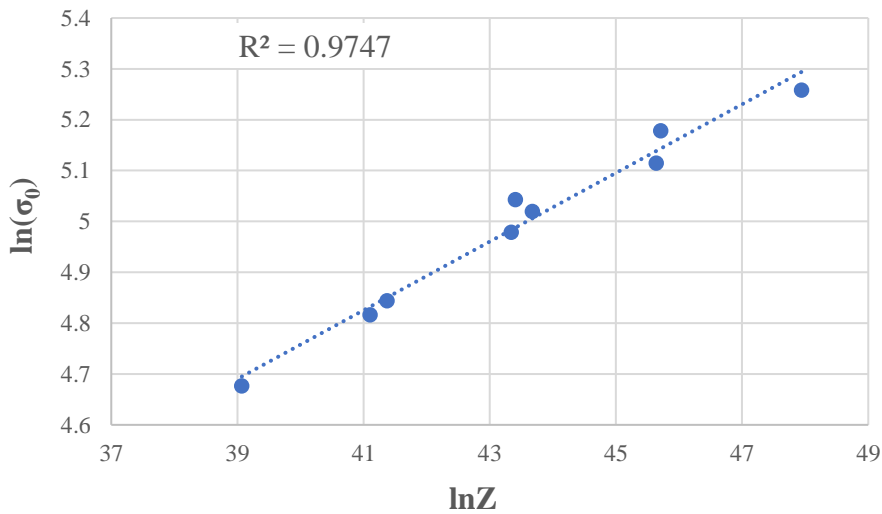


Fig. 3.41: Relationship between $\ln(\sigma_0) - \ln Z$

Linear regression was used to express σ_0 as a function of Z :

$$\sigma_0 = 7.827 * Z^{0.0675} \quad (3.33)$$

The saturation flow stress σ_{sat} can be expressed as a function of the peak stress σ_{max} , as L. Wang et al. demonstrated [62]. The dependence of σ_{sat} on σ_{max} is depicted in Figure 3.42, in which also the

linear regression line, with dashed line, represented as well as the correlation coefficient equal to 0.9964.

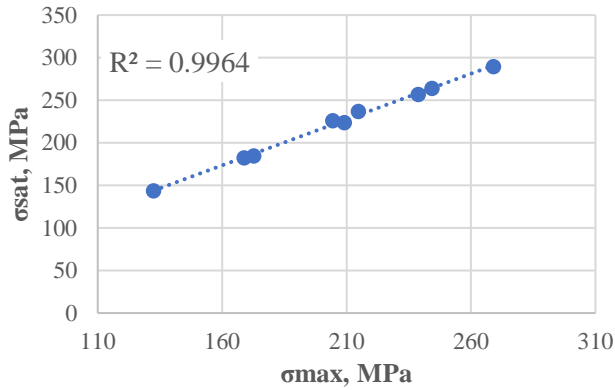


Fig. 3.42: Relationship between σ_{sat} and σ_{max}

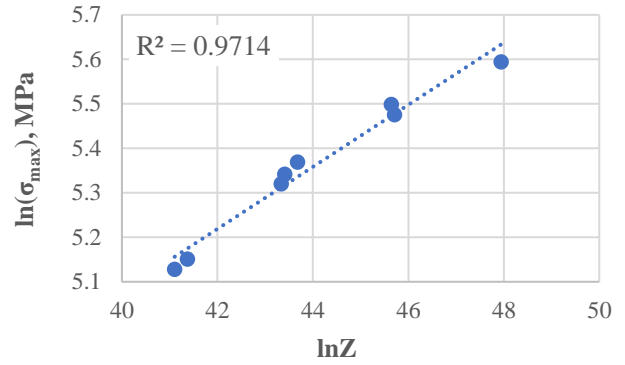


Fig. 3.43: Relationship between $\ln(\sigma_{max})$ and $\ln(Z)$

The equation that expresses the linear relationship between σ_{sat} and σ_{max} is:

$$\sigma_{sat} = 1.0766 * \sigma_{max} + 1.285 \quad (3.34)$$

However, σ_{max} can be expressed as a function of Zener-Hollomon parameter Z; this relationship is illustrated in Figure 3.43 and through the equation (3.35):

$$\sigma_{max} = 9.8631 * Z^{0.0698} \quad (3.35)$$

After expressing all quantities as a function of the Zener-Hollomon factor, it is possible to numerically calculate the predicted flow curves and compare them with the experimental ones. This comparison for all conditions investigated is shown in Figures 3.44.

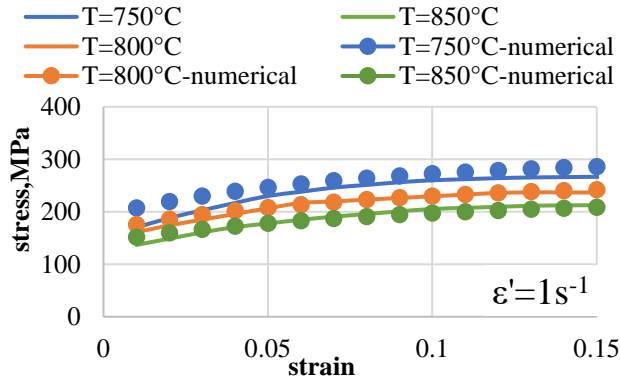


Fig. 3.44 (a): Comparison between experimental data and predicted results with DRV model under different deformation temperature at $1s^{-1}$

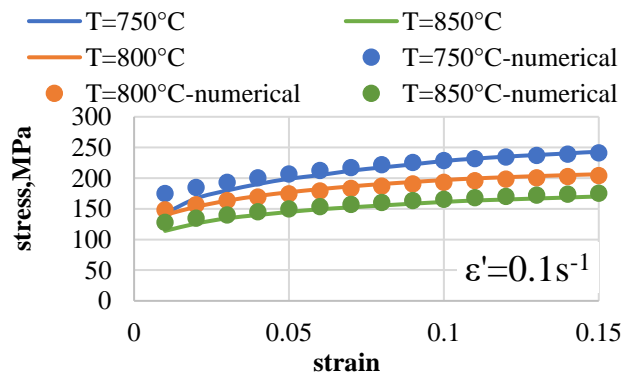


Fig. 3.44(b): Comparison between experimental data and predicted results with DRV model under different deformation temperature at $0.1s^{-1}$

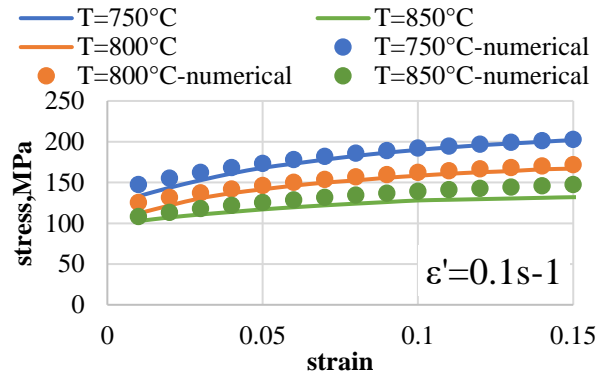


Fig. 3.44 (c): Comparison between experimental data and predicted results with DRV model under different deformation temperature at $0.01s^{-1}$

The quantitatively accuracy of the dynamic recovery model, also in this case, has been defined by the correlation coefficient, the average absolute relative error, and the root mean square error. These parameters are defined as shown in 3.2.2 section. The values of R, AARE and RMSE are respectively equal to 0.5, 0.43%, 2.3 MPa. The value of the correlation coefficient is much lower than that calculated with the Arrhenius model.

4. FE ANALYSIS OF PRESS-HARDENING TO OBTAIN TAILORED PROPERTIES

In the automotive sector, as already said, the demand for new processes to produce high-strength parts with adequate costs and productivity is growing together with weight reduction and safety improvements. The high-strength advanced boron steel responds to these requests, but to increase the formability of this alloy, the Hot Stamping process, known also as Press-Hardening process is carried out. The high strength of these parts is obtained during the quenching phase that leads to a completely martensitic microstructure. However, this process could also extend to some components that require greater toughness in some regions, with the aim to improve crashworthiness.

This section focuses on the FE modelling, in AutoForm R10 software, of the Press-Hardening processes. As a case study, an automotive B-Pillar was considered, for which two lateral ductile zones and a central resistant zone are required (Figure 4.1).

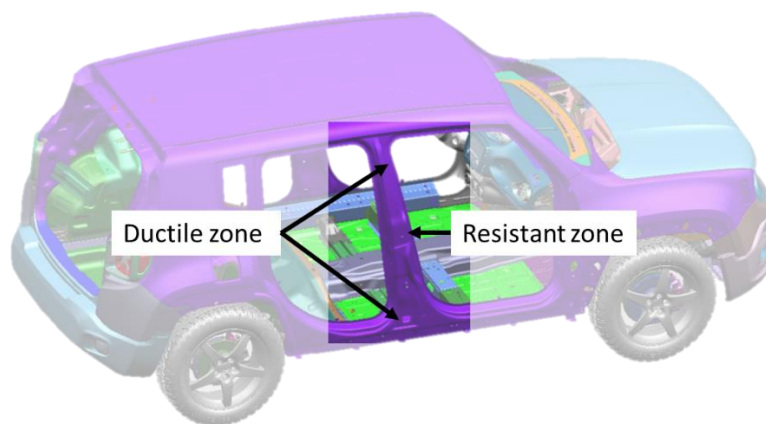


Fig. 4.1: B-Pillar investigated as a case study to model in AutoForm a Press-Hardening process with tool tempering approach

To achieve these customized properties, two tailored technologies have been taken into consideration, i.e. the Tailored Tool Tempering and the TemperBox[®]. Moreover two different ultra-high strength steels are considered, i.e. USIBOR[®]1500 and USIBOR[®]2000.

Details about the modelling of these technologies and numerical results are shown in the following.

4.1 FE model of tailored tool tempering approach

Currently, one of the main forming technologies for designing stamped parts with tailored properties include Tailored Tool Tempering approach. This approach involves that the tailored properties are achieved by exploiting different cooling conditions during the quenching phase. High cooling rate and low quenching temperature leads to a completely martensitic structure (higher resistance), while, low cooling rate and higher quenching temperature leads to a bainitic microstructures (greater ductility). To obtain an increase of quenching temperature, generally, heated tools through the use of heating cartridges are adopted. While, to have a reduction of the quenching temperature, cooled tools through cooling channels are used. Details about this tailored approach are already explain in section 1.

The numerical model provides for the definition of tools geometries (die, punch, pad and blank holder), the initial blank and their reference system and material characteristics and production plan

(defining individual operations of the production process). Figure 4.2 shows the initial blank, after positioning on the tools, and the pilots used to locate the sheet in the correct position and to prevent the sheet from moving during the process. A thickness of 2 mm was assigned to the blank. On the other hand, Figure 4.3 shows the tool surfaces with adaptive mesh. Tools, in particular die, punch and pad are modelled in hot and cold parts, as highlighted in the Figure 4.3 with the aim of implementing Tailored Tool Tempering approach.

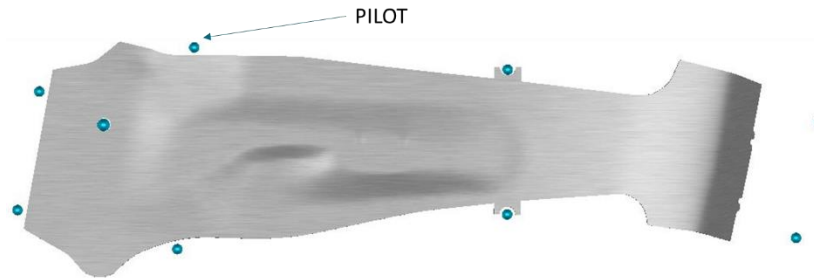


Fig.4.2. Initial blank and pilots

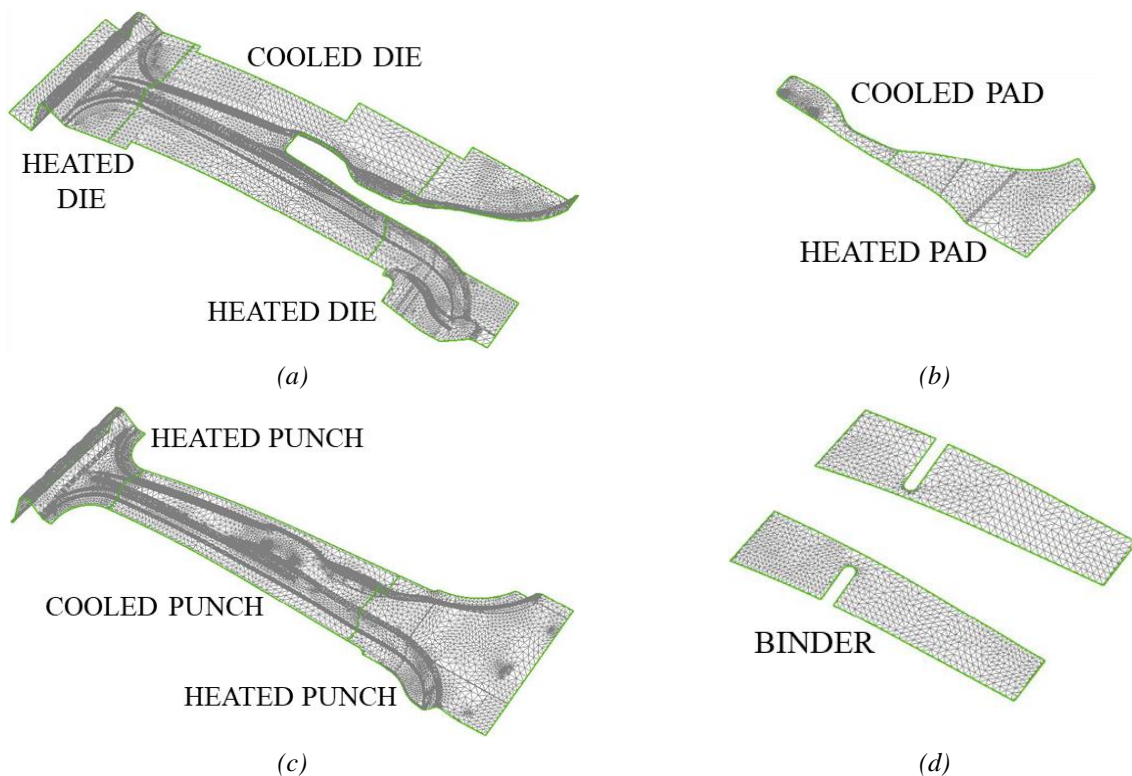


Fig.4.3: Tool surfaces geometries: (a) die, (b) punch, (c) blank holder, (d) pad

The die and the punch were imposed as rigid tool, this means that die and punch do not have a stroke and they are directly attached to ram and bed respectively. On the other hand, the pad and the blank holder were defined as gap controlled. This means that the pad and the blank holder tools must maintain a specific gap (0.20 mm) with respect to the displacing tool, which in this case is the die. The contact between tools and blank are modelled as ideally adapted, this means that the temperature distribution is more homogenous. However, during the real process the contact depends on the

thinning of the sheet. Specifically, there will be less heat transfer where thinning is greater and in areas where contact pressure is lower.

At first, the tool temperatures were considered constant, subsequently, as it will show in subsection 4.1.3, for the cooled part of the tools the cooling channels were modelled and different hot stamping cycles were simulated to understand the steady-state temperature value and the time taken to reach a steady state condition.

In the process plan definition, it is possible to define a lubrication condition. Specifically, in the model developed to simulate the hot stamping process, a constant Coulomb friction was considered. This means that the specified friction value is applied between all possible material-tool contact pairs and it remains constant during the simulation.

Usually, between the heated and cooled sections, a small air gap is introduced. The air gap produces a very abrupt temperature change across the boundary, which is designed to induce an immediate change in cooling rate of the blank across that gap [63]. Therefore, in the tools modelling phase, an air gap between heated and cooled tools is designed (Figure 4.4).

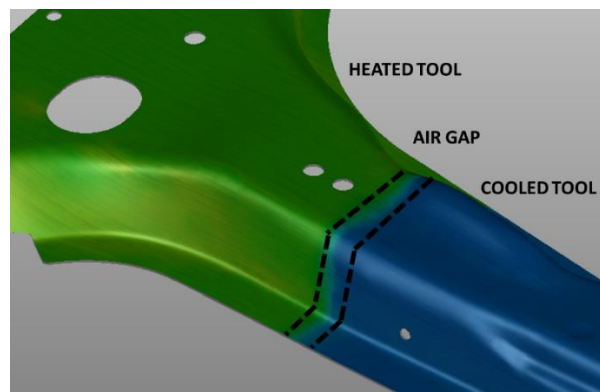


Fig. 4.4: Air gap between heated and cooled tools

The production line setup is defined as shown in Figure 4.5 (from left to right).



Fig.4.5: Production line of Press Hardening process

The first operation is H10 during which the heating of the blank is simulated. In this operation, the transport time from furnace to the press is defined. In the second operation (D20) the drawing and quenching phases are simulated; the third operation (K30) reproduce the cooling in air of the quenched part and finally, the last operation (T40) simulate the trimming of the component.

The Press-Hardening process with Tailored Tool Tempering approach was investigated for two different advanced high strength boron steel: USIBOR[®]1500 (22MnB5) and USIBOR[®]2000 (37MnB5). AutoForm software offers a default material database. The USIBOR[®]1500 can be found in this database. The data related to this steel are shown below. In particular, Figure 4.6 shows the Formability Limit Curves (FLCs) for USIBOR[®]1500 at temperatures of 600 °C and 700 °C.

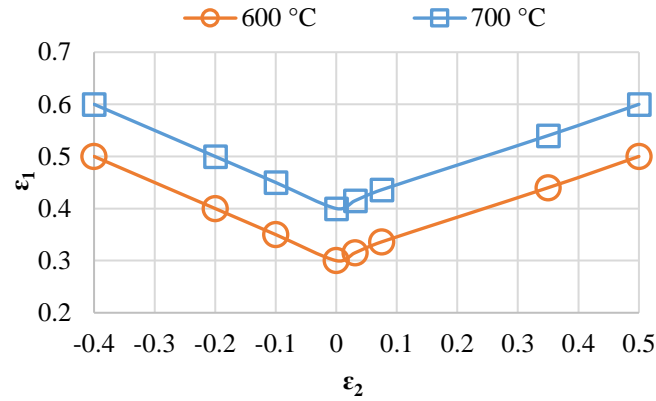


Fig. 4.6: FLCs for USIBOR®1500

The database includes also flow curves at different temperatures and different strain rates obtained in the martensitic, ferritic-pearlitic and austenitic fields. For the yield surface, the Hill 48 model was adopted; however considering that the deformation occurs at high temperature after complete austenization, an isotropic behaviour of the material was assumed ($r_0=r_{45}=r_{90}=1$).

In a Tailored Tool Tempering process the cooling rates are adjusted in such a way that the final part shows hard and soft regions with desired phase fractions and properties. Therefore, modelling of phase transformation is necessary. In fact, phase fractions and final properties (hardness, tensile strength) depend on the temperature history and the chemical composition of the material. Moreover, for an accurate computation of the temperature history it is important to consider that during phase transformation a latent heat is generated. For the USIBOR®1500 the phase transformation model is contemplated in card material definition.

Table 4.1a shows the thermo-physical properties for USIBOR®1500 and in Table 4.1b, for each microstructural phase, physical properties are highlighted through which dilatation curves can be defined.

Table 4.1a: Thermo-physical properties for USIBOR®1500

Properties	Values
Volumetric heat capacity, $\left(\frac{mJ}{mm^3K}\right)$	4.37
Conductivity, $\left(\frac{mW}{mmK}\right)$	32

Table 4.1b: Physical properties for each microstructural phase

Properties	Values for AUSTENITE	Values for FERRITE	Values for BAINITE	Values for MARTENSITE
Expansion coefficient (1/K)	2.20E-05	1.50E-05	1.50E-05	1.10E-05
Start temperature (°C)	850	780	550	400
End temperature (°C)	950	550	400	200
Transformation strain	-0.008	0.008	0.008	0.008
Latent Heat $\left(\frac{mJ}{mm^3}\right)$	-	539	563	563

Trans plastic coefficient - 0.00015 0.0001 9.00E-05

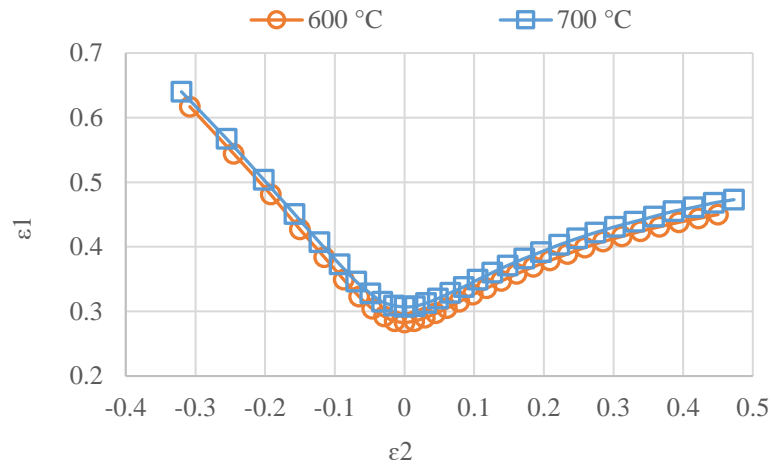


Fig. 4.7: FLCs for USIBOR®2000

The second investigated advanced high strength boron steel (USIBOR®2000), being a steel commercially available just recently, it cannot be found in AutoForm R10 material database. Therefore, a user-defined material card was developed. The hardening curves were defined with a table of strain-stress points experimentally obtained in the austenitic field at temperature of 750 °C – 850 °C and strain rate of $1 \text{ s}^{-1} - 0.01 \text{ s}^{-1}$ (section 3.2.1). Furthermore, in order to have information about the microstructure, the CCT curves of 37MnB5 steel found in the work of Naderi et al.[33] have been included in the USIBOR®2000 card material. The thermo-physical properties of USIBOR®2000 are highlighted in Table 4.2.

Table 4.2: Thermo-physical properties for USIBOR®2000

Properties	Values
Volumetric heat capacity, $\left(\frac{\text{mJ}}{\text{mm}^3\text{K}}\right)$	3.59
Conductivity, $\left(\frac{\text{mW}}{\text{mmK}}\right)$	23.3

The thermophysical properties and the FLCs, shown in Figure 4.7, were provided confidentially by the Fiat Research Center (CRF) within the PICO&PRO (Integrated and COnnected PROcesses for the industrial production evolution) project. Finally, for the yield surface, also for the USIBOR®2000 the Hill 48 model was adopted considering an isotropic behaviour of the material at high temperature ($r_0=r_{45}=r_{90}=1$). In the following subsections the numerical results obtained for the B-Pillar in USIBOR®1500 are shown. Specifically, the influence of the process parameters (transport time, quenching time and temperature of heated tools) and of the design parameters (width of the air gap between cooled and heated tools and the position of conformal cooling channels in the tools) were evaluated on final properties of the investigated component. For the analysis of the Press-Hardening process using a more hardenable steel, the USIBOR®2000, only FE thermo-mechanical cycles will be shown. The numerical microstructural and hardness results on the USIBOR®2000 are not reliable since the CCT curves taken from the bibliographic reference should be experimentally validated.

Therefore, in this case, the considerations regarding the mechanical properties of the part as the process parameters vary will be carry out by physically simulating the thermo-mechanical cycles extracted from the FE model.

4.1.1 Investigation of process parameters on mechanical properties of the part at the end of Press-Hardening process with tailored tool tempering approach

The Press-Hardening process is a complex process because the phenomena involved are both thermal (the heat transfer between tools and blank and the phase transformation occur) and mechanical (the plastic deformation occurs during drawing). Therefore, the process parameters involved are different and the use of the FE simulations can help the process design, by evaluating how process parameters influence the quality of the final product. In fact, in this way it becomes easy identify critical areas in the part, the measures that can be taken to resolve these issues as well as the effect these measures will have on other areas. Moreover, some dedicated software, such as AutoForm, can evaluate the process capability, with the aim to validate the process, minimize part rejects and maximize production efficiency. For this reason, AutoForm R10 software was adopted to evaluate how the process parameters influencing the final mechanical properties of the studied component. The investigation was carried out on a USIBOR®1500 blank with a thickness of 2 mm. For this component, ductile properties are required for regions I and III, while high strength mechanical properties are desired for region II (Figure 4.8). To ensure high ductility in regions I and III it would be desirable to have a fully bainitic microstructure. On the other hand, to ensure high mechanical strength it would be desirable to have a completely martensitic microstructure at the end of the process. Preliminary FE simulations allowed to choose range of parameters values to investigate after verifying that these parameters guarantee a good formability without problems of splits, wrinkles or thinning. Therefore, the analysis presented aims to evaluate how the microstructure changes on the component as a function of process parameters, since the microstructure affect mechanical properties of the part and, consequently, the performance in the case of impact.

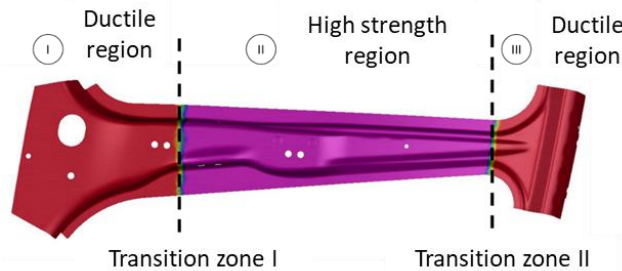


Fig. 4.8: B-Pillar investigated with required mechanical properties

Table 4.3 shows the process parameters and the range of values explored for the sensitivity analysis.

Table 4.3: Values of process parameters investigated for the study of the process

Process parameters	Values
Transport time (t _{transport})	5 s – 10 s
Quenching time (t _{quenching})	15 s – 25 s

Table 4.4: Values of constant process parameters

Process parameters	Values
Forming velocity (v)	200 mm/s
HTC to Tool	3.5 mW/(mm ² K)
Temperature of sheet	930°C

Temperature heated tools (T_hot tool)	400 °C – 460°C	Blank thickness	2 mm
		Quenching force	1.2E+04 kN
		Temperature heated tools	80 °C
		Friction coefficient	0.4
		Air gap	8 mm

The software proceeds to a sampling according to the Latin Hypercube statistical method (Latin Hypercube Sampling, LHS), generating a near-random samples of parameter values. In total, 64 numerical simulations are performed. The analysis is carried out by setting constant the parameters shown in Table 4.4. In the range chosen for the transport time, quenching time and temperature of heated tools, there is always the complete martensitic transformation in the high strength region (hard region). Therefore, the process was studied by evaluating how transport time, quenching time and temperature of heated tools influences the percentage of bainitic microstructure in ductile regions. The results of numerical simulations show that the parameter that mainly affects the homogeneity of bainitic microstructure is the temperature of heated tools, as can be seen in Figure 4.9. This result is confirmed by the metamodells shown in Figures 4.10 and 4.11. The metamodells are related to the bainitic microstructure percentage in ductile region III as temperature of heated tools, quenching time and transport time vary. For simplicity, the metamodells relating to bainite percentage in region I are not shown. However, the surfaces trends for both regions are similar.



Fig.4.9: Dominant variable that influences bainitic microstructure percentage on the final stamped component

The metamodells shown in Figures 4.10a and 4.11b confirm a greater influence of heated tool temperature on bainite percentage. In particular, a rises of bainitic microstructure phase with an increasing of heated tools temperature is observed. Moreover, a threshold temperature of about 440°C that leads a homogeneous bainitic microstructure on the component is found.

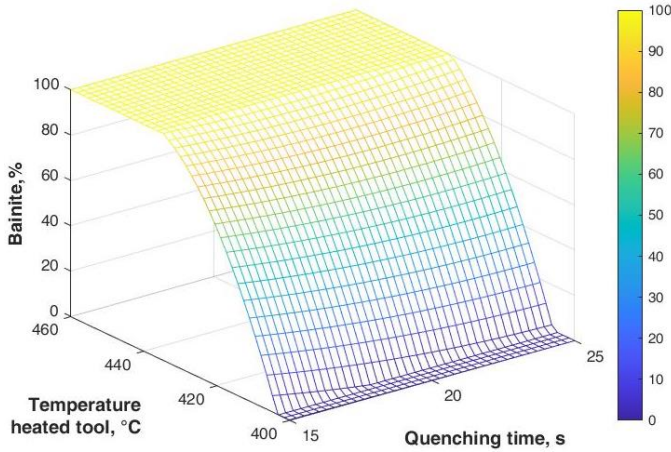


Fig.4.10a: Metamodel of bainite percentage in region III as a function of quenching time and temperature of heated tools

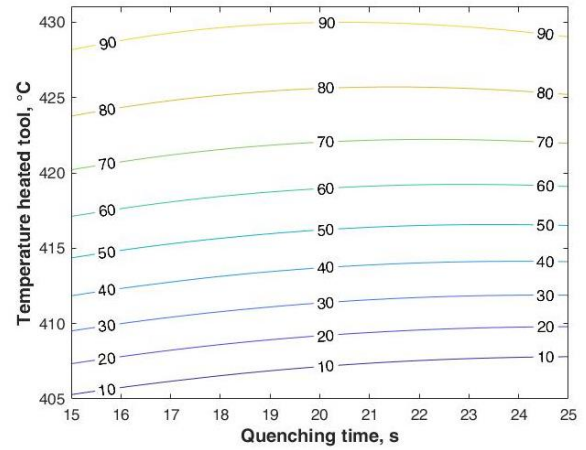


Fig.4.10b: Contour plot of bainite percentage in region III as a function of quenching time and temperature of heated tools

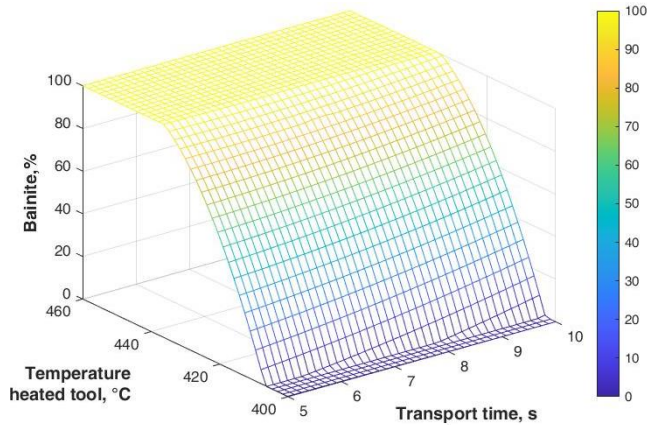


Fig.4.11a: Metamodel of bainite percentage in region III as a function of transport time and temperature of heated tools

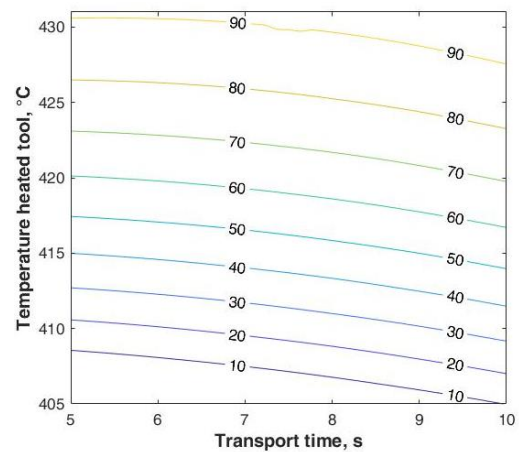


Fig.4.11b: Contour plot of bainite percentage in region III as a function of transport time and temperature of heated tools

Although the influence of transport and quenching time is negligible, from contour lines in Figures 4.10b and 4.11b it is observed that as quenching time rises and transport time reduce, bainite percentage rises for heated tools temperature values between 400 °C and 440 °C.

4.1.2 Design of air gap between cooled and heated tool

In the Tailored Tool Tempering approach, between the blank region in contact with the cooled tool and the region in contact with the heated tool a transition zone is created, due to the thermal conductance of the blank material. The transition zone is defined as the zone between the fully softened and fully hardened microstructure. The width of transition zone depends on the blank thickness and on the heating and cooling tools layout. The width and the position of transition zone can influence the crash performance of the component; therefore, an analysis of mechanical properties near the transition zone may be required. However, few scientific works investigated in detail the properties of the transition zone or the influence of process and design parameters on its width and position. Wang Zi Jian et al in [64] investigated, for an air gap width of 8 mm, the hardness trend

near the transition zone for different temperature of heated tool and for two different steel. Moreover, they compare their results with those get from George's work [63] in which an air gap width of 3 mm was considered.

In this thesis, the influence of the air gap width on the transition zone was investigated, taking into account its width and position. Moreover, the influence of the process parameters on the transition zone was also evaluated. Figure 4.12 shows the parameters relating to the transition zone. Under the assumption of having 100 % bainite in the ductile part and 0 % bainite in the resistant part, transition zone is defined as the zone between the fully softened and fully hardened microstructure and it is represented from A parameter. A reference for the position of the transition zone is provided by parameter C. This parameter indicates the distance between the cooled tool and the starting point of transition.

These considerations were carried out by adopting the numerical model that led to the results described in paragraph 4.1.1.

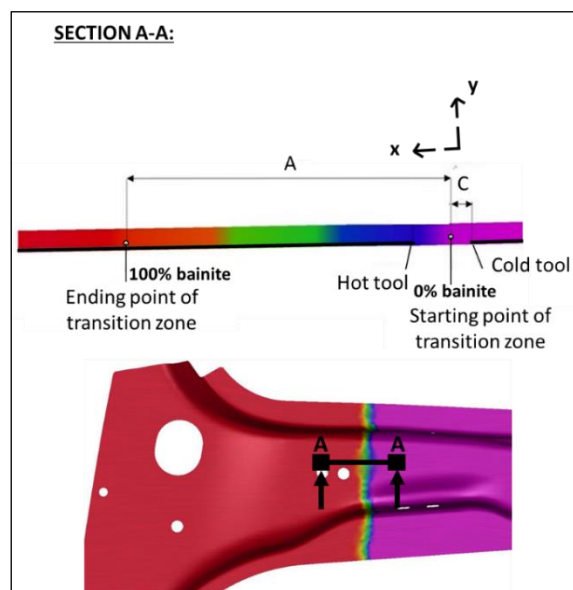


Fig. 4.12: Parameters relating to the transition zone in correspondence of section A-A of the B-Pillar

To study the influence of the air gap width on the parameters of the transition zone (A and C), the process parameters, i.e. quenching time, temperature of heated tools and transport time were set to the nominal value, 20 s, 430 °C and 7.5 s respectively. The width of air gap was varied between 3 mm and 8 mm. The variation of the air gap width does not affect the percentage of bainitic or martensitic phase formed on the component in the ductile and resistant regions. The air gap parameter affects only the width and position of the transition zone. As an example, only the results obtained in correspondence of the transition zone I are shown (Figure 4.8). Twelve points are taken, along the longitudinal section, starting from the node with a completely martensitic microstructure up to the node with a completely bainitic microstructure (Figure 4.13). Figure 4.14 shows the percentage of bainitic microstructure as a function of the abscissa x from the node with martensitic microstructure to the node with bainitic microstructure, for three different values of air gap width. The origin of the reference system coincides with the final point of the cooled tool next to the transition zone I. It can be observed that by fixing the x coordinate, the percentage of bainite increases as the air gap increases. This implies that as the gap increases, the width of transition zone is reduced. This trend is confirmed

by the graph in Figure 4.15. The values of transition zone width coincides with the values found in reference [65], where the fully softened and hardened material conditions are achieved across a 25 mm transition zone for an air gap of 3 mm.

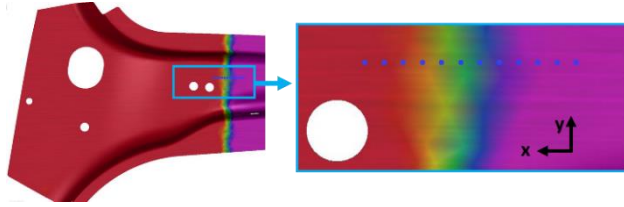


Fig.4.13: Twelve points chosen for the analysis of bainite percentage

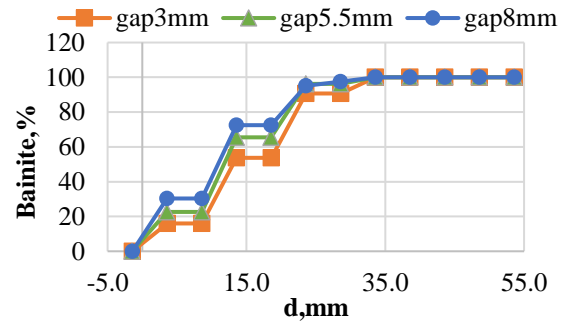


Fig.4.14: Percentage of bainitic microstructure as a function of the abscissa x for three different values of air gap

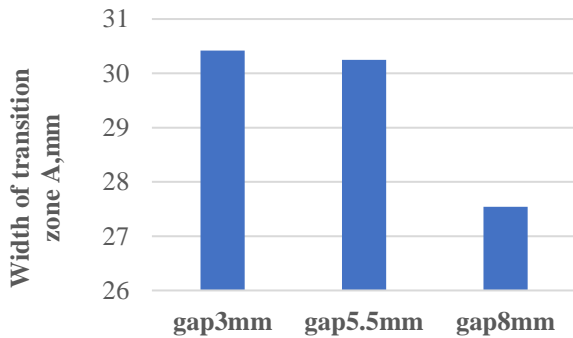


Fig.4.15: Width of transition zone for three different values of air gap

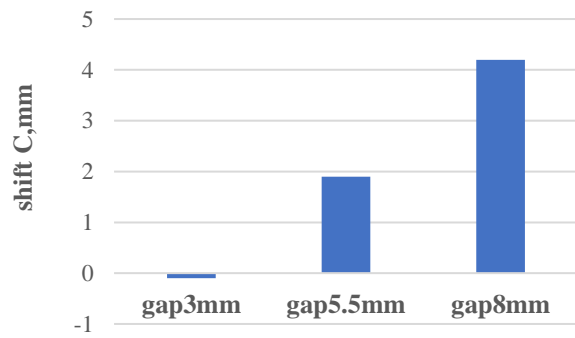


Fig. 4.16: Values of the parameter "C" for three different values of air gap

For the analysis of transition zone position, parameter "C" is evaluated. The results are shown in the graph in Figure 4.16. It emerged that as the air gap decreases, the beginning of transition zone (point with 0 % bainite microstructure) moves towards the cold tool. Therefore, by decreasing the air gap between the two tools, the heat that spreads towards the central part of the component, which must remain cold, increases.

The results presented in section 4.1.1 show that a completely bainitic microstructure is not reached below the threshold temperature (430°C). Therefore, to study the influence of process parameters on the width and position of the transition zone, a heated tool temperature range from 430 °C to 460 °C was chosen. In fact, the transition zone was defined as the zone between 100 % bainite and 100 % martensite. The results acquired from the numerical simulation were processed using the kriging technique to obtain the metamodells relating to the variation of A and C parameters as the process parameters vary.

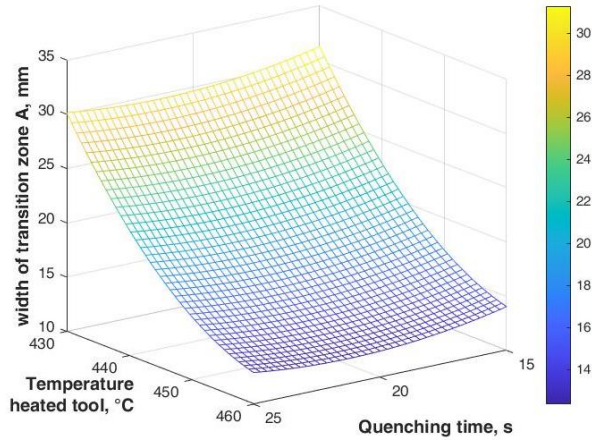


Fig.4.17a:Metamodel of transition zone I width (A) as a function of heated tool temperature and quenching time

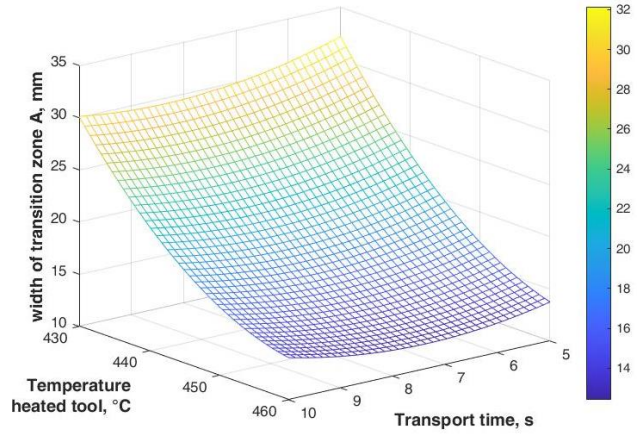


Fig.4.17b:Metamodel of transition zone I width (A) as a function of heated tool temperature and transport time

Figures 4.17a and 4.17b show the metamodels of the transition zone width A as heated tool temperature and, respectively, quenching and transport time vary.

Also for the width of transition zone, the most influential parameter is the temperature of heated tools. It is observed that as the heated tools temperature increases, the width of transition zone is reduced. In fact, the higher hot tools temperature, the greater diffusion heat towards the cold tools. The starting point with 100 % bainitic microstructure moves towards the cooled tools, thus reducing the width of the transition zone. From the metamodels in Figures 4.17a and 4.17b, it can be seen that transport time and quenching time do not affect the width of transition zone.

On the other hand, Figures 4.18a and 4.18b show the metamodels of the transition zone width C as heated tool temperature and, respectively, quenching and transport time vary.

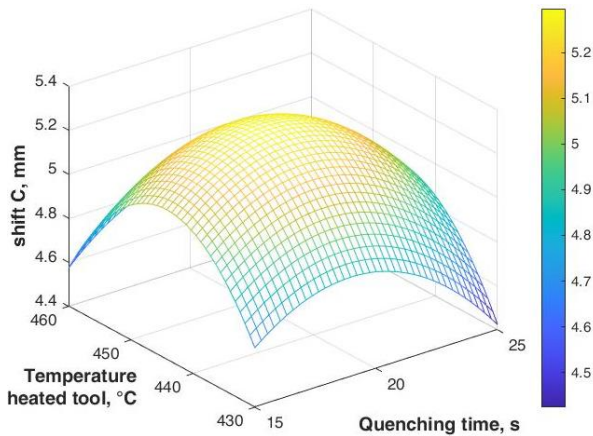


Fig.4.18a:Metamodel of shift parameter (C) as a function of heated tool temperature and quenching time

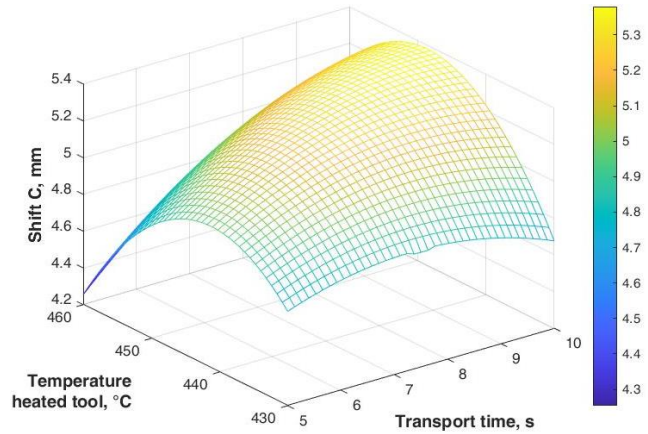


Fig.4.18b:Metamodel of shift parameter (C) as a function of heated tool temperature and transport time

It is observed that an increase in the heated tool temperature leads first to an increase and, subsequently, to a reduction in the shift of transition zone. The temperature at which the maximum shift value occurs is about 445 °C. The same trend of parameter C is found when the quenching time varies. The quenching time at which the maximum shift is obtained is about 20 s. The transport time is the parameter that has the least influence on the C parameter.

4.1.3 Design of conformal cooling channels (CCC) and evaluation of CCC parameters on mechanical properties of the final part

The FE results related to the Press Hardening process by means of tailored tool tempering approach were obtained considering the constant tool temperature. However, in the industrial process, cooling channels are inserted inside the tools, in correspondence with the part that must have a martensitic microstructure. This implies that it is necessary to wait a certain time for the tools to reach a steady temperature in order to have a homogeneous microstructure on the component. Therefore, it is interesting to understand how to optimize the cooling channels design to reduce cooling times and to ensure a uniform temperature on the component.

To meet these requirements, most of scientific works are mainly focused on optimizing cooling channel diameter, the distance between channels and the distance between tool surface and channel. Shan et al. [66] showed that the depth from the die surface to the cooling channels has the biggest impact on the cooling rate and uniformity of the workpiece. Moreover, they discovered that augmenting the cooling channel diameter near the inlet improved the water flow uniformity. Lin et al. [67] showed that the distance between the cooling channels and the distance between the cooling channel and the tools surface have significant influence on the quenching effect; in particular, better quenching effect can be achieved with the shorter distance from the tool surface and with smaller distance between cooling channels. Furthermore, thermal expansion proved to be the main reason for deformation of the hot forming tools, which causes the distortion of the cooling channels, and the stress concentration at corner of the cooling channels. Recently, Hung et al. [68] stated that the blank thickness, the distance from the tool surface to the cooling channel edge, and distance between cooling channel edges are the parameters that have marked effects on cooling performance. These studies mentioned so far are mainly focused on straight drilled channels, however to improve cooling efficiency, conformal cooling channels (CCC) are increasingly adopting thanks to opportunities offered by additive manufacturing (AM) technologies in combination with the development of powders with high thermal conductivity. Cortina et al. [69] investigated the design and manufacturing of conformal cooling ducts via additive manufacturing and they compared the conformal cooling conduits with the traditional straight channels. With regard to thermal results, a more homogeneous temperature distribution within the tool and the stamped part is attained with CCC, leading to the enhancement of the dimensional accuracy and features of the produced parts. Moreover, they stated that better temperature distribution also leads to the lowering of the process cycle times in hot stamping and the subsequent improvement of the efficiency of the process and reduction of the costs. Muvunzi et al. [70] proposed a method for designing hot stamping tools with conformal cooling channels. The suggested method involves the evaluation of the part to decide whether it is suitable for AM application, the definition of conformal cooling parameters and the design of alternative layouts. Vallas et al. [71] explored the increase of cooling capacity of tools by using the new high thermal conductivity tool steel powders FASTCOOL-50 and HTCS-230.

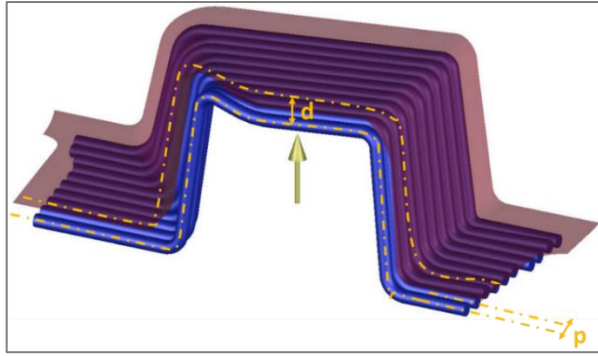


Fig. 4.19a: Tool insert of investigated B-Pillar with the geometric parameters p and d considered for the optimization

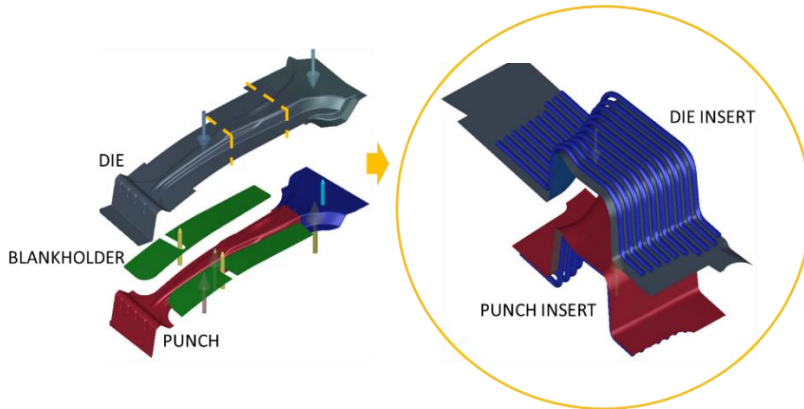


Fig. 4.19b: position of the tool insert in the investigated component

Taking these research activities into consideration, rather than consider a constant the temperature of cooled tools, conformal cooling channels were designed for the component described in section 4.1, evaluating the thermal cycle on the tools and on the blank. For the design of the conformal cooling channels, a commercially available tool steel powder with high thermal conductivity (HTCS1) was chosen and an optimization of the distance between the cooling channels (p) and distance between the tool surface and the cooling channel centre (d) was performed. Figure 4.19 shows the geometric parameters p and d on an insert of the studied component (4.19a) and the position of the insert (4.19b). Parameters p and d were varied between 12 mm - 24 mm and between 9 mm - 21 mm, respectively. The modelling of conformal cooling channels was performed through a CAD modelling software. Each configuration was imported in the AutoForm FE code and the Press-Hardening process was numerically simulated. On the base of surface thermal cycles in a tool and in the part, an optimal solution have been chosen by considering the peak temperature, time taken to reach stationary condition and percentage of martensitic microstructure on the component. In correspondence with the identified optimal solutions the temperature distribution and presence of eventual hot spots in the tool was investigated with a 3D FE thermal model developed in COMSOL Multiphysics. The diameter chosen for the conformal cooling channels is equal to 6 mm, because it was hypothesized that these CCC were manufactured with the L-PBF (Laser Powder Bed Fusion) technique. In fact, beyond this value, it is necessary to use internal supports that cannot be removed after manufacturing the tool. The presence of such supports is not recommended as it can adversely affect the flow conditions inside the channels [72].

The process parameters adopted for the numerical simulations of the hot stamping process in the AutoForm environment are shown in Table 4.5, while blank and tools parameters are reported in Tables 4.6a and 4.6b.

Table 4.5: Process parameter for hot stamping FE simulation in AutoForm environment

Process parameters	Values
Blank heating temperature (°C)	950
Transport time (s)	5
Positioning and drawing time (s)	7
Quenching time (s)	18
Cooling water temperature (°C)	20
Quenching force (ton)	400

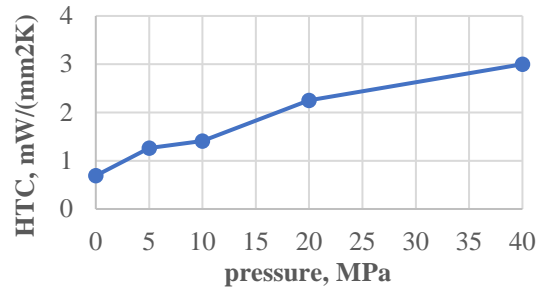


Fig. 4.20: Pressure dependent HTC

Table 4.6a: Values of tool parameters

Tool parameters	
Thermal conductivity (W/m·K)	54
Heat capacity (J/kg·K)	480
Density (kg/m³)	8040
Young's modulus (GPa)	210
Poisson ratio	0.3

Table 4.6b: Values of blank parameters

Blank parameters	
Thickness (mm)	1.7
Thermal conductivity (W/m·K)	32
Heat capacity (J/kg·K)	470
Density (kg/m³)	7800
Young's modulus (GPa)	210
Poisson ratio	0.3

The HTC coefficient has been defined as a function of gap and contact pressure between sheet and tool. The gap change the contact conditions and it can occur due to the sheet thinning. Figure 4.20 shows the influence of contact pressure on HTC coefficient. Scale factor for the variation of HTC coefficient as a function of the contact pressure and the value of the gap for which the HTC is halved have been chosen referring to the work of Lechler et al. [73].

After numerical simulation, temperatures on the central points of tools surfaces (punch and die) were analysed observing twenty hot stamping cycles, for all the nine CCC configurations.

Figure 4.21 shows the punch thermal cycles corresponding to the extreme configurations. These results confirm that an increase in d and/or p parameter leads to an increase both of the tool peak temperature and of tool temperature at the end of the stamping cycle. To better evaluate after how many hot stamping cycles the steady state condition is reached, the punch temperature difference between two consecutive hot stamping cycles at the end of quenching phase was calculated (Figure 4.22).

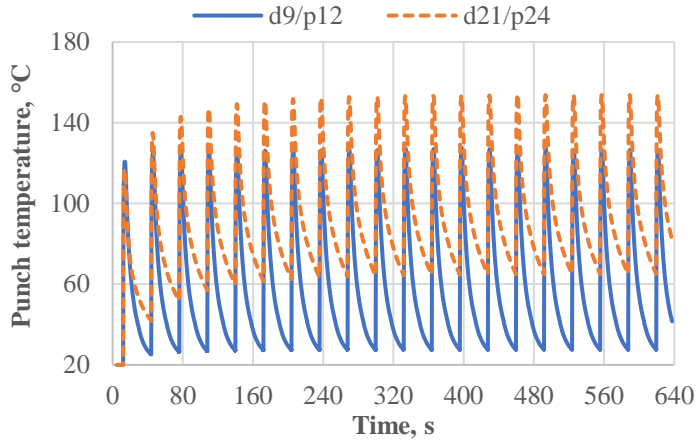


Fig. 4.21: Thermal cycles on punch surface with cooling channels in two configuration

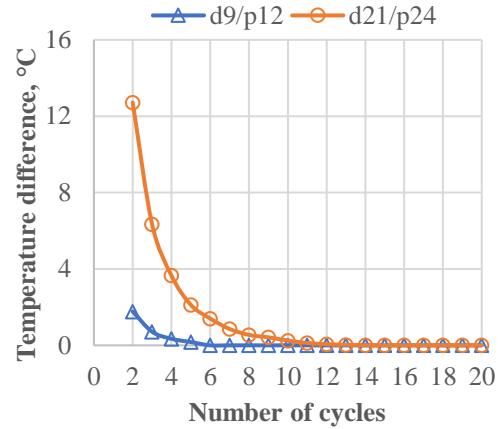


Fig.4.22: Punch temperature difference between two consecutive hot stamping cycles

It is possible to state that in the configuration with the cooling channels closest to the tool surface and closest to each other, the temperature stabilizes already starting from the sixth cycle (temperature difference equal to zero). For the configuration with cooling channels at maximum distance from the punch surface and at maximum centre distance, the temperature difference is below 1 °C starting from the seventh cycle, but the temperature difference decreases to zero in the twelfth cycle. Therefore, the twelfth cycle can be considered as the steady state condition for all the geometric configurations of the CCC.

Figure 4.23 shows the steady-state thermal cycles in the two extreme conditions and the respective temperature distributions in the tool. The results show that as the geometric parameters of the cooling channels vary, the peak temperature of the tool varies in the range 126 °C - 154 °C, while the tool temperature at the end of the hot stamping cycle varies in the range 42 °C - 82 °C. The lower values of these ranges are obtained using $d = 9$ mm and $p = 12$ mm and for this configuration it is possible to reach the steady state condition first, already from the sixth stamping cycle. In the steady state condition, all the CCC configurations investigated assure in the quenching phase cooling rate in the formed part higher than 50 K/s; therefore the complete martensitic transformation is guaranteed.

Taking as reference the less severe channels configuration ($d = 21$ mm and $p = 24$ mm), in the Figure 4.24 is shown the time evolution of the martensitic transformation on the blank during the quenching phase. This result highlights that just three seconds from the start of the quenching phase, greatest part of the formed part has a completely martensitic microstructure, while after 14 s, the formed part is fully martensitic.

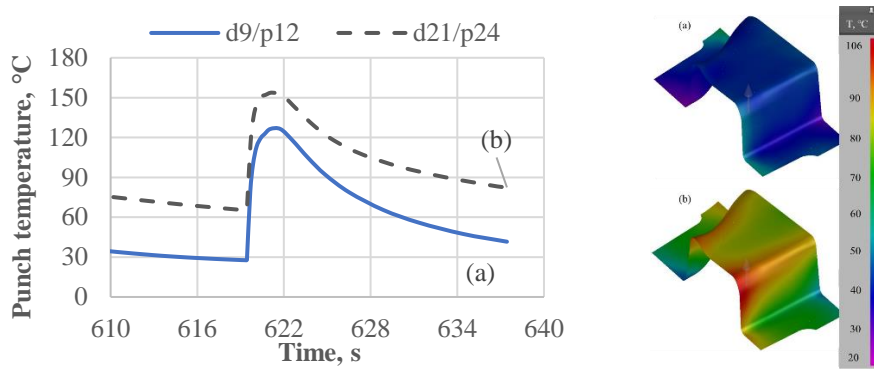


Fig. 4.23: Thermal cycles in the steady state condition for the two most extreme condition and the respective temperature distribution on the punch

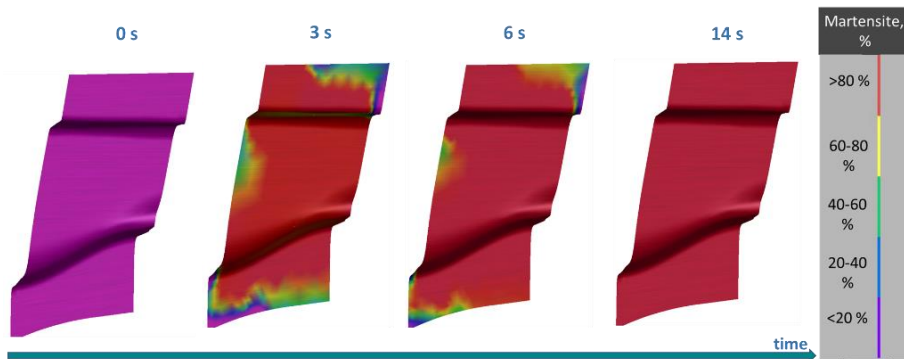


Fig.4.24: Martensite history during quenching phase ($d = 21$ mm, $p = 24$ mm)

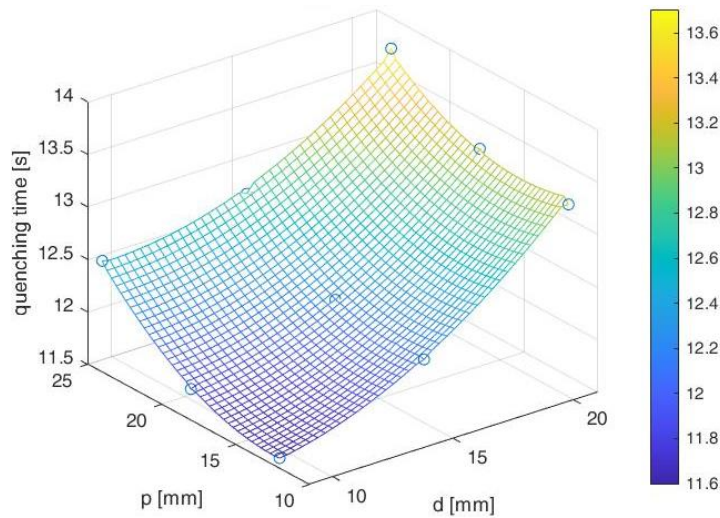


Fig.4.25: Metamodel related to the quenching time that guarantees the complete martensitic transformation as p and d vary

Therefore it can be considered that the additive manufacturing approach that ensure conformal cooling channels production and the use of materials with high thermal conductivity allows the complete martensitic transformation of the component in approximately 14 s during quenching phase, less than the 18 s imposed. By tracking the temporal evolution of the martensitic transformation during the quenching phase for all the conformal cooling channels geometric configurations, the

metamodel in Figure 4.25 can be obtained. It can be observed that as the parameters p and d are reduced, the quenching time necessary to guarantee the complete martensitic transformation is reduced. This suggests as optimal channel configuration, that obtained with $d = 9$ mm and $p = 12$ mm. This configuration is also optimal because shorter times are guaranteed to reach the stationary condition and lower peak temperatures are assured, as already highlighted.

This optimal channel configuration was investigated with the transient 3D FE thermal model developed using COMSOL Multiphysics FE software. The model simulates the quenching and the cooling in air phases during several stamping cycle in a press-hardening process. The formed part and tool parameters are the same as entered in Tables 4.5a and 4.5b, while the process parameters are the same as described in Table 4.4.

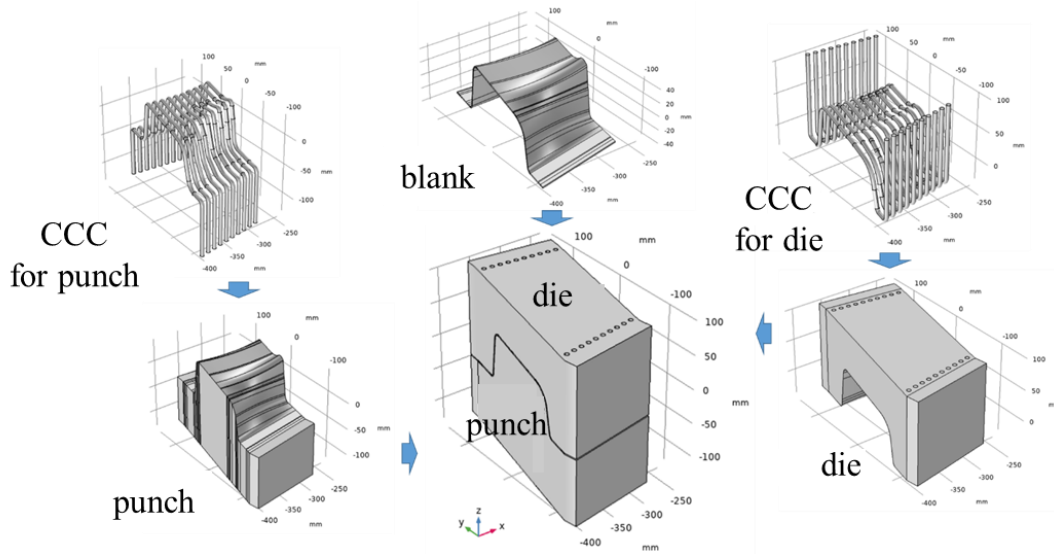


Fig. 4.26: Geometric model of the conformal cooling channels, the die, the punch and the blank

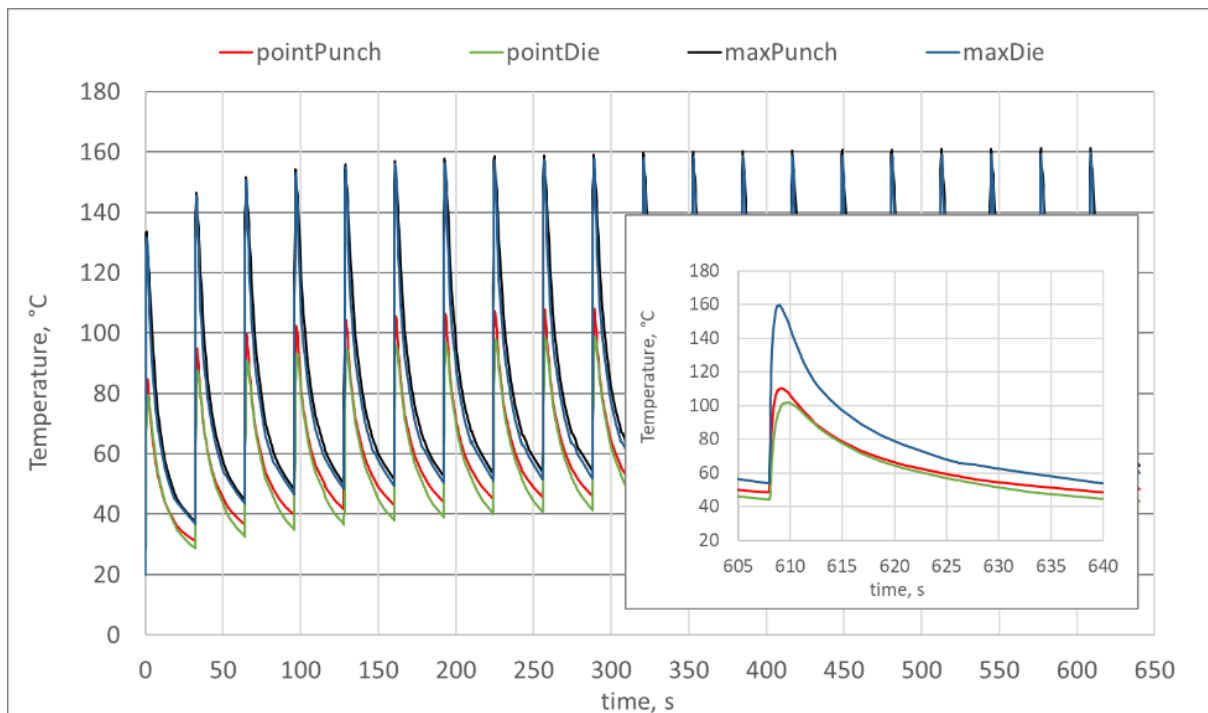


Fig. 4.27: Thermal cycles recorded during 20 hot stamping cycles at 30 mm from the punch and die surfaces and on the punch and die surfaces

Figure 4.26 shows the geometric model of the conformal cooling channels, the die, the punch and the blank. An unstructured tetrahedral mesh was chosen for the numerical simulations.

This model allowed to evaluate the temperature distribution not only on the tool surface but also on the entire tool volume. Figure 4.27 shows the thermal cycles in the punch and in the die recorded both at 30 mm from the tool surface centre (pointPunch, pointDie) and in the point of the tool surface where are observed maximum temperatures (maxPunch, maxDie), during twenty hot stamping cycles.

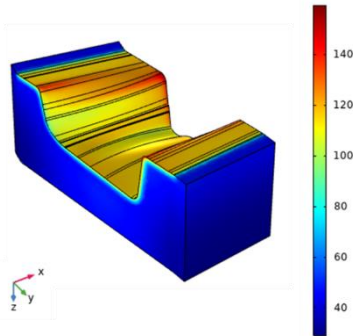


Fig.4.28a: Die temperature distribution in the steady condition at the time corresponding to the peak temperature

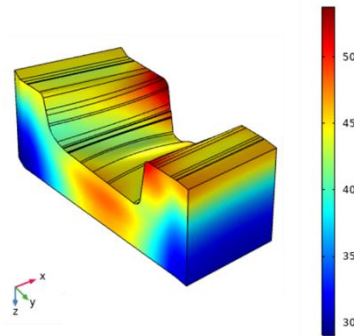


Fig.4.28b: Die temperature distribution in the steady condition at the time corresponding to the end of the hot stamping cycle

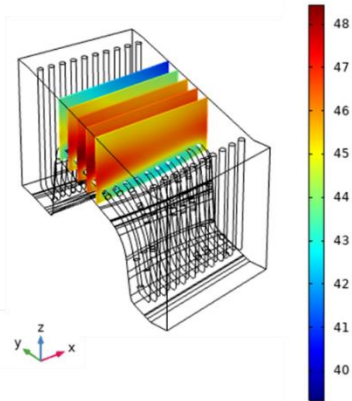


Fig.4.28c: Temperature distribution in the cross sections of the die at the end of the stamping cycle in the steady state condition.

In addition, Figure 4.28 also shows the details of the thermal cycles at steady state. It can be seen that the peak temperatures recorded at 30 mm from the tool surface are about 33% lower than those obtained on the punch and die surfaces. Moreover, it is possible to observe that, while on the tool surface the thermal cycles of the die and the punch coincide, at 30 mm from the tool surface temperatures are lower in the die respect to those recorded in the punch because they depend from the tool shape. Finally, it can be highlighted that the steady state condition is reached starting from the tenth stamping cycle. In Figure 4.28a and in Figure 4.28b, the die temperature distribution in the steady-state is shown at the time corresponding to the peak temperature and at the time corresponding to the end of the hot stamping cycle, respectively. On the other hand, Figure 4.28c shows the temperature distribution in the cross sections of the die at the end of the stamping cycle in the steady state condition. From Figure 4.28a it can be seen that the peak temperature of the die ranging between 100 °C and 160 °C on the surface, while in the remaining part of the die, not in direct contact with the hot blank, the temperature is about 40 °C. From Figure 4.28b, on the other hand, it is observed that the heat is distributed by conduction in the entire volume of the die. In particular, analyzing the temperature distribution in the cross sections of the die (Figure 4.28c), it is observed that near the cooling channels the temperature is slightly higher than 40 °C while moving away from the cooling channels the maximum temperature recorded is 50 °C. From these figures, it emerges that although there are hot spots, in these points, compared to the remaining areas of the tool, the temperature increase of about 20 °C. This temperature increase is negligible, therefore the geometric solution for conformal cooling channels with $p = 9$ mm and $d = 12$ mm is actually an optimal solution.

4.2 FE model of tailored TemperBox® approach

Another innovative approach taken into consideration in this thesis to manufacture components with tailored properties is the Tailored Blank Heating, specifically the innovative patented solution TemperBox®. Details about this technology are presented in the introduction section. First, the blank is fully austenitized. Next, the temperature of soft zones is decreased gradually, by means of convection cooling in a second furnace, over a defined duration. Finally, the blanks are transferred to the press. Next, the forming and quenching phases occur as if it was conventional direct Press-Hardening. Consequently, soft zones can be generated with different phase fractions and hardness values.

AutoForm software allowed to design and simulate the Press-Hardening process with a TemperBox® approach to manufacture the B-Pillar, shown previously in section 4.1, with two soft zones and one hard, the central one. To simulate this process, another heating station was added in the process plan (Figure 4.29) which provides for the maintenance at the complete austenitization temperature for the part of the component with high mechanical properties and cooling to a temperature lower than A_{c1} for ductile areas.

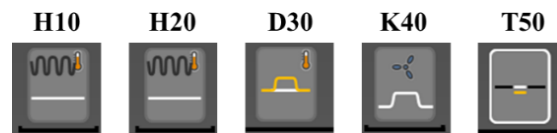


Fig. 4.29: Process plan for FE simulation of Press Hardening process with Temper Box approach

The process parameters are the same as previously highlighted in Table 4.3. No longer having to divide the tools into heated and cooled parts, the air gap was not modelled and the temperature of the tools was considered constant at 80 °C. The quenching time was set equal to 14 s, since in the previous paragraph (section 4.1.3) it has been verified that a completely martensitic microstructure is obtained for this quenching time value. Finally, the transport time from the first to the second furnace and the transport time from the second furnace to the press were set at 5 s. This section shows the numerical results obtained for the USIBOR®1500. As already said in section 4.1, for the USIBOR®2000 steel the influence of process parameters on mechanical properties were evaluated thanks to laboratory tests after physical simulation of thermal cycles. In fact, the numerical results of the TemperBox® on the USIBOR®2000 are not reliable because it is necessary to both derive the flow behaviour of the material in the ferritic-pearlitic field and verify the continuous cooling transformation curves. It is important to get the flow behaviour of the USIBOR®2000 steel also in the ferritic-pearlitic field because the process involves cooling below the A_{c3} temperature in the second furnace. By imposing in the second oven a cooling down to 600 °C in 30 s it is possible to follow the temperature at the end of each process phase (thermal history) on the blank, as can be seen in Figure 4.30.

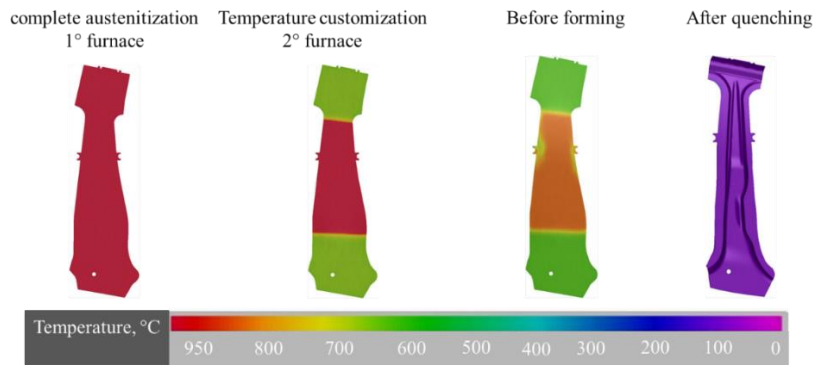


Fig. 4.30: Thermal history on the blank during Press Hardening with Temper Box approach

By comparing the FE thermal cycles recorded in the ductile region III and in the resistant region II, the graph in Figure 4.31 is obtained. FE simulation allowed to track also the phase transformation, as shown in Figure 4.32 reflecting the phase fractions in two different states: before forming (Figure 4.32a) and at the end of the process (Figure 4.32b). Immediately after the second heating station, some bainite and ferrite started to form in the soft zones, while the hard zones are still fully austenitic. In the final component, the soft zones exhibit a mixture of martensite, bainite and ferrite, while the hard zone exhibit only a martensitic microstructure. Therefore, on the final component there are zone with different hardness. The results of the FE simulation for the process parameters considered show an hardness average values of about 320 HV in the soft zones and an 490 HV in the hard zone. Therefore, a softening of about 35 % in the ductile region is reached.

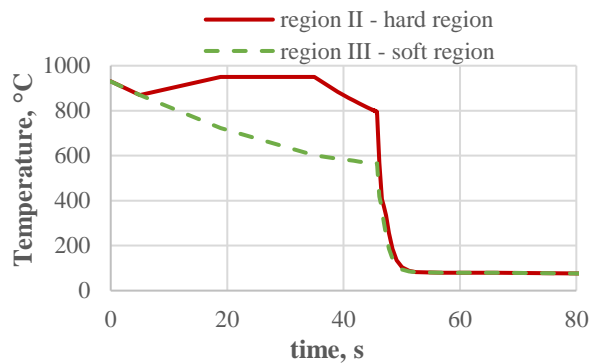


Fig. 4.31: FE thermal cycle recorded in soft and hard region

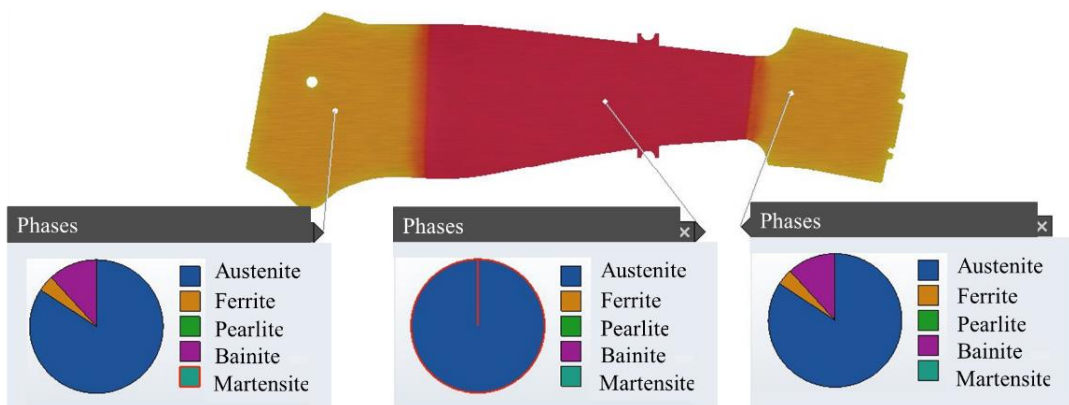


Fig.4.32a: Phase fractions before forming

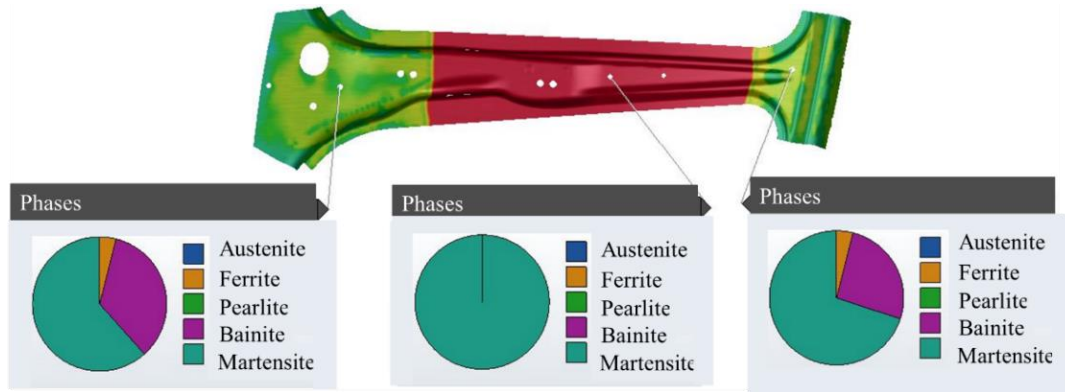


Fig.4.32b: Phase fractions at the end of the process

Table 4.7: FE results in terms of hardness and percentage of microstructural phases for different value of $T_{\text{temperbox}}$ and $t_{\text{temperbox}}$

$T_{\text{temperbox}}, ^\circ\text{C}$	$t_{\text{temperbox}}, \text{s}$	Hardness, HV	Martensite, %	Ferrite, %	Bainite, %	Pearlite, %
600	30	319	56.45	3.9	39.65	0
600	90	193	0	25.72	41.63	32.65
600	150	177	0	52.94	10.3	36.76
600	210	165	0	57.27	0	42.73
650	30	357	71.63	7.21	13.84	7.32
650	90	186	0	47.23	34.71	18.06
650	150	167	0	56.95	13.77	29.28
650	210	163	0	62.5	0	37.5
700	30	370	63.89	7.77	24.52	3.82
700	90	262	41.38	35.29	17.07	6.26
700	150	250	41.31	36.53	15.56	6.6
700	210	240	38.44	39.96	17.34	4.26

The mechanical properties of the component in ductile regions vary according to the temperature to be reached after cooling in the second oven ($T_{\text{temperbox}}$) and the time taken during this cooling ($t_{\text{temperbox}}$). In fact, when these two parameters vary, the cooling rate changes and this leads to a variation in terms of microstructures and hardness. The $T_{\text{temperbox}}$ and $t_{\text{temperbox}}$ parameters were varied respectively between 600 °C - 700 °C and 30 s - 210 s. The results obtained from AutoForm FE simulations are shown in Table 4.7. These results are related to the ductile region, specifically the region III of the investigated B-Pillar. The trend of hardness results as the two process parameters vary are better highlighted in Figures 4.33.

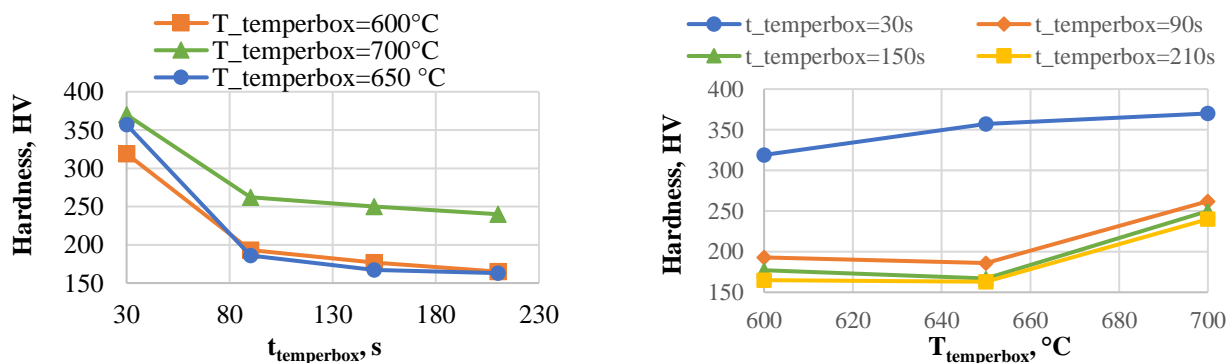


Fig.4.33a: Hardness FE results as a function of $t_{\text{temperbox}}$ for a constant $T_{\text{temperbox}}$

Fig.4.33b: Hardness FE results as a function of $T_{\text{temperbox}}$ for a constant $t_{\text{temperbox}}$

The lowest hardness is recorded, at the same value of $T_{\text{temperbox}}$, for higher $t_{\text{temperbox}}$ values (Figure 4.33a). This happens because the longer the time taken to cool the ductile part of the component, the lower the cooling rate. Low values of cooling rate lead to intersect the continuous cooling transformation (CCT) curves in correspondence of most ductile microstructural phases such as ferrite, perlite and bainite. In this way, the percentage of martensite is reduced, obtaining lower hardness values. An example is shown in Figure 4.34 where the thermal cycles recorded for $T_{\text{temperbox}}$ equal to 600 °C and $t_{\text{temperbox}}$ equal to 30 s and 210 s are superimposed on the CCT diagram of USIBOR® 1500 steel. In fact, the thermal cycle with $t_{\text{temperbox}}$ equal to 210 s lead to a ductile ferritic-pearlitic microstructure (57.27% ferrite and 42.73% perlite from Table 4.6) versus a ferritic-pearlitic-bainitic and martensitic microstructure for $t_{\text{temperbox}}$ equal to 30 s (56.45 % martensite, 3.9% ferrite, 39.65 % bainite from Table 4.6). On the other hand, for the same value of $t_{\text{temperbox}}$, an increase in $T_{\text{temperbox}}$ leads to an increase in hardness (Figure 4.33b). This effect is more marked by comparing the results obtained for $t_{\text{temperbox}}$ equal to 30 s and those obtained for $t_{\text{temperbox}}$ equal to 210 s. The higher the temperature reached in the second furnace, the higher the austenite percentage that will transform into martensite at the end of the process.

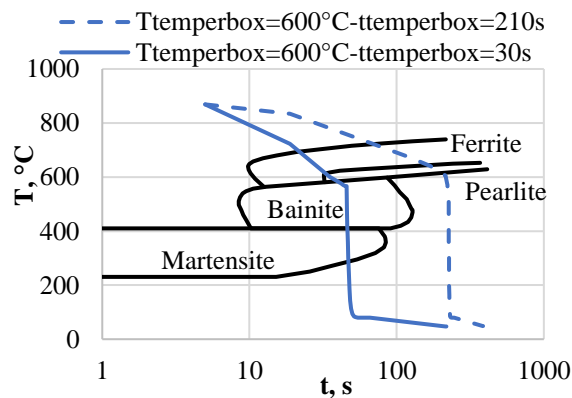


Fig. 4.34: thermal cycles in ductile region III for two different condition (i) $T_{\text{temperbox}}=600\text{ °C} - t_{\text{temperbox}}=30\text{ s}$ (ii) $T_{\text{temperbox}}=600\text{ °C} - t_{\text{temperbox}}=210\text{ s}$ superimposed on CCT diagram

The results shown so far are related to the ductile region III. However, there are no great differences with the results obtained in the ductile region I. Instead, as regards the results relative to the hard zone (region II), the numerical results confirm the presence of a completely martensitic microstructure with a hardness of about 490 HV for each value of $T_{\text{temperbox}}$ and $t_{\text{temperbox}}$ considered. An increase in the time taken for cooling in the second oven implies an increase in the holding time at the complete austenitization temperature in the hard part; Geiger et al. [74] verified that the permanence at high temperature can cause the phenomenon of the austenite grain growth. This phenomenon could lead to a variation of the hardness in the hard part of the component. This observation will be explored better in the next chapter with the experimental hardness results after physical simulation. In this regard, the possibility of reducing the keeping time at high temperature for the hard part will be explored by increasing the transport time of the blank from the first to the second furnace ($t_{\text{transport1}}$), paying attention to always remain in the austenitic field. For example, Figure 4.35a shows the thermal cycles of the hard part for two different transport times $t_{\text{transport1}}=5\text{ s}$ (solid line) and $t_{\text{transport1}}=22\text{ s}$

(dashed line). Results are obtained by performing a numerical simulation with $T_{\text{temperbox}}$ equal to 600 °C, $t_{\text{temperbox}}$ equal to 90 s, and assuming the same total process time.

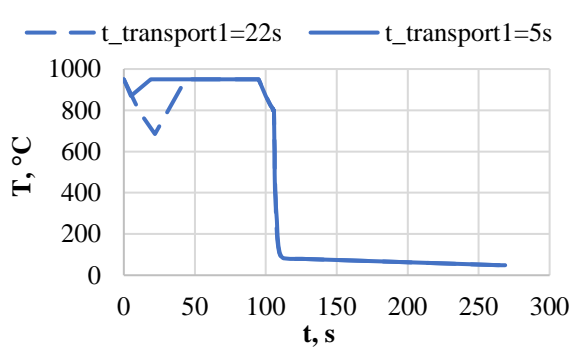


Fig.4.35a: thermal cycles of the hard part (region II) as the transport time between the first and second furnace ($t_{\text{transport1}}$) vary

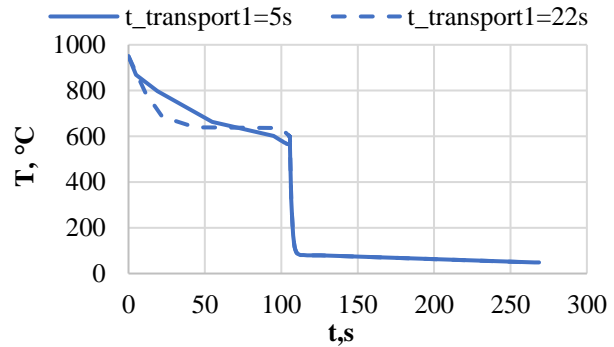


Fig.4.35b: thermal cycles of the ductile part (region III) as the transport time between the first and second furnace ($t_{\text{transport1}}$) vary

Similarly, Figure 4.35b shows the thermal cycles for the ductile zone, again for $t_{\text{transport1}}=5$ s and $t_{\text{transport1}}=22$ s. Notice that, when $t_{\text{transport1}}=22$ s, a thermal cycle similar to an isothermal treatment is observed. This leads to a final completely ferritic-pearlitic microstructure (81.77% pearlite and 18.23% ferrite) and a slightly lower hardness of about 182 HV. Such numerical prediction is performed by the CCT diagram implemented in the software. However, for isothermal treatment, Time Temperature Transformation (TTT) diagram should be adopted. Unlikely, the software procedure does not allow to implement TTT diagram and, in such case, further experimental investigation could be useful to verify numerical results.

4.3 FE thermo-mechanical cycles

Numerical simulation is an excellent tool for designing a process reducing experimental costs and time efforts. In fact, it allows to evaluate mechanical properties of the part and its possible defects, such as thinning, wrinkles, splits. Moreover, it allows to choose the optimal process parameters for obtaining a component with the desired properties. However, experimental tests are always required to validate numerical results. For this reason, in this thesis, physical simulation tests – performed with the Gleeble 3180 system – are adopted to support numerical analysis. Specifically, physical simulation tests were carried out to design the Press-Hardening process with a Tailored Tool Tempering and TemperBox® approaches. To this end, it is necessary to design thermo-mechanical cycles occurring in such approaches.

In this section, FE simulations of Press-Hardening process with Tailored Tool Tempering and TemperBox® approaches are presented; AutoForm software was used for tracking the evolution of temperature and equivalent plastic strain. In the following, thermo-mechanical cycles obtained from FE models are shown. The latter will be reproduced with experiments on Gleeble 3180 system (chapter five).

In a first set of simulations, a study was performed on the transition zone between the ductile and resistant regions of the B-Pillar. Considering the numerical model of the Tailored Tool Tempering (see section 4.1), five FE thermo-mechanical cycles were extracted near the transition zone (Figure

4.36). Simulations have been performed on USIBOR[®]1500. Table 4.8 shows the values of process parameters that have been fixed in the numerical simulation.

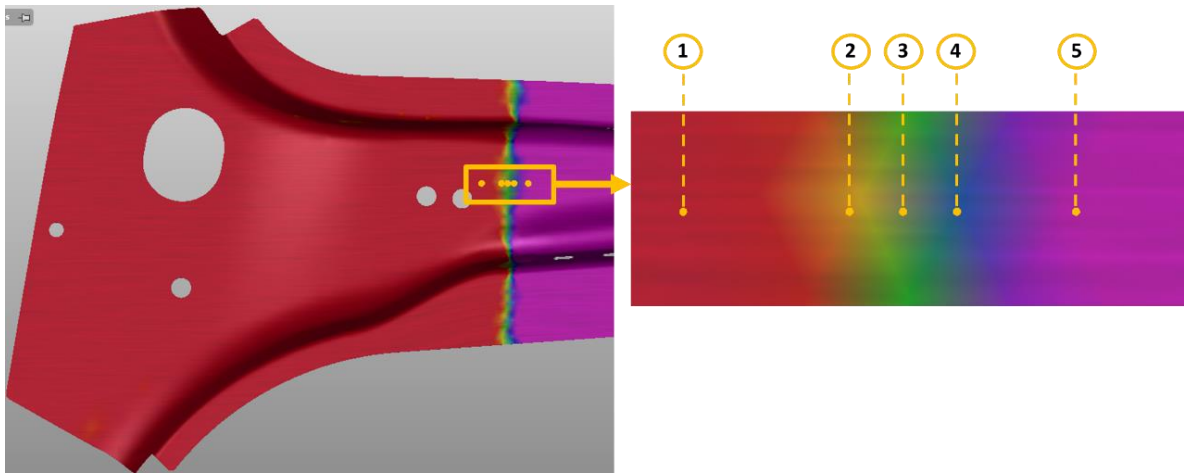


Fig. 4.36: Five points considered near the transition zone for extracting thermo-mechanical cycles

Table 4.8: Values of process parameters of FE model used for transition zone analysis

Parameter	Value
T_hot tool	455°C
t_quenching	20s
t_transport	7.5s
Friction coefficient	0.4

The five thermo-mechanical cycles are shown in Figures 4.37a and 4.37b, where the temperature and equivalent plastic strain are represented as a function of time, respectively.

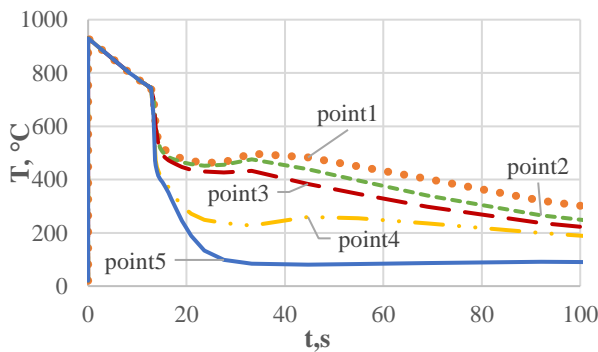


Fig. 4.37a: thermal cycle of five points considered for transition zone analysis

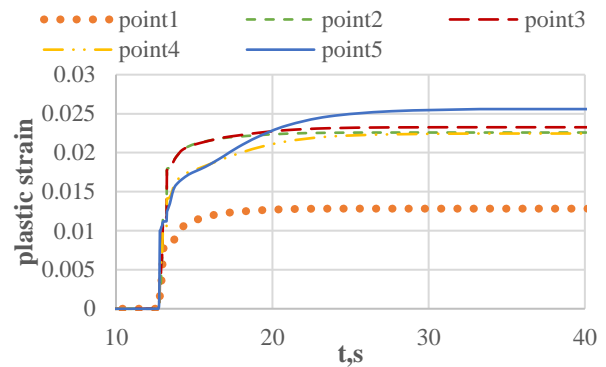


Fig. 4.37b: equivalent plastic strain of five points considered for transition zone analysis

Gleeble system allows to perform experiments under uniaxial tension, while in FE simulations, the component is subjected to a multiaxial stress. In such case, it is reasonable to extract the equivalent plastic strain from numerical model, imposing this strain value as input parameter in physical

simulation tests. Notice that the equivalent plastic strain considers the contribution of deformations in all directions. Such approximation is valid for the purposes of this thesis, as microstructure and hardness are mainly affected by the thermal cycle, which is independent of the direction of deformation.

Table 4.9: Percentage of microstructural phases and hardness value estimated from FE model in the investigated five v

Point	Bainite, %	Martensite, %	Hardness, HV
Point 1	100%	0%	300HV
Point 2	85%	15%	350HV
Point 3	44%	56%	430HV
Point 4	18%	82%	460HV
Point 5	0	100%	500HV

Table 4.9 collects numerical predictions of the percentages of microstructural phases and the corresponding hardness values in the selected five points.

In a second set of simulations, Tailored Tool Tempering numerical model was used to extract thermo-mechanical cycles for different values of process parameters, i.e. the temperature of heated tools and quenching time (Table 4.10). Simulations have been performed on both USIBOR[®]1500 and USIBOR[®]2000. However, since results are almost the same for the two materials, only thermo-mechanical cycles of USIBOR[®]2000 are shown.

Table 4.10: Values of temperature of heated tool and quenching time adopted for the second set of simulations

Temperature of heated tool, °C	Quenching time, s
430-465-500	5-10-20-50-110-150-200-250

Specifically, 24 simulations were performed considering three values of the temperature of heated tools (430-465-500 °C) and eight different quenching times (5-10-20-50-110-150-200-250 s); moreover, the transport time was set equal to 7.5 s. The values of further process parameters (friction coefficient, forming velocity, etc) are collected in section 4.1.1.

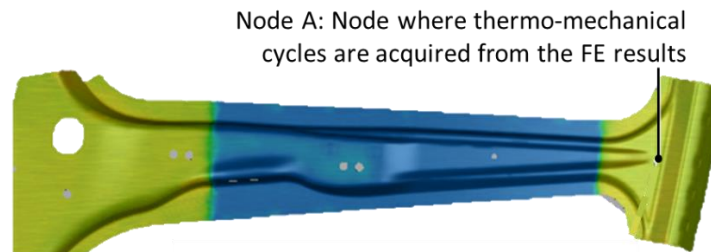


Fig. 4.38: Node chosen to follow thermal and mechanical history of the component during the process

Figures 4.38 a-b show the temperature as a function of time in node A, which is located in the ductile zone of the B-pillar (see Figure 4.38). Node A is purposely chosen far from holes or walls, to avoid spurious effects due to fast heat exchange during the cooling on air phase. This node is representative of regions where there isn't influence of the increased cooling rate, which could lead to martensitic transformations.

Specifically, results in Figure 4.39a show thermo-mechanical cycles with a temperature of the heated tools equal to 500 °C and a quenching time equal to 50 s.

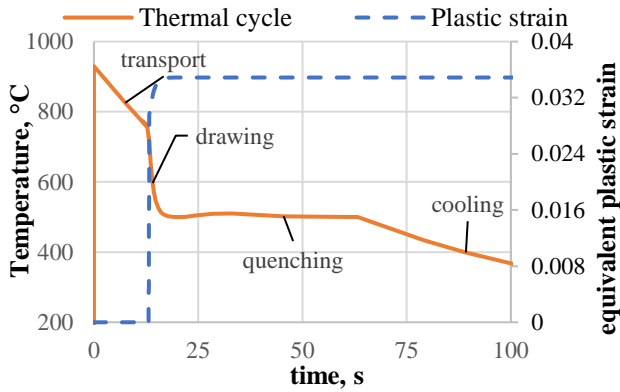


Fig. 4.39a: Example of thermo-mechanical cycle extract from FE model for USIBOR®2000 with quenching time of 50s and tool temperature of 500°C

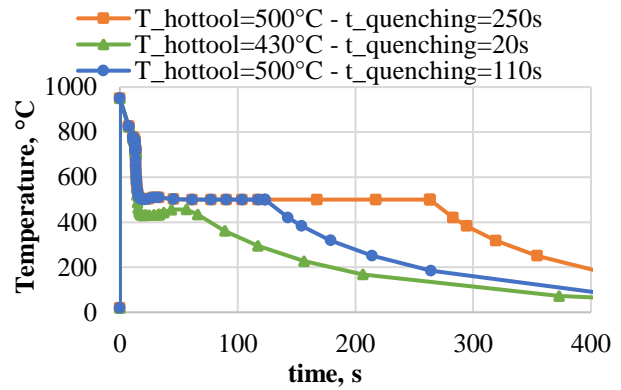


Fig. 4.39b: Thermal cycle for different condition extract from FE-model in USIBOR®2000

Since the same node A was considered in all simulations, the evolution of equivalent plastic strain over the time is equal for each value of both temperature of heated tool and quenching time. On the other hand, the thermal cycles change according to the process parameters taken into account. As a result, the dwell time in the tools and the blank temperature during quenching phase change (Figure 4.39b).

In a third set of simulations, the new TemperBox® technology (see section 4.2) was implemented instead of the classical Tailored Tool Tempering approach. Different values of $t_{\text{temperbox}}$, i.e. the time necessary to cooling the ductile part in the second oven, were considered; moreover, it was fixed $T_{\text{temperbox}} = 600 \text{ °C}$ (being $T_{\text{temperbox}}$ the final temperature reached by the ductile part in the second oven). The values of further process parameters are collected in section 4.2. Simulations were performed on USIBOR®2000.

Thermal cycles were extracted in the ductile region III (Figure 4.40a) and in the high-strength region II (Figure 4.40b).

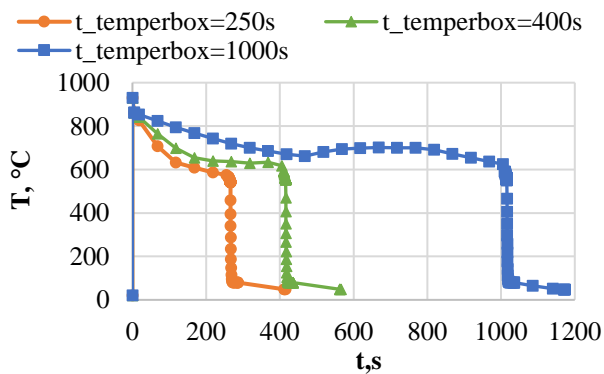


Fig. 4.40a: Thermal cycles in the ductile region III as the parameter $t_{\text{temperbox}}$ changes for $T_{\text{temperbox}}$ equal to 600 °C

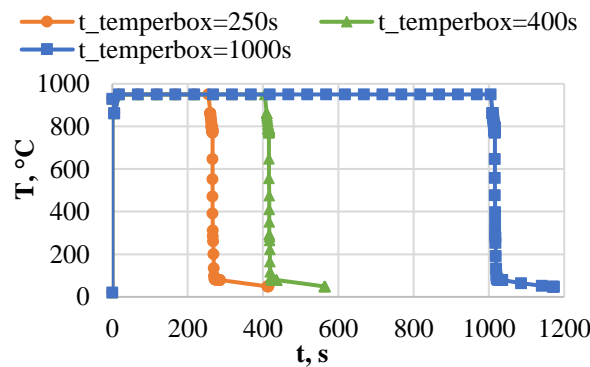


Fig. 4.40b: Thermal cycles in the resistant region II as the parameter $t_{\text{temperbox}}$ changes for $T_{\text{temperbox}}$ equal to 600 °C

As it will be discussed in section 4.3, long $t_{\text{temperbox}}$ can lead to undesired growing of grain size in the hard part during the austenitization phase in the first oven. To avoid this drawback, a first feasible solution may consist in increasing the transport time of the part from the first oven to the second one ($t_{\text{transport1}}$). Therefore numerical simulations were performed increasing the $t_{\text{transport1}}$ from 5 s to 22 s.

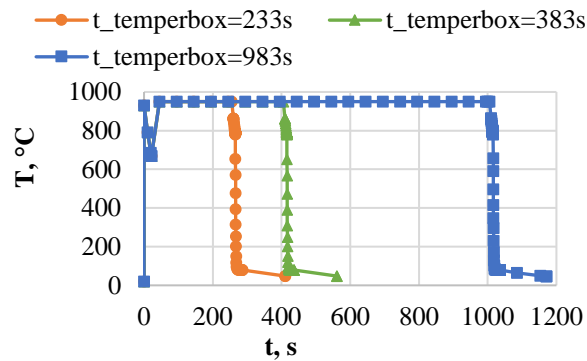


Fig. 4.41: Thermal cycles in the resistant region II as the parameter $t_{\text{temperbox}}$ changes for $T_{\text{temperbox}}$ equal to 600 °C and $t_{\text{transport1}}$ equal to 22 s

Figure 4.41 shows the new thermal cycles of the hard part when a greater transport time of 22 s is imposed.

5. Physical simulation test

In previous section, FE modelling of Press-Hardening processes and numerical results have been presented. In order to verify numerical predictions, physical simulation tests with Gleeble system were performed. To this end, first FE thermo-mechanical cycles were physically reproduced on samples, then tensile and hardness tests were performed on treated samples.

Since the numerical results on the USIBOR[®]2000 were not accurate (a check of transformation points of the CCT curves is required), the physical simulation tests allowed also to study the behaviour of this new steel during the Press-Hardening process with tailored technologies.

In this chapter results of physical simulation and subsequent tensile and hardness tests are shown.

First, results aimed at the analysis of transition zone between ductile and resistant region on the component manufactured with Tailored Tool Tempering technology are presented.

Later, the comparison between USIBOR[®]1500 and USIBOR[®]2000 for manufacturing ductile regions of B-Pillar with Tailored Tool Tempering approach is illustrated. Specifically hardness and tensile tests results are presented to evaluate the ductility and softening of the two steel after Press-Hardening process in the soft regions. Therefore, considerations on cycle times, ductility and softening are drawn.

Finally, hardness results of USIBOR[®]2000 after physical simulation of thermal cycle typical of TemperBox[®] technology are shown.

5.1 Analysis of transition zone by means of physical simulation tests

In tailored process technologies (i.e. technologies for which different heat treatment within the hot-stamping process are exploited), a transition zone between sections of different cooling rates exist and it can exhibit an intermediate or mixed microstructure. Therefore, when manufacturing components with tailored properties, attention must be paid to the mechanical properties of this zone that affect the crash performance of the component. In general, it would be advantageous to ensure a width of transition zone not too small to avoid abrupt changes in mechanical properties, but also not too large to avoid zone, that should exhibit high strength, but are characterized by low strength. From the results shown in this thesis it is observed that the Press-Hardening process with Tailored Tool Tempering approach leads to a transition zone between 20 mm - 30 mm. This width is greater respect to that measured in the classic tailored blank technologies (such as tailor welded blank) for which the transition zone is equal to 2 mm [75].

Given the importance of evaluating the mechanical properties in the transition zone, although the AutoForm software adopted for the modelling of the hot stamping process is able to predict hardness and microstructure in all mesh node of the component, experimental tests were carried out for a better prediction of the component response at the end of the process. In particular, the thermo-mechanical cycles shown in section 4.3 were physically simulated with the Gleeble system. The experimental setup is the same as shown in Figure 2.13, while the specimen geometry used for these experimental tests is the same as shown in Figure 3.28 for the mechanical characterization tests. Since the hot stamping process need to be simulate with the Gleeble physical simulator, the section reduction in central part of the specimens combined with the forced air system, allow to respect high cooling rates ($\sim 10^2$ K/s) during the quenching phase. In fact, forced air alone would not be able, without the optimization of the specimen geometry, to reproduce the thermal cycles. These specimens are obtained by laser cutting a 22MnB5 sheet 2 mm thick. For the experiments, three thermocouples are

welded onto these specimens (Figure 5.1). The control thermocouple (TC2) is welded in the centre of the specimen, the other two thermocouples (TC3 and TC4) are welded at a distance from the centre of 5 mm and 15 mm respectively.

While in the FE software the sheet temperature value is set directly to 930 °C, with the Gleeble system, on the contrary, it is necessary to heat the specimen up to the set temperature of 930 °C. Therefore, the heating from room temperature to this set temperature (temperature of complete austenitization) takes place in two steps. In the first step the specimen is heated from room temperature to 700 °C with a heating rate of 10 K/s. While, in the second step, the heating continues from 700 °C to 930 °C with a heating rate of 5 K/s. Finally, in order to have a completely austenitic homogeneous microstructure, a dwell time of 4 min at the temperature of 930 °C was set.

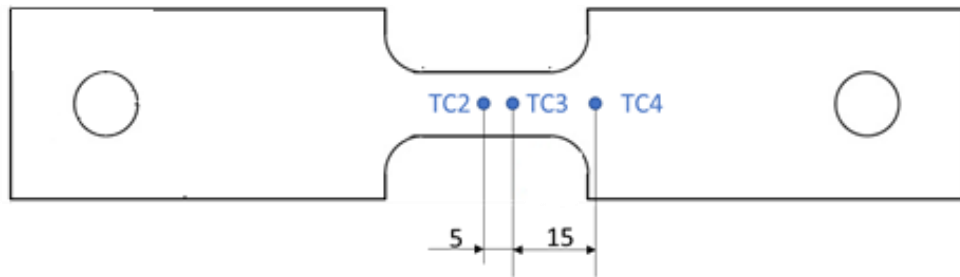


Fig. 5.1: Position of thermocouples welded on the specimen for Gleeble test

Gleeble system, as already said, exploits resistance heating thanks to the current conduction through the copper clamps. The gripping system, however, is cooled with a water-glycol solution; for this reason with increasing distance from the specimen centre, similar thermal cycles to the set one, but with lower peak temperatures, are achieved. Thanks to the thermocouples welded along the longitudinal axis of the specimen, it is possible to record all thermal cycles. Figure 5.2 shows the thermal cycles recorded by TC2, TC3 and TC4 thermocouples for the physical simulation test related to point 1, i.e. point for which thermo-mechanical cycle leads to a completely bainitic microstructure. Figure 5.3, on the other hand, shows the trend of temperature at the end of keeping phase at 930 °C along the longitudinal direction of specimen. In the figure, only one side of the temperature profile has been plotted, since this profile is symmetrical with respect to the specimen central point.

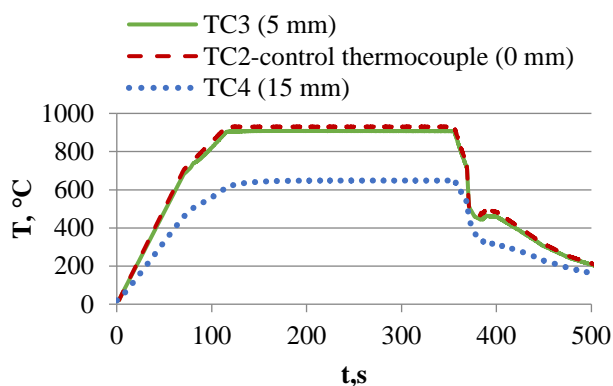


Fig. 5.2: Thermal cycles recorded by TC2, TC3 and TC4 thermocouples during the physical simulation test related to point 1

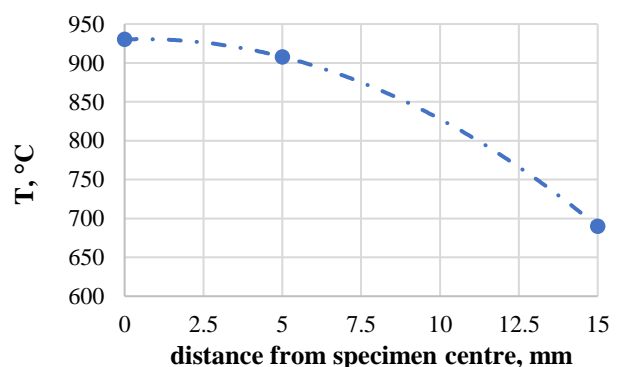


Fig.5.3: Temperature gradient along the longitudinal axis of specimen

From Figure 5.2 it can be observed that at each point along the longitudinal direction of the specimen a different thermal cycle is recorded. Moreover, from the graph in Figure 5.3 it can be observed that about 10 mm away from the specimen centre, the temperature is lower than that of complete austenitization (~850°C). Therefore, the different thermal cycles lead to a different final microstructure. For this reason, hardness value is measured only at the specimen centre. At this point, in fact, the recorded thermal cycle coincides with the set one extrapolated from the FE model.

Vickers-hardness tests are performed with the Qness Q10+ system, a load of 2 kg and a dwell time of 5 s was adopted. The initial hardness value of the specimens corresponding to the martensitic supply state of the USIBOR® 1500P sheet metal is equal to 500 HV.

Considering that only at the specimen centre the thermal cycle is exactly the same as that imposed, Figure 5.4 shows the hardness value measured at the centre of the specimen as a function of the FE predicted percentage of bainite along the width of the transition zone. The same graph also shows the error bar of experimental results and the hardness value estimated by the numerical simulation model.

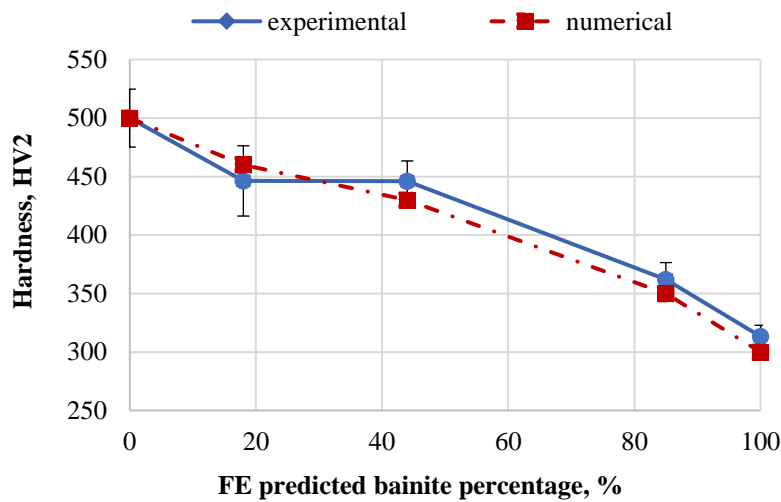


Fig.5.4: Hardness trend as a function of bainite percentage

From the graph in Figure 5.4 it can be seen that, as expected, as the bainite percentage increases, lower hardness values are obtained. An excellent correspondence is also observed between the numerical and experimental results. Therefore, the physical simulation has proven to be a valid tool for experimental verification of the results estimated with the numerical simulation.

To confirm the good correspondence between numerical and experimental results, metallographic analyses were performed on specimens subjected to Gleeble thermal cycles.

After physical simulation tests, central sections of specimens were mounted in epoxy resin and then grinded and polished to obtain a surface suitable for the metallographic observation. Finally, chemical etching (2 % Nital) was carried out. Microscopic observations were done using the Eclipse MA200 Nikon light microscope. These observations were performed at the point where the pilot thermocouple was welded.

Furthermore, to evaluate mechanical properties in the transition zone, tensile tests assisted by DIC system were performed after physical simulation of thermo-mechanical cycles extracted from FE model near the transition zone (Figure 4.36). As highlighted in paragraph 2.4, *notched* specimens, obtained by reducing the center sample section exactly where the control thermocouple was welded, were adopted.

Figures 5.5 a-b-c show micrographs relating to the specimens subjected to the Gleeble thermo-mechanical cycles of points 1, 3 and 5, respectively.

On the other hand, Figure 5.6 shows the results of the tensile tests of specimens subjected to thermo-mechanical cycles of points 1, 3 and 5 in the transition zone.

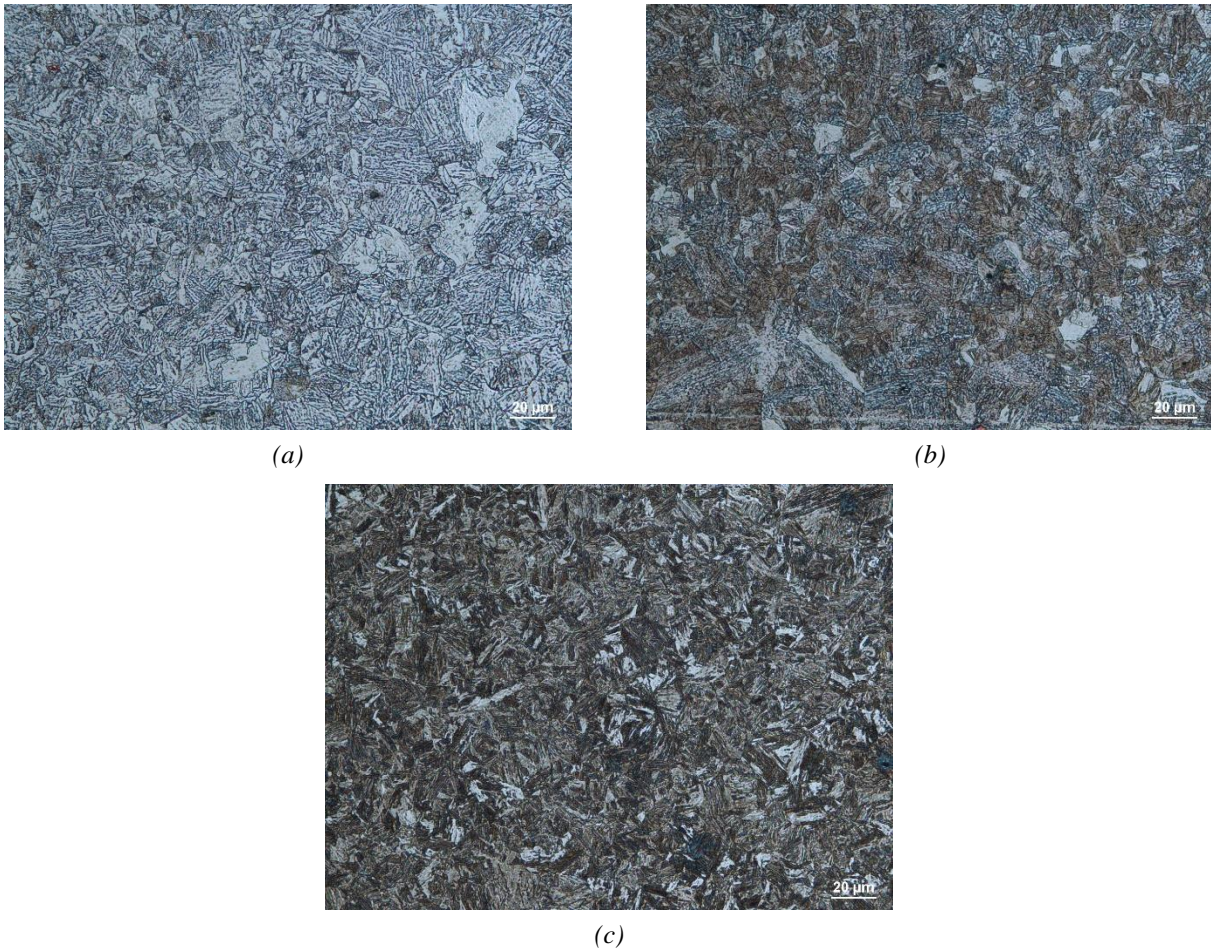


Fig. 5.5 Microstructure (500x) of the USIBOR®1500 steel obtained in the central section of specimen after physical simulation tests of thermo-mechanical cycles of point 1 (a), point 2 (b) and point 5 (c)

In accordance with the numerical prediction, the thermo-mechanical cycle of point 1 leads to a predominantly bainitic microstructure (Figure 5.5a); the thermo-mechanical cycle of point 3 leads to a mixed bainitic-martensitic microstructure (Figure 5.5b), while the thermo-mechanical cycle 5 leads to a predominantly martensitic microstructure (Figure 5.5c).

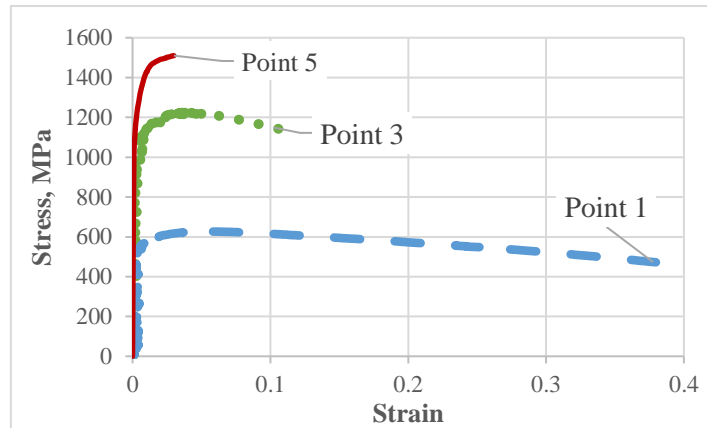


Fig. 5.6 Stress-strain curves representative of mechanical properties in three different point near transition zone

As can be seen from Figure 5.6, the highest value of rupture deformability is observed in the specimen subjected to the thermo-mechanical cycle of point 1 (predominantly bainitic microstructure). In this specimen, however, the lowest value of tensile strength is recorded. On the contrary, the highest value of tensile strength is reached in the specimen subjected to the thermo-mechanical cycle of point 5 (predominantly martensitic microstructure). From these results it is confirmed that an increase in the percentage of bainitic microstructure leads to a greater ductility of the part.

The specimen subjected to thermo-mechanical cycle of point 3 (at the center of the transition zone) shows a value of rupture deformability of about 10%, between 37% (point 1) and 5% (point 5), and a tensile strength of about 1200 MPa. Such value is between 600 MPa (point 1) and 1500 MPa (point 5). These results confirm a mixed bainitic-martensitic microstructure.

5.2 Design of Press-Hardening process by means of physical simulation tests

In the previous section, the Gleeble system was mainly adopted to verify the reliability of the numerical results. In the following sections, on the other hand, the physical simulation combined with the numerical simulation will be mainly adopted to design the hot stamping process with both a Tailored Tool Tempering and a TemperBox[®] approach. In fact, once the thermo-mechanical cycles were obtained as the process parameters vary (quenching time and heated tools temperature for the first approach – cooling time in the second furnace and temperature at which the ductile part of the blank must cool in the second furnace for the second approach), these were physically simulated using the Gleeble system. Considerations regarding the mechanical properties were drawn after subsequent hardness, tensile tests and metallographic analyses.

5.2.1. Physical simulation tests of Tailored Tool Tempering approach

In the previous section 4.3, FE thermo-mechanical cycle extracted in the ductile region of the B-Pillar are shown. With the aim to experimentally evaluate the mechanical properties of both USIBOR[®]1500 and USIBOR[®]2000 for different value of quenching time and temperature of heated tools, these cycles were reproduced on both USIBOR[®]1500 and USIBOR[®]2000 samples thanks to the Gleeble system. Samples adopted during experimental tests present the same geometry described in Figure 3.28 and the set-up is the same as shown in Figure 2.13. On these specimens, in addition to the central control thermocouple (TC2), two other thermocouples are welded at a distance from the center of 10 mm and 15 mm respectively (TC3, TC4). Because of cooling water-glycol solution in the gripping

system, with increasing distance from the specimen centre, similar thermal cycles to the set one, but with lower heating temperatures, are observed. Figure 5.7 shows the thermal cycles recorded by the thermocouples in the physical simulation test on a USIBOR®2000 steel specimen, in the condition with temperature of the heated tools equal to 430 °C and quenching time equal to 20 s (T430tq20 condition).

These results confirm the heating temperature decreasing with the increasing of the distance from the specimen centre along the longitudinal axis direction. It can therefore be highlighted that at about 10 mm away from the specimen center, the maximum temperature reached during the heating phase is lower than that of the complete austenitization of both steels, which means that in the same Gleeble test the hot stamping on a blank with the initial ferritic-pearlitic microstructure is also physically simulated.

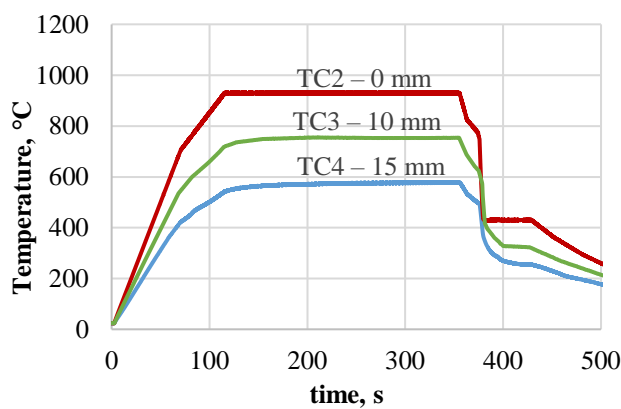


Fig. 5.7: Thermal cycles recorded by the thermocouples during the Gleeble tests on USIBOR®2000 specimen in the condition of temperature of heated tools equal to 430 °C and quenching time 20 s.

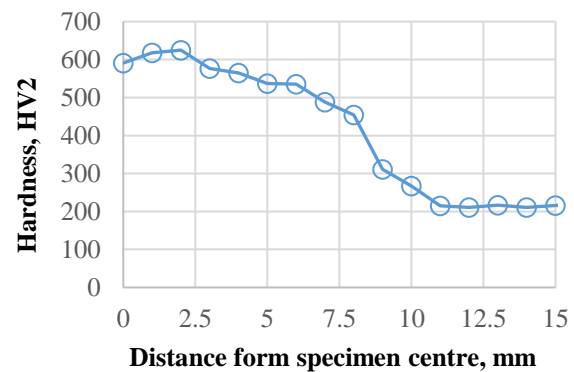


Fig. 5.8: Hardness values along longitudinal direction of USIBOR®2000 specimen for the condition of temperature of heated tools equal to 430 °C and quenching time equal to 20 s.

The effect of the reduction of the heating temperature with the increase of the distance from the specimen centre can be highlighting analysing the hardness profile (hardness as a function of distance from the specimen centre), which has been measured along the specimen longitudinal axis after the physical simulation test. Figure 5.8 shows the hardness profile achieved in a USIBOR®2000 steel specimen physically simulated with the T430tq20 condition. It can be seen that within about 2.5 mm from the specimen center the hardness can be considered constant, highlighting a negligible temperature gradient in the specimen central area. Moving towards cooled grips, the hardness value decreases up to a constant value that corresponds to the hardness value in the supply state (ferritic-pearlitic micro-structure) for the USIBOR®2000 (~215HV). Only in the specimen center, the thermo-mechanical cycle recorded coincides with the set one; therefore, only the hardness value close the central point has been used to analyse the effect of the thermo-mechanical cycle set. These considerations can also apply to the USIBOR®1500 steel specimens.

After physical simulation tests were carried out, by varying the most influential process parameters, on both steels taken into consideration, hardness tests were performed. These allowed both to compare the two steels and to understand the optimal process parameters to obtain the greater softening in ductile regions.

By averaging five hardness values measured on the specimen surface closed to the specimen center, the graphs in Figure 5.9 can be plotted. In particular Figures 5.9a, 5.9b and 5.9c show hardness values of the specimen center for different quenching times and a temperature of the heated tools equal to 430 °C, 465 °C and 500 °C, respectively.

The hardness is an indicative parameter of the microstructure. Therefore, it can be assume that as the hardness value decreases, the percentage of transformed martensite decreases and the bainite percentage increases. When the hardness value remains constant, it can be suppose that there has been a complete bainitic transformation.

By observing the behavior of the USIBOR[®]1500, the complete bainitic transformation is obtained for quenching times of 20 s when the temperature of heated tools is 430 °C (blue curve with circular markers in Figure 5.9a). When the temperature of the heated tools is equal to 465 °C or 500 °C, the complete bainitic transformation is reached earlier, for quenching times of 5 s (blue curve with circular markers in Figure 5.9b and Figure 5.9c). In fact, the higher the temperature of heated tools, the higher the part metal temperature at the end of the quenching phase and the lower the cooling rate during the cooling on air phase, leading to the complete bainitic transformation.

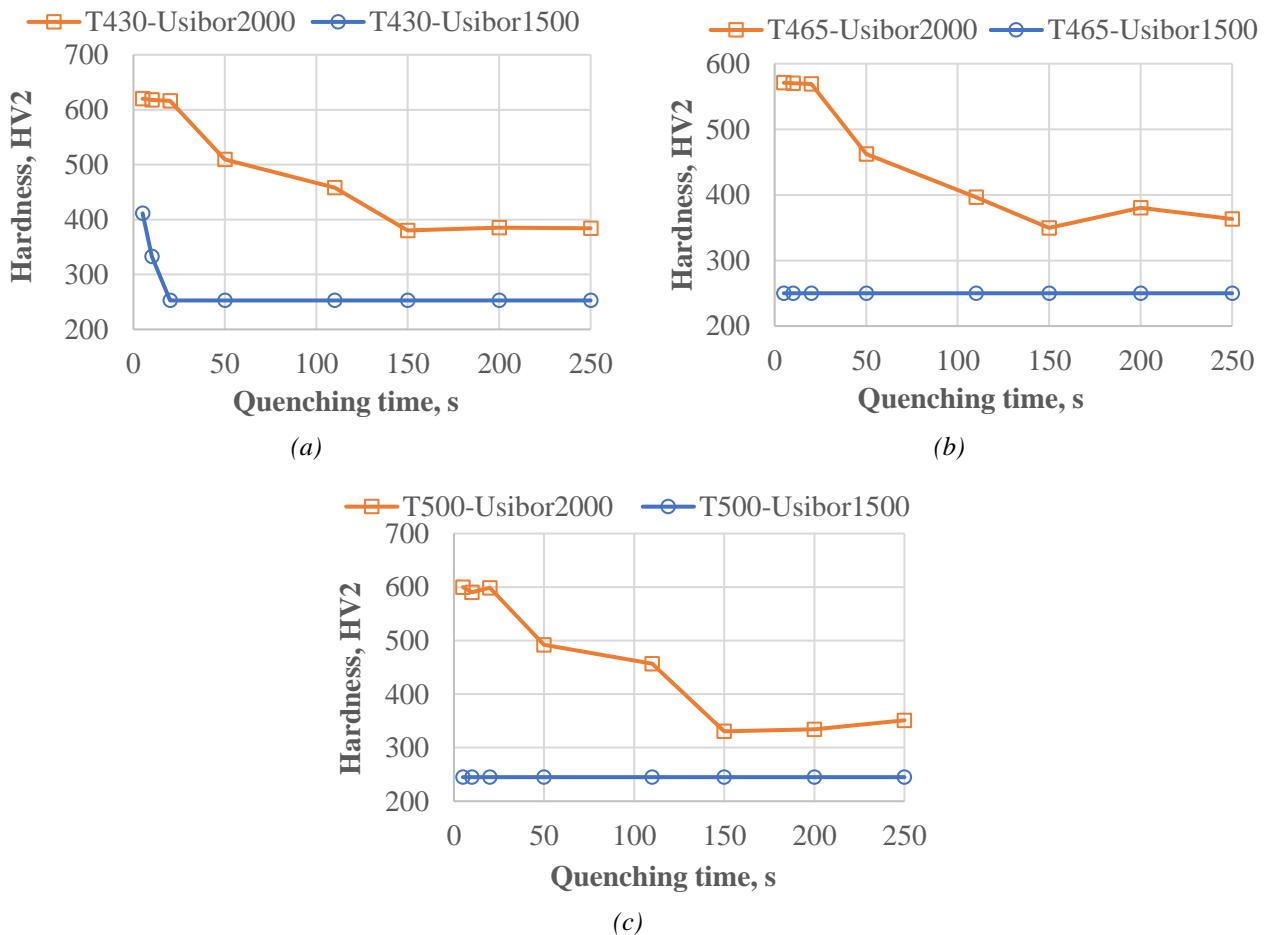


Fig.5.9: (a) Hardness values for different quenching time at temperature of 430 °C; (b) Hardness values for different quenching time at temperature of 465 °C; (c) Hardness values for different quenching time at temperature of 500 °C

For the USIBOR®2000, however, it is observed that the hardness remains constant starting from a quenching time of 150 s (orange curve with square markers in Figures 5.9a, 5.9b and 5.9c).

The observation of metallographic samples confirms the interpretation of the obtained hardness results. Figure 5.10 shows some micrographs obtained observing USIBOR®2000 steel metallographic samples with a Nikon Ig_ma200In optical microscope. Figure 5.10a refers to the steel in the supply state. Figures 5.10b and 5.10c were obtained in specimens centre after physical simulation of the thermomechanical cycles corresponding to an hot tool temperature of 500 °C and quenching times of 20 s (Figure 5.10b) and 250 s (Figure 5.10c).

Micrographs were obtained by etching metallographic samples for 18-20 s in a 4 % picral etchant (4 gm dry picric acid in 100 ml ethanol). In the thermomechanical cycle carried out with a quenching time of 20 s, the ferritic-pearlitic structure oriented in the rolling direction observed in Figure 5.10a is transformed into a predominantly martensitic structure with small islands of residual austenite (Figure 5.10b). With a quenching time of 250 s (Figure 5.10c), on the other hand, a predominantly bainitic structure is observed.

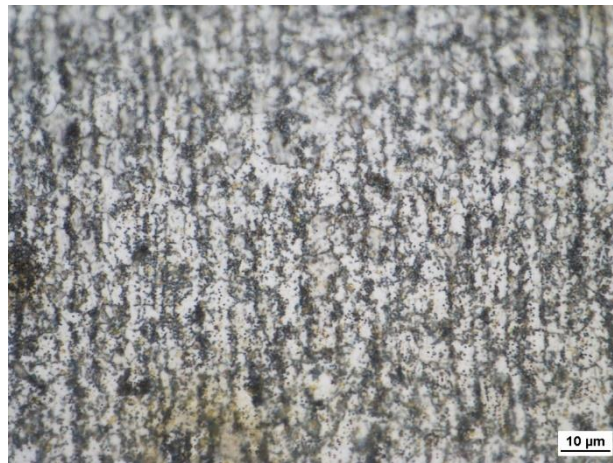


Figure 5.10a: Microstructure of USIBOR®2000 steel in the supply state (1000x)

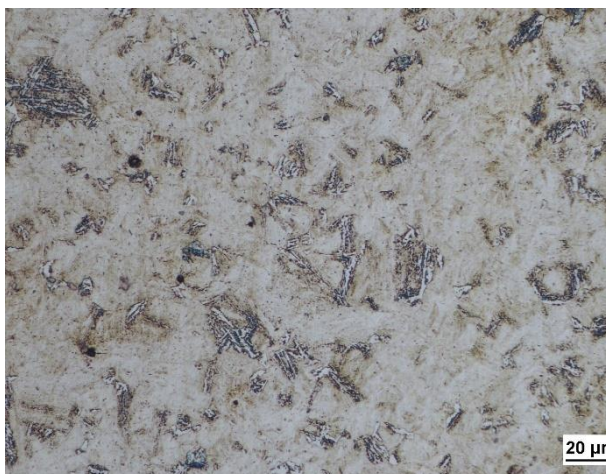


Figure 5.10b: Microstructure of the USIBOR®2000 steel obtained in the specimen central point with the T500tq20 condition (1000x)

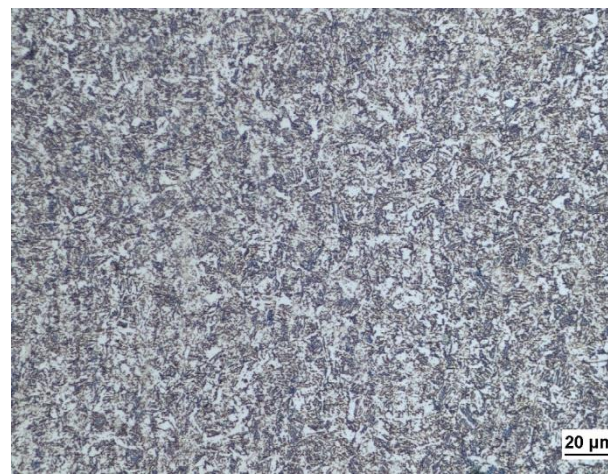


Figure 5.10c: Microstructure of the USIBOR®2000 steel obtained in the specimen central point with the T500tq250 condition (1000x)

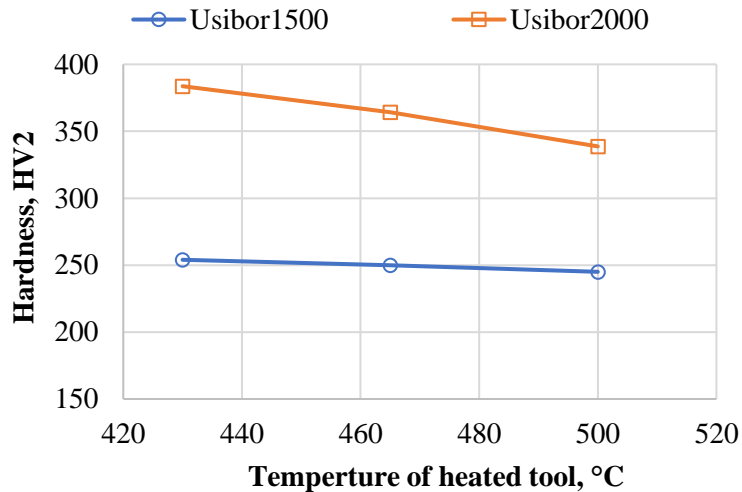


Fig. 5.11: Bainite hardness trend (100%) as a function of temperature of heated tools

The results shown in Figure 5.11 highlight that USIBOR[®]2000 steel hardness is always greater than that of the USIBOR[®]1500 steel. The higher hardness before the complete bainitic transformation is given by the higher percentage of martensite (for the higher hardenability) and by the higher hardness of the martensite (for the higher percentage of carbon). By comparing, however, the value of the quenching time at which the two steels reach the complete bainitic transformation, it is possible to state that the complete bainitic transformation is reached earlier for the USIBOR[®]1500. This is a consequence of the shifting of the CCT (Continuous Cooling Transformation) curves at higher transformation times. This shift is observed by comparing the CCT curves of 22MnB5 obtained in [33, 76-77] and the CCT curves of 37MnB5 described in the work of [33].

Further considerations can be made analyzing the minimum hardness value (higher softening) as a function of temperature of heated tools for both steels (Figure 5.11); in particular the hardness values of the USIBOR[®]2000 steel are an average of the tests at quenching time equal to 150 s, 200 s and 250 s. It is possible to observe that hardness decreases with the increase of the temperature of the heated tools, especially for USIBOR[®]2000 steel. This can be justified by the variation of morphology of the bainitic microstructure with the transformation temperature. The hardness differences between the two AHSS steel at each temperature of the heated tool can be again justified due to the greater carbon percentage of the USIBOR[®]2000 steel.

To verify the difference between the two UHSS steels also in terms of elongation at break in the condition of greater softening, Gleeble thermo-mechanical cycles in the conditions that guarantee the minimum hardness are repeated to subsequently perform tensile tests. For all temperatures of the heated tools investigated, the physically simulated thermo-mechanical cycles are those relating to a quenching time equal to 200 s for the USIBOR[®]2000 and equal to 20 s for the USIBOR[®]1500.

The tensile tests were performed by means of the Instron 4485 universal testing machine and they were assisted by the Digital Image Correlation (DIC) system ARAMIS 3D (provided by GOM). The DIC system allowed to evaluate the local elongation of the specimen. Uniaxial tensile tests were carried out on the notched specimens shown in Figure 5.12, obtained machining the specimens subjected to physical simulation. Notched specimens are adopted in order to force plastic deformation exactly in the central point of the specimen which is the point where thermo-mechanical cycle is imposed because it is the point where the control thermocouple is welded during the Gleeble test.

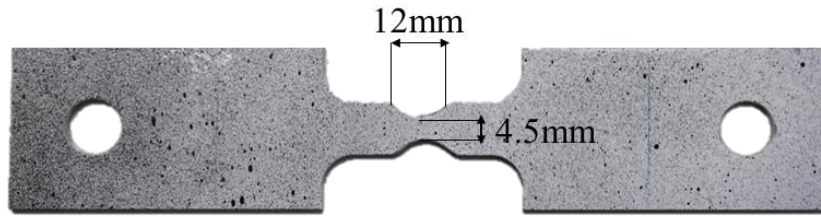


Fig.5.12: speckled notched specimen adopted for tensile tests

The stress-strain curves obtained are compared in Figure 5.13. Only the extremes values of the temperatures of the heated tools investigated are shown: 430 °C (Figure 5.13a) and 500 °C (Figure 5.13b). From these graphs, as expected, a greater ultimate tensile strength as well as a lower elongation at break is observed for the USIBOR®2000 compared to the USIBOR®1500. Furthermore, for both investigated steel, by reducing the temperature of heated tools, there is an increase in mechanical strength and a decrease in elongation.

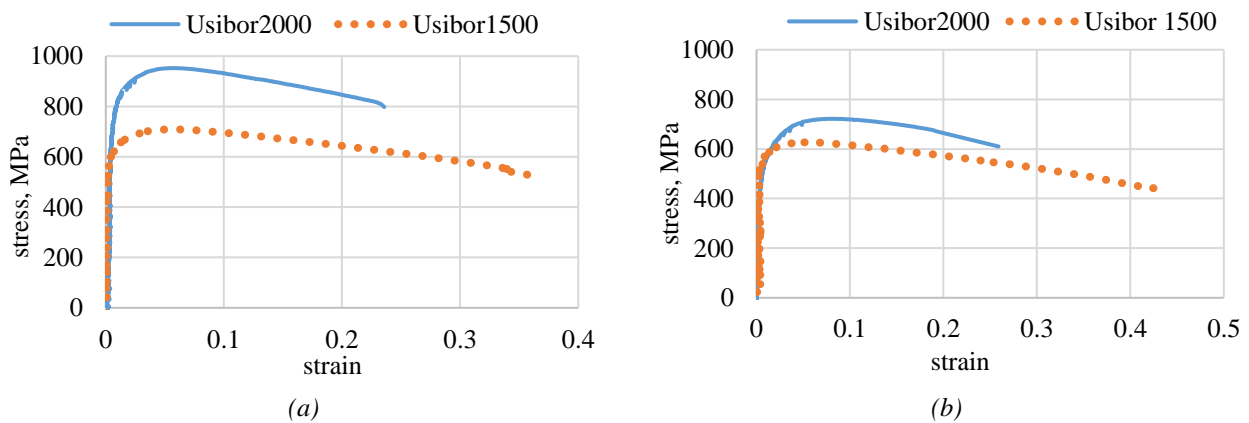


Fig. 5.13: (a) Stress-strain curves for the two UHSS in the condition of heated tools temperature of 430 °C; (b) Stress-strain curves for the two UHSS in the condition of heated tools temperature of 500 °C

The results shown in Figure 5.13 evidence that the ductile zone of the B-Pillar in USIBOR®1500 steel has elongations greater than 30 % and 40 % by varying the temperature of the heated tool from 430 °C to 500 °C. The sufficiently low quenching time used is interesting for an industrial application of the Press-Hardening process with the Tailored Tool Tempering approach. The ductile zone of the Pillar in USIBOR®2000 steel shows a more contained increase in elongation, but always greater than 20 %. However, due to the higher hardenability of USIBOR®2000 steel, quenching time are excessive.

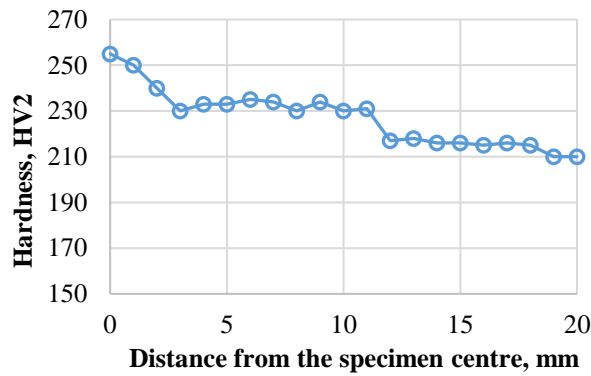


Fig. 5.14: Hardness trend along the longitudinal direction of the specimen in USIBOR®2000 after physical simulation of Tailored Heated Blank approach

Observing the hardness profile shown previously in Figure 5.8, at 10 mm from the specimen center a hardness of about 270 HV is reached (equivalent to the hardness value obtained on the USIBOR®1500 in the condition of complete bainitic transformation). This suggests that a reduction in the quenching time could be obtained by differentiating the blank heating temperature (following a Tailored Blank Heating approach).

The physical simulation of the corresponding hot stamping process is designed with a heating phase up to 750 °C, a tool temperature of 80 °C and a quenching time equal to 20 s. This new thermal cycle was imposed in the central point of USIBOR®2000 steel specimen. Hardness tests after physical simulation confirms about 250 HV in the specimen centre (Hardness profile is illustrated in Figure 5.14), while tensile test shows an elongation of about 20 %. This elongation value is lower than those obtained with the Tailored Tool Tempering approach with a quenching time of 200 s, probably due the lower microstructure homogeneity obtained with the partial austenitization of the steel in the supply state (Figure 5.10a).

This solution requires more in-depth analysis, but it is potentially of interest for the industrial production of part in USIBOR®2000 steel by Press-Hardening with a Tailored Blank Heating approach.

Details about results of physical simulation tests of tailored tool tempering approach are in reference [78].

5.2.2. Physical simulation tests of TemperBox® approach

In section 4.3, finite element (FE) simulations of TemperBox® approach were presented for different values of $t_{\text{temperbox}}$. With $t_{\text{temperbox}}$, it has been denoted the time necessary for the temperature of the ductile zone to decrease from T1 to T2, being T1 the value of complete austenitization and T2 the final value in the second oven. The FE thermal cycles (see Fig. 4.39) have been extracted and simulated during experiments through the Gleeble physical simulator on USIBOR®2000 samples. The latter present a thickness of 2 mm and the same geometry shown in Figure 3.28.

After the physical simulation of Press-Hardening process, specimens were subjected to Vickers hardness tests to estimate the mechanical properties of the part. A load of 2 kg and a dwell time of 5 s were adopted for hardness tests.

Three thermocouples were welded along the longitudinal section of the specimen, in order to record the temperature variation. The control thermocouple, which controls the imposed thermal cycle, was

located at the centre of the specimen. Figures 5.15a-b show the hardness obtained by averaging the values measured at the location of the control thermocouple. Specifically, Figure 5.15a shows results related to the thermal cycles extracted from the ductile part. In agreement with FE predictions (see section 4.3), if $t_{\text{temperbox}}$ increases, a reduction in hardness is observed on the ductile part. On the other hand, FE simulations returned a constant hardness for the resistant part, while experiments show a clear reduction of hardness with increasing $t_{\text{temperbox}}$, as observed in figure 5.15b, where experimental measurements on the resistant part are collected. Such discordance may be related to the fact that FE model does not take into account the growing of grains due to prolonged time at high temperature.

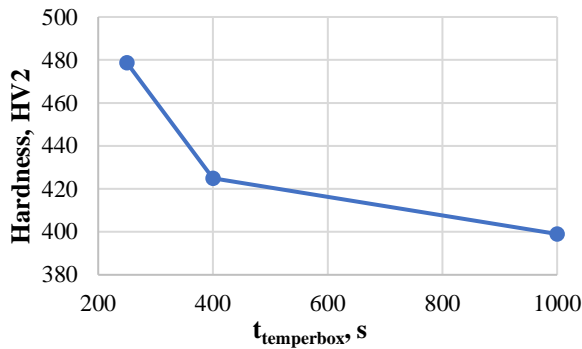


Fig. 5.15a: Hardness values for different values of $t_{\text{temperbox}}$ related to the thermal cycles in ductile zone of investigated component

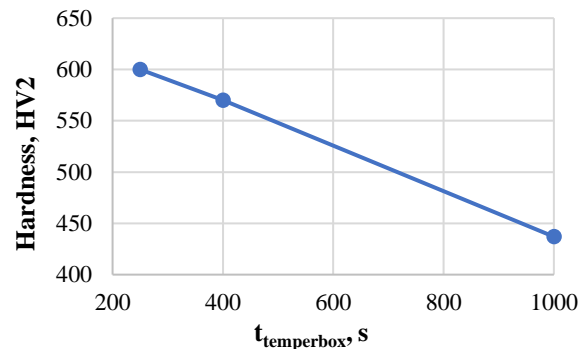


Fig. 5.15b: Hardness values for different values of $t_{\text{temperbox}}$ related to the thermal cycles in hard zone of investigated component

The phenomena determining the reduction of hardness are different for the ductile and resistant parts. In the ductile part, enhancing $t_{\text{temperbox}}$ leads to an increase in the fraction of the ferritic-pearlitic microstructure and, therefore, to a decrease in the martensitic fraction (that is the harder one).

In the resistant part, long $t_{\text{temperbox}}$ leads to an increase in the total time the blank remains at high temperature (930 °C). In such conditions, microstructure grains grow and a notable reduction in hardness occurs (Figure 5.15b). However, these aspects were deeper investigated by means of metallographic analyses.

Once thermal cycles of the TemperBox process relating to the resistant part were physically reproduced with Gleeble system for all values of the $t_{\text{temperbox}}$ parameter, specimens were prepared for metallographic analyses. A 2% Nital chemical etching was carried out. Figures 5.16 show micrographs observed at the center of specimens (where the pilot thermocouple was welded). Specifically, Figure 5.16a shows the microstructure obtained after the TemperBox® treatment cycle with a $t_{\text{temperbox}}$ value of 250 s, while Figure 5.16b shows the microstructure observed at the end of the TemperBox® thermal cycle for $t_{\text{temperbox}}$ of 1000 s.

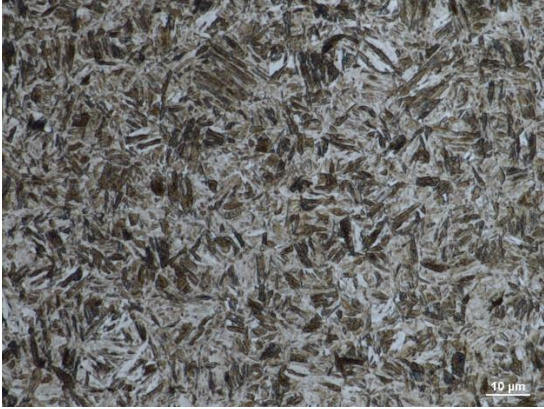


Fig. 5.16a: Microstructure observed with the optical microscope (100X) after the TemperBox® thermal cycle in the resistant part for $t_{\text{temperbox}}$ of 250 s.

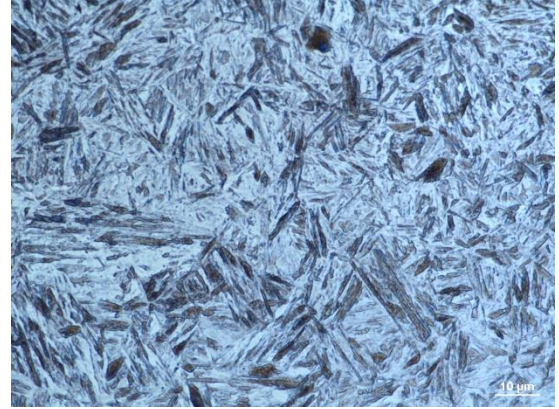


Fig. 5.16b: Microstructure observed with the optical microscope (100X) after the TemperBox® thermal cycle in the resistant part for $t_{\text{temperbox}}$ of 1000 s.

Comparing the two figures, it is possible to observe larger martensitic laths in Figure 5.16b respect to those observed in Figure 5.16a.

Results of metallographic analyses confirm that the reduction in hardness is due to an increase in the grain size, caused by a great value of dwell time at the complete austenitization temperature.

At $t_{\text{temperbox}} = 250$ s, a hardness of 480 HV2 is measured in the ductile part and 600 HV2 in the resistant one. Therefore, it is possible to guarantee a differentiation of the mechanical properties on the component. The resulting softening is equal to 20%, while greater percentages could be required by automotive companies. To this end, one could increase $t_{\text{temperbox}}$. However, at $t_{\text{temperbox}} = 1000$ s, the values of hardness in the ductile and resistant part are almost the same, 399 HV2 and 437 HV2, respectively. Such value is acceptable for the ductile part (with a softening of about 34%), but not for the resistant one. In fact, there is no clear difference between the two zones and, consequently, the tailored properties on the component are not guaranteed.

In order to obtain higher hardness in the resistant part, one could decrease the total time the blank remains at high temperature. A feasible solution could be to increase the transport time $t_{\text{transport1}}$ of the blank from the first to the second oven (as already discussed in section 4.3); in this way, grains growing should be less important. To verify such solution, physical simulations with $t_{\text{transport1}} = 5$ s and $t_{\text{transport1}} = 22$ s were performed on the resistant part, but no significant variation of hardness was measured after the processes. Unlikely, it is not convenient to fix $t_{\text{transport1}} \gg 5$ s, as austenitic field will not be longer guaranteed. These results suggest that high $t_{\text{temperbox}}$ should be avoided.

At short $t_{\text{temperbox}}$, softening of the ductile part is about 20%. To increase such value, a new technique was investigated for manufacturing components in USIBOR®2000 with tailored properties. This new approach is sketched in Figure 5.17.

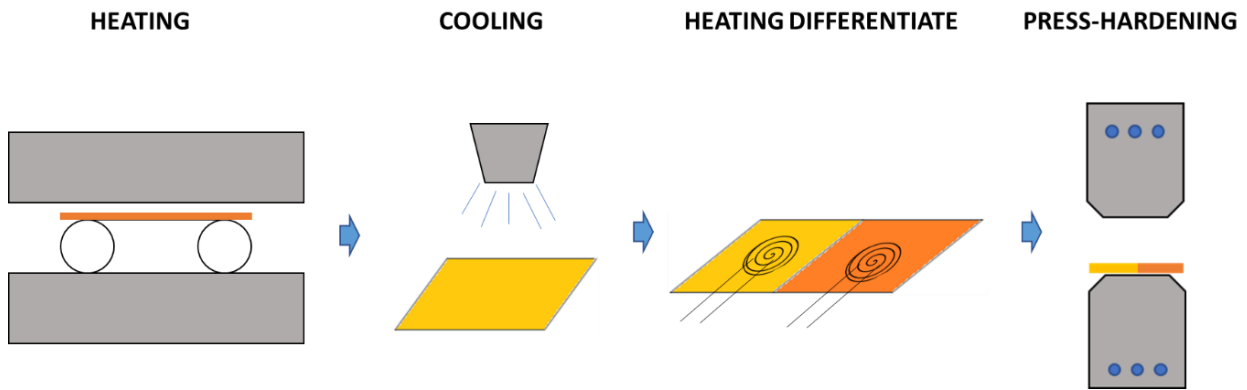


Figure 5.17: Proposed tailored hot stamping process

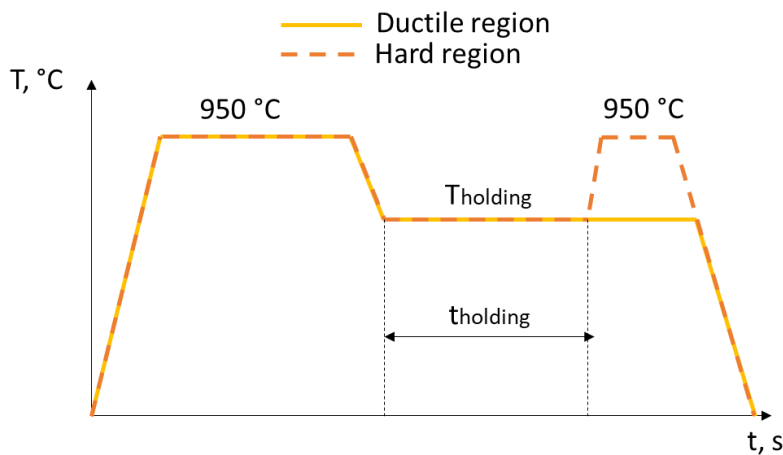


Fig. 5.18: Thermal cycles of ductile and hard region in the proposed tailored Press-Hardening process

In the first phase, the component is subjected to heating at $T = 930 \text{ }^\circ\text{C}$ for four minutes (time required for obtaining a homogeneous austenitic microstructure). In the second phase, the component is rapidly cooled down to a fixed temperature (for example $600 \text{ }^\circ\text{C} - T_{\text{holding}}$). In the third phase, ductile and hard regions are maintained at this constant temperature thanks to the use of two inductors (the use of inductors can be a possible technological solution). Before the end of the third phase, the hard part is again heated up to $T = 930 \text{ }^\circ\text{C}$ for four minutes. The final phase consists in classical press-hardening process. The thermal cycles related to the ductile and the resistant part are schematized in Figure 5.18. Rapid cooling (between the first and third phases) allows to remain in the austenitic field and control the final desired microstructure.

This new approach has been tested by means of physical simulation on the ductile part. USIBOR[®]2000 sample, presenting thickness of 2 mm and the same geometry shown in Figure 3.28. Experiments were performed by imposing a temperature of $600 \text{ }^\circ\text{C}$ in the third phase, and investigating different holding times t_{holding} at this temperature. Figure 5.19 shows the thermal cycles that were physically simulated. The holding times explored are equal to $t_{\text{holding}} = 300 - 400 - 600 - 1000 \text{ s}$.

At the end of the Gleeble treatment, Vickers hardness tests were carried out in the point where the control thermocouple was welded, adopting a load of 2 kg and a dwell time of 5 s. Results are shown

in Figure 5.20, where hardness is given in terms of the holding time. As expected, hardness decreases at higher holding time, because greater portion of austenitic phase is transformed into ductile phase. Figure 5.21a shows hardness measurement on the ductile part, after the classical TemperBox® approach (blue curve) and the new technique (orange curve).

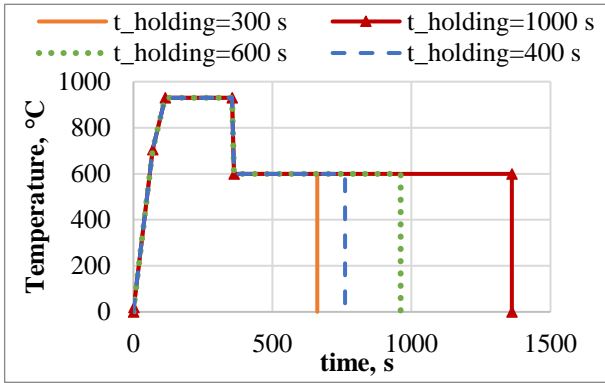


Fig.5.19: thermal cycles imposed on Gleeble system to investigate the proposed tailored approach

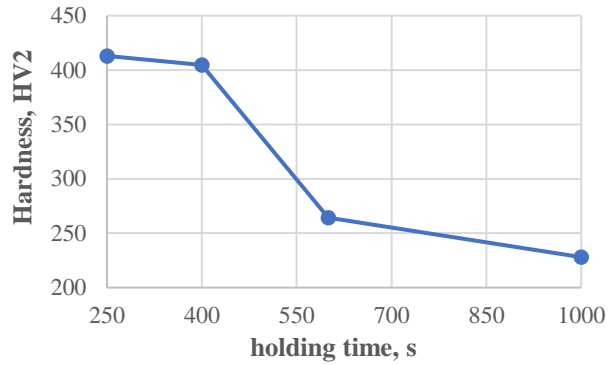


Fig. 5.20: Hardness value for different holding time values after physical simulation test of tailored Press-Hardening process proposed

Interestingly, the new approach leads to a greater softening, especially at high holding time. In the new approach, keeping a constant temperature for a certain t_{holding} leads to a thermal cycle that is similar to isothermal treatments. Therefore, lower hardness is justified considering that the transformation fields in an isothermal treatment are shifted to lower times [79].

Notice that, in order to compare the two approaches, the holding time t_{holding} of the new approach is confused with $t_{\text{temperbox}}$ of the classical approach. In fact, Figure 5.21b shows that a negligible difference occurs between t_{holding} and $t_{\text{temperbox}}$.

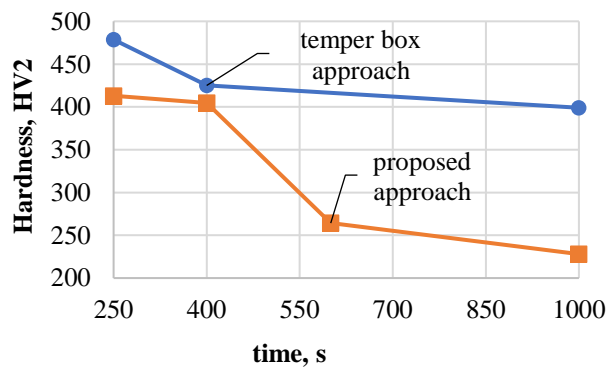


Fig. 5.21a: Hardness comparison between temper box and new proposed approach

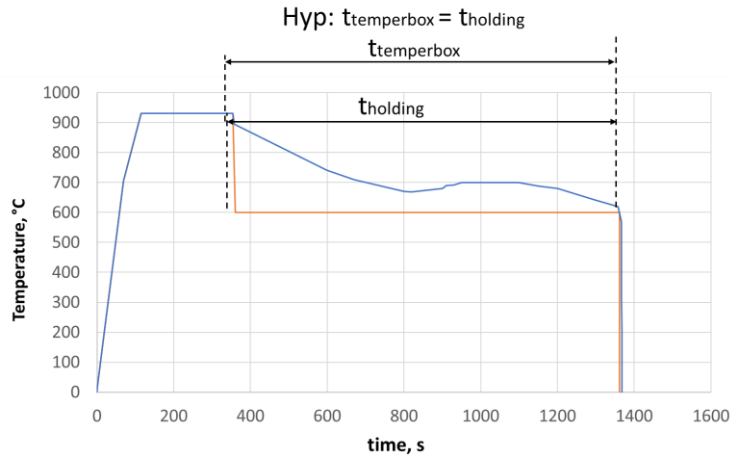


Fig. 5.21b: Comparison between the thermal cycle of the temper box approach and that of the new proposed approach

Finally, it was interesting to verify that this proposed approach also allows to avoid the softening of the steel in the resistant part, by reproducing with Gleeble physical simulator the cycle similar to that shown in Figure 5.18 with the dashed line in orange. In fact, hardness tests performed after physical simulation tests show that this imposed thermal cycle leads to a mean hardness value of 620 HV2.

5.3. Process map

As seen so far, process parameters are crucial for the Press-Hardening process, because they affect the final microstructure and mechanical properties of the component. For this reason, it is necessary to design the process correctly so that the desired mechanical properties can be achieved. To support the design, several researchers have developed Finite Element (FE) models that allow to estimate the mechanical properties of the component at the end of the process. Abdollahpoor et al. [80] developed a thermal-mechanical-metallurgical model to investigate microstructure sensitivity and hardness for different input parameters such as tool temperature, punch speed, contact pressure, friction coefficient, tool conductivity. George et al. [81] developed a FE code in LS-DYNA to predict hardness on a B-Pillar component as a function of tool temperature. Moreover, Cui et al. [82] developed a numerical model for hot stamping process to study the effect of the number of process cycles and holding time on the microstructure. Akerstrom and Oldenburg [83] used a model based on Kirkaldy's equations to predict the austenite decomposition into perlite, ferrite, bainite and martensite. This model was implemented in the FE software LS-DYNA to evaluate hardness and microstructure at the end of the process. Later, Zhang et al. [84] established a theoretical model for phase transformation of USIBOR[®]1500 based on Kirkaldy-Venugopalan model. They exploited the theoretical model to estimate the martensite fraction on the formed part at the end of Press-Hardening process, which was numerically simulated in DYNAFORM. Kim et al. [85] used FE simulation coupled with quench factor analysis to determine the process window adopted to predict hardness for different quenching time and tool temperature. In general, current scientific research aims at improving the prediction of mechanical properties by combining numerical simulations with experimental investigations. For this purpose, in this thesis, numerical simulation is combined with physical simulation, by reproducing at the laboratory scale thermo-mechanical Press-Hardening cycles.

The results of hardness and tensile tests after physical simulation tests typical of ductile region of the investigated component manufactured by Press-Hardening process with tailored tool tempering approach were elaborated to obtain a process window for estimating the mechanical properties. Some of the results of the tensile and hardness tests have already been shown in section 5.2.1. In this section, instead, all the results of the hardness and tensile tests for each temperature of heated tool (430 °C - 500 °C) and quenching time (20 s - 250 s) were elaborated to derive, by means of an artificial neural network, a process window. A two-layer feed-forward neural network with sigmoid hidden neurons and linear output neurons was considered. Figure 5.22 shows a schematic diagram of neural network. In particular, for this case study, the ANN model is characterized by two input parameters that are quenching time and temperature of heated tool, and three output parameters that are hardness (Hardness), ultimate tensile strength (Tensile strength) and elongation (Rupture deformability). The number of neurons in the input and output layer is equal to the number of input and output parameters, respectively. Finally, a single neuron is chosen for hidden layers. If too many neurons in the hidden layers are chosen, overfitting problem can occurs.

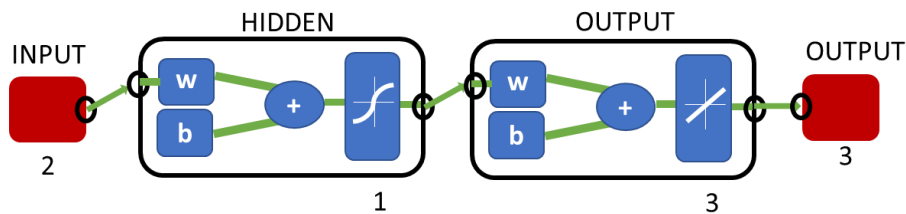


Fig. 5.22: Diagram of neural network

A random initial distribution of weights was implemented. The available data set was divided into three parts: training, validation and testing data. The ANN model was trained using 80 % of the total data randomly selected, while the remaining data 10 % was used for validation and the other 10 % for testing. The training set was used to teach the network. Training continues as long as the network continues improving on the validation set. The test set provides a completely independent measure of network accuracy.

After being trained, the ANN model can map the relationship between quenching parameters and mechanical properties of the B-Pillar soft zones. It can then be used as process window to predict mechanical properties for combinations of process parameters not yet investigated or to choose quenching parameters to achieve certain desired mechanical properties. To verify the reliability of neural network results, new combinations of process parameter were then used to realize FE simulations that allow to obtain new thermo-mechanical cycle to physically simulate by means of Gleeble system. Finally, experimental results of hardness and tensile tests were compared with neural network prediction.

Figures 5.23a, 5.23b and 5.23c show, respectively, the process window to predict hardness, tensile strength and elongation of low strength region for investigated quenching parameters. It has been found that the hardness decreases as the quenching time increases. Moreover, for low values of the quenching time, the hardness decreases as the temperature of the heated tools increases. The trend of tensile strength follows the hardness one. In particular, the ratio between tensile strength and hardness is on average 2.6 (Figure 5.23b). On the contrary, the elongation decreases with the reduction of the quenching time and the temperature of the heated tools (Figure 5.23c).

These results are justified by a generation of bainite microstructure with the increase of tool temperature and quenching time. In fact the bainite microstructure is characterized by greater

toughness and ductility compared to martensite one, formed for low quenching time and tool temperature.

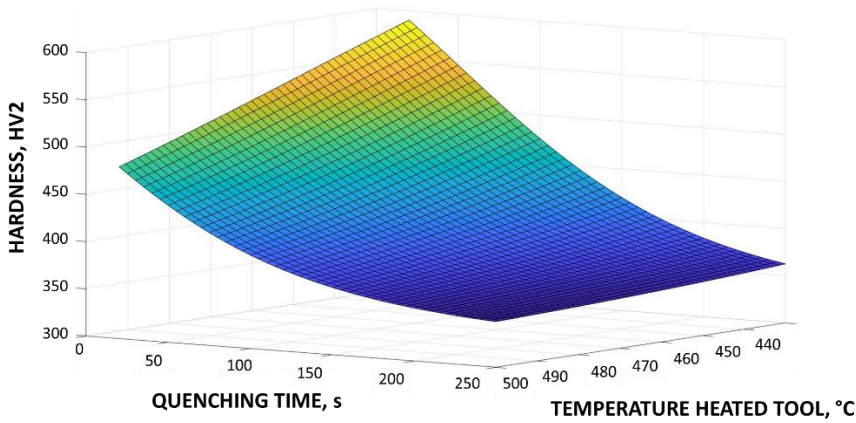


Fig. 5.23a: Process window to predict hardness of low strength region as a function of heated tool temperature and quenching time

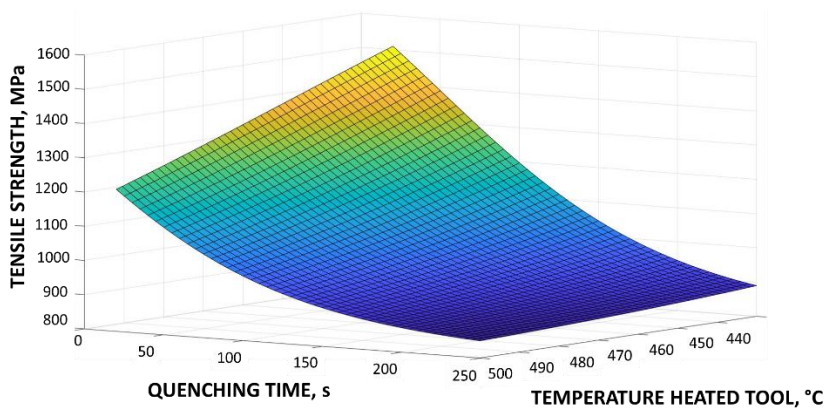


Fig. 5.23b: Process window to predict tensile strength of low strength region as a function of heated tool temperature and quenching time

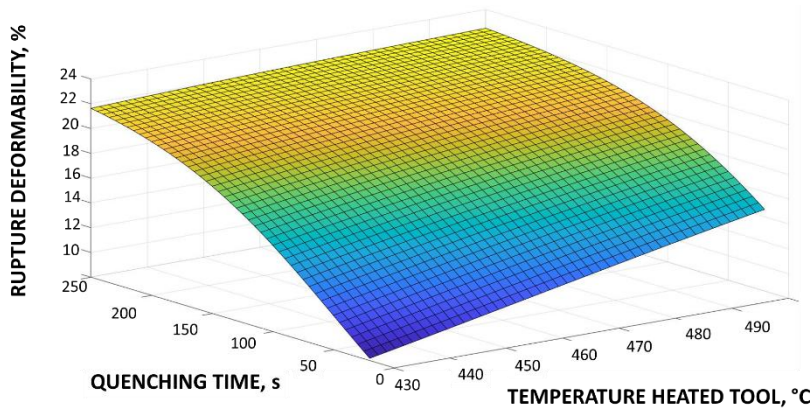


Fig. 5.23c: Process window to predict rupture deformability of low strength region as a function of heated tool temperature and quenching time

For quenching times between 150 s and 250 s, all three process maps show a plateau. Within this plateau, the maximum rupture deformability (between 20% and 24%), the lowest tensile strength (between 800 MPa and 900 MPa) and the minimum hardness (between 300 HV2 and 350 HV2) are obtained. On the other hand, in correspondence with lowest quenching time (20 s) and lowest heated tools temperature (430 °C), a hardness slightly higher than 600 HV2, a tensile strength between 1500-1600 MPa and a rupture deformability less than 10 % are recorded. These values are typical of a fully martensitic microstructure.

A measurement of how well neural network has fit the data is the regression analysis and the error histogram. Figure 5.24a shows the regression plot, instead, Figure 5.24b shows the error histogram. For a perfect fit, the data should fall along a 45 degree line, where the network outputs are equal to the responses. For this problem, as it is possible to see in Figure 5.24a, the fit is good with a R-value equal to 0.99851. The error histogram in Figure 5.24b shows how the error sizes are distributed. The blue bars represent training data, the green bars represent validation data, and the red bars represent testing data. It is possible to observe that most errors are near zero, with very few errors far from that.

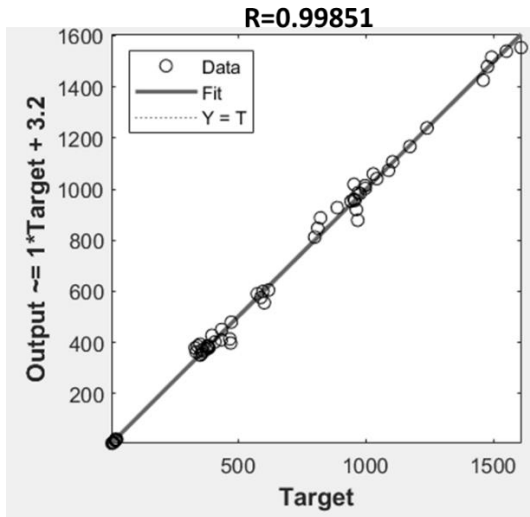


Fig. 5.24a: Regression plot that shows the neural network predictions (output) with respect to responses (target)

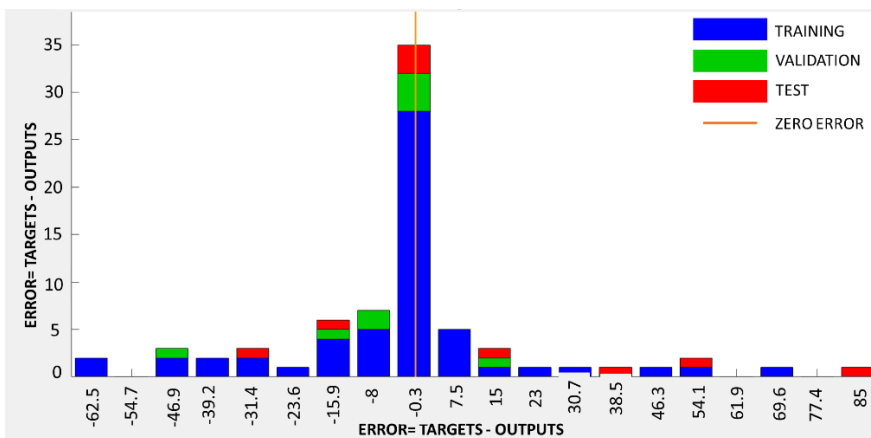


Fig. 5.24b: Error histogram for additional verification of neural network performance

Effectiveness of process window for mechanical properties prediction was verified. In particular, new values for quenching time and tool temperature, within the investigated range, are chosen and imposed for FE-simulations, by adopting the FE model described in section 4 for USIBOR[®]2000. Once new thermo-mechanical cycles were obtained, physical simulation tests were carried out. Finally, experimental results of hardness and tensile tests were compared with neural network prediction.

Table 5.1: Comparison between experimental and ANN model results

	Experimental results	ANN model results	Error, %
Hardness (HV2)	492	450	8.5
Tensile strength (MPa)	1281	11140	11

Rupture deformability (%)	15	16.7	11.3
---------------------------	----	------	------

Table 5.1 shows, for example, a comparison between the experimental results and the results estimated from the neural network model for a heated tool temperature of 500 °C and a quenching temperature of 50 s. From Table 5.1 it is observed that the maximum percentage errors are obtained for the results of the tensile strength and rupture deformability, however these values are within the experimental scatter. Therefore, the ANN model is reliable.

Conclusion

The Press-Hardening process is a thermal-mechanical-metallurgical process that involves different process parameter, especially if tailored technologies are adopted. Knowing as the process parameters affect the mechanical properties and the quality of the stamped part is of crucial importance in industrial production. The design of industrial production line aims at guaranteeing desirable properties of components, avoiding material and time wastes. To this end, Finite Element (FE) simulations are usually adopted to carry out a sensitivity analysis of Press-Hardening process. However, numerical predictions should be always validated by experimental investigations that, on the other hand, may be expensive. In fact, classical post-forming experiments are performed at the end of the production line on samples obtained from the final component.

In this dissertation, an efficient strategy that combine experimental and numerical investigations has been presented. Experimental physical simulation has been combined with FE models to design the Press-Hardening process on components with tailored properties, i.e. with distinct zones exhibiting high ductility or strength.

The investigated tailored technologies were the *Tailored Tool Tempering* and *TemperBox®* approaches. The automotive component that has been taken as a case study is the B-Pillar, for which ductile areas are required to improve crashworthiness and areas with high mechanical strength are necessary for good intrusion resistance. Two advanced high strength steels with different hardenability has been compared in the applications of tailored Press-Hardening processes. The two steels are the highly utilized USIBOR®1500 and the new generation one, namely USIBOR®2000.

The physical simulator exploited in the present study was the Gleeble 3180 system, which allows to reproduce at the lab scale thermo-mechanical cycles typical of Press Hardening process. In quenching phase of classical Press Hardening process, the cooling rate may increase up to 100 K/s. In order to reach high cooling rates in the Gleeble system, a preliminary design of the USIBOR specimens geometry has been necessary. In this work, the specimen geometry was identified by optimizing the length and width of the central section (shaped zone) of the specimen. To this end, a FE thermo-electric model has been developed in COMSOL Multiphysics. FE results show that reductions in the width and length of the shaped zone lead to an increase in cooling rate up to 30 K/s; however, an increase in the thermal gradient is also observed. Although high cooling rates are desirable, an increase in the thermal gradient leads to non-uniform temperature at the center of the specimen. Moreover, it was verified that an increase in the specimen thickness leads to a reduction in the cooling rate, as the mass involved is greater and the heat is dissipated more slowly. On the other hand, an increase in thickness leads to negligible increase in the thermal gradient.

For a sample with 2 mm thickness, the chosen geometry presents a length of 25 mm and a width of 10 mm of the shaped zone. With this geometry, a cooling rate of 25 K/s and a thermal gradient of 4 K on 5 mm width are guaranteed in the Gleeble system. Such parameters are feasible to perform mechanical characterization of USIBOR, as a low cooling rate allows to remain in austenitic field, while low thermal gradient leads to quasi-uniform temperature.

However, a cooling rate of 25 K/s is lower than typical values of Press-Hardening process; therefore, the forced air system of the Gleeble simulator was adopted to enhance the cooling rate and perform physical simulation tests. The effects due to the forced air system combined with the chosen geometry of the specimen allowed to reach cooling rate of about 100 K/s.

The mechanical characterization of USIBOR 2000 was performed by measuring the flow curves at different temperatures and strain rates, typical of Press-Hardening process. Results showed that an increase of temperature (decrease of strain rates) determines a decrease of the steel strength, as well as an increase of the steel elongation. Arrhenius constitutive equation was applied to describe the relationship between the obtained flow behaviors and the material coefficients for the investigated steel. A fifth order polynomial function was used to describe the effect of the strain on the material coefficients. Then, the flow stress-strain curves predicted by the established constitutive model were compared with those obtained from experimental tests. A statistical analyses showed a good agreement between numerical prediction and experimental measurement of the stress. Finally, flow behavior of USIBOR®1500 steel was compared with that of USIBOR®2000; the latter achieves higher activation energy values than the former, showing higher deformation resistance at high temperature. USIBOR®2000 is a new advanced high strength steel and, as a result, its material data are not available in the literature. Therefore, experimental results were exploited to implement the flow curves of USIBOR®2000 into FE models of Press Hardening process.

First, *Tailored Tool Tempering* approach has been investigated by means of numerical and physical simulations. This tailored technology involves that the component is formed within a die presenting heated sections in correspondence of the ductile part (see section 1.2).

Numerical simulations were carried out by means of AutoForm FE software. FE model allowed to evaluate the influence of *process parameters* (quenching time, transport time and temperature of the heated tools) and *design parameter* (air gap between cold and hot tools) on mechanical properties of the component. Results for USIBOR®1500 showed that, in the resistant part, the mechanical properties are almost the same for all the investigated values of the process parameters. On the other hand, in the ductile part, mechanical properties are strongly affected by process parameters. In particular, greater quenching time, transport time and temperature of heated tools lead to a greater ductility, which is due to the greater portion of bainitic microstructure of the component. Specifically, the formation of homogeneous bainitic microstructure is mainly affected by the temperature of heated tools. When the latter ranges between 440 °C and 460 °C a completely bainitic microstructure is always guaranteed in the ductile regions, independently of the values of other process parameters.

The design parameter, i.e. the width of air gap between cooled and heated tools, greatly affects the width and the position of the transition zone, namely the area between the hard and ductile parts. If the air gap increases, a lower heat flow is expected and, as a result, the transition zone is closer to the heated tool and its width reduces.

FE model allowed to track thermo-mechanical cycles of the component during the simulation of Press-Hardening process. Specifically, the temperature and equivalent plastic strain of the ductile part were obtained as a function of time, and for different process parameters, i.e. temperature of heated tools and quenching time. In a second phase of the study, thermo-mechanical cycles were experimentally reproduced on USIBOR®1500 and USIBOR®2000 specimens. Physical simulations were performed by means of Gleeble 3180 system and classical tensile and hardness tests were carried out to compare mechanical properties of the two Advanced High Strength Steels (AHSS).

For both materials, an increase in the quenching time leads to a reduction in the hardness, as complete bainitic transformation occurs. The latter is expected at quenching time of about 20 s and 150 s for

USIBOR®1500 and USIBOR®2000, respectively. Such difference is justified by greater carbon content (and greater hardenability) in USIBOR®2000. Short quenching times are feasible for industrial applications. For a complete bainitic microstructure, USIBOR®2000 presents higher hardness than USIBOR®1500, while softening of the ductile part is almost the same (50% for USIBOR®1500 and 55-60 % for the USIBOR®2000).

Tensile tests confirmed that USIBOR®2000 presents higher mechanical strength, which is due to its greater carbon percentage with respect to USIBOR®1500. In previous studies on USIBOR®1500, the elongation at break of the resistant part was found to be about 5%. In this work, we measured an elongation at break of the ductile part of about 30-40% for USIBOR®1500 and greater than 20 % for USIBOR®2000, showing that i) tailored properties can be obtained with Tailored Tool Tempering approach, ii) USIBOR®1500 exhibits greater ductility than USIBOR®2000.

Physical simulation on USIBOR®2000 steel specimens showed that softening of B-Pillar areas with short quenching times, could be obtained by differentiating the blank heating temperature (following a Tailored Blank Heating approach). For example, heating up to 750 °C and assuming a tool temperature of 80 °C and a quenching time of 20 s, experimental results showed a ductile zone and an elongation of about 250 HV and 20 %, respectively.

The second tailored technology that was investigated is the *TemperBox*® approach, which has been recently developed in the framework of Tailored Blank heating technology. Again, physical and numerical simulations have been exploited. As discussed in section 1.2, in the *TemperBox*® process, soft zones of the component are obtained through convective cooling below the temperature A_{c3} in the second oven.

AutoForm FE software was exploited to perform numerical simulations aimed at evaluating the influence of *process parameters* ($T_{\text{temperbox}}$ and $t_{\text{temperbox}}$) on the mechanical properties of the component. For USIBOR®1500, results showed that greater ductility in the soft part is achieved when increasing $t_{\text{temperbox}}$ (lower cooling rate) and decreasing $T_{\text{temperbox}}$. For the investigated process parameters, the softening of the ductile part falls in the range 25%-66%, approximately.

In a second phase, FE thermal cycles were extracted and reproduced by means of physical simulator on samples in USIBOR®2000. Subsequently, hardness tests were performed.

Hardness measurements on the ductile part confirmed that an increase in $T_{\text{temperbox}}$ and $t_{\text{temperbox}}$ leads to greater ductility, in agreement with numerical predictions. On the other hand, measurements on the resistant part showed a clear reduction in the hardness with increasing $t_{\text{temperbox}}$. In fact, long $t_{\text{temperbox}}$ leads to an increase in the total time the blank remains at high temperature (930 °C). In such conditions, growth of microstructure grains may occur, causing undesired hardness reduction. To overcome this problem, one could decrease the total time the blank remains at high temperature. To this end, physical simulations were performed at greater $t_{\text{transport1}}$, which is the transport time of the blank from the first to the second oven. Anyway, no significant variation of hardness was measured respect to lower value of $t_{\text{transport1}}$. These results suggested that high $t_{\text{temperbox}}$ should be avoided in the *TemperBox*® process. However, short $t_{\text{temperbox}}$ leads to softening of the ductile part of about 20%, while greater values could be required for automotive components. To increase softening, a new technique was investigated for manufacturing components in USIBOR®2000 with tailored properties. The proposed approach predicts, for the ductile part, a thermal treatment similar to an isothermal one.

Interestingly, the new approach leads to a greater softening (from 30% to 60%) with respect to the classical *TemperBox*[®] approach.

Modern industry 4.0 aims at developing systems with online-control technologies that act on process parameters. In the final part of the dissertation, a process window was developed by training an artificial neural network (ANN) with the experimental data obtained from physical simulation. In particular, data referred to the ductile region of the B-Pillar manufactured by means of tailored tool tempering approach. Predictions of ANN algorithm were found in good agreement with experimental data, showing the potentiality of such fascinating approach.

This dissertation showed that physical simulation is a valid tool for experimental verification of numerical predictions, which can be affected by limitations and assumptions of theoretical models. The combination of physical and numerical simulations has proved to be an efficient methodology for designing the Press-Hardening process, as it was possible to predict the mechanical properties of the component without material waste. In fact, differently from classical post-forming experiments, tests were performed on small samples at the lab scale. Moreover, it was shown that the use of modern artificial intelligence algorithms (such as ANN) can help in increasing efficiency and quality of production. As a result, this work can be of great interest for automotive industry. Moreover, the study of mechanical properties of innovative materials, such as the recent USIBOR[®]2000, is a topic of crucial importance also in the academic field.

References

- [1] Lechler, Jürgen, Marion Merklein, and Manfred Geiger. "Determination of thermal and mechanical material properties of ultra-high strength steels for hot stamping." *steel research international* 79.2 (2008): 98-104.].
- [2] Karbasian, Hossein, and A. Erman Tekkaya. "A review on hot stamping." *Journal of Materials Processing Technology* 210.15 (2010): 2103-2118.
- [3] Behrens, B. A., S. Hübner, and M. Demir. "Conductive heating system for hot sheet metal forming." *Proceedings of 1st International Conference on Hot Sheet Metal Forming of High-Performance Steel*. 2008.
- [4] Steinbeiss, Heinz, et al. "Method for optimizing the cooling design of hot stamping tools." *Production Engineering* 1.2 (2007): 149-155.
- [5] Hoffmann, H., H. So, and HI Steinbeiss. "Design of hot stamping tools with cooling system." *CIRP annals* 56.1 (2007): 269-272.
- [6] Chen, Jieshi, et al. "Optimization of hot stamping cooling system using segmented model." *The International Journal of Advanced Manufacturing Technology* 93.1 (2017): 1357-1365.
- [7] Shan, Zhong-de, et al. "Hot-stamping die-cooling system for vehicle door beams." *International Journal of Precision Engineering and Manufacturing* 14.7 (2013): 1251-1255.
- [8] Lim, Woo-Seung, et al. "Cooling channel design of hot stamping tools for uniform high-strength components in hot stamping process." *The International Journal of Advanced Manufacturing Technology* 70.5-8 (2014): 1189-1203.
- [9] Lv, Mengmeng, et al. "Optimal design for cooling system of hot stamping dies." *ISIJ International* (2016): ISIJINT-2016.
- [10] Shan, Zhong-de, et al. "Hot-stamping die-cooling system for vehicle door beams." *International Journal of Precision Engineering and Manufacturing* 14.7 (2013): 1251-1255.
- [11] Lin, Tao, et al. "Cooling systems design in hot stamping tools by a thermal-fluid-mechanical coupled approach." *Advances in Mechanical Engineering* 6 (2014): 545727.
- [12] Hung, Tzu-Hao, et al. "Performance of die cooling system design in hot stamping process." *Journal of the Chinese Institute of Engineers* 42.6 (2019): 479-487.
- [13] Cortina, Magdalena, et al. "Case study to illustrate the potential of conformal cooling channels for hot stamping dies manufactured using hybrid process of laser metal deposition (LMD) and milling." *Metals* 8.2 (2018): 102.
- [14] Muvunzi, Rumbidzai, et al. "A case study on the design of a hot stamping tool with conformal cooling channels." *The International Journal of Advanced Manufacturing Technology* 114.5 (2021): 1833-1846.
- [15] Valls, I., A. Hamasaiid, and A. Padré. "New approaches to thermal tool performance, cooling and machining strategy: the strongly correlated triple that determines the cost effectiveness of the process." *IOP Conference Series: Materials Science and Engineering*. Vol. 418. No. 1. IOP Publishing, 2018.
- [16] Taylor, T. and, and A. Clough. "Critical review of automotive hot-stamped sheet steel from an industrial perspective." *Materials Science and Technology* 34.7 (2018): 809-861.

- [17] Munera, Daniel Duque, et al. "Innovative press hardened steel based laser welded blanks solutions for weight savings and crash safety improvements." *SAE International Journal of Materials and Manufacturing* 1.1 (2009): 472-479.
- [18] Lei, Chengxi, et al. "Hot stamping of patchwork blanks: modelling and experimental investigation." *The International Journal of Advanced Manufacturing Technology* 92.5 (2017): 2609-2617.
- [19] M. Merklein et al. , 2016 "Hot stamping of boron steel sheets with tailored properties: A review". *Journal of Materials Processing Technology* 228, 11–24.
- [20] Mu, Yanhong, et al. "Numerical simulation of hot stamping by partition heating based on advanced constitutive modelling of 22MnB5 behaviour." *Finite Elements in Analysis and Design* 147 (2018): 34-44.
- [21] Mori, K-I., T. Maeno, and K. Mongkolkaji. "Tailored die quenching of steel parts having strength distribution using bypass resistance heating in hot stamping." *Journal of Materials Processing Technology* 213.3 (2013): 508-514.
- [22] Available on <https://aptgroup.com/company/news/apt-launching-temperbox%C2%AE-new-cycle-time-neutral-production-solution-enables-tailored>
- [23] Mori, K-I., T. Maeno, and K. Mongkolkaji. "Tailored die quenching of steel parts having strength distribution using bypass resistance heating in hot stamping." *Journal of Materials Processing Technology* 213.3 (2013): 508-514.
- [24] Palmieri, Maria Emanuela, Vincenzo Domenico Lorusso, and Luigi Tricarico. "Investigation of material properties of tailored press hardening parts using numerical and physical simulation." *Procedia Manufacturing* 50 (2020): 104-109.
- [25] Tang, B. T., et al. "Influence of temperature and deformation on phase transformation and Vickers hardness in tailored tempering process: numerical and experimental verifications." *Journal of Manufacturing Science and Engineering* 136.5 (2014).
- [26] Totten, George E. *Steel Heat Treatment Handbook-2 Volume Set*. CRC press, 2006.
- [27] S. Graff, T. Gerber, F.J. Lenze, S. Sikora, About the simulation of microstructure evolution in hot sheet stamping process and the correlation of resulting mechanical properties and crash performance, in 3rd International Conference on Hot Sheet Metal Forming of High Performance Steel, CHS2, Kassel, Germany (2011), pp. 323–330
- [28] ArcelorMittal Flat Carbon Europe S.A. *ArcelorMittal Automotive Product Offer Europe*, Android App, V1.0 (2015)
- [29] Mohrbacher, Hardy. "Martensitic automotive steel sheet-Fundamentals and metallurgical optimization strategies." *Advanced Materials Research*. Vol. 1063. Trans Tech Publications Ltd, 2015.
- [30] W. D. Callister, Jr, *Materials science and engineering-an introduction*, New York: John Wiley & Sons, Inc, 2007.
- [31] Reed-Hill, Robert E., Reza Abbaschian, and Reza Abbaschian. *Physical metallurgy principles*. Vol. 17. New York: Van Nostrand, 1973.

- [32] Taylor, Tom, and John McCulloch. "Effect of Part/Die Boundary Conditions on Microstructural Evolution during Hot Stamping 2000 MPa Class Boron Steel." *steel research international* 89.6 (2018): 1700495.
- [33] Naderi, Malek, and Wolfgang Bleck. Hot stamping of ultra high strength steels. No. RWTH-CONV-112497. Lehrstuhl und Institut für Eisenhüttenkunde, 2008.
- [34] Available on Manual AutoForm R10
- [35] Liapis, S. "A review of error estimation and adaptivity in the boundary element method." *Engineering analysis with boundary elements* 14.4 (1994): 315-323.
- [36] Wang, Q. F., Shang, C. J., Fu, R. D., Wang, Y. N., & Chen, W. (2005). Physical simulation and metallurgical evaluation of heat-affected zone during laser welding of ultrafine grain steel. In *Materials Science Forum* (Vol. 475, pp. 2717-2720). Trans Tech Publications.
- [37] Pasquale Guglielmi, Vincenzo Domenico Lorusso, Maria Emanuela Palmieri, Luigi Tricarico. Physical Simulation of Laser-Induced Softening of a High Strength Aluminum Alloy Sheet. XIV Convegno dell'Associazione Italiana Tecnologie Manifatturiere AITEM 2019.
- [38] Palmieri, Maria Emanuela, Vincenzo Domenico Lorusso, and Luigi Tricarico. "Laser-induced softening analysis of a hardened aluminum alloy by physical simulation." *The International Journal of Advanced Manufacturing Technology* 111.5 (2020): 1503-1515.
- [39] Javaheri E, Lubritz J, Graf B, et al. Mechanical properties characterization of welded automotive steels. *Metals*. 2020; 10(1): 1.
- [40] Zhang ZL, Hauge M, Thaulow C, et al. A notched cross weld tensile testing method for determining true stress–strain curves for weldments. *Eng fracture mechanics*. 2002; 69(3): 353-366.
- [41] DACE - A MATLAB Kriging Toolbox-Version 2.0, August 1, 2002. Søren N. Lophaven, Hans Bruun Nielsen, Jacob Søndergaard
- [42] Simpson, Timothy W., et al. "Metamodels for computer-based engineering design: survey and recommendations." *Engineering with computers* 17.2 (2001): 129-150.
- [43] Sacks, Jerome, et al. "Design and analysis of computer experiments." *Statistical science* 4.4 (1989): 409-423.
- [44] Dang, Van-Tuan, Carl Labergere, and Pascal Lafon. "Adaptive metamodel-assisted shape optimization for springback in metal forming processes." *International Journal of Material Forming* 12.4 (2019): 535-552.
- [45] Available on <https://www.mathworks.com/discovery/neural-network.html>
- [46] Available on <https://www.mathworks.com/help/deeplearning/ug/shallow-neural-networks-bibliography.html>
- [47] Available on <https://www.mathworks.com/help/deeplearning/ref/trainlm.html>
- [48] Merklein, Marion, Matthias Graser, and Michael Lechner. "Experimental investigation of heat-treated aluminum profiles." *Key Engineering Materials*. Vol. 651. Trans Tech Publications Ltd, 2015.
- [49] Merklein, Marion, et al. "Tailored Heat Treated Profiles-Enhancement of the forming limit of aluminum profiles under bending load." *Key Engineering Materials*. Vol. 504. Trans Tech Publications Ltd, 2012.
- [50] Geiger, Manfred, Marion Merklein, and Uwe Vogt. "Aluminum tailored heat treated blanks." *Production Engineering* 3.4-5 (2009): 401.

- [51] Zhou, Jing, et al. "Effect of hot stamping parameters on the mechanical properties and microstructure of cold-rolled 22MnB5 steel strips." *International Journal of Minerals, Metallurgy, and Materials* 21.6 (2014): 544-555.
- [52] Estrin, Yu, and H. Mecking. "A unified phenomenological description of work hardening and creep based on one-parameter models." *Acta metallurgica* 32.1 (1984): 57-70.
- [53] Li, Muyu, et al. "Constitutive model and flow behavior of B1500HS high-strength steel during the hot deformation process." *Metals* 10.1 (2020): 64.
- [54] Ghosh, Sumit, et al. "Hot Deformation Characteristic and Strain Dependent Constitutive Flow Stress Modelling of Ti+ Nb Stabilized Interstitial Free Steel." *Metals and Materials International* 27.8 (2021): 2481-2498.
- [55] Zener, Clarence, and John Herbert Hollomon. "Effect of strain rate upon plastic flow of steel." *Journal of Applied physics* 15.1 (1944): 22-32.
- [56] Fei, Wei-Jie, et al. "Flow behaviors of 22MnB5 steel at a high temperature." *Materials Research Express* 6.7 (2019): 076527.
- [57] Montazeri-Pour, Mehdi, and Mohammad Habibi Parsa. "Constitutive analysis of tensile deformation behavior for AA1100 aluminum subjected to multi-axial incremental forging and shearing." *Mechanics of Materials* 94 (2016): 117-131.
- [58] Rakhshkhorshid, M., and S. H. Hashemi. "Experimental study of hot deformation behavior in API X65 steel." *Materials Science and Engineering: A* 573 (2013): 37-44.
- [59] Xu, Yakun, et al. "Investigation of constitutive relationship and dynamic recrystallization behavior of 22MnB5 during hot deformation." *Results in Physics* 14 (2019): 102426.
- [60] Estrin, Yu, and H. Mecking. "A unified phenomenological description of work hardening and creep based on one-parameter models." *Acta metallurgica* 32.1 (1984): 57-70.
- [61] Jonas, John J., et al. "The Avrami kinetics of dynamic recrystallization." *Acta materialia* 57.9 (2009): 2748-2756.
- [62] Wang, Lei, et al. "Prediction of flow stress for N08028 alloy under hot working conditions." *Materials & Design* 47 (2013): 737-745.
- [63] George, R., A. Bardelcik, and M. J. Worswick. "Hot forming of boron steels using heated and cooled tooling for tailored properties." *Journal of Materials Processing Technology* 212.11 (2012): 2386-2399.
- [64] Wang, Zi Jian, et al. "Hot stamping of two different high strength steel with tailored properties." *Applied Mechanics and Materials*. Vol. 395. Trans Tech Publications Ltd, 2013.
- [65] Bardelcik, Alexander, Ryan George, and Michael J. Worswick. *Transition Zone Tensile Properties within a Tailored Hot Stamping*. No. 2012-01-0531. SAE Technical Paper, 2012.
- [66] Shan, Zhong-de, et al. "Hot-stamping die-cooling system for vehicle door beams." *International Journal of Precision Engineering and Manufacturing* 14.7 (2013): 1251-1255.
- [67] Lin, Tao, et al. "Cooling systems design in hot stamping tools by a thermal-fluid-mechanical coupled approach." *Advances in Mechanical Engineering* 6 (2014): 545727.
- [68] Hung, Tzu-Hao, et al. "Performance of die cooling system design in hot stamping process." *Journal of the Chinese Institute of Engineers* 42.6 (2019): 479-487.

- [69] Cortina, Magdalena, et al. "Case study to illustrate the potential of conformal cooling channels for hot stamping dies manufactured using hybrid process of laser metal deposition (LMD) and milling." *Metals* 8.2 (2018): 102.
- [70] Muvunzi, Rumbidzai, et al. "A case study on the design of a hot stamping tool with conformal cooling channels." *The International Journal of Advanced Manufacturing Technology* 114.5 (2021): 1833-1846.
- [71] Valls, I., A. Hamasaid, and A. Padré. "New approaches to thermal tool performance, cooling and machining strategy: the strongly correlated triple that determines the cost effectiveness of the process." *IOP Conference Series: Materials Science and Engineering*. Vol. 418. No. 1. IOP Publishing, 2018.
- [72] Feng, Shaochuan, Amar M. Kamat, and Yutao Pei. "Design and fabrication of conformal cooling channels in molds: Review and progress updates." *International Journal of Heat and Mass Transfer* 171 (2021): 121082.
- [73] Lechler, Jürgen, Marion Merklein, and Manfred Geiger. "Determination of thermal and mechanical material properties of ultra-high strength steels for hot stamping." *steel research international* 79.2 (2008): 98-104.
- [74] Geiger, Manfred, Marion Merklein, and Cornelia Hoff. "Basic investigations on the hot stamping steel 22MnB5." *Advanced Materials Research*. Vol. 6. Trans Tech Publications Ltd, 2005.
- [75] Peister, C., et al. "Forming of an axially tailored automotive channel section through hot stamping of tailor-welded blanks." *Journal of Physics: Conference Series*. Vol. 896. No. 1. IOP Publishing, 2017.
- [76] Xu, Yaowen, et al. "effect of cooling path on microstructures and hardness of hot-stamped steel." *Metals* 10.12 (2020): 1692.
- [77] Naderi, M., et al. "Constitutive relationships for 22MnB5 boron steel deformed isothermally at high temperatures." *Materials Science and Engineering: A* 478.1-2 (2008): 130-139.
- [78] Palmieri, Maria Emanuela, Francesco Rocco Galetta, and Luigi Tricarico. "Study of Tailored Hot Stamping Process on Advanced High-Strength Steels." *Journal of Manufacturing and Materials Processing* 6.1 (2022): 11.
- [79] Zhao, Ji-Cheng, and Michael R. Notis. "Continuous cooling transformation kinetics versus isothermal transformation kinetics of steels: a phenomenological rationalization of experimental observations." *Materials Science and Engineering: R: Reports* 15.4-5 (1995): 135-207.
- [80] Abdollahpoor, Amir, et al. "Sensitivity of the final properties of tailored hot stamping components to the process and material parameters." *Journal of Materials Processing Technology* 228 (2016): 125-136.
- [81] George, R., A. Bardelcik, and M. J. Worswick. "Hot forming of boron steels using heated and cooled tooling for tailored properties." *Journal of Materials Processing Technology* 212.11 (2012): 2386-2399.
- [82] Cui, Junjia, et al. "Predictions of the mechanical properties and microstructure evolution of high strength steel in hot stamping." *Journal of materials engineering and performance* 21.11 (2012): 2244-2254.

- [83] Åkerström, Paul, and Mats Oldenburg. "Austenite decomposition during press hardening of a boron steel—Computer simulation and test." *Journal of Materials Processing Technology* 174.1-3 (2006): 399-406.
- [84] Zhang, Pengyun, et al. "Study on Phase Transformation in Hot Stamping Process of USIBOR® 1500 High-Strength Steel." *Metals* 9.10 (2019): 1119.
- [85] Kim, Jae-Hong, Seon-Bong Lee, and Byung-Min Kim. "Construction of process window to predict hardness in tailored tool thermomechanical treatment and its application." *Metals* 9.1 (2019): 50.